Ice and gas in protostellar clouds and planet-forming disks: a combined laboratory and observational study

Terwisscha van Scheltinga, J.

Citation

Terwisscha van Scheltinga, J. (2021, November 30). *Ice and gas in protostellar clouds and planet-forming disks: a combined laboratory and observational study*. Retrieved from https://hdl.handle.net/1887/3245869

Ice and Gas in Protostellar Clouds and Planet-forming Disks

- A Combined Laboratory and Observational Study -

Proefschrift

ter verkrijging van
de graad van doctor aan de Universiteit Leiden,
op gezag van rector magnificus prof. dr. ir. H. Bijl,
volgens besluit van het college voor promoties
te verdedigen op dinsdag 30 november 2021
klokke 13.45 uur
door

Jeroen Terwisscha van Scheltinga

geboren te Delft, Nederland
in 1990

Promotiecommissie

Promotores:	Prof. dr. H. V. J. Linnartz	
	Prof. dr. M. R. Hogerheijde	
Overige leden:	Prof. dr. H. J. A. Röttgering	
	Prof. dr. S. Viti	
	Prof. dr. E. A. Bergin	University of Michigan
	Dr. A. C. A. Boogert	University of Hawaii
	Dr. P. A. Gerakines	NASA Goddard Space Flight Center

ISBN: 978-94-6419-363-3

Cover:
Design and layout by author

Image credit:
Purple night sky by Kierancwhite on Unsplash
JWST adapted from NASA GSFC/CIL/Adriana Manrique Gutierrez

“Greed has poisoned men’s souls,
has barricaded the world with hate,
has goose-stepped us into misery and bloodshed.
We have developed speed, but we have shut ourselves in.
Machinery that gives abundance has left us in want.
Our knowledge has made us cynical.
Our cleverness, hard and unkind.
We think too much and feel too little.
More than machinery we need humanity.
More than cleverness we need kindness and gentleness.
Without these qualities, life will be violent and all will be lost...”

- *The Great Dictator*, Charlie Chaplin (1940)

CONTENTS

1 | Introduction

It is easy to forget in the rush of our daily lives that planet Earth is an extraordinary place. A small rocky planet at the right distance from our Sun that formed approximately 4.6 billion years ago, where everything aligned to eventually harbour us and every other living being. Throughout human existence, we have looked at the stars and wondered, are we alone? After the first confirmed detection of two exoplanets in 1992 by Wolszczan & Frail (1992), many others followed. As of writing, almost 5000 exoplanets have been discovered, and it is suggested that on average every star is accompanied by at least one planet. Although many of these planets may not harbour life as we know it, the population of stars and planets is unfathomable. It is rather unimaginable that there is no other place besides Earth in the vastness of the universe where physical and chemical evolution have also aligned to create life or will do so in the future.

In order for life, as we know it, to start on a planet certain organic building blocks have to be available. On Earth, organisms require different types of molecular structures to survive, thrive, and evolve. Be it an unicellular or multicellur organism, proteins, nucleic acids, carbohydrates, and lipids are a necessity. Each of these fulfill different functions, for instance, lipids are used to create cell membranes, and nucleic acids form DNA where genetic information is stored. This raises the question, were these building blocks of life formed on Earth, or are they formed in a universal way during star and planet formation filling the entire universe with the seeds of life?

In the last 100 years, our understanding of the physical and chemical processes that occur in the universe have greatly improved. It was once believed that under the harsh conditions in space, that is extremely low temperatures and strong radiation fields, no molecule could survive. However, the detection of CH by Swings & Rosenfeld (1937) and subsequent detections of many other molecules contradicted this, and showed that molecules can be formed and sustained in space. Today, over 240 different molecules have been detected (McGuire 2018). These molecules range from diatomics and small molecules, both stable and radicals, to fullerenes, such as C_{60} and C_{70}. A subgroup of these molecules are defined as complex organic molecules (COMs), where a COM is a molecule consisting of six or more atoms of which at least one is carbon and another is either nitrogen, oxygen, phosphorus, or sulfur. COMs are of particular interest as they are the smaller siblings of the previously mentioned building blocks of life. Whether and how these organic molecules are formed and incorporated in the different stages of star and planet formation is key in understanding the formation of life on Earth, and potentially in other planet-forming systems (see e.g., reviews by Herbst & van Dishoeck 2009; Öberg & Bergin 2021).

1.1 Star and planet formation

Our Solar system is a mature system in which no significant physical and chemical evolution takes place anymore, at least at Solar system size. However, at a “young” age, that is, below 10 million years, it went through different evolutionary stages in which conditions varied significantly. It started with a molecular cloud that initially contained only gas and small dust particles, and turned into the Sun and planets we know today. One way to look at the composition of the material available at these early stages, and if they contained COMs, is through comets. Comets are essentially large and dirty snowballs that are created from the same material and at the same time as planets, and contain large amounts of the most pristine material available in our Solar system.

On the 2nd of March 2004, the European Space Agency launched its *Rosetta* mission. Its goal was to intercept the comet 67P/Churyumov–Gerasimenko, henceforth 67P, and, among other science tasks, teach us about its molecular composition. As the comet approached perihelion, that is, the closest distance to the Sun, more and more of 67P’s icy surface layer started to sublimate. Once arrived at 67P, the ROSINA instrument on board the *Rosetta* spacecraft allowed for *in situ* measurements of the coma surrounding 67P created by this release of ice. Molecules, such as water (H_2O), oxygen (O_2), nitrogen (N_2), and methanol (CH_3OH) were readily detected, but most intriguing was the detection of glycine (NH_2CH_2COOH; Altwegg et al. 2016, 2019). The significance of this detection is high, as glycine is the simplest amino acid, and is part in the creation of protein molecules. This suggests that prebiotic molecules are already available in the very early stages of our Solar system, and may have played a role in the development of life on Earth.

Another way to investigate the presence of organic molecules is through astronomical observations of distant objects in our skies that are still in their early stages. The stellar evolution starts in molecular clouds, where as the name suggests the first generation of molecules are formed, such as hydrogen (H_2), carbon monoxide (CO), and water. In the diffuse interstellar medium (ISM) these molecules have a high chance to get dissociated or ionized due to the harsh radiation field, but in a dark molecular cloud the densities are high enough to shield these molecules from the harsh external radiation field. Moreover, in these clouds temperatures are approximately 10–20 K, which is important for the formation of these molecules as will be discussed later.

Molecular clouds are also known as stellar nurseries, because in the dense cores of these clouds star formation starts through gravitational collapse. In this process denser regions become even denser as more and more material is pulled in through its own gravitational interaction, and starless cores are formed. If enough material accretes onto a starless core, enough to eventually form a star, it is called a prestellar core. The angular momentum at large molecular cloud scales (several pc) is conveyed into the scales of prestellar cores (~ 10000 au). This angular momentum in combination with the gravitational pull results in the rotation of the material toward the gravitational center. The material at this center forms a point source, and in this process the release of gravitational energy heats the surrounding material. It is at this stage that we consider that a protostar has formed, which is known as a Class 0 object. The evolution between a prestellar core and planetary system is divided into four stages, that is, Class 0, Class I, Class II, and Class III (Shu et al. 1987). This classification is based on the appearance of the object in the infrared, which informs us on the

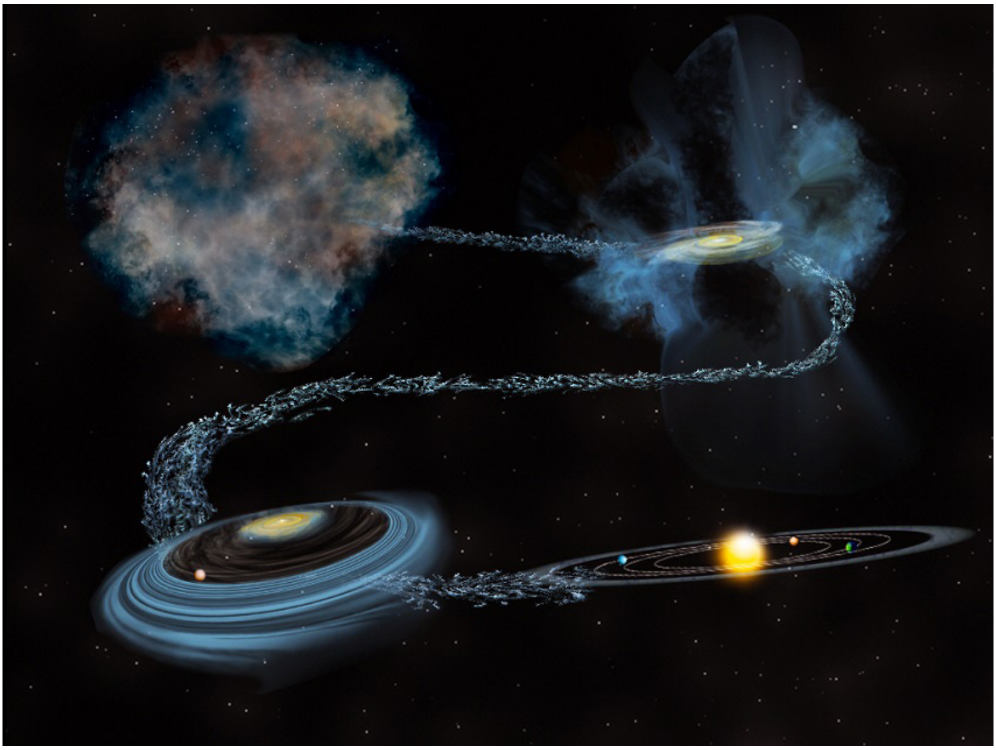

Figure 1.1: Artist impression of the evolution of stars and planets. It starts in a molecular cloud (top left), which through its own gravity collapses and starts forming protostars with envelopes (top right, only one is shown). The star enters the pre-main sequence once the majority of the envelope has accreted and only a disk is left, a so-called protoplanetary disk (bottom left). This protoplanetary disk eventually evolves into a planetary system (bottom right; Credit: Bill Saxton, NSF/AUI/NRAO).

protostar and the surrounding material. Figure 1.1 shows a visual representation of these different stages of star and planet formation.

The angular momentum of the infalling rotating material has to be preserved, and results in the formation of an embedded disk in the envelope. Another result of the preservation of angular momentum is the appearance of outflows and jets, perpendicular to the rotational plane, which partially opens the envelope (see e.g., review by Larson 2003). In the Class 0 stage, the majority of the mass is still in the envelope surrounding the protostar. However, as time progresses more of the envelope material accretes onto the protostar. Eventually, the envelope mass is significantly smaller than the mass of the protostar. The system is now classified as a Class I object. After this, the protostar starts contracting and turns into a pre-main-sequence star. The temperature of the star has increased significantly. However, it is not yet enough to start the fusion process of hydrogen in its core, but its radiation is strong enough to blow away the remainder of the envelope. With the envelope dissipated, a protoplanetary disk is left rotating around the pre-main-sequence star, classified as a Class II object. The dust in the protoplanetary disk keeps evolving into larger bodies, and the protoplanetary disk itself evolves into a debris disk, which is classified as a

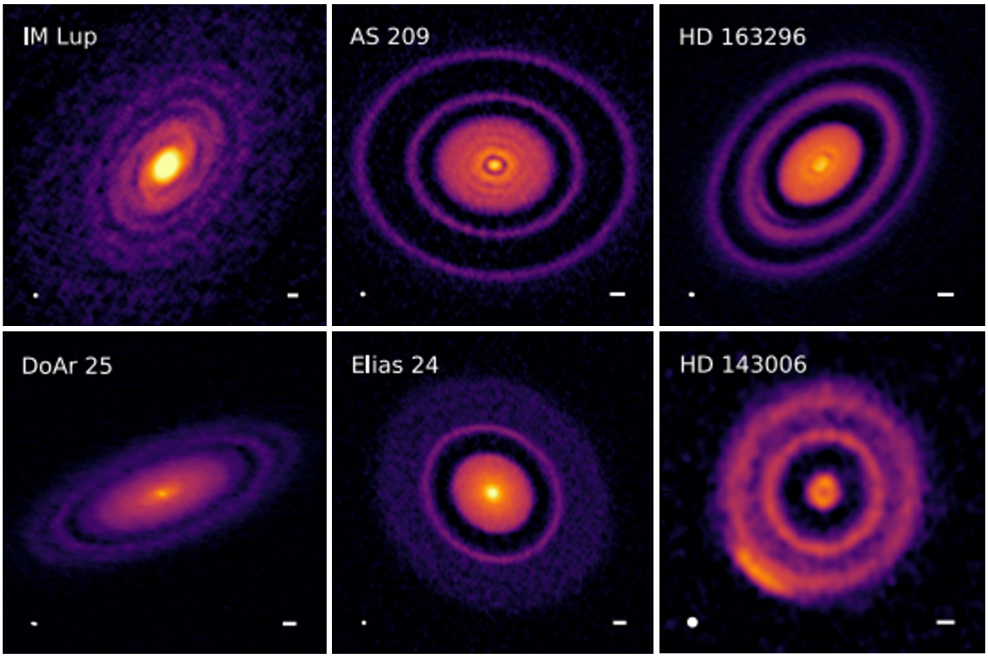

Figure 1.2: Six sources taken from the large ALMA program DSHARP observed at 240 GHz, that is, 1.25 millimeter-dust continuum emission. Beam sizes are shown in the bottom left and the width of the bar in the bottom right depicts 10 au (Adopted from Andrews et al. 2018).

Class III object. Once the star starts burning its hydrogen through fusion it enters the main sequence, and any of the residual dust and gas is blown away leaving a planetary system such as our Solar system.

The embedded disks around protostars set the scene for planet formation. As the system evolves on large scales, there is also significant evolution on the small scales. In the molecular cloud, the cold dust particles have sizes ranging from a few nm to 0.1 micron. However, by the time they reach the protoplanetary disk stage, the majority of the dust population has aggregated and grown to mm-sized dust grains. Although there are still gaps in our knowledge on the formation of large bodies, exoplanets are readily detected. An example is the meter-size barrier, which is a long-standing issue in planet formation (Weidenschilling 1977). It seems that bodies of approximately a meter quickly drift into the young star or are destroyed due to collisions instead of growing into larger bodies. In the last decade, observations with the Atacama Large Millimeter/submillimeter Array (ALMA) and Very Large Array (VLA) suggest that planet formation starts in the Class 0/I stage, as dust masses in protoplanetary disks (Class II) are not sufficient to form planetary systems (e.g., Tychoniec et al. 2020).

The amount of substructure seen in dust disks of Class II objects seems to suggest that indeed large bodies are present. The ALMA DSHARP program looked at the millimeter-dust distribution of 20 nearby protoplanetary disks at a spatial resolution of 5 au, roughly the distance from the Sun to Jupiter (Andrews et al. 2018). Figure 1.2 shows a select few of the protoplanetary disks observed in this program. Dust rings and gaps are seen from a few au away from the pre-main-sequence star, to all the way to the edge of the dust disk. Hydrodynamical simulations of both the gas and dust show excellent agreement with the observed substructures in AS 209 with a planet in the 100 au gap (Zhang et al. 2018). However, other scenarios, such as snow lines, dead zone transition, and secular gravitational instability, can produce substructures in disks (e.g., review by Andrews 2020, and references therein).

Besides the dust, there is also a substantial amount of gas in the regions where stars and planets are formed. On average the gas-to-dust ratio is found to be 100 in the ISM. It is generally assumed that this value is preserved throughout the different stages of star and planet formation. This gas and dust interacts with each other in both physical processes, such as viscous evolution, and chemical processes, such as formation of organic molecules. Given the amount of substructure seen in protoplanetary disks it is very likely that the organic content and its evolution are linked to these changes in physical structure. Preliminary results from the ALMA large program Molecules with ALMA at Planet-forming Scales (MAPS) does indeed show that this is the case.

An example of a crucial interaction between gas and dust is the formation of H_2O, one of the most important molecules to sustain life on Earth. The formation of water occurs in the molecular cloud on the surface of dust grains. Specifically, the increasing density results in shielding of the material which in turn lowers the temperature of the dust grains. An effect of this lower temperature, that is, 10–20 K, is that species from the gas phase, such as atomic hydrogen and oxygen, can adsorb on the surface and diffuse across it. When these diffusing atoms find each other they can react and form H_2O. Besides the formation of water, many other molecules are formed on the dust grains, also those that fall under the category potential building blocks of life (see e.g., Linnartz et al. 2011, 2015, and references therein). The processes that result in the formation of molecules on the dust grains are discussed later in more detail.

1.2 Organics through the eyes of telescopes

Probing the full organic inventory in star- and planet-forming regions is challenging. Low abundant organics are hidden in the noise, while line opacities can result in underestimated column densities and dust opacities hide molecules in plain sight. Telescopes such as the Infrared Space Observatory (ISO) and the *Spitzer* telescope have shown that simple species, such as H_2O, CO, CO_2, and NH_3, but also CH_3OH are present in the icy layers on top of dust grains in star- and planet-forming regions (e.g., review by Boogert et al. 2015). An example of such an observation is given in Figure 1.3, where absorption features toward AFGL 7009 S, as observed by ISO, are assigned to solid-state molecules. With the exception of methanol, no other COMs have been securely identified. Two other COMs have been tentatively detected, namely acetaldehyde (CH_3CHO) and ethanol (CH_3CH_2OH), in the massive protostar W33A (Schutte et al. 1999; Öberg et al. 2011). This is because space-based telescopes, such as the infrared space observatory (ISO) and the *Spitzer* telescope, lacked spectral resolution and sensitivity to detect larger COMs. Ground-based infrared telescopes suffer from telluric contamination and have so far only detected methanol in the solid state (e.g., Boogert et al. 2011, PhD thesis D. Qasim).

There is, however, an upcoming infrared space telescope, namely the *James Webb* Space Telescope (JWST), which will bring new impetus to the investigation of solid-state species that cover dust grains. In preparation to observations with JWST, this thesis contains two chapters, that is, Chapters 3 and 4, in which infrared spectra of

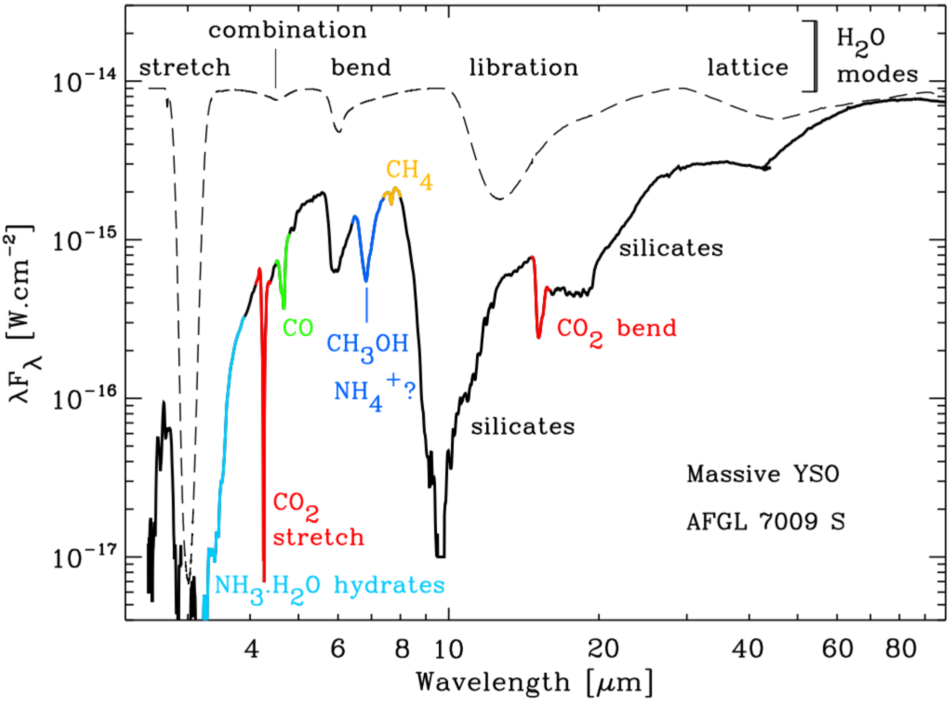

Figure 1.3: Infrared spectrum of the massive young stellar object AFGL 7009 S in black, where the colored parts are assigned to accompanied species in the solid state. The dashed line represents pure H_2O ice (Credit: Boogert et al. 2015).

astronomically relevant COMs are characterized to help identification of these COMs in JWST spectra of star- and planet-forming regions.

In contrast to the solid state, COMs are readily detected in the gas phase, especially in the early Class 0 stages of star and planet formation. As accretion of material onto the protostar continues, the star's temperature and that of its surrounding material increases and this creates a so-called hot core. In these hot cores, the temperature increases enough to thermally desorb ice constituents on dust grains into the gas phase. ALMA observations of gas-phase species of such hot cores have revealed that they are rich in both O- and N-bearing COMs (see e.g., Bøgelund et al. 2018, 2019b; van Gelder et al. 2020; Nazari et al. 2021).

In the following stage, that is, Class I, the detection of gas-phase COMs is already slightly more challenging. In general these sources do not show COM emission, but there are exceptions. For example, the Class I outbursting protostar V883 Ori has episodes of highly increased luminosity, which temporarily increases the temperature profile in the embedded disk surrounding the young star. This sudden increase in temperature pushes the snowlines, that is, the location in the disk midplane where significant amounts of a species start freezing out, outward and sublimates molecules that otherwise would not have been released. ALMA observations of V883 Ori have shown COMs, such as methanol, acetone (CH_3COCH_3), acetonitrile (CH_3CN), acetaldehyde (CH_3CHO), and methyl formate ($HCOOCH_3$) in the gas phase (van 't Hoff et al. 2018b; Lee et al. 2019).

Only in a handful of the protoplanetary disks methanol has been detected. The most likely reason for this is that the envelope has completely dissipated at this stage and the remaining ice reservoirs are shielded in the disk midplane. Even methanol itself is challenging to detect at this stage. Physical-chemical models of the disk around TW Hya predicted up to a 100 times more methanol than eventually was detected (Walsh et al. 2016). Surprisingly, the protoplanetary disk around HD 100546 does show significant amounts of gas-phase methanol. In fact, the HD 100546 disk shows so much methanol, that physical chemical models suggest that this methanol must have been inherited from the molecular cloud (Booth et al. 2021). The gas-phase abundance of methanol in HD 100546 is explained by thermal desorption of large ice resevoirs. This is possible in HD 100546 as it has a large inner cavity (13 au) in its dust structure, which allows heating of a large solid-state reservoir. In contrast to HD 100546, a stringent upper limit was derived for methanol in a similar source, namely HD 163296. Deep ALMA observations of this source showed that there is at least one order of magnitude less gas-phase methanol compared to HD 100546. HD 163296 has a substantially colder disk as it does not have a large inner cavity (< 5 au) and thus shielding the methanol ice reservoir (Carney et al. 2019).

The formation of methanol through reactions in the gas phase is extremely inefficient at the temperatures and densities of these regions. However, formation of methanol on the dust grains is found to be efficient at low temperatures and is deemed the origin of most observed gas-phase methanol in these regions (e.g., review by Linnartz et al. 2015). In order to better understand the formation of methanol one can look at its chemical precursor formaldehyde (H_2CO). The ratio of methanol to formaldehyde is said to trace how chemically evolved the ice is. However, opposite to methanol, formaldehyde also has an efficient gas-phase formation pathway. It is thus important to verify if the observed formaldehyde originates from the solid state or from the gas phase in order to link it to methanol. In Chapter 5 of this thesis, observations of TW Hya with ALMA are used to constrain the formation pathway of formaldehyde.

A lot of the organics, especially COMs, are present in the solid state or when detected in the gas phase seem to originate from the solid state. In the next section, the different processes that occur on and in the icy layers on dust grains are described. This is important as it holds the key to understanding how the potential building blocks of life are formed.

1.3 Grain processes

In a similar way as the formation of water, molecular hydrogen (H_2) is formed on the surface of dust grains when two diffusing hydrogen atoms meet and react with each other. However, the H_2 is released into the gas phase after formation, as the temperature of the dust grain is higher than the desorption temperature. This processes is know as thermal desorption. The temperature at which a species desorbs is dependent on its binding energy to the surface and can even vary with different surfaces. These binding energies determine under which physical conditions molecules are either in the gas phase or in the solid state. At the time that H_2O is formed, carbon monoxide (CO) is present in the gas phase, and since its binding energy is low compared to the dust grain temperature at this stage the majority of CO remains in gas phase above temperatures of ~ 20 K.

However, as the dark cloud contracts under its own gravity, the density increases and subsequently the temperature drops, allowing gas-phase CO to freeze out on top of the water-rich ice layer. This freeze out of gas-phase CO is an important step in creating the building blocks of life. Once CO is in the solid state, it can interact with atomic hydrogen and proceed through tunneling into the formyl (HCO) radical. This process is called hydrogenation and occurs sequentially, after HCO the molecule formaldehyde is formed, one of the simplest organic molecules. The hydrogenation process does not stop at formaldehyde, after two more hydrogen are added one of the simplest COMs is formed, namely methanol (Watanabe & Kouchi 2002a; Fuchs et al. 2009). The intermediate radicals created through hydrogenation, that is, formyl, methoxy (OCH_3), and hydroxymethyl (CH_2OH), are able to react with each other and form COMs, such as methyl formate ($HCOOCH_3$), glycolaldehyde ($HOCH_2CHO$), and ethylene glycol ($HOCH_2CH_2OH$; Fedoseev et al. 2015a; Chuang et al. 2016). Atoms additions and radical recombination reactions are considered as non-energetic processes, as they do not require external energy (e.g., UV photons or cosmic rays) to proceed. Recent laboratory results showed that through these types of non-energetic processes glycine can be formed in the molecular cloud stage (Ioppolo et al. 2021). This could explain the origin of glycine detected in 67P, as mentioned earlier.

The densities of the dark cloud do not allow the external radiation field to penetrate and induce photoprocessing of the ice. Cosmic rays, however, induce an internal UV field through the excitation of H_2, which subsequently emits UV photons upon relaxation. Additionally, in the Class I stage the external radiation field is able to penetrate again, and as the star enters the pre-main-sequence stage the SED contains significant amounts of high energy photons to break bonds and induce chemical reactions. Processes induced by UV, shorter-wavelength photons, and other energetic particles (e.g., electrons or cosmic rays) are considered as energetic processes. An example of such energetic processing is the interaction of UV photons with ices on dust grains. A molecule absorbs an UV photon and is raised into an excited state. This results in the nonthermal desorption (of itself or neighboring molecule), or dissociation of the molecule. The desorption of molecules through photons, that is, photodesorption, is a nonthermal desorption process, which explains the presence of, for example, gas-phase CO in regions where freeze-out timescales are short.

Dissociation of molecules through energetic processes is another way to increase the molecular complexity in star- and planet-forming regions. The dissociation products diffuse across and through the ice to form larger molecules. Laboratory experiments where pure methanol and methanol mixed with CO or CH_4 were irradiated with UV photons show formation of COMs, such as acetaldehyde, ethanol, dimethyl ether, methyl formate, glycolaldehyde, and ethylene glycol (Öberg et al. 2009b). Another example is the work by Ligterink et al. (2017) who looked at the formation of methyl isocyanate (CH_3NCO) from an ice mixture of isocyanic acid (HNCO) and methane (CH_4). The formation of methyl isocyanate is of particular interest as it has a similar chemical structure as a peptide bond, which connect amino acids, such as glycine, in long protein chains. In a follow-up study other amides were detected in the solid state after UV irradiation, such as formamide, carbamide, acetamide, and N-Methyl formamide (Ligterink et al. 2018a). Similar experiments, but with electrons or other high energy particles produce similar COMs (see e.g., Modica & Palumbo 2010; de Barros et al. 2011; Boamah et al. 2014; Maity et al. 2015; Inostroza-Pino et al. 2020).

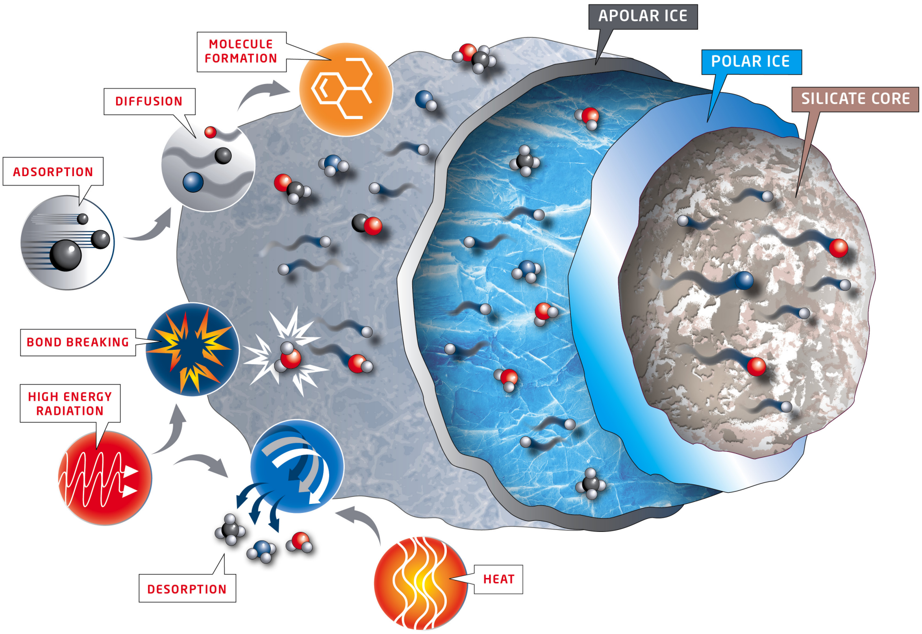

Figure 1.4: Artist impression of a dust grain covered with ice. Through adsorption, diffusion, and high energy radiation species are formed on top of the silicate core, forming a polar and an apolar ice layer (Credit: Leibundgut Design & Center for Space and Habitability).

To summarize, due to the decreasing temperature atoms are able to diffuse across the surface of the dust grains and form simple species, such as H_2O, NH_3, and CH_4. These species have significant dipole moments and the layer they form on top of the dust grain is called polar ice. A further decrease of the temperature allows CO to freeze out on top of the polar layer. This layer is called apolar ice, because it mainly consists out of CO, which does not have a significant dipole moment. The hydrogenation of CO results in H_2CO, CH_3OH, and larger COMs. Additionally, irradiation of these ices, with for example, UV photons or electrons, induces chemical reactions further increasing the molecular complexity. All the above described processes are visualized in Figure 1.4.

1.4 Laboratory astrochemistry

In order to gain better understanding of the molecular complexity in astronomical environments it is key to investigate in the laboratory, quantitatively, their characteristic properties, such as spectroscopic features, and the processes that result in their formation and/or destruction. Such information is needed to interpret astronomical observations and as input for astrochemical models. Laboratory experiments allow careful control of the parameters, while only looking at one or a few processes at the time. These experiments are performed on setups that mimic the conditions in which the icy grains reside. In general, space is associated with extreme conditions where it either extremely hot or cold, extremely dense or and highly dilute. In this thesis the focus is on the cold and dilute regions. The number density in the interstellar medium is many orders of magnitude lower than in the Earth's atmosphere. For example, in molecular clouds the number density is roughly 10^6 molecules per cm^3, whereas on Earth at sea level, this is approximately 10^{19} molecules per cm^3. The temperatures in the laboratory range from a few K up to a couple of hundred K when investigating the processes in the solid state. This is representative of the temperature in which the majority of the icy dust grains reside in star- and planet-forming regions. In contrast, processes at these low temperatures on Earth are considered ineffective.

In astrophysical and astrochemical laboratories around the world highly specialized setups are used that exploit different techniques to learn more about the processes that determine star and planet formation, either directly by providing spectra that can be compared with astronomical data or with insight in the underlying processes. For this thesis, two experimental setups are used in the Laboratory for Astrophysics at Leiden Observatory to investigate ice processes on dust grains. These setups are the high-vacuum setup (HV setup) and the Cryogenic Photoproduct Analysis Device 2 (CryoPAD2). A short introduction to the setups and techniques is given here, while in Chapter 2 a more detailed description will be given. The main chambers of the HV setup and CryoPAD2 are pumped down to high vacuum and ultra-high vacuum, respectively. The pressure on CryoPAD2 is the lowest pressure commercially available and approaches the pressure in a molecular cloud. However, the pressure in the diffuse ISM is still many orders of magnitude lower. At the center of these chambers a substrate is placed as an analogue for a dust grain surface. These substrates are cryogenically cooled to mimic the temperatures in star- and planet-forming regions. Growing ices on these cold substrate allows for characterization of icy analogues and studying irradiation processes under astrophysical conditions. In the following two sections the diagnostic techniques used by these setups are described, namely vibrational spectroscopy and mass spectrometry.

1.4.1 Vibrational spectroscopy

The molecules adsorbed onto the dust grains in star- and planet-forming regions or those on the substrate of laboratory setups cannot rotate. This makes it impossible to observe them through rotational spectroscopy, as with gas-phase species, with telescopes such as ALMA or microwave spectroscopy in the lab. Although the molecules are rotationally hindered, they are still able to vibrate in the solid state. The vibrational transitions of molecules can be excited by absorption of infrared photons, and thus provides a tool to investigate solid-state molecules. In the laboratory this is generally realized through the use of Fourier transform infrared spectroscopy (FTIRS).

In this thesis two types of FTIR spectroscopy are applied, namely transmission spectroscopy and reflection adsorption infrared spectroscopy (RAIRS). In transmission spectroscopy the infrared light passes, under normal incidence, through an infrared transmissive window on which species are deposited, while in RAIRS the infrared is incident under a grazing angle, and reflected of the surface on which species are deposited. The latter has increased sensitivity over the former as the optical path length through the adsorbed ice is increased, but spectra could look slightly different and thus should not be used for comparison to infrared observations. This is because in transmission spectroscopy, under normal incidence, only transverse optical (TO) phonon modes are recorded, while in RAIRS longitudinal optical (LO) phonon modes can appear (see e.g., Palumbo et al. 2006).

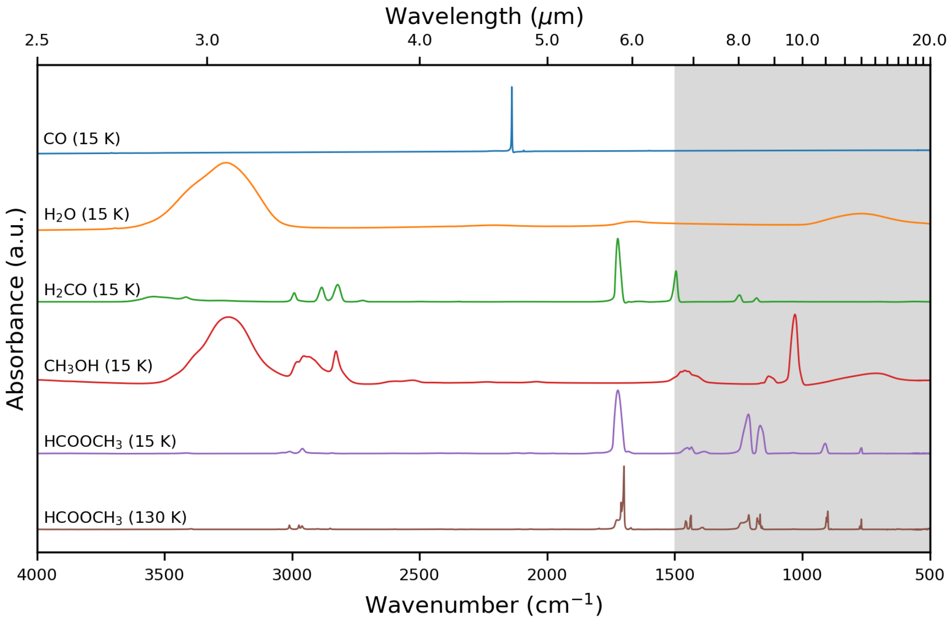

Figure 1.5: Normalized transmission infrared spectra of carbon monoxide (CO), H_2O, formaldehyde (H_2CO), methanol (CH_3OH), and methyl formate ($HCOOCH_3$) at 15 K. The spectrum of methyl formate ($HCOOCH_3$) at 130 K is added to show the effects of crystallinity on the infrared absorption bands. The shaded area indicates the fingerprint region in which identification of species is most likely.

In laboratory astrochemistry, vibrational spectroscopy is used to trace the chemical and physical evolution of the ice during processing and to supply reference spectra to compare with observational spectra. Since each molecule has its own distinct vibrational spectrum, it is possible to determine which molecules have formed during an experiment or are present in the early stages of star and planet formation. Especially, the fingerprint region, that is, 1500–500 cm^{-1} (6.6–20 μm), is well suited for identification of molecules in the solid state. Figure 1.5 shows the vibrational spectra of carbon monoxide, H_2O, formaldehyde, methanol, and methyl formate. As molecular complexity increases, so does the number of absorption modes for each spectrum. This is because the amount of atoms in a molecule determines the number of vibrational modes a molecule has. The number of vibrational modes equals $3N - 5$ for linear molecules and $3N - 6$ for nonlinear molecules, where N equals the amount of atoms in the molecule. For example, CO is a linear molecule and consists of two atoms and thus has one vibrational mode. Methyl formate is a nonlinear molecule and consists of eight atoms. Through the above rule, this gives 18 vibrational modes for methyl formate. However, at 15 K we see at most 11 vibrational modes, while at 130 K the number of absorption features is above 18. The former is because vibrational modes can be inactive or degenerate with each other, that is, adsorb photons of similar frequencies. The latter is either because not all the molecules are in a similar crystalline structure and/or because molecules interact with each other and have combined vibrational modes. A way to eliminate this is to heavily dilute the molecule in an infrared inactive species, such as argon. However, this is of course not representative of the conditions in which molecules reside on dust grains.

The measured spectra of ices are not only dependent on the composition, but also on the orientation of the molecules. When molecules adsorb onto a cold substrate they do so in a random orientation, forming an amorphous ice. As the temperature of the ice increases, molecules gain mobility and move themselves in a more energetically favourable configuration. The change in orientation slightly changes the resonant frequency of the molecules and results in spectral features with distinct shapes and at subtly different wavelengths. When the molecules have oriented themselves in their most favourable configuration, it is called a crystalline ice. Different ice constituents reach crystallinity at different temperatures. Once an ice has become crystalline, it normally does not turn amorphous anymore. The difference between amorphous and crystalline methyl formate ice is shown in Figure 1.5 (see also Chapter 4).

So far only pure ices have been discussed, but in the star- and planet-forming regions different molecules are formed at the same time. This means they are intimately mixed with each other in the ice layers on top of the dust grains. The presence of different molecules also changes the vibrational properties of a molecule. One can expect shifts in peak position, change in peak profile, increase or decrease of amplitude, or even peak splitting. At first this seems to complicate the identification of species, but once these changes are properly characterized they allow for an additional tool to investigate the ice environment in which the molecules reside.

1.4.2 Mass spectrometry

Another commonly used analysis technique in laboratory astrochemistry is mass spectrometry. This technique exploits that different molecules are composed of different atoms, and thus have different weights. The weight of a molecule is commonly expressed in the dalton standard, where one Da is defined as 1/12 of the mass of a carbon atom. For instance H_2O consists out of two hydrogen atoms and one oxygen atom, and thus a total mass of 18 Da. Another example is carbon monoxide (CO), which consists out of one carbon and one oxygen atom, and thus a total mass of 28 Da. By measuring the mass of a molecule, one can deduct from the mass what atoms build up that molecule. However, there are molecules that have a similar mass. For example carbon monoxide (CO) and molecular N_2 both weigh 28 Da, because atomic nitrogen equals 14 Da. A more general example are isomers, isomers are molecules that consist out of the same atoms, and thus have the same weight, but have different chemical structures. An example of an isomer is C_2H_6O, which can be either ethanol (CH_3CH_2OH) or dimethyl ether (CH_3OCH_3).

Instead of actually weighing the molecules, a mass spectrometer relies on a mass filter. Without such filter, the spectrometer would measures every particles that arrives at the detector at once. There are several ways to make a mass spectrometer mass selective, for example, with a quadrupole mass filter, time of flight system, or an ion trap. In this thesis the focus is on quadrupole mass spectrometry (QMS) as this is the technique used on CryoPAD2. A QMS works on the principle that ionized species can be manipulated by an electric field. Before molecules enter the mass filter, the molecules are ionized with electrons at 70 eV. After ionization they are “pushed” by ion optics into the mass filter. Here, four rods, in pairs of two, are placed in such a way that once an oscillating electric field is applied to those rods only ions with

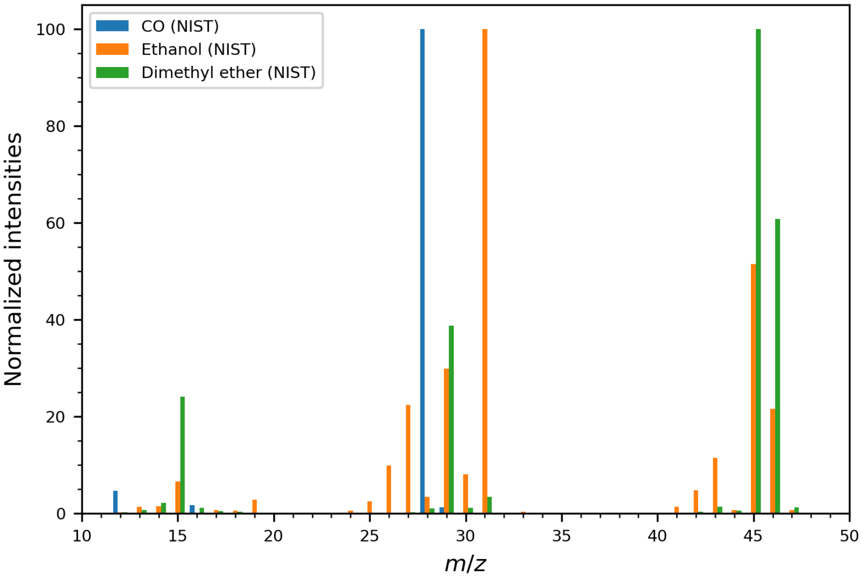

Figure 1.6: Normalized fragmentation patterns of carbon monoxide (CO) and the two isomers of C_2H_6O, namely ethanol (CH_3CH_2OH) and dimethyl ether (CH_3OCH_3). Values are retrieved from the NIST database.

the correct mass-to-charge ratio (m/z) pass through and others are deflected. By scanning through a range of different electric fields applied to those rods different m/z are measured as a function of time, that is, a mass spectrum.

However, upon ionization many molecules fragment as bonds are broken. This complicates the mass spectrum of molecules, as multiple masses now represent a molecule. For instance, carbon monoxide (CO) has small fragmentation channels into C^+ and O^+ besides CO^+ as is shown in Figure 1.6. However, the fragmentation of a molecule upon ionization is unique and once properly characterized it can be used to distinguish between species. The ionization of N_2, which has a similar mass as CO, results in a fragmentation channel at $m/z = 14$. Because N_2 and CO have a different fragmentation pattern they are distinguishable from each other, which would not be possible if measuring at $m/z = 28$ only. Similarly, this can be use to distinguish isomers. Figure 1.6 also shows the fragmentation pattern of the two isomers of C_2H_6O, ethanol and dimethyl ether.

Since each molecule has its own distinct binding energy to a surface, different molecules can be distinguished from each other by looking at their desorption temperature. This is exploited in a so-called temperature programmed desorption (TPD) experiment in which the temperature of the sample is linearly increased and species desorb at their characteristic desorption temperature. During this temperature increase, the QMS continuously probes the gas phase for desorbing species from the solid state. In a sense, the ice is distilled and in order to assign molecules to the measured signals both the desorption temperature and fragmentation pattern should match. This technique is complementary to vibrational spectroscopy and allows for unambiguous assignment of species formed during experiments in Chapter 6.

1.5 This thesis

This thesis aims to take steps toward understanding the interaction between gas phase and solid state (organic) molecules in star- and planet-forming regions. Observations of hot cores show many different COMs in the gas phase. It is generally accepted that the majority of these COMs originate from the solid state. Providing astronomers with reference spectra of solid-state COMs mixed in astronomically relevant matrices will allow them to look for these COMs inside the ices where they are formed and bridge the gap between gas-phase and solid-state COMs.

Another way of tracing the chemical evolution is looking at the ratio between two closely related species: methanol and formaldehyde. Formaldehyde is the intermediate product in CO hydrogenation to methanol, and thus a high CH_3OH/H_2CO would suggest that the ice is significantly chemically evolved. However, this ratio is predominantly measured in the gas phase, and requires good understanding of the release into the gas phase and if gas phase chemistry is contributing to the observed abundances of these species. Formaldehyde has both efficient gas-phase and solid-state formation pathways. Understanding which chemical pathway is active under which physical conditions is crucial to link gas-phase formaldehyde to methanol formed in the solid state.

The interaction between gas and dust is not only important for the building blocks of life, but also for the material available for formation of planets themselves. Observations of protoplanetary disks suggest that they are generally either poor in gas or depleted in gas-phase CO. The general lack of gas in protoplanetary disks would hinder formation of gas giants as there is not sufficient gas to accrete. Since the gas mass is traced through CO and its isotopologues, it is proposed that CO may be chemically depleted. One of the pathways to chemical depletion would be through interaction of gas-phase CO with radicals on the surface of the icy dust grains.

The three aspects introduced above, that is, the spectroscopic identification of solid-state COM features, the gas or grain origin of gas-phase H_2CO, and the chemical conversion of gas-phase CO, are investigated in the remaining chapters of this thesis. Below a summary is given of the findings of each chapter, and afterward some overarching conclusions.

Chapter 2 describes the different tools and methods used in the subsequent chapters. Laboratory: the HV setup is a high-vacuum experimental system in which solid-state COMs are spectroscopically investigated through transmission FTIR. CryoPAD2 is an ultra-high-vacuum system in which chemical and physical processes through vacuum-UV irradiation can be investigated in the solid state. Temperatures can be as low as 15 K, and the probing techniques are RAIRS and QMS. Observational: ALMA is a millimeter/submillimeter interferometer, which allows to measure gas-phase species with high sensitivity and high spatial and spectral resolution in star- and planet-forming regions.

Chapter 3 presents the characterization of infrared spectra of three solid-state COMs, that is, acetaldehyde (CH_3CHO), ethanol (CH_3CH_2OH), and dimethyl ether (CH_3OCH_3), in pure form and mixed with astronomically relevant matrices. Infrared spectra are continuously acquired on the HV setup through FTIR with increasing temperature from 15 K until desorption occurs. Select vibrational modes, that is, those deemed most suited for detection with JWST, are characterized in peak position, full width half maximum (FWHM), and relative band intensities. Additionally, the recorded spectra are used to reanalyze the ISO spectrum of the massive protostar W33A.

Chapter 4 continues the work of Chapter 3, but now for the COM methyl formate ($HCOOCH_3$) in pure form and mixed with astronomically relevant matrices. Once again the HV setup is used to measure the infrared spectra as a function of temperature between 15 K and thermal desorption of the adsorbed species. The most promising features for detection with JWST are characterized in peak position, FWHM, and relative band intensities. A tentative assignment of methyl formate is made to the *Spitzer* observation of HH 46. The idea of looking for vibrational modes of molecules with similar functional groups is introduced.

Chapter 5 contains the observations and analysis of gas-phase formaldehyde (H_2CO) in the protoplanetary disk of TW Hya with ALMA. Specifically, this chapter presents seven transitions of H_2CO of which four are of the ortho-spin isomer and three of the para-spin isomer. Rotational diagram analysis of each separate spin isomer allows investigation of the excitation temperature, column density, and ortho-to-para ratio as a function of radius. It is found that the ortho-to-para ratio hints at formation above the CO freeze-out temperature, and thus suggests that the majority of the observed H_2CO is formed in the gas phase.

Chapter 6 investigates the interaction of gas-phase CO above its canonical desorption temperature with vacuum-UV irradiated water ice. It is found that gas-phase CO spends sufficient time on the water ice to react with OH radicals to form CO_2. This conversion of gas-phase CO into CO_2 at temperatures above the desorption temperature of CO can help explain the low observed CO abundances in protoplanetary disk. Additionally, it may explain how CO_2 embedded in the water-rich ice layer on top of dust grains in the cloud stage is formed.

The main conclusions of this thesis research project are:

1) Detection of COMs in the solid state is the next step in understanding the formation and incorporation of the building blocks of life in planet formation. Chapter 3 and 4 prepare for the observations of the COMs: acetaldehyde, dimethyl ether, ethanol, and methyl formate. The most likely candidates for identification of these frozen COMs are the following features:

- the 7.427 and 5.803 μm bands are recommended for acetaldehyde,
- the 9.141 and 8.011 μm bands should be used for dimethyl ether,
- the 11.36 and 7.240 μm bands are good candidates for ethanol, and
- the 13.02 and 10.98 μm bands are most suited for methyl formate.

However, even with JWST the detection of COMs in the solid state will be challenging. The MIRI instrument is expected to have a continuum signal-to-noise ratio of at most 300. This translates into a 3σ detection at 1% of the continuum flux, which would require significant column densities of COMs to reach. In addition to this, multiple features of a single COM will have to be detected, preferably also with the correct intensity ratio, to ensure it is a robust detection. Besides looking at individual molecules, it will be worthwhile to investigate column densities of similarly structured molecules through common vibrational modes of functional groups.

2) One should be careful using the gas-phase CH_3OH/H_2CO ratio as a tracer of the chemical evolution of the CO hydrogenated ice on dust grains. The results in Chapter 5 suggest that the observed gas-phase H_2CO in TW Hya is formed in the gas phase in an elevated layer. This would mean that it holds little information about the solid-state H_2CO in the midplane. Detection of H_2CO closer to the disk midplane outside of the snowline is prohibited due to dust opacities at (sub)millimeter wavelengths. Detections with current facilities at longer wavelengths are not possible due to unfavourable Einstein A coefficients. Observing H_2CO inside its snowline, however, is more likely, especially in the case that dust opacities are lowered because of substructures. The temperature at which H_2CO thermally desorbs is $\sim$ 50 K, which would require high spatial resolution and long integration times with ALMA to probe this region. For example, the derived temperature structure for TW Hya puts a midplane temperature of 50 K at approximately 10 AU. This would require spatial resolution of at least $0\farcs15$ to spatially resolve the thermal desorption of the solid-state H_2CO reservoir in TW Hya, one of the closest protoplanetary disks.

3) In order to understand planet formation and the material incorporated into those forming planets it is important to not only look at the interaction between gas and dust in a physical way, but also in a chemical way. The laboratory experiments in Chapter 6 show the conversion of gas-phase CO above its canonical desorption temperature into CO_2 with OH radicals on the surface of water ice. This specific interaction between gas and dust holds the potential to explain embedded solid-state CO_2 in water-rich environments and low gas-phase CO abundances in protoplanetary disks. Besides this reaction between CO and OH radicals, other ice and gas interactions might also take place and be able to explain observations. For example, one of the postulated pathways in Chapter 5 is to form the observed gas-phase H_2CO through a combined ice and gas reaction.

4) The results in Chapter 6 suggest a conversion factor of 0.06 for the conversion of CO into CO_2 per adsorbed UV photon. The limiting step in this conversion factor is the production of OH radicals. This suggests that either the dissociation of H_2O is not unity upon UV absorption or there is significant more recombination back into H_2O, more than suggested by molecular dynamics calculations. It is important to understand if this is due to laboratory conditions, that is, high UV fluxes, or if the dissociation efficiency upon absorption of UV photons of solid-state H_2O is not unity. More in-depth investigation is required to understand how water dissociates under laboratory conditions and to translate this into physical-chemical models that represent star- and planet-forming regions.

1.6 Future Outlook

The launch date of the *James Webb* Space Telescope should be shortly after the defence date of this thesis. JWST will open a whole new avenue of research that was previously not possible. It is equiped with four instruments, namely NIRSpec, MIRI, NIRCam, and FGS/NIRISS. NIRSpec and MIRI are most valuable for detections of solid-state molecules, as they cover the 0.6–5.3 μm and 5–28 μm wavelength range, respectively. Especially MIRI is well suited for detection of organic molecules as it covers the entire molecular fingerprint region, that is, 6.6–20 μm. Even though molecules with similar molecular structures have similar vibrational modes, the combination of different vibrational modes is unique in the fingerprint region. This emphasizes the need for the spectral characterizations performed in Chapter 3 and 4 for vibrational modes of COMs in pure form, but also mixed with astronomically relevant precursor molecules. Besides COMs, JWST will supply us with a wealth of knowledge on the main ice constituents, such as H_2O, CO, CO_2, NH_3, and CH_4. The high sensitivity and spectral resolution will allow for accurate determination of solid-state column densities, while the high spatial resolution of JWST will allow to spatially probe ice constituents as a function of distance from young stars. Combining our knowledge from ALMA with for instance the ERS program Ice Age will greatly improve our knowledge on star- and planet-forming regions, which can be used to make physical-chemical models more accurate.

CryoPAD2 is a state-of-the-art experimental setup, which allows to investigate vacuum-UV photon induced chemical and physical processes. The extremely sensitive QMS, which is able to detected partial pressures of at least 10^{-15} mbar, and recently improved RAIRS sensitivity will allow for further investigation of ices under UV light. For example, it is possible that organic species such as formic acid (HCOOH) and carbonic acid (H_2CO_3) form from the interaction between gas-phase CO and solid-state OH radicals in Chapter 6. The improved sensitivity will allow for them to be detected or put stringent upper limits on their formation if not detected. The calibration of the QMS will allow to look at potential chemical- and photodesorption of organics during UV irradiation and get better insight on the processes that occur in star- and planet-forming regions. Installation of a different light source, for instance one that simulates stellar radiation, can be used to investigate processes in our own Solar system on ice moons, such as Enceladus.

ALMA has been fully operational since March 2013, and many plans exist to improve even further its capabilities over the upcoming years. One of such upgrades is the implementation of the Band 1 receivers. These receivers cover a frequency range between 35 and 50 GHz, and will allow ALMA to observe deeper into the protoplanetary disks as there is less dust opacity at these wavelengths. Additionally, at these frequencies lower energy rotational transitions are probed, which inherently allows probing of gas at colder temperatures, that is, closer to the disk midplane. This will allow for probing of organics in the gas-phase closer to the midplane. Another proposed upgrade is to add additional antennas at longer baselines, which would increase the spatial resolution at which ALMA can observe. This would allow for observations of gas and dust in the terrestrial planet zone of young planet-forming systems, but also investigate at higher spatial resulution the interaction between gas and dust. These and other upgrades will significantly increase our understanding of the incorporation of organic molecules in star- and planet-forming regions.

The Square Kilometre Array (SKA, currently being build) and proposed next generation Very Large Array (ngVLA), will operate in the 50 MHz to 20 GHz and 1.2–116 GHz frequency range, respectively. In this centimeter wavelength regime protoplanetary disks do not suffer from dust opacities. The SKA and ngVLA will be able to observe gas and dust all the way to the midplane of protoplanetary disks, where planets are formed from accreting dust and gas onto larger bodies. Many organic molecules, such as formaldehyde, have transitions with low upper energies in this frequency range, which will allow probing the organic inventory in the midplane. This will be complementary to what ALMA observes in the elevated layers, and will allow for a complete picture of the organic gas-phase inventory in star- and planet-forming regions. Now combine this with the solid-state species observed with JWST and our knowledge of the total budget of organic molecules, and its potential to feed life throughout the universe, will drastically improve.

2 | METHODS

The data presented in this thesis is either measured in the Laboratory for Astrophysics at Leiden Observatory or with the Atacama Large millimiter/submillimeter Array (ALMA). This chapter is for the reader who is less familiar with laboratory astrophysics and radio interferometry in general and acts as a bridge between Chapter 1 and the subsequent research chapters. It adds detail to the rather concise information presented in Chapters 3, 4, 5, and 6, focusing on general procedures and calibrations.

2.1 HV setup

The HV setup is used to measure the infrared spectra of COMs in pure form and mixed with astronomically relevant ice matrices in Chapters 3 and 4. At the heart of this setup is a stainless steel chamber, which is positioned in the sample compartment of a Varian 670 Fourier transform infrared (FTIR) spectrometer, see Figure 2.1. The chamber is pumped by a 350 l s^{-1} turbomolecular pump (Oerlikon Leybold TurboVac 361), which is backed by a double-stage rotary vane pump (8 m^3 h^{-1}, Edwards E2M8). This allows for a base pressure of $\sim 2 \times 10^{-7}$ mbar at room temperature, and is monitored with a Agilent FRG-720 full range gauge. The center of the vacuum chamber houses a ZnSe window that is cooled down to a temperature of 12 K by a closed-cycle helium refrigerator (Air Products Displex DE-202). The temperature of the ZnSe window is measured by a temperature sensor (silicon diode DT-670-CU), which is connected to a LakeShore 330 temperature controller. This PID controller actively controls the temperature by measuring the difference between the measured and desired temperature. If there is a difference, the PID controller changes the Joule heating of the ZnSe window to reach the desired temperature. ZnSe is largely transparent for infrared light, and allows for transmission vibrational spectroscopy of species deposited on the window. The FTIR spectrometer records spectra at a resolution as accurate as 0.1 cm^{-1} in the 4000–400 cm^{-1} (2.5–25 μm) range. The optical path of the infrared light is purged with dry air to prevent absorption by CO_2 and H_2O in the atmosphere (Balston 75-62 FT-IR Purge Gas Generator). The deposition of species on the ZnSe window occurs through careful admission of gas-phase samples with a needle valve.

The samples of gas or vapor are stored in a 2 liter glass bulb, which is connected to the deposition line of the HV setup. The glass bulb is filled on a different setup, namely our mixing line, see Figure 2.2. This mixing line has its own pre-vacuum pump and turbomolecular pump and allows pumping down to pressures $< 10^{-5}$ mbar to ensure there is no contamination of atmosphere or previously used gasses or vapors.

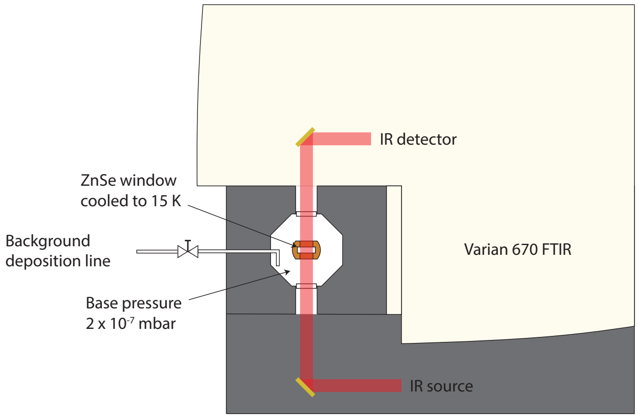

Figure 2.1: Schematic drawing of the HV setup. A simplified pathway of the infrared is shown in red. The ZnSe window is mounted at the bottom of the second stage of the closed-cycle helium refrigerator.

The mixing line features two gas-independent pressure gauges (Edwards 600AB Trans 10MB and 1000MB) that measure in the range of 0–10 and 0–1000 mbar. In general, glass bulbs are filled with 20 mbar of a pure or mixed gasses and vapors. This pressure is not arbitrarily chosen as it ensures that H_2O does not condense on the glass surface. This is because the vapor pressure of H_2O at room temperature is approximately 23 mbar. By careful measuring the exact volume of the mixing line and the glass bulb, the ideal gas law can be used to make accurate mixtures. Additionally, the bottom of the glass bulb can be placed in a liquid nitrogen (LN_2) bath, which allows molecules such as water, methanol, or any COM to freeze out at the bottom of the glass bulb. An advantage of this is that as long as the bulb is in placed in LN_2 bath, other mixture components can be added sequentially as long as their freeze-out temperature is above the temperature of LN_2, approximately 77 K. For example, assuming that the ratio between the glass bulb and mixing line is 10. A mixture with a total pressure of 20 mbar of CO, methanol, and ethanol in a ratio of 10:10:1 (9.5:9.5:0.95 mbar) is realized as follows:

1. Connect glass bulb to mixing line and evacuate both to a pressure of at least $< 10^{-5}$ mbar.

2. Close valve between the glass bulb and mixing line, henceforth valve, and place a LN_2 bath around the bottom of the glass bulb.

3. Fill the mixing line with 9.5 (10×0.95) mbar of ethanol and open the valve. The ethanol freezes out at the bottom, and given that the glass bulb volume is 10 times larger it will have a pressure of 0.95 mbar once sublimated.

4. Once ethanol is frozen out, close the valve, pump the mixing line, and fill the mixing line with 95 (10×9.5) mbar methanol.

5. Open the valve and the methanol will also freeze out.

6. Once methanol is frozen out, close the valve, pump the mixing line, and fill the mixing line with 104.5 (11×9.5) mbar CO. The pressure of CO is higher because CO does not freeze out at the temperature of LN_2 and thus $1/11^{\text{th}}$ of the CO will remain in the mixing line.

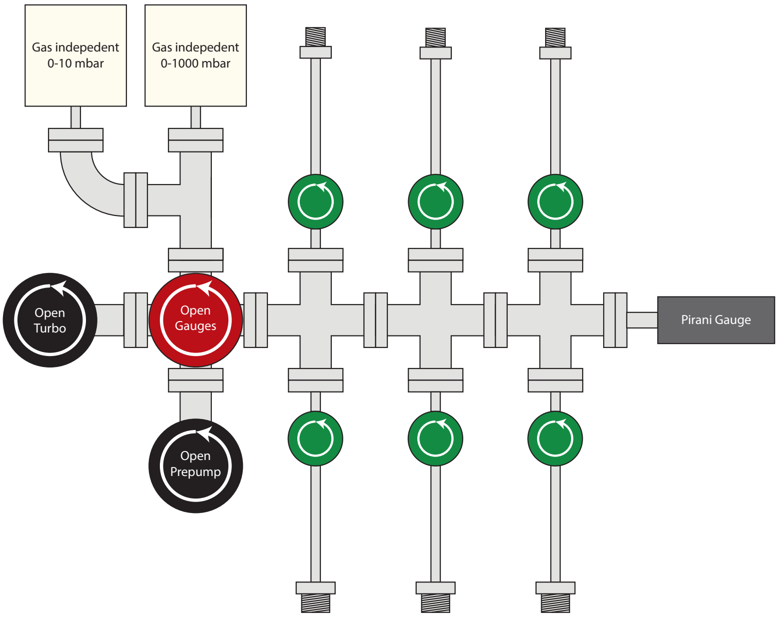

Figure 2.2: Schematic diagram of the mixing line used to prepare samples for the HV setup.

7. Open the valve and close the valve once the pressure between the glass bulb and mixing line is in equilibrium at 9.5 mbar.
8. Remove the LN_2 bath and wait for it to reach room temperature before use.

The relative accuracy of the mixture ratio is mostly dependent on the level of human reproducibility as the volume ratio is determined to be 6.9 ± 0.2 and the repeatability of the gauges is ±0.01% of the full range. For instance, when adding CO to the glass bulb when it is placed inside a LN_2 bath the pressure-to-volume ratio is not preserved. This is because the temperature of the CO gas drops once it collides with the cold surface and thus also the pressure. It is found that it is best to close the valve when the pressure gauge reads the desired pressure. This is prone to human error and was found to introduce errors up to 10% in the mixing ratios.

Typically, these gas samples are background deposited onto the ZnSe window at 15 K. This means that when molecules enter the chamber through the needle valve, they are pointed away from the substrate and interact first with the vacuum-chamber walls before adsorbing onto the window. The idea behind background deposition is that it mimics the adsorption of molecules in space onto dust grains with a random approach trajectory. Once the desired amount of molecules is deposited the deposition is stopped and infrared spectra are recorded. First a spectrum at 15 K is acquired after which the temperature of the ZnSe window is linearly increased with time. During the increase of the temperature, spectra are continuously acquired until all adsorbed species have sublimated. This allows to trace all changes in spectroscopic features as a function of temperature. This is done for acetaldehyde, dimethyl ether, and ethanol in Chapter 3 and for methyl formate in Chapter 4.

2.2 CryoPAD2

CryoPAD2 is an ultra-high-vacuum (UHV) system, which is used for the research presented in Chapter 6. It houses multiple diagnostic tools to investigate UV induced physical and chemical processes on analogue dust grains. The setup is build around a 9" spherical stainless steel chamber, which is fitted with 14 ports (one DN200CF, two DN100CF, three DN63CF, and eight DN40CF ports). The chamber is turbomolecular pumped by an Agilent TV 1001 navigator, which is connected at the bottom of the chamber and is backed by a Leybold Scrollvac 15 Plus. This turbo's pumping speed is specified at approximately 900 L s^{-1} for helium and hydrogen and results in a base pressure of low 10^{-10} mbar at room temperature and 4×10^{-11} mbar at cryogenic temperatures. The pressure is measured with a hot-cathode ionization gauge (DeMaco, Bayard-Alpert nude ion gauge) connected to a Granville-Phillips 350 vacuum gauge controller.

A closed-cycle helium refrigerator (ARS, DE202NB) is mounted vertically to the top port of the stainless chamber. This refrigerator allows for cooling of a gold-coated copper block that acts as an analogue substrate for a dust grain. The substrate is attached to the bottom of the second stage of the refrigerator where temperatures as low as 12 K can be reached. Typically, the substrate is aligned in the center of the chamber with other instruments. The refrigerator is connected to the chamber with both a two-stage differentially pumped rotary platform and Z-axis translator. The former allows for 360 degrees rotation of the substrate inside the chamber with 0.1 degree accuracy, and the latter allows the substrate to move up and down. This is particularly useful for characterizing the microwave-discharge hydrogen-flow lamp (MDHL), see Section 2.2.1.

The refrigerator has a certain cooling power and is either on or off, which means that in order to control the temperature of the substrate, heating power has to be applied. This is generally done through Joule heating, and allows us to control the temperature of the substrate from 12–300 K. A heating strip is attached to the second stage of the refrigerator, which can counteract some or all of the cooling power. The heating power is set by a PID controlled LakeShore 350 temperature controller that uses two Chromel–$\mathrm{AuFe}_{0.07\%}$ thermocouple (TC) temperature sensors as a feedback loop to probe the temperature of the substrate. One TC is mounted near the heating strip and one at the bottom of the substrate. The temperature is controlled on the TC near the heating strip and the experimental temperature is recorded with the TC at the bottom. The latter cannot be used for temperature control, as there is significant thermal mass between the heating strip and the bottom of the substrate. This would result in undesired oscillations in the temperature as the PID cannot compensate for this thermal lag. The TCs have an absolute accuracy of 2 K and a relative accuracy with respect to each other of 0.5 K. Molecular species can be deposited onto the substrate if the temperature of the substrate is below the desorption temperature of said species. The column densities, that is, molecules cm^{-2}, at which molecules are deposited can be controlled by the partial pressure at which the molecules are leaked into the chamber and the total exposure time. CryoPAD2 features a high-precision leak valve (Hositrad, VML14CFR16) followed by a glass-extruded capillary array. This deposition array allows for accurate control of the partial pressure and guarantees that the beam of molecules is close to collimated.

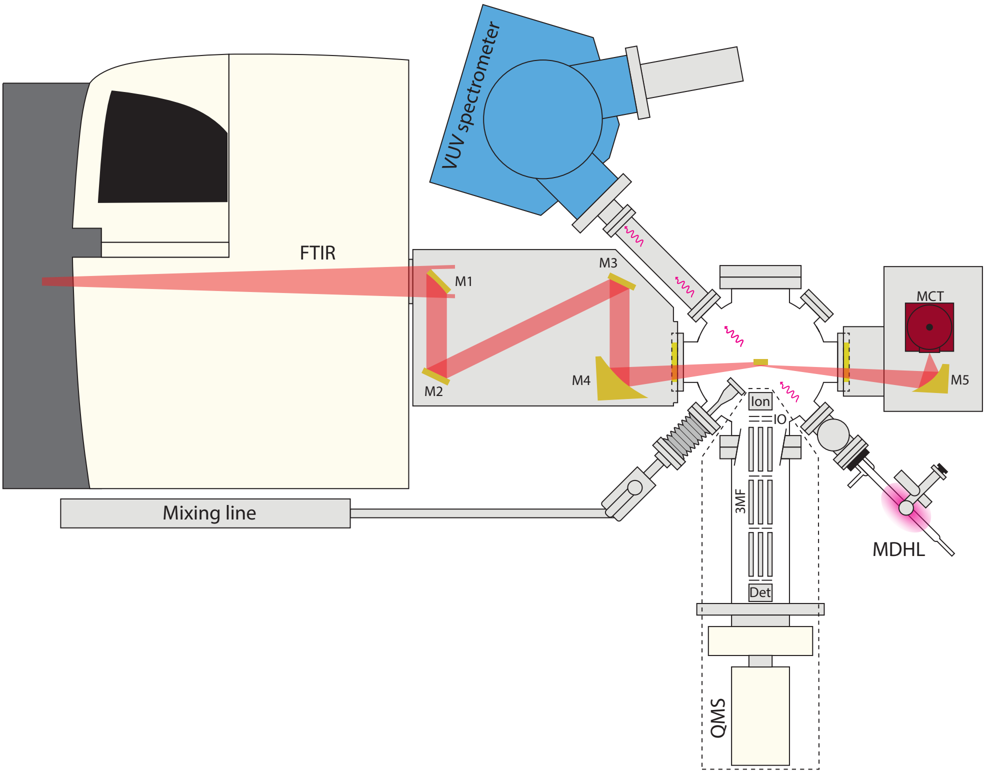

Figure 2.3: Top view schematic diagram of CryoPAD2 in the Laboratory for Astrophysics at Leiden Observatory.

Additionally, the deposition array is mounted on a linear UHV translator, which allows moving the deposition array from 50 mm to within 10 mm away from the substrate. The close proximity and collimated beam ensure that the majority of the molecules adsorb onto the subtrate, which reduces chamber contamination for subsequent measurements. The leak valve is directly connected to the mixing line of CryoPAD2. This mixing line is of similar design as that used for the HV setup, see Figure 2.2. However, here the sample is not stored in a glass bulb, but in the backbone of the mixing line, which allows direct deposition into the main chamber of CryoPAD2.

Once the desired species have been deposited, the experiment is usually continued by vacuum-UV irradiation of the sample. This radiation has the potential to break bonds of the parent deposited species, which can subsequently react with each other and form new species. Additionally, the excitation of species can result in the desorption of solid-state species into the gas phase. These processes are probed on CryoPAD2 through vibrational spectroscopy and mass spectrometry. The following sections describe the procedures and calibration used for the MDHL, reflection adsorption infrared spectroscopy (RAIRS), and quadrupole mass spectrometry (QMS).

2.2.1 Vacuum-UV irradiation

UV photons can get absorbed in the icy layer that cover the dust grains in the star- and planet-forming regions. In general, the absorption of a UV photon results in the increase of molecular complexity in these ices or the release into the gas phase through photodesorption. There are different sources of UV in these regions, that is, from the star itself, the external UV field from other stars, or through excitation of H or H_2. The UV emission from stars is broad band, while the excitation of hydrogen results in a rather discrete emission. The latter is simulated and used on CryoPAD2 with the use of a microwave-discharge hydrogen-flow lamp (MDHL).

Specifically, a T-type HDML is used through which H_2 (Linde, 99.999%) flows. The flow rate is set such that when the MDHL is pumped (Agilent TriScroll 300) the flow pressure equals 0.5 mbar, as measured by a Granville-Phillips Convectron gauge. The H_2 is initially excited with a high frequency generator (Electro-Technic Products BD-10A), and the plasma is sustained with a microwave cavity that is placed around the center of the lamp. The microwave cavity is air cooled and powered by a Sairem GMP 03 K/SM microwave generator. The spectral energy distribution (SED) of the MDHL is measured *in situ* on CryoPAD2 by a McPherson Model 234/302 VUV spectrometer. This spectrometer is mounted opposite of the MDHL and requires the gold-coated substrate to be raised with the Z-axis translator to clear the line of sight toward the spectrometer. The absolute UV flux is also measured *in situ* with a NIST calibrated SXUV-100 photodiode, which is mounted on two posts of PEEK at the bottom of the substrate. Full extension of the Z-axis translator puts the photodiode at the nominal height of the substrate, and allows for accurate determination of the vacuum-UV flux to which the samples are exposed.

Here only a brief description is given of the MDHL flux calibration, for more details see Ligterink et al. (2015). The photodiode has a relatively small band gap, which results in it being sensitive to photons with wavelengths < 1100 nm. Since the MDHL also produces photons in the visible range, these have to be excluded when measuring the photocurrent for flux calibration. The photocurrent is measured by a Keithley 485 picoammeter for both a standard open MDHL and a MDHL closed with a fused-silica window. The fused silica has a transmission wavelength of approximately > 200 nm, which means that the photocurrent measured with the closed MDHL is that attributed to visible photons. Subtracting this visible contribution from the total photocurrent of the open MDHL results in a photocurrent in the 115–200 nm range. However, fused silica is not fully transmissive and absorbs on general 10% of the visible photons. The vacuum-UV photocurrent, I_{VUV}, is then given by

$$I_{VUV} = I_{tot} - \frac{I_{vis}}{0.9}, \tag{2.1}$$

where I_{tot} is the total measured photocurrent with the open MDHL, I_{vis} the measured photocurrent with the closed MDHL, and 0.9 the correction for absorption of visible photons by the fused-silica window. However, this is not directly translatable into a photon flux as we lack the information on the contribution of each wavelength and the quantum efficiency of the photodiode. The percentage contribution of each wavelength is taken from Ligterink et al. (2015) and is used to scale the I_{VUV} to its respective wavelength bins. With the wavelength dependent quantum efficiency (η_q) supplied by the manufacturer, the photon flux for a given wavelength bin, $\Phi(\lambda)$, equals

$$\Phi(\lambda) = \frac{I_{VUV}(\lambda)}{e \cdot \eta_q(\lambda)}, \tag{2.2}$$

where e equals the charge of an electron in C. The photon flux as a function of wavelength is then integrated for the total vacuum-UV flux. In general, the flux is dependent on the conditions under which the lamp operates and is thus setup specific. Here the UV flux is $(2.5 \pm 0.3) \times 10^{14}$ photons s^{-1} cm^{-2}.

2.2.2 RAIRS

Species adsorbed on the gold-coated substrate are probed with an Agilent Cary 660 FTIR set up in reflection absorption infrared spectroscopy (RAIRS) mode. In this configuration, the infrared beam is coupled out of the FTIR, angled onto the gold-coated substrate under a grazing incidence, and reflected toward an external mercury cadmium telluride (MCT) detector. Atmosphere infrared absorption, that is absorption of infrared light by gas-phase H_2O and CO_2, is prevented by purging the infrared beam path outside the vacuum with dry air. The dry air is generated with a Pure Gas CO_2-PG80-2. The infrared beam from the FTIR is guided and focused by four gold-coated mirrors in the first purge box. The first mirror (M1, Thorlabs CM508-1000-M01) has a focal length of 1000 mm, which collimates the slightly diverging beam as it exits the FTIR, and M2 and M3 (Thorlabs PF20-03-M01) are two flat mirrors, which guide the collimated beam toward the off-axis parabolic mirror (M4, Thorlabs MPD399-M01). The off-axis parabolic mirror focuses the infrared beam under grazing incidence onto the gold-coated substrate. The reflected infrared beam is collected by a second off-axis parabolic mirror (M5), which focuses the infrared beam onto the MCT detector area in the second purge box. The infrared beam enters and leaves the vacuum chamber through two ZnSe windows. These windows are transparent in the infrared, but allow UHV conditions inside the main chamber.

An advantage of RAIRS is its increased sensitivity, which allows for detection of species with lower column densities over transmission spectroscopy. However, a downside of this is that the apparent transmission band strengths A' from literature are not applicable. When using RAIRS, a calibration is required to correct for the increased sensitivity in order to derive accurate column densities. Even this correction constant cannot be taken from literature, as it is dependent on the geometry of the infrared beam path and thus setup specific. In general, the column density of a species, $N_{species}$, measured through RAIRS is derived as follows

$$N_{species} = \ln(10) \cdot \frac{\int_{band} \log_{10}\left(\frac{I_0(\tilde{\nu})}{I(\tilde{\nu})}\right) d\tilde{\nu}}{R \cdot A'}, \tag{2.3}$$

where the prefactor ln(10) is the conversion from absorbance to optical depth, the numerator contains the integral of the absorption band of said species, and the denominator contains the RAIRS correction factor R and apparent transmission band strength A' for the integrated infrared band.

When the column density, $N_{species}$, is known, the RAIRS correction factor R can de derived by solving Eq. 2.3. A way to approximate the column density is through the change in binding energy of CO at different interfaces. The binding energy of

CO is lower when adsorbed on other CO molecules compared to adsorbed on the gold-coated substrate. This change in binding energy should become apparent when there is approximately one monolayer of CO on the substrate. Measuring the absorption band of CO at this turnover point in binding energy will allow solving for R when $N_{species}$ is set to 10^{15} molecules cm^{-2} in Eq. 2.3, where 10^{15} equals the column density of one layer of molecules on a surface.

Two methods have been used in the past on CryoPAD2 to find this turnover point in binding energy of CO. The first method is isothermal desorption of CO, here a multilayer of CO ice is heated to 27.5 K and is kept at this temperature. The CO starts to desorb at a slow rate, dependent on the temperature and binding energy, and once the majority of the "bulk" CO ice has desorbed the desorption rate slows down. This is because the average binding energy increases, as the remaining CO is adsorbed with a higher binding energy to the gold-coated substrate. By continuously acquiring infrared spectra during isothermal desorption the decrease in absorbance can be fitted by two slopes, one for the bulk CO and the other for CO on the substrate. The intercept of these slopes is where there is approximately one monolayer of CO on the surface (see e.g., Öberg et al. 2009c).

The second method that can be used is temperature programmed desorption (TPD) of different coverage of CO adsorbed on the substrate. Here the temperature at which CO desorbs is an indication of the binding energy of CO. By deposition of different column densities, one can derive from the TPD plot at what coverage there is approximately one monolayer on the surface and correlate this to the infrared absorption band measured for that coverage. A full description of this method is given in Chapter 2.3 of the PhD thesis of Ligterink (2017).

2.2.3 QMS

Molecules that desorb from the solid state into the gas phase, be it temperature induced or by photon processes, are recorded on CryoPAD2 by a Hiden HAL/3F PIC 1000 series quadrupole mass spectrometer (QMS). The QMS is mounted opposite of the RAIRS substrate surface at a distance of approximately 50 mm. This close proximity ensures the highest possible sensitivity of the QMS for desorbing species from the substrate. The basic principles of a QMS are described in Chapter 1.4.2, while here the calibration of the Hiden QMS for the mass sensitivity is discussed. A QMS is in general not equally sensitive to each mass over its measurable mass range. This is known as the mass sensitivity function (MSF) and once properly characterized it is used to correct the measured signals appropriately. This is important as without correction comparison with other experimental setups or databases, such as NIST[1], are very challenging.

The MSF is determined with a commercial mixture of noble gasses, that is, He, Ar, Kr, and Xe with a ratio of 0.884:0.0382:0.0390:0.0388, respectively. These noble gasses each have a different mass, and even different individual natural isotopes, which allows to probe the MSF in a range of different masses. The measured signals by the QMS, as a result of a constant leak rate of this noble gas mixture into the chamber, have to be corrected in order to compare them and derive the MSF.

---

[1] https://webbook.nist.gov/chemistry/

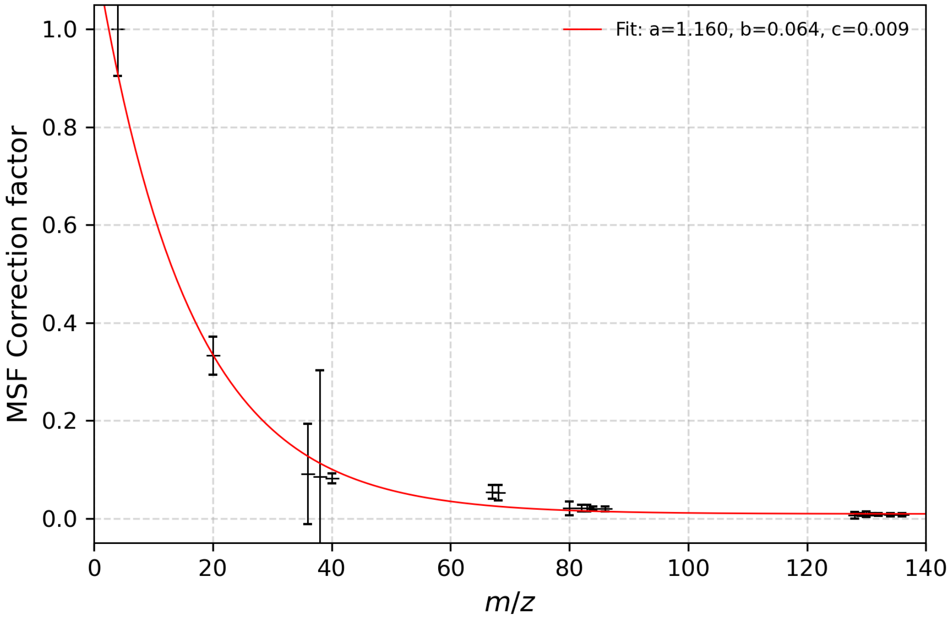

Figure 2.4: Mass sensitivity function derived with a noble gas mixture of He, Ar, Kr, and Xe. Black points shows the normalized signals after correction for the gas concentration, isotope abundance, and electron-impact ionization cross section and the red line is the fit to the data. The electron-impact ionization cross sections are take from Rejoub et al. (2002). The error bars on the data points are 2σ and derived from the standard deviation on the signals.

For example, the signal of ^{40}Ar is corrected as follows

$$S_{corr}(^{40}\mathrm{Ar}) = \frac{S_{QMS}(^{40}\mathrm{Ar})}{F(^{40}\mathrm{Ar}) \cdot I(^{40}\mathrm{Ar}) \cdot \sigma(^{40}\mathrm{Ar})}, \tag{2.4}$$

where S_{QMS} is the raw signal measure by the QMS, F the fraction of a species in a mixture, I the isotope ratio of that species in the fraction, and σ the electron-impact ionization cross section of that species. After this correction, each signal would be equal if the MSF was unity across the mass range. However, since this is not the case, the MSF for each mass can be approximated by fitting an exponential decay function, of the form $\mathrm{a} \cdot \exp(-\mathrm{b} \cdot \mathrm{x}) + \mathrm{c}$, to the normalized signals of the noble gasses as measured by the QMS after corrections. This fit and the normalized noble gas data after correction are shown in Figure 2.4. The fit of the MSF is used to find the correction factor for a given mass and is applied to all presented QMS data in this thesis.

2.3 ALMA

The Atacama Large Millimeter/submillimeter Array (ALMA) is a state-of-the-art radio interferometer, which consists of 54 12-meter and 12 7-meter diameter antennas. ALMA is the result of nearly 80 years of radio interferometry development. Radio interferometry dates back to the 1940s, where radio waves directly from a source and reflected on the surface of the sea interfered with each other and were observed with a single dish (sea-cliff interferometer). Great advances in the field were made with radio interferometers, such as the Owens Valley Radio Observatory (OVRO), Very Large Array (VLA), Combined Array for Research in Millimeter-wave Astronomy (CARMA), Westerbork Synthesis Radio Telescope (WSRT), Submillimeter Array (SMA), and Plateau de Bure (IRAM), that eventually led to development and construction of ALMA in the Atacama Desert of northern Chile. A full explanation of radio interferometry is beyond the scope of this thesis. However, a generalized basis is included to build a foundation for the methods used in Chapter 6.

In radio interferometry, aperture synthesis is used to combine the signals of all the antennas to produce a single image. This image is, however, not a true image of the sky, but a reconstruction that is retrieved from the phases and amplitudes of each of the antenna pairs. The use of aperture synthesis allows for high angular resolution observations with respect to the diameter of the antenna dish. This is because in interferometry, the Rayleigh criterion is not set by the individual antenna diameters, but the longest distance between antenna pairs. However, one cannot place two antennas at large distance and expect high image fidelity. In fact, this antenna pair is only sensitive to emission at those particular scales. In order to reach high fidelity the array of antennas needs to be configured in such a way that they cover a wide range of baseline lengths, where a baseline is the projected distance between an antenna pair.

Each antenna measures the phase and amplitude of the source they are pointing to. The signals of the different antennas are matched with each other by the correlator to create all the different baselines of the array configuration. In short, the correlators multiply and average the signals of all the antenna pairs and create a visibility for each baseline spatial frequency coordinate (u, v). Due to the rotation of the Earth, the baseline coordinates move across the uv-plane, which increases the uv-coverage. Figure 2.5 shows an example of the uv-coverage and visibilities as function of uv-distance of an ALMA execution block used in Chapter 5. One can directly work with these visibilities or Fourier transform them into the image plane. In this thesis, data reduction and analysis is performed in the image plane. Before looking into image restoration, it is however, important to first discuss calibration of the visibilities, the angular resolution, and the resulting maximum recoverable scale.

The amplitudes and phases measured for a source by each antenna pair are affected by several factors, such as amplitude changes and phase delays by the atmosphere. Without corrections for these errors, the observed brightness will be smeared out across the “sky” in the image plane. Through careful calibration of the data these errors can be removed or minimized. There are several types of calibration procedures and here we shortly discuss bandpass, phase, and flux calibration. These procedures are part of the ALMA pipeline and take place before the data is delivered to the principal investigator (PI). The initial step is to correct for variation in phase and amplitude as a function of frequency. This is achieved through bandpass calibration,

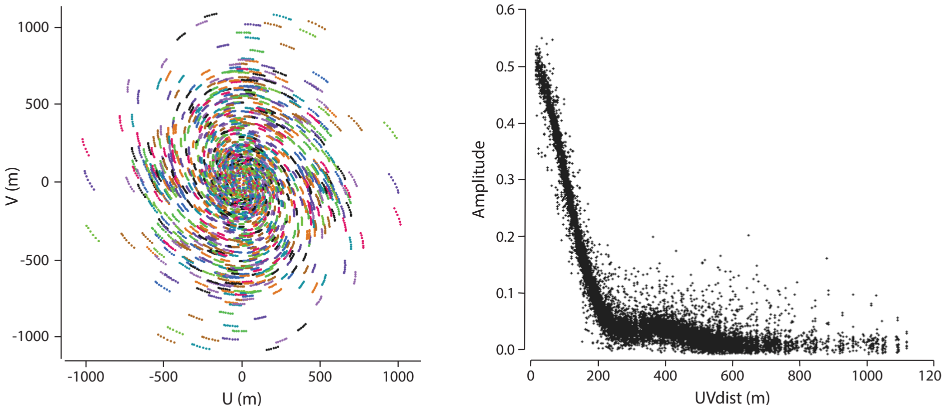

Figure 2.5: Left: Different baselines in the uv-plane from an observation of TW Hya with ALMA in Chapter 5. Right: Visibilities as a function of uv-distance for the baselines showed on the left.

which requires the observation of an additional source that is preferably unresolved and has a bright and flat featureless spectrum. After bandpass calibration, the phase and amplitude is calibrated as a function of time. In order to perform this phase calibration, the antenna array pointing is regularly switched between the science target and a nearby well defined source, often a quasar. Because these calibrator sources are well characterized, one can solve for the phase and amplitude of the science target as a function of time, assuming that between calibrator pointings the conditions are stable, such as the atmospheric conditions. The last step is flux calibration in which the absolute amplitude is scaled to a source of which the brightness is known. After the standard calibration is applied, provided that the signal-to-noise ratio is sufficiently high, minor residual errors can be removed with extra iterations of phase and amplitude calibration. This is known as self-calibration, and helps to increase the signal-to-noise ratio and the quality of the final image of the science target.

It is important to realize that an array of antennas in a specific configuration observes with a specific angular resolution and is only sensitive to those scales for which it is configured. For example, when observing a point source with an interferometer it does not appear as a point source in the image plane, as the interferometer has a finite resolution. The point source is observed with a certain point spread function (PSF), also known as the dirty beam, and the width of this beam determines how far apart two point sources on the sky can be spatially resolved from each other, that is, angular resolution. In star-forming regions the observed sources with ALMA are in general extended and resolved. This allows us to look at for instance the gas and dust of a protoplanetary disk as a function of radius from the star. However, one should be careful with high angular resolution observations of extended sources. Interferometers have a finite amount of antennas available to create baselines, and in order to create high angular resolution observations, many of these antennas are placed at long distances from each other. As mentioned earlier, a baseline is only susceptible to a specific scale and by removing short baselines in favor of long baselines, sensitivity to the larger angular scales on the sky is lost. This results in a so-called maximum recoverable scale (MRS) of a particular array configuration. In general, an array configuration with finite antennas can have an increased angular resolution, but at the cost of a loss of information on the true sky distribution at scales larger than the MRS.

The shape of the PSF is determined by the array configuration and its resulting *uv*-coverage. However, it is also dependent on how each baseline is weighted. There are several ways in which the baselines can be weighted. The possible weighting schemes are natural, uniform, Briggs, or tapering. In natural weighting, each baseline is weighted equally and results in the highest possible signal-to-noise ratio at modest angular resolution. The uniform weighting scheme decreases the weighting of a baseline depending on the number of baselines in a certain *uv*-grid cell (for fast Fourier transform the *uv*-plane is divided into a 2D grid), and results in the highest possible angular resolution of the array configuration at the cost of poorer signal-to-noise ratio. A balance between uniform and natural weighting can be found with Briggs weighting, where the robust parameter determines how weighting is applied. The robust parameter ranges from -2 to 2, where -2 is close to uniform and 2 is close to natural weighting (Briggs 1995). In general, for ALMA the advised weighting scheme is Briggs with a robust parameter of 0.5, as this gives the best balance between angular resolution and signal-to-noise ratios for the designed array configurations. Tapering is a weighting scheme in which the visibilities are scaled in the *uv*-plane with an elliptical Gaussian, which reduces the weight as the baseline length increases with a Gaussian profile. This is particularly useful for improvement of the synthesized beam shape, but comes at the cost of angular resolution.

Once the desired weighting scheme is chosen, image restoration algorithms can be used to improve the image quality. The image created from the initial Fourier transform is called a dirty image because the true on sky distribution is observed with a PSF that contains sidelobes. These sidelobes smear out the emission and create artifacts that do not represent the on sky distribution. These sidelobes exist because the *uv*-plane is not complete, it is only measured at discrete *uv*-coordinates. The gaps in the *uv*-plane can contain any value and result in an infinite amount of solutions for the Fourier transform into the image plane. A solution to this is setting all the unknown values to zero, the so-called principle solution. However, a result of this is that the PSF can have very significant sidelobes that distort the dirty image.

A way to improve this is through a restoration algorithm, which can guess more reasonable values than zero for these unknown values. A commonly used algorithm is the CLEAN algorithm developed by Högbom (1974). In this algorithm, a model of point sources is created, which is then convolved with a synthesized beam that represents the PSF without sidelobes. This model is created by scaling the PSF to the brightest position in the dirty image and subtracting a portion (gain factor < 1) of the PSF from the dirty image. The subtracted flux is stored and represented as a point source in the model. This is an iterative process that is repeated until a user specified threshold level is reached. What remains below the threshold level is called the residuals and in general this should contain noise or emission not distinguishable from noise. A good rule of thumb is to set the threshold to three times the noise level. After the threshold is reached the model is convolved with a synthesized beam representing the PSF and the residuals are added to form a CLEANed image. An example of a dirty image and CLEANed image is shown in Figure 2.6.

In this thesis, the Common Astronomy Software Applications (`CASA`) 5.6.1 is used to reconstruct the images with the `TCLEAN` task (McMullin et al. 2007). However, instead

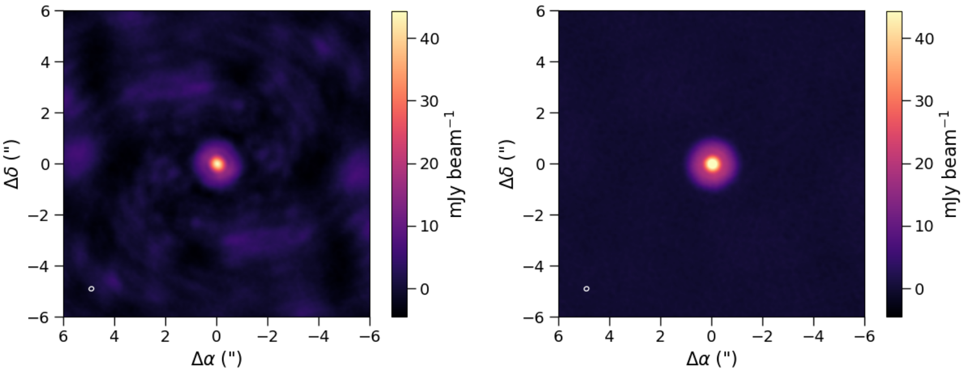

Figure 2.6: Dirty (left) and CLEANed (right) image of the 351 GHz continuum of TW Hya observed with the band 7 receivers. The angular resolution of these observations is shown shown in the bottom left with a white ellipse.

of the default Högbom deconvolver the multiscale deconvolver is used, which was developed by Cornwell (2008). This particular deconvolver creates a model consisting of Gaussian objects of a given set of scales rather than only points sources. It is found that this type of deconvolver is more accurate at guessing/predicting the unsampled regions in the *uv*-plane for extended sources compared to the Högbom deconvolver. One should, however, always keep in mind that the restored images are only one of the infinite solutions possible through Fourier transform of a discrete sampled *uv*-plane. The user and algorithm try to infer the best possible values for unsampled *uv*-coordinates, but they can under- or over-predict flux at scales that the array inherently was not sensitive to.

2.3.1 Keplerian masking of rotating disks

Figure 2.6 shows the spatially resolved continuum emission of the dust at approximately 351 Ghz in the disk of TW Hya. Besides the unprecedented spatial resolution, ALMA also has high spectral resolution. Because of this spectral resolution, ALMA is able to spectrally resolve emission of gas-phase molecules. This is particularly useful as it allows to resolve the Keplerian rotating gas around a young star into different channels. An example of Keplerian rotating gas can be seen in Figure 5.1 of Chapter 5. The observed H_2CO gas moves at different velocities with respect to us due to the inclination of the disk around TW Hya. This Doppler shift in velocity can be predicted for each pixel when the stellar mass is known and used to mask the pixels in channels where Keplerian rotating gas is expected. The shaded areas in Figure 5.1 show where Keplerian rotating gas is expected.

It is common to integrate over velocity spaces to create a single image that displays the emission of a gas. The velocity integrated emission map, also known as moment-zero map, is basically the summation of the different channels that contain emission of Keplerian rotating gas. The signal-to-noise ratio of these maps can be improved by exploiting the knowledge of Keplerian rotation and exclude the regions that only contain noise and no Keplerian emission. This method is used in Chapter 5, but for example also in the studies by Walsh et al. (2016) and Salinas et al. (2017).

3 | Infrared spectra of complex organic molecules in astronomically relevant ice matrices. I. Acetaldehyde, ethanol, and dimethyl ether

Jeroen Terwisscha van Scheltinga, Niels F.W. Ligterink, Adwin C.A. Boogert,
Ewine F. van Dishoeck, Harold Linnartz, 2018, A&A, 611 A35

Abstract

The number of identified complex organic molecules (COMs) in inter- and circumstellar gas-phase environments is steadily increasing. Recent laboratory studies show that many such species form on icy dust grains. At present only smaller molecular species have been directly identified in space in the solid state. Accurate spectroscopic laboratory data of frozen COMs, embedded in ice matrices containing ingredients related to their formation scheme, are still largely lacking.

The work described in this thesis chapter provides infrared reference spectra of acetaldehyde (CH_3CHO), ethanol (CH_3CH_2OH), and dimethyl ether (CH_3OCH_3) recorded in a variety of ice environments and for astronomically relevant temperatures, as needed to guide or interpret astronomical observations, specifically for upcoming *James Webb* Space Telescope observations.

Fourier transform transmission spectroscopy (500–4000 cm^{-1} / 20–2.5 μm, 1.0 cm^{-1} resolution) was used to investigate solid acetaldehyde, ethanol and dimethyl ether, pure or mixed with water, CO, methanol, or CO:methanol. These species were deposited on a cryogenically cooled infrared transmissive window at 15 K. A heating ramp was applied, during which infrared spectra were recorded until all ice constituents were thermally desorbed.

In this chapter a large number of reference spectra is presented that can be compared with astronomical data. Accurate band positions and band widths are provided for the studied ice mixtures and temperatures. Special efforts have been put into those bands of each molecule that are best suited for identification. For acetaldehyde the 7.427 and 5.803 μm bands are recommended, for ethanol the 11.36 and 7.240 μm bands are good candidates, and for dimethyl ether bands at 9.141 and 8.011 μm can be used. All spectra are publicly available in the Leiden Database for Ice.

3.1 Introduction

Water was the first molecule to be detected in the solid state in the interstellar medium (Gillett & Forrest 1973). Since then more than 10 other molecules have been identified in icy form (i.e., CO, CO_2, CH_4, NH_3, and CH_3OH) and it has become clear that icy dust grains play a key role in the formation of both these small molecules and more complex organic molecules (COMs), such as glycolaldehyde ($HOCH_2CHO$) and ethylene glycol ($HOCH_2CH_2OH$). The combined outcome of astronomical observations, specifically space based missions such as the Infrared Space Observatory (ISO) and *Spitzer* Space Telescope (Kessler et al. 1996; Werner et al. 2004), laboratory, and astrochemical modelling studies have resulted in a detailed picture of the composition and structure of ice mantles on interstellar dust grains and the chemical processes taking place (see reviews by Gibb et al. 2000b; Herbst & van Dishoeck 2009; Öberg et al. 2011; Caselli & Ceccarelli 2012; Tielens 2013; Boogert et al. 2015; Linnartz et al. 2015; Öberg 2016). It is generally accepted that interstellar ices form on the surface of dust grains in cold dark clouds through accretion in two distinct layers: a polar H_2O-rich and an apolar CO-rich layer. Water, together with NH_3, CO_2, and CH_4, forms through atom addition reactions in lower density environments (Hiraoka et al. 1995; Miyauchi et al. 2008; Oba et al. 2009, 2012; Dulieu et al. 2010; Hidaka et al. 2011; Linnartz et al. 2011; Lamberts et al. 2013, 2014; Fedoseev et al. 2015b). At later stages, when densities increase and temperatures decrease along with the ongoing cloud collapse, CO freeze-out from the gas phase occurs, forming a CO coating on top of the water rich layer (Tielens et al. 1991; Pontoppidan 2006). Subsequent hydrogenation processes transform CO to H_2CO and H_2CO to CH_3OH (Watanabe & Kouchi 2002a; Fuchs et al. 2009), resulting in CO ice intimately mixed with methanol (Cuppen et al. 2011; Penteado et al. 2015). Radical recombination processes in various starting mixtures, triggered by energetic (i.e., UV photons or cosmic rays) or non-energetic (i.e., atom additions) were shown to provide pathways towards the formation of more complex molecules (see reviews of Linnartz et al. 2015; Öberg 2016).

The molecules H_2O, CO, CO_2, CH_4, NH_3, and CH_3OH make up the bulk of interstellar ice (Ehrenfreund & Charnley 2000; Öberg et al. 2011), but less abundant species have been observed as well. These include species such as OCS and OCN^- (Palumbo et al. 1995; van Broekhuizen et al. 2004). A number of COMs, such as formic acid (HCOOH), acetaldehyde (CH_3CHO), and ethanol (CH_3CH_2OH), have been tentatively detected based on spectroscopic features at 7.2 and 7.4 μm (Schutte et al. 1999; Öberg et al. 2011). Several other spectroscopic features, such as the 6.0 and 6.8 μm bands, remain only partly identified (Schutte et al. 1996; Boudin et al. 1998; Gibb & Whittet 2002; Boogert et al. 2008). Limited astronomical detection sensitivity combined with a lack of high resolution laboratory data have thus far prohibited secure solid state identifications of COMs other than methanol, but their presence in interstellar ices is generally accepted and also further supported by the recent detection of a number of COMs on comet 67P/Churyumov-Gerasimenko and in its coma (Goesmann et al. 2015; Altwegg et al. 2017).

With the upcoming launch of the *James Webb* Space Telescope (JWST), new instruments such as MIRI (Mid InfraRed Instrument; Wright et al. 2015) and NIRSpec (Near InfraRed Spectrograph; Posselt et al. 2004) will become available to record telluric free spectra of interstellar ices at higher spectral and spatial resolution and with higher sensitivity than possible so far. This opens up new possibilities to search for and study the level of molecular complexity in interstellar ices. To aid in the search for larger molecules in the solid state, high resolution infrared laboratory spectra are required. The ice matrix environment and its temperature have to be taken into account since these influence the spectral appearance of vibrational bands.

In this work we present the infrared spectra of acetaldehyde, ethanol, and dimethyl ether, respectively, CH_3CHO, CH_3CH_2OH, and CH_3OCH_3. The choice for these three species, an aldehyde, an alcohol, and an ether, is motivated by previous tentative identifications (Boudin et al. 1998; Schutte et al. 1999; Öberg et al. 2011), their astronomical gas-phase identification and high abundance (e.g., Turner 1991; Gibb et al. 2000a; Cazaux et al. 2003; Bisschop et al. 2007b; Taquet et al. 2015; Müller et al. 2016), and their common formation scheme upon UV irradiation of methanol ice (Öberg et al. 2009b). Formation of these molecules is seen in energetic processing experiments of methanol ice (Gerakines et al. 1996; Bennett et al. 2007; Öberg et al. 2009b; Boamah et al. 2014) and starts with cleavage of the CH_3OH bonds. This results in a reservoir of radicals that can be used for their formation as follows:

$$^{\bullet}CH_3 + {}^{\bullet}CHO \rightarrow CH_3CHO$$

$$^{\bullet}CH_3 + {}^{\bullet}CH_2OH \rightarrow CH_3CH_2OH$$

$$^{\bullet}CH_3 + {}^{\bullet}OCH_3 \rightarrow CH_3OCH_3$$

Formation of dimethyl ether and ethanol has also been studied by radical recombination reactions starting from CH_4:H_2O mixtures (Bergantini et al. 2017). Besides energetic radical recombination reactions, other formation pathways and links between the three molecules exist as well. For example, acetaldehyde has been proposed as a solid state precursor of ethanol. A hydrogen atom addition experiment showed that acetaldehyde can at least partially ($> 20\%$) be transformed into ethanol (Bisschop et al. 2007a).

Acetaldehyde itself has been proposed to form as a spin-off in the well-studied $CO + H \rightarrow HCO \rightarrow H_2CO \rightarrow H_3CO \rightarrow CH_3OH$ chain (Charnley 2004); HCO may directly interact with a C-atom, to form HCCO that upon hydrogenation yields CH_3CHO (Charnley & Rodgers 2005).

This work presents a detailed study of the infrared spectral characteristics of CH_3CHO, CH_3CH_2OH, and CH_3OCH_3 in pure form and mixed in the interstellar relevant ice matrices H_2O, CO, CH_3OH, and CO:CH_3OH. Section 3.2 contains the experimental details and measurement protocols. The results of the measurements are presented and discussed in Section 3.3. In Section 3.4 the astronomical relevance of the new data is illustrated. The conclusions are summarized in Section 3.5. A complete overview with all data obtained in this study is available from the Appendices.

3.2 Experimental

3.2.1 Setup

The ice spectra are recorded in a high-vacuum (HV) setup, which is described in detail by Bossa et al. (2015). A central stainless steel chamber is evacuated by a 300 l s^{-1} turbomolecular pump, backed by a double stage rotary vane pump (8 m^3 hr^{-1}). This allows a base pressure of $\sim 10^{-7}$ mbar at room temperature. The pressure is monitored by an Agilent FRG-720 full range gauge. Ices are grown on an infrared transmissive ZnSe window that is cryogenically cooled to a lowest temperature of 12 K by a closed-cycle helium refrigerator. The temperature of the window is monitored by a LakeShore 330 temperature controller, which regulates a feedback loop between a resistive heating wire and a silicon diode temperature sensor. An absolute temperature accuracy of 2 K and a relative accuracy of 1 K is acquired with this diode. The infrared beam of a Fourier transform infrared spectrometer (FTIR; Varian 670-IR) is aligned through the window to obtain infrared spectra of the samples. The spectrometer covers a range of 4000 to 500 cm^{-1} (2.5–20 μm) at spectral resolutions as high as 0.1 cm^{-1}. Samples are externally prepared in a 2 liter glass bulb using a separate multi-line gas mixing system. The gas mixing line is turbomolecularly pumped to pressures $< 1 \times 10^{-4}$ mbar. Gas mixtures are made by sequential addition of its components. Two gas independent gauges, covering various pressure ranges ensure that accurate mixing ratios are obtained with a maximum error of < 10%. The liquids and gases used in these experiments are acetaldehyde (Sigma-Aldrich, 99.5%), ethanol (Biosolve, 99.9%), dimethyl ether (Sigma-Aldrich, 99.9%), water (Milli-Q, Type I), carbon monoxide (Linde gas, 99.997%), and methanol (Sigma-Aldrich, 99.9%). Liquid samples are purified with freeze-pump-thaw cycles before use.

3.2.2 Measurement protocol

Pure or premixed gases are background deposited onto the 15 K cold sample via an inlet valve. A standard pressure of 20 mbar in the glass bulb is used to prevent a decreasing inlet pressure gradient during deposition. Bi-mixed gases are prepared in a 1:20 ratio and tri-mixed gases in a 1:20:20 ratio, where the smallest fraction is the COM under investigation. These dilution factors ensure that the COM mainly interacts with the surrounding matrix, resulting in matrix shifted infrared vibrational bands. Ices are grown at 15 K to a column density of $\sim$ 4500 ML (1 monolayer equals 1×10^{15} mol cm^{-2}) on the window. This coverage ensures that any influence of background contamination, mainly water depositing at a rate of less than 30 ML h^{-1}, can be neglected. During deposition, infrared spectra are recorded at 1 cm^{-1} resolution (0.5 cm^{-1} step size) and averaged over 61 scans (equals 2 min) to trace the ice growth and determine when the ice is $\sim$ 4500 ML thick. From the integration of the infrared band absorption, the column density of the species N_{species} is determined according to

$$N_{\mathrm{species}} = \ln(10) \frac{\int_{\mathrm{band}} \log_{10}\left(\frac{\mathrm{I}_0(\tilde{\nu})}{\mathrm{I}(\tilde{\nu})}\right) \mathrm{d}\tilde{\nu}}{A'}, \tag{3.1}$$

where $\int_{\mathrm{band}} log_{10} \left(\frac{I_0(\tilde{\nu})}{I(\tilde{\nu})}\right) d\tilde{\nu}$ is the integrated absorbance of the band and $I_0(\tilde{\nu})$ and $I(\tilde{\nu})$ are the flux received and transmitted by the sample, respectively, and A' is the apparent band strength in cm mol^{-1}. It is important to realize that strongly absorbing bands may get saturated at high coverages, resulting in unreliable column density measurements. In the experiments conducted, the CO band at 2135 cm^{-1} reaches saturation at high coverage, as do certain bands of pure acetaldehyde and dimethyl ether. For these species, bands with a lower band strength or isotopologues can be used. The measured column densities give an indication whether the mixed ice composition still matches the gas-phase mixing ratio and whether the COMs are sufficiently diluted in the matrix. Small variations in the composition of the gas mixture and matrix interactions complicate accurate ice mixing ratio determinations. The apparent band strengths are listed in Table 3.1 and taken from literature for acetaldehyde and ethanol. For the dimethyl ether bands at 923, 1095, and 1164 cm^{-1} the band strength value is approximated from a CH_4:CH_3OCH_3 mixture, prepared at a one-to-one ratio in the gas phase. Assuming this ratio is maintained in the ice and matrix interactions are negligible, the apparent band strength is determined from a comparison with the methane 1302 cm^{-1} band area and its known apparent band strength of 8.0×10^{-18} cm mol^{-1} (Bouilloud et al. 2015).

After deposition the sample is linearly heated at a rate of 25 K h^{-1}, until it is fully desorbed from the window. The low temperature ramp ensures that the ice has sufficient time to undergo structural changes, particularly from the amorphous to the crystalline phase. During heating infrared spectra are continuously recorded and averaged over 256 scans to trace spectral changes vs. temperature.

3.2.3 Analysis protocol

Owing to the very large amount of spectra that are recorded during the experiments, we only present samples of representative infrared spectra for temperatures at which significant spectral changes occur. These spectra are baseline subtracted and the peak position and band width at full width at half maximum (FWHM) are determined for selected spectral features. When the band of a COM overlaps with a spectral feature of a matrix molecule, also the matrix feature is subtracted where possible. In the case of band splitting, the least intense component is only taken into account when its peak position is clearly distinguishable. In a few cases splitted peaks rival in intensity and are heavily overlapping and it is not possible to fit a FWHM for the individual components. Here the FWHM of the combined peaks is determined. Peaks are selected for analysis mainly based on their intensity and potential as an ice tracer, that is, selecting wavelengths for which no strong overlap with known interstellar features exist.

Identification of vibrational modes of the three species studied here is realized by comparison with available spectra from liquid and solid state literature (Plyler 1952; Evans & Bernstein 1956; Barnes & Hallam 1970; Allan et al. 1971; Hollenstein & Günthard 1971; Mikawa et al. 1971; Coussan et al. 1998). Optical effects such as longitudinal optical – transverse optical (LO–TO) splitting and particle shape effects are not explicitly taken into account. Since spectra are recorded at normal incidence with unpolarized light, only the TO modes are recorded. However, certain combinations of polarized light and angles of incidence can result in the LO phonon mode showing up (Baratta et al. 2000; Palumbo et al. 2006). Also particle shape effects can shift transition bands with respect to recorded laboratory spectra (Baratta & Palumbo 1998). Such effects affect only the spectra of more abundant species, such as CO or CO_2, and are not considered to be relevant for COMs.

Table 3.1: Selected transitions of acetaldehyde, ethanol, and dimethyl ether.

Species	Vibrational mode	Peak position*		A'
		cm^{-1}	μm	cm mol^{-1}
Acetaldehyde	CH_3 rock. + CC stretch. + CCO bend.	1122.3	8.909	
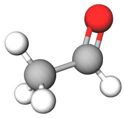	CH_3 s-deform. + CH wag.	1346.2	7.427	
	CH_3 deform.	1429.4	6.995	
	CO stretch.	1723.0	5.803	1.3×10^{-17} [a]
Ethanol	CC stretch.	879.8	11.36	3.24×10^{-18} [b]
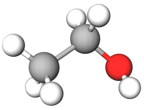	CO stretch.	1051.0	9.514	1.41×10^{-17} [b]
	CH_3 rock.	1090.5	9.170	7.35×10^{-18} [b]
	CH_2 tors.	1275.2	7.842	
	OH deform.	1330.2	7.518	
	CH_3 s-deform.	1381.3	7.240	
Dimethyl ether	COC stretch.	921.3	10.85	5.0×10^{-18} [c]
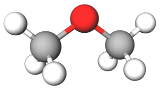	COC stretch. + CH_3 rock.	1093.9	9.141	9.2×10^{-18} [c]
	COC stretch. + CH_3 rock.	1163.8	8.592	9.8×10^{-18} [c]
	CH_3 rock.	1248.2	8.011	

Notes. (*) Peak position of the pure molecule at 15 K. Note that throughout literature there seems to be disagreement in the assignment of certain modes, particularly for ethanol.

References. (a) Schutte et al. (1999). (b) Hudson (2017). (c) This work.

3.3 Results and discussion

In this section selected results of the acetaldehyde, ethanol, and dimethyl ether experiments are presented. These are representative for the much larger data set given in the appendix. All the selected spectra used in this work are publicly available from the Leiden Ice Database[1], spectra recorded for other temperatures are available on request. Figure 3.1 shows the infrared spectra of pure acetaldehyde, ethanol, and dimethyl ether ice at 15 K; the bands that are fully analysed are indicated with an asterisk (*) and spectra of pure water, CO, and methanol ice. Figures of the spectra of COMs mixed in water, CO, methanol, and CO:methanol at 15 K are shown in Appendix 3.A. In Table 3.1, these selected bands are listed together with their peak positions and, if available, apparent band strength in pure ices at 15 K. Appendix 3.B presents the results of the analysis of the selected bands, listing peak positions, FWHMs, and integrated absorbance ratios at various temperatures and for different ice matrices. A representative example of the tables listed in the appendix is shown in Table 3.2 for the acetaldehyde CH_3 s-deformation + CH wagging mode at 1346.6 cm^{-1} at 15 K.

For easier interpretation the results are represented in a number of plots; see Figures 3.2, 3.3, and 3.4 for examples. Each plot covers the data of one band. In all plots, the top panels show spectroscopic changes of the band under thermal processing in

---

[1] (https://icedb.strw.leidenuniv.nl)

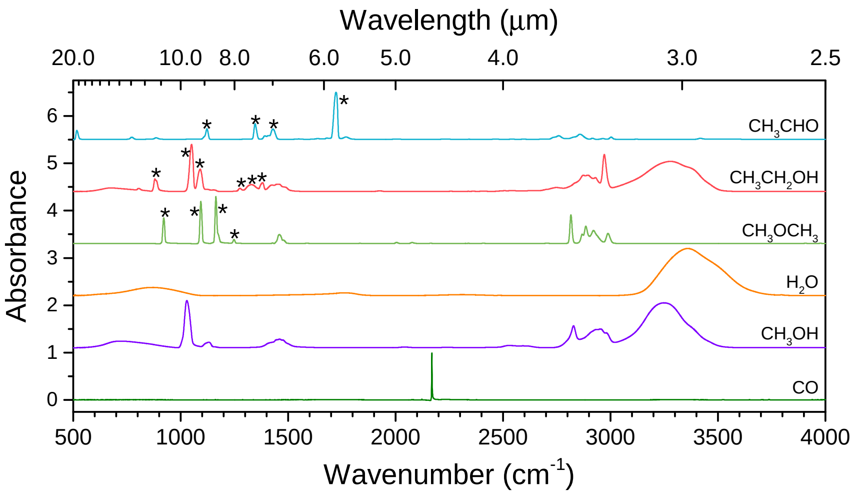

Figure 3.1: Spectra of pure acetaldehyde (blue), ethanol (red), dimethyl ether (green), water (orange) methanol (purple), and CO (dark green) normalized to one in the range of 2.5 to 20.0 μm. The bands investigated in this work are indicated with an asterisk (*).

Table 3.2: Peak position and FWHM of the acetaldehyde CH_3 s-deformation + CH wagging mode at 15 K in various matrices.

Mixture	Temp.	$\lambda_{\mathrm{peak,-baseline}}$		$\lambda_{\mathrm{peak,-matrix}}$		FWHM	
	(K)	(cm^{-1})	(μm)	(cm^{-1})	(μm)	(cm^{-1})	(μm)
CH_3CHO		1346.6	7.4264	–	–	13.5	0.0744*
CH_3CHO : H_2O		1349.9	7.4078	1349.9	7.4078	9.2	0.0502
CH_3CHO : CO	15	1349.4	7.4104	–	–	4.8	0.0262
CH_3CHO : CH_3OH		1347.5	7.4211	–	–	13.0	0.0714
CH_3CHO : CO : CH_3OH		1349.4	7.4105	–	–	12.6	0.0691

Notes. Excerpt from Table 3.5. $^{(*)}$ FWHM result of two or more blended peaks.

pure and mixed ices. The bottom left panels plot peak position vs. FWHM, showing trends in the band. The bottom right panels give an indication of how the band strengths change relative to each other in various matrices. Assuming that the ice column density is roughly the same for each experiment and that the gas mixing ratio is close to the ice mixing ratio, the mixed ices are corrected for their dilution factor. Owing to various uncertainties in this method, this results in relatively large error bars for the band strengths. This is unfortunate as this would allow us to interpret the spectroscopic identifications – the primary goal of this work – also in terms of accurate column densities. The remaining figures of other bands can be found in Appendix 3.C.

A few general statements can be made. Most peaks display peak narrowing under thermal processing, which is due to the ice changing to a crystalline phase with increasing temperature. Mixed ice in CO and CO:CH_3OH are exceptions due to the volatility of CO and its removal from the ice at relatively low temperatures. Above 30 K, the desorption temperature of CO (Öberg et al. 2005), these ices are often seen to display peak broadening.

Peak splitting, especially at high temperatures is another effect that is generally seen. This can be caused by two or more modes contributing to a single feature at low temperatures and becoming visible as the peaks begin to narrow at higher temperatures. Alternatively, the matrix can play a role and a peak is split owing to different interactions of a functional group with its surroundings. For example, an ice can segregate under thermal processing and have part of the COM still intimately mixed with the matrix molecule, while another part is forming COM clusters. Segregation is an effect most clearly seen in the COM:CO ice mixtures.

Integrated absorbance ratios are given for the bands under investigation in each ice mixture. These ratios can provide a tool to estimate the likelihood of observing other bands upon detection of a specific transition. They can also be used as conversion factors to determine band strengths from known band strengths. The bands are normalized on the band with highest integrated absorbance at 15 K, unless this band is suspected to be in saturation or when the data set is incomplete over the investigated temperature range.

3.3.1 Acetaldehyde

Acetaldehyde hosts four significant features in the 5.5–12.5 μm region (see Figure 3.1). Some smaller features are also visible, such as the CC stretching + CH_3 rocking mode close to 11 μm, however, its intensity is very small compared to the other bands. Two characteristic vibrational modes of acetaldehyde at 6.995 and 8.909 μm coincide with methanol CH_3 rocking and deformation modes and are likely obscured in interstellar spectra. A solid state identification of acetaldehyde based on these vibrational modes is unlikely. The CO stretching mode is the most prominent band in this spectrum. However, its location at 5.8 μm coincides with the CO stretching mode of many other molecules, such as formaldehyde (H_2CO), formic acid (HCOOH), or formamide (NH_2CHO), which are expected to be present in interstellar ice, making it likely that this band is blended. The fourth band is the CH_3 s-deformation + CH wagging mode around 7.427 μm, which is found to have no substantial overlap with abundant bulk interstellar ice components and therefore is most suited for a successful solid state identification of this molecule.

Figure 3.2 shows the results of the analysed data of the CH_3 s-deformation + CH wagging band. Under thermal processing the band widths are generally seen to decrease; this is caused by crystallization in the ice. Peak positions shift as well, with clear blue shifting trends visible for the CO:CH_3OH and water mixtures. In the case of the CO:CH_3OH mixture this is likely because of the loss of CO from the matrix, while for the water mixture the interaction between acetaldehyde and crystalline water is more likely the cause. In some cases, at high temperature CH_3CHO undergoes peak splitting, making identification through FWHM challenging. However, this can also be used as a tool to determine the ice temperature. The comparison of peak position makes it in general easy to distinguish between pure acetaldehyde, acetaldehyde mixed in CH_3OH, and CO:CH_3OH, acetaldehyde mixed in CO, and acetaldehyde mixed in water. The 7.427 μm band shows a substantial decrease in band strength by about 40% when acetaldehyde is surrounded by matrix molecules.

The acetaldehyde CO stretching band underlines the above findings, given it is clearly observed (see Figure 3.12). Especially at low ice temperatures of 15 and 30 K clear peak shifts are visible between the CO:CH_3OH matrix at 5.84 μm, the water matrix at 5.825 μm, and the pure matrix, or in a CH_3OH matrix at around 5.805 μm.

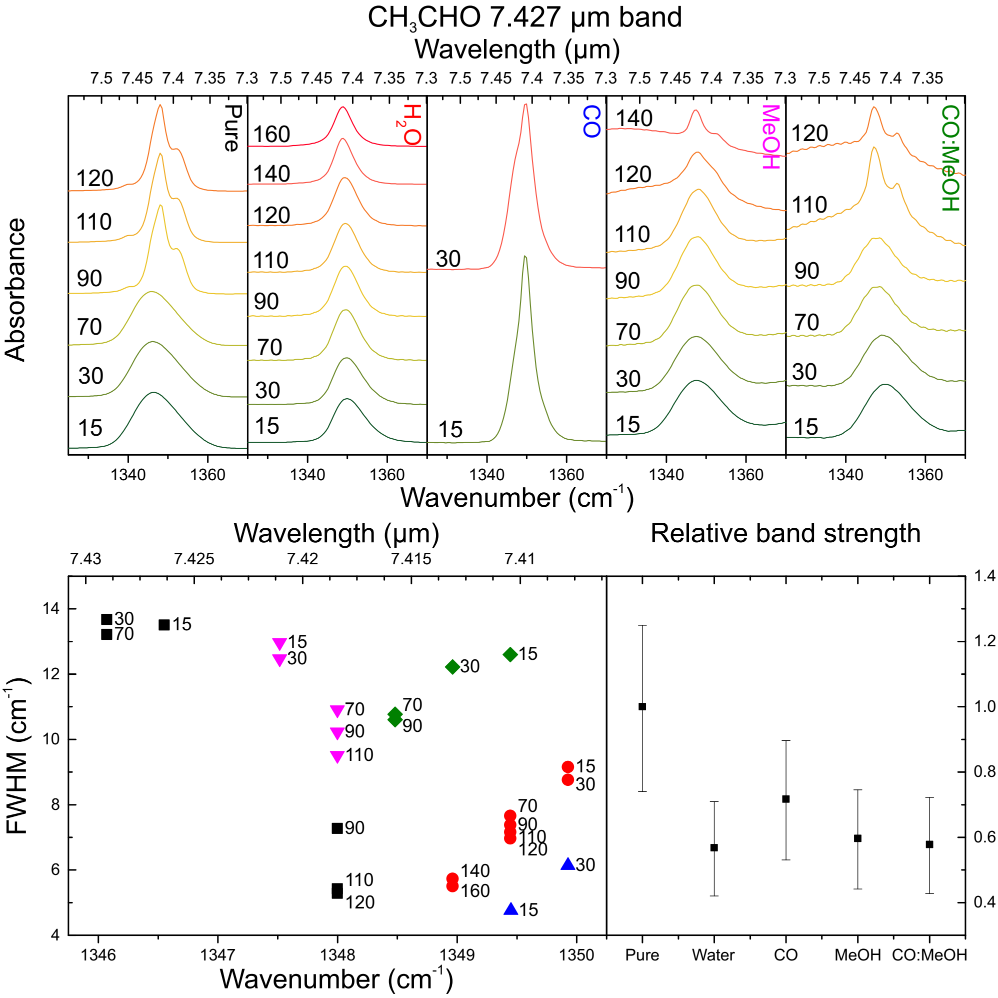

Figure 3.2: Top: from left to right the acetaldehyde 7.427 μm band pure (black) and in water (red), CO (blue), methanol (purple), and CO:CH_3OH (green) at various temperatures. Bottom left: peak position vs. FWHM plot, using the same colour coding. Bottom right: the relative band strength for the 7.427 μm band at 15 K in various matrices.

3.3.2 Ethanol

The spectrum of pure ethanol in Figure 3.1 shows a strong CC stretching band at 11.36 μm, CO stretching mode at 9.514 μm, and CH_3 rocking mode at 9.170 μm. A number of weaker modes are seen between 6.5 and 8.5 μm: specifically the CH_2 torsion mode at 7.842 μm, the OH deformation mode at 7.518 μm, and the CH_3 symmetric deformation mode at 7.240 μm. Overlap with spectral features of bulk interstellar ice species such as water and methanol is an issue for the three strongest bands, coinciding with either the water libration mode or CO stretching and CH_3 rocking modes of methanol. Also the prominent broad silicate feature is present at $\sim 9.7\mu$m. Although the other ethanol modes are substantially weaker, they fall within a spectral region that is generally clean of strong transitions.

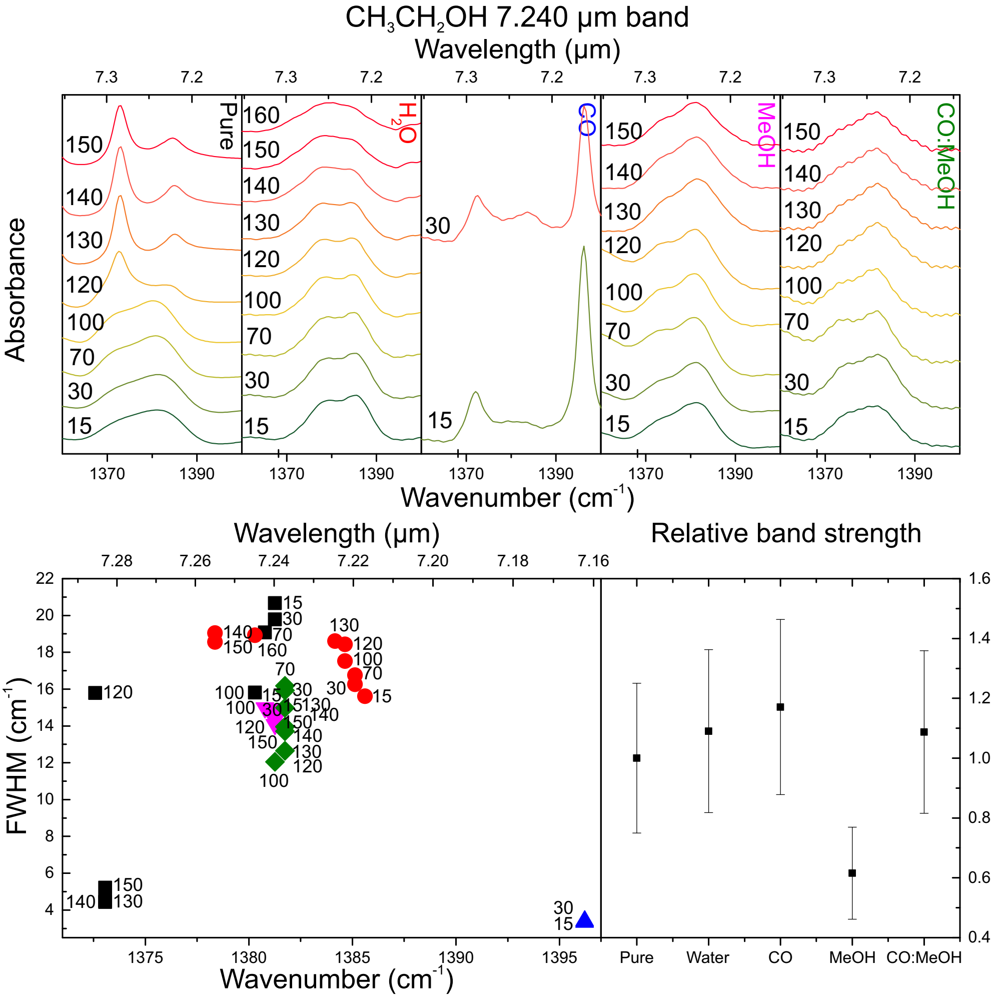

Figure 3.3: Top: from left to right the ethanol 7.240 μm band pure (black) and in water (red), CO (blue), methanol (purple), and CO:CH_3OH (green) at various temperatures. Bottom left: peak position vs. FWHM plot, using the same colour coding. Bottom right: the relative band strength for the 7.240 μm band at 15 K in various matrices.

The ethanol 7.240 μm band is a possible candidate for identification. Figure 3.3 shows the data of this band. Ethanol mixed in water can be distinguished from other features by a ~ 3 cm^{-1} peak shift from other mixtures. In general it is found that the CH_3CH_2OH:H_2O mixture is relatively easy to distinguish, but the other mixtures display much overlap in peak position and FWHM. The CH_2 torsion, OH deformation mode, and CH_3 symmetric deformation mode are hard to identify in the CH_3CH_2OH:CO mixture owing to the appearance of many more modes. Band areas and relative band strengths of these modes are therefore not considered. The band strength is seen to vary substantially for the various bands, but does not show a clear trend.

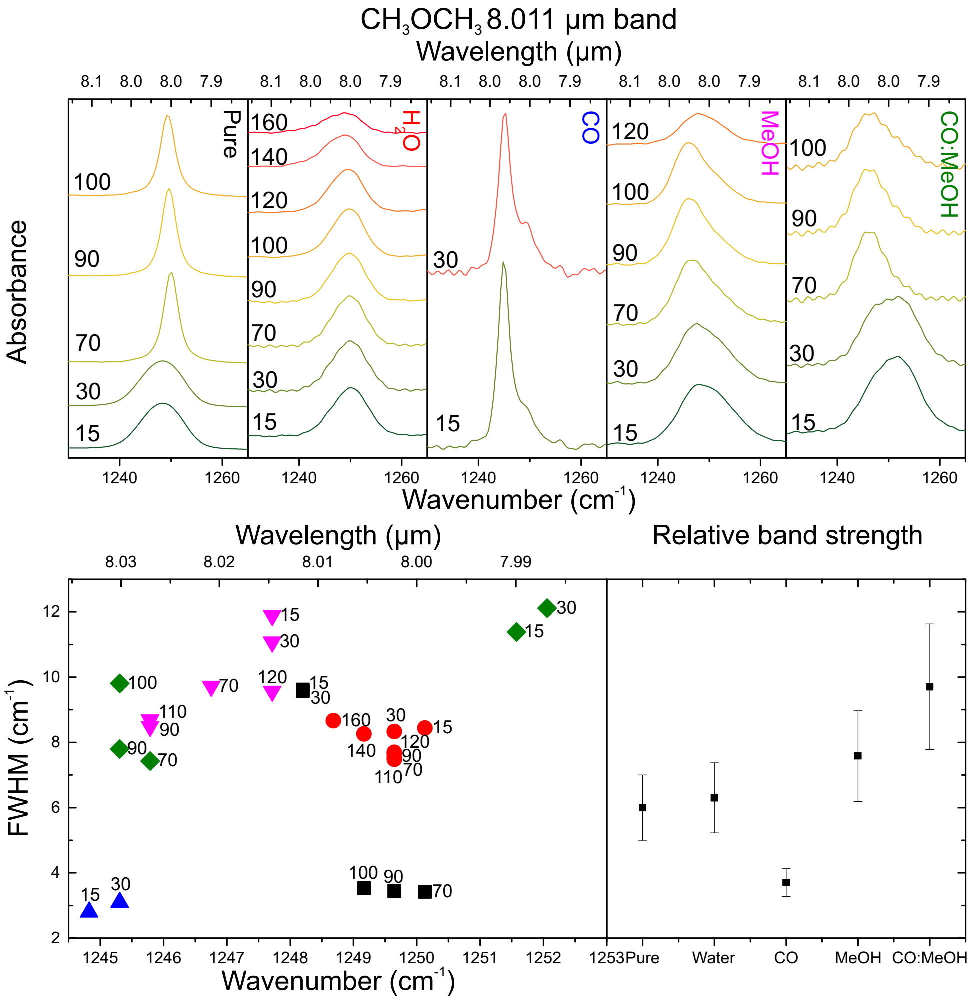

Figure 3.4: Top: from left to right the dimethyl ether 8.011 μm band pure (black) and in water (red), CO (blue), methanol (purple), and CO:CH_3OH (green) at various temperatures. Bottom left: peak position vs. FWHM plot, using the same colour coding. Bottom right: the relative band strength for the 8.011 μm band at 15 K in various matrices.

3.3.3 Dimethyl ether

Three strong bands of dimethyl ether are found at 10.85, 9.141, and 8.592 μm for the COC stretching and two COC stretching + CH_3 rocking modes, respectively. A much weaker CH_3 rocking mode is found at 8.011 μm. The first two overlap with known interstellar ice features of methanol, water, and silicates and are therefore less suited for an identification, while the third likely falls in the wing of such features and may still be used. Even though it is a weak mode, the 8.011 μm band falls in a relatively empty region of interstellar ice spectra. This feature could therefore be most suited for a dimethyl ether identification; see Figure 3.4.

For the 8.011 μm band clear differences are seen depending on the matrix. The spectra of pure and methanol mixture are distinguishable from those of the water and CO:CH_3OH mixtures by a ~ 2 cm^{-1} peak shift of the low temperature spectra at 15 and 30 K. In water this band displays a narrower peak compared to the other ices. The other bands also show many clear differences in peak position and FWHM between the various ice mixtures. A characteristic peak splitting structure at low temperatures is seen for the 10.85 μm band when mixed in water, methanol, or CO:CH_3OH. Interestingly, the relative band strength shows a substantial increase in the CH_3OH and CO:CH_3OH mixtures for the 8.011 μm band. Other modes do not show such clear differences. Also it is interesting to note the fact that the COC stretching mode has the largest band area when mixed in water, while in the other mixtures this is always the CH_3 rocking mode at 8.592 μm (see Appendix 3.B.6).

3.4 COM ice features in W33A

Our extensive measurements of frozen COMs are needed in the analysis of the many spectra of dense clouds, embedded protostars, and inclined protoplanetary disks that will be obtained with the upcoming JWST mission at high sensitivity and medium spectral resolution (R of up to 3,500). Here, we demonstrate their use by a reanalysis of a spectrum of the massive protostar W33A obtained with the Infrared Space Observatory's Short Wavelength Spectrometer (Astronomical Observation Template 1; $R = 800$). This is one of the few sources for which a high quality mid-IR spectrum is available (Gibb et al. 2000b). In the 7 to 8 μm region three prominent features at 7.25, 7.41, and 7.67 μm have been described previously in the literature. The 7.25 μm feature has been attributed to both CH_3CH_2OH and HCOOH (Schutte et al. 1999; Öberg et al. 2011), the 7.41 μm feature has been attributed to $HCOO^-$ and CH_3CHO (Schutte et al. 1999), and the 7.67 μm band has been identified as solid methane with potentially contributions of SO_2 (Boogert et al. 1996).

In this work we make use of the water and silicate subtracted spectrum of W33A, shown in Figure 3.5 with a straight line local continuum subtraction. The aforementioned features are visible, although the 7.41 μm feature seems to have two contributions at 7.47 and 7.40 μm and the 7.25 μm feature is found at 7.22 μm. The spectra of ethanol and acetaldehyde mixed in CO:CH_3OH and H_2O are plotted in the same figure. The peak position of the 7.40 μm feature can be reproduced well by the acetaldehyde CH_3 s-deformation mode in both mixtures. However, the band in CO:CH_3OH mixture seems to be too broad to justly reproduce the W33A 7.40 μm feature and also this band covers the 7.47 μm feature next to it. The other two features at 7.22 and 7.47 μm could be the result of the CH_3 s-deformation and OH deformation modes of ethanol. Particularly, the CH_3CH_2OH:H_2O mixture coincides with the peak locations of the 7.22 and 7.47 μm features in the W33A spectrum. While the identification of acetaldehyde and ethanol are plausible, detection of additional features would strengthen the assignment. We checked and found that none of the other CH_3CHO and CH_3CH_2OH bands have an anti-coincidence with the W33A spectrum.

Upper limits to the ice column densities of ethanol and acetaldehyde can be given based on the integrated optical depth of their potential features. Schutte et al. (1999) give integrated τ values of 2.0 ± 0.3 and 1.6 ± 0.5 cm^{-1}, respectively. Band strength values of ethanol and acetaldehyde are taken from the literature and used to calculate the column densities of the two features. The ethanol band strength of the CO stretch

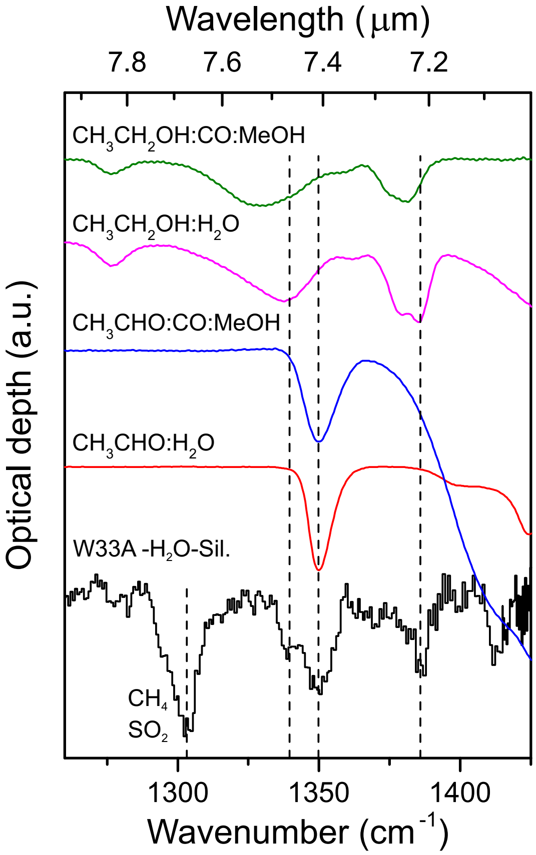

Figure 3.5: Continuum and water and silicate subtracted spectrum of W33A plotted together with ice spectra of ethanol and acetaldehyde at 15 K, mixed in CO:CH_3OH and H_2O. Features in the W33A spectrum are indicated with dashed lines at 7.22, 7.40, and 7.47 μm. The large spectral feature at 7.67 μm is due to CH_4 and SO_2.

mode at 9.514 μm has been determined to be 1.41×10^{-17} cm mol^{-1} by (Hudson 2017). Using the integrated absorbance ratio CH_3 s-def. / CO str. = 0.20 at 15 K from Table 3.19, the band strength of the CH_3 stretch mode is determined to be 2.8×10^{-18} cm mol^{-1}. The effect of the matrix on the relative band strength is small for both the ethanol CO stretch and CH_3 s-deformation modes, as can be seen from Figures 3.3 and 3.14, and therefore assumed to be negligible. Assuming the entire 7.22 μm feature is caused by ethanol, this results in a column density of $(7.1 \pm 0.2) \times 10^{17}$ cm^{-2}.

In Schutte et al. (1999), the acetaldehyde band strength is given as 1.3×10^{-17} cm mol^{-1} for the CO stretch mode based on data from Wexler (1967). The integrated absorbance ratio of CO stretching / CH_3 s-deforming + CH wagging = 4.32 in pure acetaldehyde at 15 K in laboratory experiments. As the CO stretching mode is likely saturated, the ratio may thus be higher. Using this ratio, the band strength of the CH_3 s-deformation mode is found to be 3.0×10^{-18} cm mol^{-1}. As can be seen in Figure 3.2, the relative band strength of this mode decreases substantially in mixtures by about 40%. The band strength of the CH_3 s-deformation mode in mixed ices is thus 1.8×10^{-18} cm mol^{-1}. If the entire 7.40 μm feature is attributed to CH_3CHO, the resulting column density is $(8.9 \pm 3) \times 10^{17}$ cm^{-2}.

Table 3.3: Ice upper limits and gas-phase abundances of ethanol and acetaldehyde towards W33A.

Species	Ice		Gas phase^c
	$/N(H_2O)^a$	$/N(CH_3OH)^b$	$/N(CH_3OH)$
CH_3CH_2OH	≤ 1.9	≤ 42	2.4
CH_3CHO	≤ 2.3	≤ 52	≤ 0.2

Notes. Abundances given in %.
References. $^{(a)}$ Keane et al. (2001). $^{(b)}$ Dartois et al. (1999). $^{(c)}$ Bisschop et al. (2007b).

In all likelihood the 7.22 and 7.40 μm features contain contributions of other molecules, mainly HCOOH and $HCOO^-$ and the reported values should therefore be seen as upper limits. Using solid water and methanol column densities of 3.8×10^{19} and 1.7×10^{18} cm^{-2}, respectively, towards W33A (Dartois et al. 1999; Keane et al. 2001), the upper limit abundance ratios of ethanol and acetaldehyde can be determined. The abundance ratio $N(\mathrm{COM})/N(\mathrm{H_2O})$ is found to be $\leq$ 1.9% and $\leq$ 2.3%, while $N(\mathrm{COM})/N(\mathrm{CH_3OH})$ is $\leq$ 42% and $\leq$ 52% for ethanol and acetaldehyde, respectively. The abundances with respect to water are in good agreement with previously reported values of $\leq$ 4% and $\leq$ 3.6% for ethanol and acetaldehyde, respectively (Boudin et al. 1998; Schutte et al. 1999).

The $N(\mathrm{COM})/N(\mathrm{CH_3OH})$ upper limit ice abundance can be compared with known gas-phase abundances towards W33A. These are given as $N(\mathrm{CH_3CH_2OH})/N(\mathrm{CH_3OH})$ = 2.4% and $N(\mathrm{CH_3CHO})/N(\mathrm{CH_3OH}) \leq$ 0.2% (Bisschop et al. 2007b) and are substantially lower than the ice upper limits. Interferometric observations with the Atacama Large Millimeter/submillimeter Array are needed to spatially resolve these molecules and determine more accurate abundances. Beside being upper limits, this difference may be linked to the process that transfers solid-state species into the gas phase, causing molecules to fragment, or to other destruction of species in the gas phase. An overview of the COM abundances in ice and in the gas phase towards W33A is given in Table 3.3.

The spectroscopic data presented in this paper, combined with the improvements in terms of sensitivity and resolution of JWST, will aid in confirming these detections and distinguish other potential contributors to these features. More observations, particularly towards low-mass sources, will give additional information about the carriers of these features.

3.5 Conclusions

This paper adds to and extends on data of three important interstellar ice candidates: acetaldehyde, ethanol, and dimethyl ether. A number of selected bands are fully characterized in FWHM and peak positions and show clear changes in various matrices. Our conclusions are summarized as follows:

1. The most promising bands to identify the COMs studied here in interstellar ice spectra are the 7.427 and 5.88 μm bands of acetaldehyde, the 7.240 and 11.36 μm bands of ethanol, and the 8.011 and 8.592 μm bands of dimethyl ether.

2. Matrix characteristic shifts in peak position and FWHM are seen for several bands. The acetaldehyde CH_3 deformation and CO stretching mode can be distinguished in the H_2O, CO, CH_3OH, and CO:CH_3OH matrices. Ethanol shows generally less distinctive shifts and only bands in the water matrix are unique. At low temperatures matrix specific dimethyl ether band shifts can be identified, specifically for the CH_3 rocking mode at 8.011 μm.

3. Given the higher complexity of the involved spectra, unambiguous identifications need to involve different bands that reflect bandwidths and intensity ratios as found in the laboratory studies. The dependence on matrix environment and temperature provides a tool to use these transitions as a remote diagnostic instrument.

4. Analysis of the ISO W33A spectrum in the 7 μm region shows a number of features that can be assigned to the COMs studied in this work. The 7.40 μm feature matches the position of the CH_3 s-deformation mode of acetaldehyde, and the 7.22 μm feature is plausibly caused by the CH_3 s-deformation mode of ethanol. It is likely that 7.22 μm band is specifically caused by ethanol mixed in water. Abundances of both molecules with respect to water ice are determined to be $\leq 2.3\%$ and $\leq 3.4\%$ for acetaldehyde and ethanol, respectively.

Appendix

3.A Spectra

The following figures show the spectra of acetaldehyde, ethanol, and dimethyl ether mixed in water, CO, methanol, and CO:methanol in the range of 2.5 to 20.0 μm. All spectra are taken at 15 K.

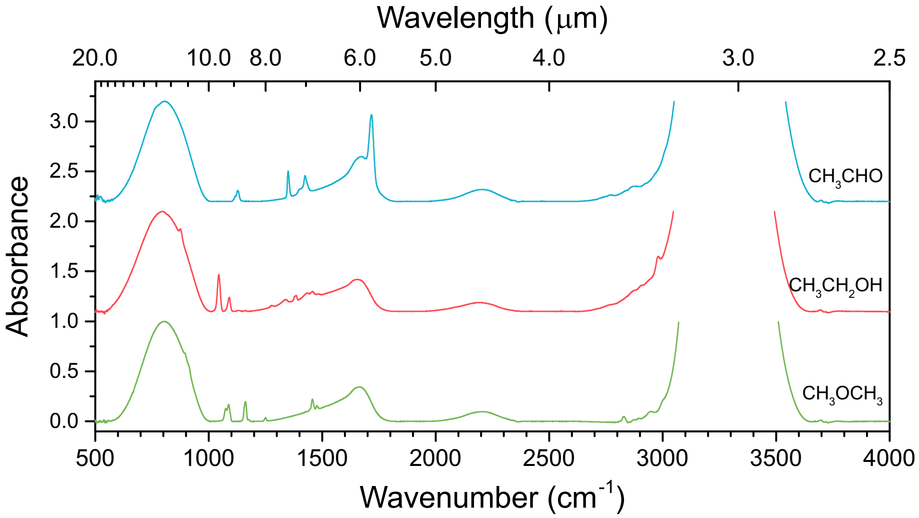

Figure 3.6: Spectra of acetaldehyde (blue), ethanol (red), and dimethyl ether (green) mixed in water at 15 K in the range of 2.5 to 20.0 μm.

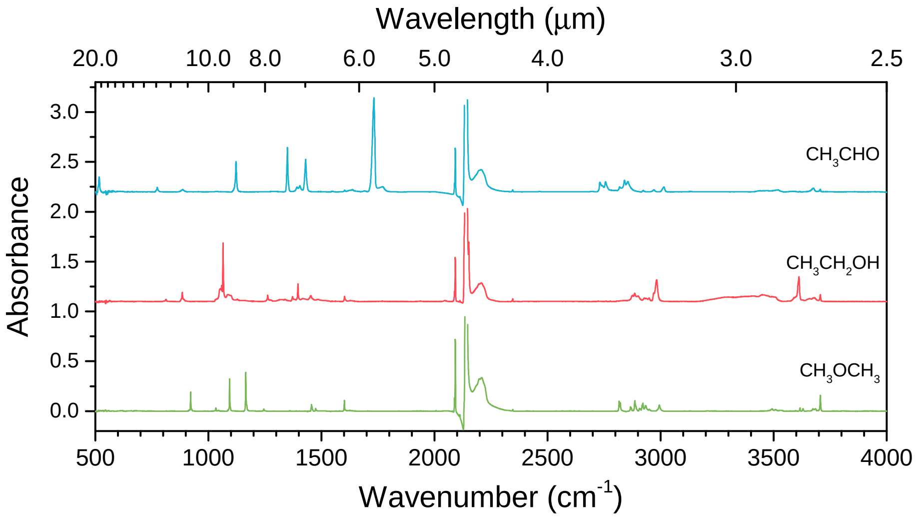

Figure 3.7: Spectra of acetaldehyde (blue), ethanol (red), and dimethyl ether (green) mixed in CO at 15 K in the range of 2.5 to 20.0 μm.

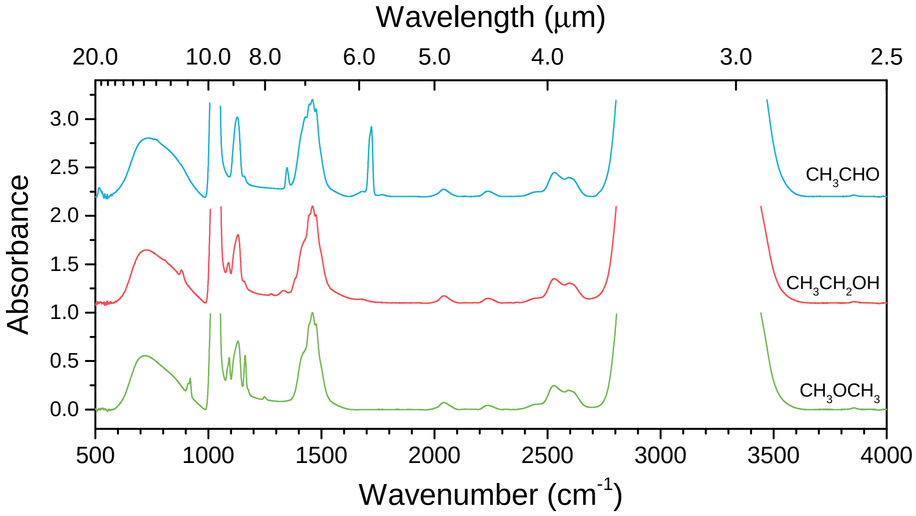

Figure 3.8: Spectra of acetaldehyde (blue), ethanol (red), and dimethyl ether (green) mixed in methanol at 15 K in the range of 2.5 to 20.0 μm.

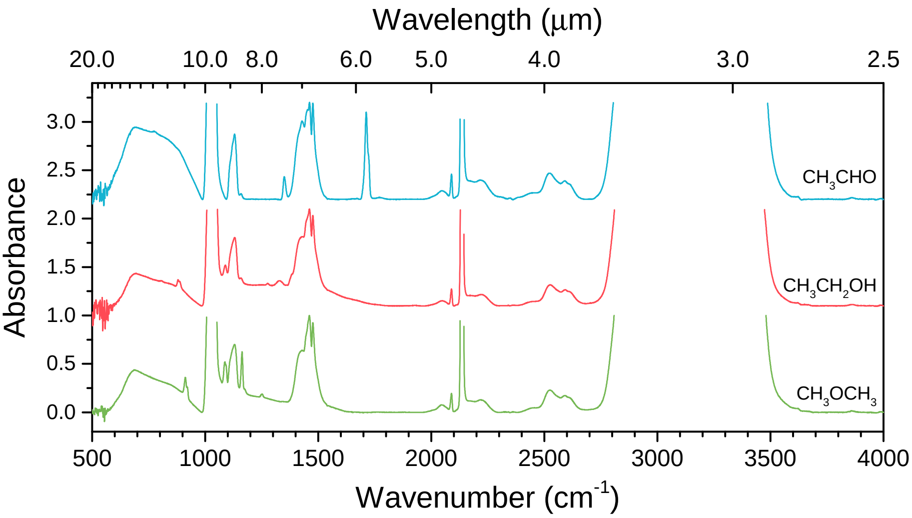

Figure 3.9: Spectra of acetaldehyde (blue), ethanol (red), and dimethyl ether (green) mixed in CO:CH$_3$OH at 15 K in the range of 2.5 to 20.0 μm.

3.B Overview of peak position, FWHM, and integrated absorbance ratios of selected transitions

In this section tables are presented that list peak positions, FWHMs, and integrated absorbance ratios of selected acetaldehyde, ethanol, and dimethyl ether transitions. Where necessary, peak positions are given of both baseline corrected and matrix subtracted spectra. The peak position and FWHM are given in wavenumber (cm^{-1}) and wavelength (μm). Separate tables list the variation in band intensities over a range of temperatures for each mixture (e.g., Table 3.8). Values in these tables are usually normalized to the strongest transition at 15 K, which also remains identifiable over the entire temperature range. Exceptions are made for bands that are potentially in saturation, for example the CO stretching mode in pure acetaldehyde ice.

In the tables various asterisks are used to indicate special circumstances. An asterisk indicates that the FWHM is the result of two or more blended peaks. Double asterisks indicate multiple peaks, which are often caused by a different matrix or surrounding interactions of the band. Occasionally the matrix cannot be properly subtracted from the feature under investigation, which results in FWHMs with higher uncertainty or in FWHMs that cannot be determined at all. Finally, a triple asterisks indicates ice transitions that are thought to be strong enough to saturate the infrared spectrometer signal.

3.B.1 Acetaldehyde

Table 3.4: Peak positions and FWHM of the acetaldehyde CH_3 rocking + CC stretching + CCO bending mode at 8.909 μm.

Mixture	Temp.	$\lambda_{\text{peak},-\text{baseline}}$		$\lambda_{\text{peak},-\text{matrix}}$		FWHM	
	(K)	(cm^{-1})	(μm)	(cm^{-1})	(μm)	(cm^{-1})	(μm)
CH_3CHO	15	1122.4	8.9097	–	–	13.0	0.1032
$CH_3CHO : H_2O$		1116.1	8.9598	1116.1	8.9598	–	–
		1127.7	8.8678	1127.7	8.8678	14.3	0.1121
$CH_3CHO : CO$		1121.9	8.9136	–	–	5.0	0.0394
$CH_3CHO : CH_3OH$		–	–	–	–	–	–
$CH_3CHO : CO : CH_3OH$		–	–	–	–	–	–
CH_3CHO	30	1122.4	8.9097	–	–	13.0	0.1031
$CH_3CHO : H_2O$		1117.5	8.9482	1117.5	8.9482	–	–
		1126.7	8.8754	1126.7	8.8754	14.3	0.1124
$CH_3CHO : CO$		1121.9	8.9136	–	–	5.5	0.0439
$CH_3CHO : CH_3OH$		–	–	–	–	–	–
$CH_3CHO : CO : CH_3OH$		–	–	–	–	–	–
CH_3CHO	70	1122.4	8.9097	–	–	12.5	0.0993
$CH_3CHO : H_2O$		1118.0	8.9443	1118.0	8.9443	–	–
		1124.8	8.8906	1124.8	8.8906	16.3	0.1290
$CH_3CHO : CO$		–	–	–	–	–	–
$CH_3CHO : CH_3OH$		–	–	–	–	–	–
$CH_3CHO : CO : CH_3OH$		–	–	–	–	–	–
CH_3CHO	90	1119.0	8.9366	–	–	6.4	0.0513*
		1120.9	8.9212	–	–	–	–
$CH_3CHO : H_2O$		1118.0	8.9443	1118.0	8.9443	–	–
		1124.3	8.8945	1124.3	8.8945	16.0	0.1268*
$CH_3CHO : CO$		–	–	–	–	–	–
$CH_3CHO : CH_3OH$		–	–	–	–	–	–
$CH_3CHO : CO : CH_3OH$		–	–	–	–	–	–
CH_3CHO	110	1118.5	8.9405	–	–	6.1	0.0485*
		1120.9	8.9212	–	–	–	–
$CH_3CHO : H_2O$		1118.0	8.9443	1118.0	8.9443	–	–
		1124.3	8.8945	1124.3	8.8945	16.0	0.1274*
$CH_3CHO : CO$		–	–	–	–	–	–
$CH_3CHO : CH_3OH$		–	–	–	–	–	–
$CH_3CHO : CO : CH_3OH$		–	–	–	–	–	–
CH_3CHO	120	1118.5	8.9405	–	–	5.9	0.0473
		1120.9	8.9212	–	–	–	–
$CH_3CHO : H_2O$		1117.5	8.9482	1117.5	8.9482	16.2	0.1291
		1122.4	8.9097	1122.4	8.9097	–	–
$CH_3CHO : CO$		–	–	–	–	–	–
$CH_3CHO : CH_3OH$		–	–	–	–	–	–
$CH_3CHO : CO : CH_3OH$		–	–	–	–	–	–

Continued on next page

Table 3.4 – continued from previous page

Mixture	Temp.	$\lambda_{\mathrm{peak,-baseline}}$		$\lambda_{\mathrm{peak,-matrix}}$		FWHM	
	(K)	(cm^{-1})	(μm)	(cm^{-1})	(μm)	(cm^{-1})	(μm)
CH_3CHO	140	–	–	–	–	–	–
CH_3CHO : H_2O		1116.1	8.9598	1116.1	8.9598	10.0	0.0804
CH_3CHO : CO		–	–	–	–	–	–
CH_3CHO : CH_3OH		–	–	–	–	–	–
CH_3CHO : CO : CH_3OH		–	–	–	–	–	–
CH_3CHO	160	–	–	–	–	–	–
CH_3CHO : H_2O		1116.6	8.9559	1116.6	8.9559	10.1	0.0813
CH_3CHO : CO		–	–	–	–	–	–
CH_3CHO : CH_3OH		–	–	–	–	–	–
CH_3CHO : CO : CH_3OH		–	–	–	–	–	–

Notes. $^{(*)}$FWHM result of two or more blended peaks.

Table 3.5: Peak position and FWHM of the acetaldehyde CH_3 s-deformation + CH waging mode at 7.427 μm.

Mixture	Temp.	$\lambda_{\mathrm{peak,-baseline}}$		$\lambda_{\mathrm{peak,-matrix}}$		FWHM	
	(K)	(cm^{-1})	(μm)	(cm^{-1})	(μm)	(cm^{-1})	(μm)
CH_3CHO	15	1346.6	7.4264	–	–	13.5	0.0744*
CH_3CHO : H_2O		1349.9	7.4078	1349.9	7.4078	9.2	0.0502
CH_3CHO : CO		1349.4	7.4104	–	–	4.8	0.0262
CH_3CHO : CH_3OH		1347.5	7.4211	–	–	13.0	0.0714
CH_3CHO : CO : CH_3OH		1349.4	7.4105	–	–	12.6	0.0691
CH_3CHO	30	1346.1	7.4290	–	–	13.7	0.0754
CH_3CHO : H_2O		1349.9	7.4078	1349.9	7.4078	8.8	0.0481
CH_3CHO : CO		1349.9	7.4078	–	–	6.1	0.0337*
CH_3CHO : CH_3OH		1347.5	7.4211	–	–	12.5	0.0686
CH_3CHO : CO : CH_3OH		1349.0	7.4131	–	–	12.2	0.0671
CH_3CHO	70	1346.1	7.4290	–	–	13.2	0.0729
CH_3CHO : H_2O		1349.4	7.4105	1349.4	7.4105	7.7	0.0420
CH_3CHO : CO		–	–	–	–	–	–
CH_3CHO : CH_3OH		1348.0	7.4184	–	–	10.9	0.0600
CH_3CHO : CO : CH_3OH		1348.5	7.4158	–	–	10.8	0.0592
CH_3CHO	90	1348.0	7.4184	–	–	7.3	0.0400*
		1351.9	7.3972	–	–	–	–
CH_3CHO : H_2O		1349.4	7.4105	1349.4	7.4105	7.4	0.0405
CH_3CHO : CO		–	–	–	–	–	–
CH_3CHO : CH_3OH		1348.0	7.4184	–	–	10.2	0.0563
CH_3CHO : CO : CH_3OH		1348.5	7.4158	–	–	10.6	0.0584

Continued on next page

Table 3.5 – continued from previous page

Mixture	Temp.	$\lambda_{\mathrm{peak,-baseline}}$		$\lambda_{\mathrm{peak,-matrix}}$		FWHM	
	(K)	(cm^{-1})	(μm)	(cm^{-1})	(μm)	(cm^{-1})	(μm)
CH_3CHO	110	1348.0	7.4184	–	–	5.4	0.0298
		1351.9	7.3972	–	–	–	–
CH_3CHO : H_2O		1349.4	7.4105	1349.4	7.4105	7.2	0.0393
CH_3CHO : CO		–	–	–	–	–	–
CH_3CHO : CH_3OH		1348.0	7.4184	–	–	9.5	0.0524
CH_3CHO : CO : CH_3OH		1347.0	7.4237	–	–	–	–**
		1352.8	7.3920	–	–	–	–**
CH_3CHO	120	1348.0	7.4184	–	–	5.3	0.0291
		1352.3	7.3946	–	–	–	–
CH_3CHO : H_2O		1349.4	7.4105	1349.4	7.4105	7.0	0.0383
CH_3CHO : CO		–	–	–	–	–	–
CH_3CHO : CH_3OH		1348.0	7.4184	–	–	–	–**
CH_3CHO : CO : CH_3OH		1347.0	7.4237	–	–	–	–**
		1352.8	7.3920	–	–	–	–**
CH_3CHO	140	–	–	–	–	–	–
CH_3CHO : H_2O		1349.0	7.4131	1349.0	7.4131	5.7	0.0315
CH_3CHO : CO		–	–	–	–	–	–
CH_3CHO : CH_3OH		1347.5	7.4211	–	–	–	–**
CH_3CHO : CO : CH_3OH		–	–	–	–	–	–
CH_3CHO	160	–	–	–	–	–	–
CH_3CHO : H_2O		1349.0	7.4131	1349.0	7.4131	5.5	0.0302
CH_3CHO : CO		–	–	–	–	–	–
CH_3CHO : CH_3OH		–	–	–	–	–	–
CH_3CHO : CO : CH_3OH		–	–	–	–	–	–

Notes. (*)FWHM result of two or more blended peaks. (**)FWHM uncertain/not determined owing to uncertain matrix subtraction.

Table 3.6: Peak position and FWHM of the acetaldehyde CH_3 deformation mode at 6.995 μm.

Mixture	Temp.	$\lambda_{\mathrm{peak,-baseline}}$		$\lambda_{\mathrm{peak,-matrix}}$		FWHM	
	(K)	(cm^{-1})	(μm)	(cm^{-1})	(μm)	(cm^{-1})	(μm)
CH_3CHO	15	1429.5	6.9956	–	–	22.6	0.1105
CH_3CHO : H_2O		1424.2	7.0216	1424.2	7.0216	17.0	0.0837
CH_3CHO : CO		1430.4	6.9909	–	–	7.7	0.0379
CH_3CHO : CH_3OH		–	–	–	–	–	–
CH_3CHO : CO : CH_3OH		–	–	–	–	–	–
CH_3CHO	30	1429.5	6.9956	–	–	22.8	0.1115
CH_3CHO : H_2O		1424.7	7.0192	1424.2	7.0216	15.7	0.0772
CH_3CHO : CO		1430.4	6.9909	–	–	9.0	0.0438
CH_3CHO : CH_3OH		–	–	–	–	–	–
CH_3CHO : CO : CH_3OH		–	–	–	–	–	–

Continued on next page

Table 3.6 – continued from previous page

Mixture	Temp.	$\lambda_{\text{peak},-\text{baseline}}$		$\lambda_{\text{peak},-\text{matrix}}$		FWHM	
	(K)	(cm^{-1})	(μm)	(cm^{-1})	(μm)	(cm^{-1})	(μm)
CH_3CHO	70	1428.5	7.0003	–	–	22.6	0.1106
$CH_3CHO : H_2O$		1424.7	7.0192	1424.7	7.0192	14.2	0.0697
$CH_3CHO : CO$		–	–	–	–	–	–
$CH_3CHO : CH_3OH$		–	–	–	–	–	–
$CH_3CHO : CO : CH_3OH$		–	–	–	–	–	–
CH_3CHO	90	1422.7	7.0288	–	–	–	–
		1430.4	6.9909	–	–	13.3	0.0655*
$CH_3CHO : H_2O$		1425.1	7.0169	1425.1	7.0169	13.7	0.0676
$CH_3CHO : CO$		–	–	–	–	–	–
$CH_3CHO : CH_3OH$		–	–	–	–	–	–
$CH_3CHO : CO : CH_3OH$		–	–	–	–	–	–
CH_3CHO	110	1422.7	7.0288	–	–	–	–
		1430.4	6.9909	–	–	13.3	0.0653*
$CH_3CHO : H_2O$		1425.1	7.0169	1425.1	7.0169	13.1	0.0645
$CH_3CHO : CO$		–	–	–	–	–	–
$CH_3CHO : CH_3OH$		–	–	–	–	–	–
$CH_3CHO : CO : CH_3OH$		–	–	–	–	–	–
CH_3CHO	120	1422.7	7.0288	–	–	–	–
		1430.4	6.9909	–	–	13.4	0.0656*
$CH_3CHO : H_2O$		1425.1	7.0169	1425.1	7.0169	12.3	0.0603
$CH_3CHO : CO$		–	–	–	–	–	–
$CH_3CHO : CH_3OH$		–	–	–	–	–	–
$CH_3CHO : CO : CH_3OH$		–	–	–	–	–	–
CH_3CHO	140	–	–	–	–	–	–
$CH_3CHO : H_2O$		1425.1	7.0169	1425.1	7.0169	9.9	0.0488
$CH_3CHO : CO$		–	–	–	–	–	–
$CH_3CHO : CH_3OH$		–	–	–	–	–	–
$CH_3CHO : CO : CH_3OH$		–	–	–	–	–	–
CH_3CHO	160	–	–	–	–	–	–
$CH_3CHO : H_2O$		1425.1	7.0169	1424.7	7.0192	9.9	0.0488
$CH_3CHO : CO$		–	–	–	–	–	–
$CH_3CHO : CH_3OH$		–	–	–	–	–	–
$CH_3CHO : CO : CH_3OH$		–	–	–	–	–	–

Notes. $^{(*)}$FWHM result of two or more blended peaks.

Table 3.7: Peak position and FWHM of the acetaldehyde CO stretching mode at 5.803 μm.

Mixture	Temp.	$\lambda_{\mathrm{peak,-baseline}}$		$\lambda_{\mathrm{peak,-matrix}}$		FWHM	
	(K)	(cm^{-1})	(μm)	(cm^{-1})	(μm)	(cm^{-1})	(μm)
CH_3CHO***	15	1723.6	5.8019	–	–	19.5	0.0659
$CH_3CHO : H_2O$		1716.8	5.8247	1717.8	5.8215	20.9	0.0709
$CH_3CHO : CO$		1732.2	5.7729	–	–	12.6	0.0419
$CH_3CHO : CH_3OH$		1721.2	5.8101	–	–	20.4	0.0690
$CH_3CHO : CO : CH_3OH$		1712.5	5.8395	–	–	17.3	0.0589*
CH_3CHO***	30	1723.6	5.8019	–	–	20.2	0.0682
$CH_3CHO : H_2O$		1716.8	5.8247	1717.8	5.8215	21.2	0.0719
$CH_3CHO : CO$		1732.2	5.7729	–	–	12.9	–
$CH_3CHO : CH_3OH$		1721.6	5.8084	–	–	18.6	0.0630
$CH_3CHO : CO : CH_3OH$		1712.0	5.8411	–	–	19.3	0.0654*
		1722.6	5.8052	–	–	–	–
CH_3CHO***	70	1721.2	5.8101	–	–	21.1	0.0713
$CH_3CHO : H_2O$		1719.2	5.8166	1719.2	5.8166	20.2	0.0685
$CH_3CHO : CO$		–	–	–	–	–	–
$CH_3CHO : CH_3OH$		1722.1	5.8068	–	–	11.9	0.0401
$CH_3CHO : CO : CH_3OH$		1723.1	5.8035	–	–	9.2	0.0311
CH_3CHO***	90	1717.8	5.8215	–	–	18.9	0.0640*
		1722.6	5.8052	–	–	–	–
$CH_3CHO : H_2O$		1719.2	5.8166	1719.7	5.8149	19.8	0.0669
$CH_3CHO : CO$		–	–	–	–	–	–
$CH_3CHO : CH_3OH$		1722.6	5.8052	–	–	10.6	0.0356
$CH_3CHO : CO : CH_3OH$		1723.1	5.8035	–	–	9.5	0.0320
CH_3CHO***	110	1717.8	5.8215	–	–	18.2	0.0615*
		1722.6	5.8052	–	–	–	–
$CH_3CHO : H_2O$		1719.7	5.8149	1719.7	5.8149	20.3	0.0684
$CH_3CHO : CO$		–	–	–	–	–	–
$CH_3CHO : CH_3OH$		1723.1	5.8035	–	–	10.3	0.0347
$CH_3CHO : CO : CH_3OH$		1717.8	5.8215	–	–	–	–
		1720.2	5.8133	–	–	–	–
		1725.0	5.7971	–	–	13.2	0.0445*
CH_3CHO***	120	1718.3	5.8198	–	–	17.6	0.0595*
		1722.6	5.8052	–	–	–	–
$CH_3CHO : H_2O$		1719.7	5.8149	1720.7	5.8117	21.4	0.0722*
$CH_3CHO : CO$		–	–	–	–	–	–
$CH_3CHO : CH_3OH$		1716.8	5.8247	–	–	18.5	0.0627*
		1722.1	5.8068	–	–	–	–
$CH_3CHO : CO : CH_3OH$		1717.8	5.8215	–	–	–	–
		1720.2	5.8133	–	–	–	–
		1725.0	5.7971	–	–	12.3	0.0415*

Continued on next page

Table 3.7 – continued from previous page

Mixture	Temp.	$\lambda_{\mathrm{peak,-baseline}}$		$\lambda_{\mathrm{peak,-matrix}}$		FWHM	
	(K)	(cm^{-1})	(μm)	(cm^{-1})	(μm)	(cm^{-1})	(μm)
CH_3CHO***	140	–	–	–	–	–	–
$CH_3CHO : H_2O$		1730.8	5.7777	1730.8	5.7777	17.2	0.0576*
$CH_3CHO : CO$		–	–	–	–	–	–
$CH_3CHO : CH_3OH$		1717.8	5.8215	–	9.1495	–	–
		1724.5	5.7987	–	8.5959	12.2	0.0412*
$CH_3CHO : CO : CH_3OH$		–	–	–	–	–	–
CH_3CHO***	160	–	–	–	–	–	–
$CH_3CHO : H_2O$		1731.8	5.7745	1731.8	5.7745	12.5	0.0417
$CH_3CHO : CO$		–	–	–	–	–	–
$CH_3CHO : CH_3OH$		–	–	–	–	–	–
$CH_3CHO : CO : CH_3OH$		–	–	–	–	–	–

Notes. $^{(*)}$FWHM result of two or more blended peaks. $^{(***)}$Transition likely saturated.

3.B.2 Acetaldehyde normalized band areas

Table 3.8: Integrated absorbance ratios of selected transitions in pure acetaldehyde.

Temperature (K)	CH_3 rock. + CC stretch. + CCO bend. 8.909μm	CH_3 deform. + CH wag. 7.427μm	CH_3 deform. 6.995 μm	CO stretch. 5.803 μm
15	0.72	1.00	1.07	4.32
30	0.73	1.00	1.07	4.36
70	0.70	0.95	0.99	4.27
90	0.59	0.85	0.87	4.16
110	0.58	0.83	0.85	4.09
120	0.57	0.81	0.82	4.01

Notes. Owing to possible saturation of the C=O stretch mode the band intensities are normalized on the CH_3 s-deformation band at 15 K.

Table 3.9: Integrated absorbance ratios of selected transitions in CH_3CHO:H_2O.

Temperature (K)	CH_3 rock. + CC stretch. + CCO bend. 8.909μm	CH_3 deform. + CH wag. 7.427μm	CH_3 deform. 6.995 μm	CO stretch. 5.803 μm
15	0.15	0.21	0.27	1.00
30	0.16	0.21	0.25	1.02
70	0.15	0.21	0.22	1.00
90	0.15	0.03	0.22	1.01
110	0.15	0.19	0.20	0.94
120	0.15	0.18	0.19	0.83
140	0.12	0.15	0.17	0.61
160	0.11	0.13	0.12	0.57

Table 3.10: Integrated absorbance ratios of selected transitions in CH_3CHO:CO.

Temperature (K)	CH_3 rock. + CC stretch. + CCO bend. 8.909μm	CH_3 deform. + CH wag. 7.427μm	CH_3 deform. 6.995 μm	CO stretch. 5.803 μm
15	0.18	0.21	0.25	1.00
30	0.18	0.22	0.24	1.00

Table 3.11: Integrated absorbance ratios of selected transitions in CH_3CHO:CH_3OH.

Temperature (K)	CH_3 rock. + CC stretch. + CCO bend. 8.909μm	CH_3 deform. + CH wag. 7.427μm	CH_3 deform. 6.995 μm	CO stretch. 5.803 μm
15	–	0.19	–	1.00
30	–	0.19	–	0.99
70	–	0.18	–	0.95
90	–	0.17	–	0.94
110	–	0.16	–	0.96
120	–	–	–	0.62
140	–	–	–	0.35

Table 3.12: Integrated absorbance ratios of selected transitions in CH_3CHO:CO:CH_3OH.

Temperature (K)	CH_3 rock. + CC stretch. + CCO bend. 8.909μm	CH_3 deform. + CH wag. 7.427μm	CH_3 deform. 6.995 μm	CO stretch. 5.803 μm
15	–	0.17	–	1.00
30	–	0.17	–	0.94
70	–	0.15	–	0.76
90	–	0.14	–	0.78
110	–	–	–	0.82
120	–	–	–	0.48

3.B.3 Ethanol

Table 3.13: Peak position and FWHM of the ethanol CC stretching mode at 11.36 μm.

Mixture	Temp.	$\lambda_{\text{peak},-\text{baseline}}$		$\lambda_{\text{peak},-\text{matrix}}$		FWHM	
	(K)	(cm^{-1})	(μm)	(cm^{-1})	(μm)	(cm^{-1})	(μm)
CH_3CH_2OH	15	879.9	11.3654	–	–	18.3	0.2344*
CH_3CH_2OH : H_2O		875.0	11.4280	877.0	11.4029	11.7	0.1526
CH_3CH_2OH : CO		884.7	11.3035	–	–	3.8	0.0482
CH_3CH_2OH : CH_3OH		880.3	11.3592	882.3	11.3344	16.4	0.2105
CH_3CH_2OH : CO : CH_3OH		880.3	11.3592	880.8	11.3530	16.4	0.2097*
		887.6	11.2666	888.1	11.2605	–	–
CH_3CH_2OH	30	880.3	11.3592	–	–	17.9	0.2292*
CH_3CH_2OH : H_2O		874.6	11.4343	877.0	11.4029	12.1	0.1574
CH_3CH_2OH : CO		884.2	11.3096	–	–	4.1	0.0528
CH_3CH_2OH : CH_3OH		880.8	11.3530	882.3	11.3344	16.2	0.2074
CH_3CH_2OH : CO : CH_3OH		880.8	11.3530	880.8	11.3530	16.2	0.2073*
		888.1	11.2605	888.1	11.2605	–	–
CH_3CH_2OH	70	881.8	11.3406	–	–	17.3	0.2211*
CH_3CH_2OH : H_2O		874.1	11.4406	876.5	11.4092	11.8	0.1540
CH_3CH_2OH : CO		–	–	–	–	–	–
CH_3CH_2OH : CH_3OH		881.3	11.3468	882.8	11.3282	15.5	0.1976
CH_3CH_2OH : CO : CH_3OH		881.3	11.3468	–	–	–	–
		887.6	11.2666	888.1	11.2605	14.3	0.1830*
CH_3CH_2OH	100	881.8	11.3406	–	–	16.8	0.2144*
CH_3CH_2OH : H_2O		874.1	11.4406	876.5	11.4092	11.0	0.1429
CH_3CH_2OH : CO		–	–	–	–	–	–
CH_3CH_2OH : CH_3OH		881.3	11.3468	883.2	11.3220	14.8	0.1894
CH_3CH_2OH : CO : CH_3OH		883.2	11.3220	887.6	11.2666	14.4	0.1838*
CH_3CH_2OH	120	882.3	11.3344	–	–	14.2	0.1805*
		891.0	11.2240	–	–	–	–
CH_3CH_2OH : H_2O		873.1	11.4533	876.0	11.4154	11.5	0.1493
CH_3CH_2OH : CO		–	–	–	–	–	–
CH_3CH_2OH : CH_3OH		880.8	11.3530	882.3	11.3344	16.5	0.2107
CH_3CH_2OH : CO : CH_3OH		880.8	11.3530	883.2	11.3220	–	–
		889.5	11.2422	889.5	11.2422	18.5	0.2355*
CH_3CH_2OH	130	882.8	11.3282	–	–	5.2	0.0662
		891.4	11.2179	–	–	5.4	0.0678
CH_3CH_2OH : H_2O		873.6	11.4469	876.0	11.4154	11.4	0.1485
CH_3CH_2OH : CO		–	–	–	–	–	–
CH_3CH_2OH : CH_3OH		878.9	11.3779	882.3	11.3344	18.2	0.2319
CH_3CH_2OH : CO : CH_3OH		880.8	11.3530	883.2	11.3220	16.4	0.2098*

Continued on next page

Table 3.13 – continued from previous page

Mixture	Temp.	$\lambda_{\text{peak},-\text{baseline}}$		$\lambda_{\text{peak},-\text{matrix}}$		FWHM	
	(K)	(cm^{-1})	(μm)	(cm^{-1})	(μm)	(cm^{-1})	(μm)
CH_3CH_2OH	140	882.8	11.3282	–	–	5.0	0.0642
		891.4	11.2179	–	–	5.2	0.0659
$CH_3CH_2OH : H_2O$		872.6	11.4596	876.0	11.4154	11.7	0.1518
$CH_3CH_2OH : CO$		–	–	–	–	–	–
$CH_3CH_2OH : CH_3OH$		880.8	11.3530	881.8	11.3406	15.4	0.1964
$CH_3CH_2OH : CO : CH_3OH$		880.8	11.3530	881.3	11.3468	15.1	0.1934
CH_3CH_2OH	150	882.8	11.3282	–	–	5.6	0.0713
		891.0	11.2240	–	–	5.5	0.0688
$CH_3CH_2OH : H_2O$		873.1	11.4533	876.0	11.4154	12.2	0.1582
$CH_3CH_2OH : CO$		–	–	–	–	–	–
$CH_3CH_2OH : CH_3OH$		880.8	11.3530	881.3	11.3468	14.0	0.1800
$CH_3CH_2OH : CO : CH_3OH$		880.8	11.3530	881.3	11.3468	13.6	0.1740
CH_3CH_2OH	160	–	–	–	–	–	–
$CH_3CH_2OH : H_2O$		872.1	11.4659	876.0	11.4154	12.3	0.1605
$CH_3CH_2OH : CO$		–	–	–	–	–	–
$CH_3CH_2OH : CH_3OH$		–	–	–	–	–	–
$CH_3CH_2OH : CO : CH_3OH$		–	–	–	–	–	–

Notes. $^{(*)}$FWHM result of two or more blended peaks.

Table 3.14: Peak position and FWHM of the ethanol CO stretching mode at 9.514 μm.

Mixture	Temp.	$\lambda_{\text{peak},-\text{baseline}}$		$\lambda_{\text{peak},-\text{matrix}}$		FWHM	
	(K)	(cm^{-1})	(μm)	(cm^{-1})	(μm)	(cm^{-1})	(μm)
CH_3CH_2OH	15	1051.0	9.5146	–	–	19.0	0.1724
$CH_3CH_2OH : H_2O$		1044.3	9.5761	1044.3	9.5761	14.3	0.1315
$CH_3CH_2OH : CO$		1065.0	9.3897	–	–	2.9	0.0253
$CH_3CH_2OH : CH_3OH$		–	–	–	–	–	–
$CH_3CH_2OH : CO : CH_3OH$		–	–	–	–	–	–
CH_3CH_2OH	30	1051.0	9.5146	–	–	17.6	0.1598
$CH_3CH_2OH : H_2O$		1044.3	9.5761	1044.3	9.5761	14.2	0.1307
$CH_3CH_2OH : CO$		1065.0	9.3897	–	–	2.8	0.0243
$CH_3CH_2OH : CH_3OH$		–	–	–	–	–	–
$CH_3CH_2OH : CO : CH_3OH$		–	–	–	–	–	–
CH_3CH_2OH	70	1051.0	9.5146	–	–	16.0	0.1442
$CH_3CH_2OH : H_2O$		1043.8	9.5805	1043.8	9.5805	14.0	0.1288
$CH_3CH_2OH : CO$		–	–	–	–	–	–
$CH_3CH_2OH : CH_3OH$		–	–	–	–	–	–
$CH_3CH_2OH : CO : CH_3OH$		–	–	–	–	–	–

Continued on next page

Table 3.14 – continued from previous page

Mixture	Temp.	$\lambda_{\mathrm{peak,-baseline}}$		$\lambda_{\mathrm{peak,-matrix}}$		FWHM	
	(K)	(cm^{-1})	(μm)	(cm^{-1})	(μm)	(cm^{-1})	(μm)
CH_3CH_2OH	100	1051.0	9.5146	–	–	15.0	0.1358
$CH_3CH_2OH : H_2O$		1043.8	9.5805	1043.8	9.5805	14.0	0.1282
$CH_3CH_2OH : CO$		–	–	–	–	–	–
$CH_3CH_2OH : CH_3OH$		–	–	–	–	–	–
$CH_3CH_2OH : CO : CH_3OH$		–	–	–	–	–	–
CH_3CH_2OH	120	1046.2	9.5585	–	–	14.3	0.1296*
		1055.4	9.4755	–	–	–	–
$CH_3CH_2OH : H_2O$		1043.8	9.5805	1043.8	9.5805	14.1	0.1294
$CH_3CH_2OH : CO$		–	–	–	–	–	–
$CH_3CH_2OH : CH_3OH$		–	–	–	–	–	–
$CH_3CH_2OH : CO : CH_3OH$		–	–	–	–	–	–
CH_3CH_2OH	130	1045.7	9.5629	–	–	6.8	0.0624
		1056.3	9.4669		–	–	–
$CH_3CH_2OH : H_2O$		1043.8	9.5805	1043.8	9.5805	14.4	0.1325
$CH_3CH_2OH : CO$		–	–	–	–	–	–
$CH_3CH_2OH : CH_3OH$		–	–	–	–	–	–
$CH_3CH_2OH : CO : CH_3OH$		–	–	–	–	–	–
CH_3CH_2OH	140	1045.7	9.5629	–	–	6.7	0.0611
		1056.3	9.4669	–	–	6.5	0.0586
$CH_3CH_2OH : H_2O$		1044.3	9.5761	1044.3	9.5761	16.0	0.1469
$CH_3CH_2OH : CO$		–	–	–	–	–	–
$CH_3CH_2OH : CH_3OH$		–	–	–	–	–	–
$CH_3CH_2OH : CO : CH_3OH$		–	–	–	–	–	–
CH_3CH_2OH	150	1045.7	9.5629	–	–	7.6	0.0690
		1055.8	9.4712	–	–	–	–
$CH_3CH_2OH : H_2O$		1044.3	9.5761	1044.3	9.5761	17.1	0.1564
$CH_3CH_2OH : CO$		–	–	–	–	–	–
$CH_3CH_2OH : CH_3OH$		–	–	–	–	–	–
$CH_3CH_2OH : CO : CH_3OH$		–	–	–	–	–	–
CH_3CH_2OH	160	–	–	–	–	–	–
$CH_3CH_2OH : H_2O$		1044.7	9.5717	1044.7	9.5717	17.9	0.1641
$CH_3CH_2OH : CO$		–	–	–	–	–	–
$CH_3CH_2OH : CH_3OH$		–	–	–	–	–	–
$CH_3CH_2OH : CO : CH_3OH$		–	–	–	–	–	–

Notes. $^{(*)}$FWHM result of two or more blended peaks.

Table 3.15: Peak position and FWHM of the ethanol CH_3 rocking mode at 9.170 μm.

Mixture	Temp.	$\lambda_{\mathrm{peak,-baseline}}$		$\lambda_{\mathrm{peak,-matrix}}$		FWHM	
	(K)	(cm^{-1})	(μm)	(cm^{-1})	(μm)	(cm^{-1})	(μm)
CH_3CH_2OH	15	1090.5	9.1697	–	–	24.4	0.2057
$CH_3CH_2OH : H_2O$		1090.1	9.1738	1090.1	9.1738	12.9	0.1085
$CH_3CH_2OH : CO$		1084.8	9.2186	–	–	–	–
$CH_3CH_2OH : CH_3OH$		1088.6	9.1859	1088.6	9.1859	11.8	0.0996
$CH_3CH_2OH : CO : CH_3OH$		1089.6	9.1778	1087.7	9.1941	11.8	0.1001
CH_3CH_2OH	30	1091.0	9.1657	–	–	23.5	0.1978
$CH_3CH_2OH : H_2O$		1090.1	9.1738	1090.1	9.1738	13.0	0.1097
$CH_3CH_2OH : CO$		1097.8	9.1093	–	–	25.3	0.2122
$CH_3CH_2OH : CH_3OH$		1089.1	9.1819	1089.6	9.1778	11.3	0.0954
$CH_3CH_2OH : CO : CH_3OH$		1090.1	9.1738	1089.6	9.1778	11.3	0.0955
CH_3CH_2OH	70	1091.5	9.1616	–	–	21.4	0.1799
$CH_3CH_2OH : H_2O$		1090.1	9.1738	1090.1	9.1738	12.7	0.1067
$CH_3CH_2OH : CO$		–	–	–	–	–	–
$CH_3CH_2OH : CH_3OH$		1089.6	9.1778	1090.1	9.1738	11.0	0.0926
$CH_3CH_2OH : CO : CH_3OH$		1091.5	9.1616	1091.5	9.1616	10.9	0.0915
CH_3CH_2OH	100	1091.5	9.1616	–	–	20.6	0.1732
$CH_3CH_2OH : H_2O$		1089.6	9.1778	1089.6	9.1778	12.6	0.1064
$CH_3CH_2OH : CO$		–	–	–	–	–	–
$CH_3CH_2OH : CH_3OH$		1089.6	9.1778	1090.1	9.1738	10.7	0.0901
$CH_3CH_2OH : CO : CH_3OH$		1089.6	9.1778	1089.6	9.1778	10.9	0.0921
CH_3CH_2OH	120	1093.0	9.1495	–	–	20.4	0.1711
$CH_3CH_2OH : H_2O$		1089.6	9.1778	1089.6	9.1778	12.8	0.1076
$CH_3CH_2OH : CO$		–	–	–	–	–	–
$CH_3CH_2OH : CH_3OH$		1089.1	9.1819	1089.6	9.1778	10.5	0.0881
$CH_3CH_2OH : CO : CH_3OH$		1089.6	9.1778	1089.6	9.1778	10.7	0.0903
CH_3CH_2OH	130	1095.9	9.1253	–	–	17.8	0.1492
$CH_3CH_2OH : H_2O$		1089.6	9.1778	1089.6	9.1778	12.8	0.1080
$CH_3CH_2OH : CO$		–	–	–	–	–	–
$CH_3CH_2OH : CH_3OH$		1089.1	9.1819	1089.1	9.1819	10.2	0.0857
$CH_3CH_2OH : CO : CH_3OH$		1089.6	9.1778	1089.6	9.1778	9.7	0.0815
CH_3CH_2OH	140	1095.9	9.1253	–	–	16.9	0.1414
$CH_3CH_2OH : H_2O$		1089.6	9.1778	1089.6	9.1778	13.4	0.1127
$CH_3CH_2OH : CO$		–	–	–	–	–	–
$CH_3CH_2OH : CH_3OH$		1089.6	9.1778	1090.1	9.1738	12.1	0.1019
$CH_3CH_2OH : CO : CH_3OH$		1089.6	9.1778	1089.6	9.1778	12.6	0.1063
CH_3CH_2OH	150	1094.9	9.1334	–	–	17.2	0.1444
$CH_3CH_2OH : H_2O$		1088.6	9.1859	1088.6	9.1860	14.6	0.1230
$CH_3CH_2OH : CO$		–	–	–	–	–	–
$CH_3CH_2OH : CH_3OH$		1090.1	9.1738	1090.1	9.1738	12.2	0.1024
$CH_3CH_2OH : CO : CH_3OH$		1089.6	9.1778	1089.6	9.1778	12.4	0.1043

Continued on next page

Table 3.15 – continued from previous page

Mixture	Temp.	$\lambda_{\text{peak},-\text{baseline}}$		$\lambda_{\text{peak},-\text{matrix}}$		FWHM	
	(K)	(cm^{-1})	(μm)	(cm^{-1})	(μm)	(cm^{-1})	(μm)
CH_3CH_2OH	160	–	–	–	–	–	–
CH_3CH_2OH : H_2O		1088.6	9.1859	1088.6	9.1859	15.1	0.1275
CH_3CH_2OH : CO		–	–	–	–	–	–
CH_3CH_2OH : CH_3OH		–	–	–	–	–	–
CH_3CH_2OH : CO : CH_3OH		–	–	–	–	–	–

Table 3.16: Peak position and FWHM of the ethanol CH_2 torsion mode at 7.842 μm.

Mixture	Temp.	$\lambda_{\text{peak},-\text{baseline}}$		$\lambda_{\text{peak},-\text{matrix}}$		FWHM	
	(K)	(cm^{-1})	(μm)	(cm^{-1})	(μm)	(cm^{-1})	(μm)
CH_3CH_2OH	15	1275.2	7.8419	–	–	18.5	0.1133
CH_3CH_2OH : H_2O		1278.1	7.8242	1276.2	7.8360	11.9	0.0728
CH_3CH_2OH : CO		1262.2	7.9228	–	–	3.7	0.0231
		1273.8	7.8508	–	–	–	–
CH_3CH_2OH : CH_3OH		1278.6	7.8212	1278.6	7.8212	12.2	0.0746
CH_3CH_2OH : CO : CH_3OH		1276.2	7.8360	1276.2	7.8360	11.5	0.0707
CH_3CH_2OH	30	1275.7	7.8390	–	–	16.9	0.1035
CH_3CH_2OH : H_2O		1276.2	7.8360	1276.2	7.8360	12.8	0.0784
CH_3CH_2OH : CO		1262.7	7.9198	–	–	3.1	0.0193
		1276.2	7.8360	–	–	20.6	0.1257
CH_3CH_2OH : CH_3OH		1278.6	7.8212	1278.6	7.8212	11.1	0.0680
CH_3CH_2OH : CO : CH_3OH		1276.2	7.8360	1276.2	7.8360	10.3	0.0630
CH_3CH_2OH	70	1276.2	7.8360	–	–	14.4	0.0881
CH_3CH_2OH : H_2O		1278.1	7.8242	1276.2	7.8360	12.5	0.0766
CH_3CH_2OH : CO		–	–	–	–	–	–
CH_3CH_2OH : CH_3OH		1278.6	7.8212	1278.6	7.8212	12.1	0.0738
CH_3CH_2OH : CO : CH_3OH		1278.6	7.8212	1278.6	7.8212	10.0	0.0612
CH_3CH_2OH	100	1276.2	7.8360	–	–	13.9	0.0853
CH_3CH_2OH : H_2O		1278.1	7.8242	1278.1	7.8242	13.0	0.0796
CH_3CH_2OH : CO		–	–	–	–	–	–
CH_3CH_2OH : CH_3OH		1278.6	7.8212	1278.6	7.8212	11.6	0.0711**
CH_3CH_2OH : CO : CH_3OH		1278.6	7.8212	1278.6	7.8212	12.2	0.0744
CH_3CH_2OH	120	1277.6	7.8271	–	–	10.5	0.0643
CH_3CH_2OH : H_2O		1278.1	7.8242	1276.2	7.8360	13.4	0.0823
CH_3CH_2OH : CO		–	–	–	–	–	–
CH_3CH_2OH : CH_3OH		1279.1	7.8183	1278.6	7.8212	9.1	0.0556**
CH_3CH_2OH : CO : CH_3OH		1280.5	7.8094	1278.6	7.8212	8.2	0.0501
CH_3CH_2OH	130	1278.1	7.8242	–	–	7.3	0.0448
CH_3CH_2OH : H_2O		1277.6	7.8271	1276.6	7.8330	13.5	0.0829
CH_3CH_2OH : CO		–	–	–	–	–	–
CH_3CH_2OH : CH_3OH		1280.5	7.8094	1278.6	7.8212	8.9	0.0547
CH_3CH_2OH : CO : CH_3OH		1278.6	7.8212	1278.6	7.8212	8.1	0.0495

Continued on next page

Table 3.16 – continued from previous page

Mixture	Temp.	$\lambda_{\mathrm{peak,-baseline}}$		$\lambda_{\mathrm{peak,-matrix}}$		FWHM	
	(K)	(cm^{-1})	(μm)	(cm^{-1})	(μm)	(cm^{-1})	(μm)
CH_3CH_2OH	140	1277.6	7.8271	–	–	7.0	0.0427
$CH_3CH_2OH : H_2O$		1277.6	7.8271	1276.2	7.8360	14.0	0.0862
$CH_3CH_2OH : CO$		–	–	–	–	–	–
$CH_3CH_2OH : CH_3OH$		1279.1	7.8183	1278.1	7.8242	8.5	0.0519
$CH_3CH_2OH : CO : CH_3OH$		1280.5	7.8094	1276.2	7.8360	9.8	0.0604
CH_3CH_2OH	150	1277.6	7.8271	–	–	7.7	0.0471
$CH_3CH_2OH : H_2O$		1277.6	7.8271	1275.2	7.8419	13.5	0.0827
$CH_3CH_2OH : CO$		–	–	–	–	–	–
$CH_3CH_2OH : CH_3OH$		1278.1	7.8242	1276.2	7.8360	9.6	0.0590
$CH_3CH_2OH : CO : CH_3OH$		1278.6	7.8212	1276.2	7.8360	9.9	0.0609
CH_3CH_2OH	160	–	–	–	–	–	–
$CH_3CH_2OH : H_2O$		1277.1	7.8301	1275.2	7.8419	13.5	0.0831
$CH_3CH_2OH : CO$		–	–	–	–	–	–
$CH_3CH_2OH : CH_3OH$		–	–	–	–	–	–
$CH_3CH_2OH : CO : CH_3OH$		–	–	–	–	–	–

Notes. $^{(**)}$FWHM uncertain/not determined owing to uncertain matrix subtraction.

Table 3.17: Peak position and FWHM of the ethanol OH deformation mode at 7.518 μm.

Mixture	Temp.	$\lambda_{\mathrm{peak,-baseline}}$		$\lambda_{\mathrm{peak,-matrix}}$		FWHM	
	(K)	(cm^{-1})	(μm)	(cm^{-1})	(μm)	(cm^{-1})	(μm)
CH_3CH_2OH	15	1330.2	7.5179	–	–	50.9	0.2865
$CH_3CH_2OH : H_2O$		1337.9	7.4745	1337.4	7.4772	30.1	0.1690
$CH_3CH_2OH : CO$		1339.3	7.4665	–	–	40.6	0.2306*
$CH_3CH_2OH : CH_3OH$		1332.6	7.5043	1332.6	7.5043	33.6	0.1894
$CH_3CH_2OH : CO : CH_3OH$		1328.7	7.5261	1329.2	7.5233	33.7	0.1904
CH_3CH_2OH	30	1330.2	7.5179	–	–	48.6	0.2726
$CH_3CH_2OH : H_2O$		1337.9	7.4745	1337.9	7.4745	32.3	0.1816
$CH_3CH_2OH : CO$		1326.8	7.5370	–	–	38.4	0.2176*
$CH_3CH_2OH : CH_3OH$		1335.5	7.4880	1333.1	7.5016	35.0	0.1967
$CH_3CH_2OH : CO : CH_3OH$		1331.1	7.5125	1331.1	7.5125	30.1	0.1698
CH_3CH_2OH	70	1329.7	7.5206	–	–	49.4	0.2770
$CH_3CH_2OH : H_2O$		1339.8	7.4638	1337.9	7.4745	31.3	0.1758
$CH_3CH_2OH : CO$		–	–	–	–	–	–
$CH_3CH_2OH : CH_3OH$		1335.5	7.4880	1333053.0	7.5016	43.4	0.2426
$CH_3CH_2OH : CO : CH_3OH$		1335.5	7.4880	1331.1	7.5125	38.8	0.2165
CH_3CH_2OH	100	1329.7	7.5206	–	–	49.4	0.2770
$CH_3CH_2OH : H_2O$		1339.8	7.4638	1337.9	7.4745	31.6	0.1771
$CH_3CH_2OH : CO$		–	–	–	–	–	–
$CH_3CH_2OH : CH_3OH$		1335.5	7.4880	1331.1	7.5125	33.3	0.1875
$CH_3CH_2OH : CO : CH_3OH$		1335.5	7.4880	1331.1	7.5125	32.1	0.1807

Continued on next page

Table 3.17 – continued from previous page

Mixture	Temp.	$\lambda_{\text{peak},-\text{baseline}}$		$\lambda_{\text{peak},-\text{matrix}}$		FWHM	
	(K)	(cm^{-1})	(μm)	(cm^{-1})	(μm)	(cm^{-1})	(μm)
CH_3CH_2OH	120	1325.3	7.5452	–	–	20.5	0.1166*
		1357.6	7.3657	–	–	–	–
CH_3CH_2OH : H_2O		1340.3	7.4611	1337.4	7.4772	32.9	0.1844
CH_3CH_2OH : CO		–	–	–	–	–	–
CH_3CH_2OH : CH_3OH		–	–	–	–	–	–**
CH_3CH_2OH : CO : CH_3OH		–	–	–	–	–	–**
CH_3CH_2OH	130	1324.4	7.5507	–	–	13.6	0.0778
		1357.6	7.3657	–	–	4.9	0.0264
CH_3CH_2OH : H_2O		1341.2	7.4557	1337.4	7.4772	32.8	0.1843
CH_3CH_2OH : CO		–	–	–	–	–	–
CH_3CH_2OH : CH_3OH		–	–	–	–	–	–**
CH_3CH_2OH : CO : CH_3OH		–	–	–	–	–	–**
CH_3CH_2OH	140	1324.4	7.5507	–	–	13.7	0.0783
		1357.6	7.3657	–	–	5.2	0.0281
CH_3CH_2OH : H_2O		1341.2	7.4557	1337.4	7.4772	34.4	0.1933
CH_3CH_2OH : CO		–	–	–	–	–	–
CH_3CH_2OH : CH_3OH		–	–	–	–	–	–**
CH_3CH_2OH : CO : CH_3OH		–	–	–	–	–	–**
CH_3CH_2OH	150	1324.4	7.5507	–	–	14.3	0.0819
		1357.6	7.3657	–	–	6.7	0.0362
CH_3CH_2OH : H_2O		1341.2	7.4557	1338.4	7.4719	32.4	0.1825
CH_3CH_2OH : CO		–	–	–	–	–	–
CH_3CH_2OH : CH_3OH		–	–	–	–	–	–**
CH_3CH_2OH : CO : CH_3OH		–	–	–	–	–	–**
CH_3CH_2OH	160	–	–	–	–	–	–
CH_3CH_2OH : H_2O		1341.2	7.4557	1335.0	7.4907	34.8	0.1960
CH_3CH_2OH : CO		–	–	–	–	–	–
CH_3CH_2OH : CH_3OH		–	–	–	–	–	–
CH_3CH_2OH : CO : CH_3OH		–	–	–	–	–	–

Notes. (*)FWHM result of two or more blended peaks. (**)FWHM uncertain/not determined owing to uncertain matrix subtraction.

Table 3.18: Peak position and FWHM of the ethanol CH_3 s-deformation mode at 7.24 μm.

Mixture	Temp.	$\lambda_{\mathrm{peak,-baseline}}$		$\lambda_{\mathrm{peak,-matrix}}$		FWHM	
	(K)	(cm^{-1})	(μm)	(cm^{-1})	(μm)	(cm^{-1})	(μm)
CH_3CH_2OH	15	1381.3	7.2397	–	–	20.7	0.1088*
$CH_3CH_2OH : H_2O$		1379.8	7.2473	1379.3	7.2499	–	–
		1385.6	7.2171	1385.6	7.2171	15.6	0.0817
$CH_3CH_2OH : CO$		1372.1	7.2881	–	–	5.7	0.0304
		1396.2	7.1622	–	–	3.4	0.0175
$CH_3CH_2OH : CH_3OH$		1383.7	7.2271	1381.3	7.2397	14.9	0.0782**
$CH_3CH_2OH : CO : CH_3OH$		1384.2	7.2246	1381.7	7.2372	15.0	0.0788**
CH_3CH_2OH	30	1381.3	7.2397	–	–	19.8	0.1042*
$CH_3CH_2OH : H_2O$		1379.8	7.2473	1379.3	7.2499	–	–
		1385.6	7.2171	1385.1	7.2196	16.3	0.0852*
$CH_3CH_2OH : CO$		1372.6	7.2855	–	–	7.5	0.0397
		1383.7	7.2271	–	–	–	–
		1396.2	7.1622	–	–	3.3	0.0171
$CH_3CH_2OH : CH_3OH$		1384.2	7.2246	1381.3	7.2397	14.9	0.0784**
$CH_3CH_2OH : CO : CH_3OH$		1383.7	7.2271	1381.7	7.2372	15.9	0.0838**
CH_3CH_2OH	70	1380.8	7.2423	–	–	19.1	0.1005*
$CH_3CH_2OH : H_2O$		1379.3	7.2499	1379.3	7.2499	–	–
		1385.1	7.2196	1385.1	7.2196	16.7	0.0878
$CH_3CH_2OH : CO$		–	–	–	–	–	–
$CH_3CH_2OH : CH_3OH$		1383.2	7.2297	1380.8	7.2423	–	–
$CH_3CH_2OH : CO : CH_3OH$		1381.7	7.2372	1381.7	7.2372	16.2	0.0853**
CH_3CH_2OH	100	1380.3	7.2448	–	–	15.8	0.0833*
$CH_3CH_2OH : H_2O$		1379.3	7.2499	1378.9	7.2524	–	–
		1385.1	7.2196	1384.6	7.2221	17.5	0.0919*
$CH_3CH_2OH : CO$		–	–	–	–	–	–
$CH_3CH_2OH : CH_3OH$		1382.2	7.2347	1380.8	7.2423	15.0	0.0790**
$CH_3CH_2OH : CO : CH_3OH$		1381.7	7.2372	1381.3	7.2397	12.1	0.0635**
CH_3CH_2OH	120	1372.6	7.2855	–	–	15.8	0.0833
		1382.7	7.2322	–	–	–	–
$CH_3CH_2OH : H_2O$		1378.9	7.2524	1378.4	7.2549	–	–
		1384.6	7.2221	1384.6	7.2221	18.4	0.0967*
$CH_3CH_2OH : CO$		–	–	–	–	–	–
$CH_3CH_2OH : CH_3OH$		1381.7	7.2372	1381.3	7.2397	14.1	0.0740**
$CH_3CH_2OH : CO : CH_3OH$		1381.7	7.2372	1381.7	7.2372	12.6	0.0664**
CH_3CH_2OH	130	1373.1	7.2830	–	–	4.4	0.0235
		1385.1	7.2196	–	–	–	–
$CH_3CH_2OH : H_2O$		1378.4	7.2549	1378.4	7.2549	–	–
		1384.6	7.2221	1384.2	7.2246	18.6	0.0977*
$CH_3CH_2OH : CO$		–	–	–	–	–	–
$CH_3CH_2OH : CH_3OH$		1381.3	7.2397	1381.3	7.2397	14.6	0.0767**
$CH_3CH_2OH : CO : CH_3OH$		1381.7	7.2372	1381.7	7.2372	13.7	0.0721**

Continued on next page

Table 3.18 – continued from previous page

Mixture	Temp.	$\lambda_{\mathrm{peak},-\mathrm{baseline}}$		$\lambda_{\mathrm{peak},-\mathrm{matrix}}$		FWHM	
	(K)	(cm^{-1})	(μm)	(cm^{-1})	(μm)	(cm^{-1})	(μm)
CH_3CH_2OH	140	1373.1	7.2830	–	–	4.5	0.0239
		1385.1	7.2196	–	–	–	–
CH_3CH_2OH : H_2O		1380.3	7.2448	1378.4	7.2549	19.0	0.1000*
		1384.2	7.2246	1383.7	7.2271	–	–
CH_3CH_2OH : CO		–	–	–	–	–	–
CH_3CH_2OH : CH_3OH		1381.3	7.2397	1381.3	7.2397	14.6	0.0769**
CH_3CH_2OH : CO : CH_3OH		1381.3	7.2397	1381.7	7.2372	13.9	0.0733**
CH_3CH_2OH	150	1373.1	7.2830	–	–	5.2	0.0277
		1384.6	7.2221	–	–	–	–
CH_3CH_2OH : H_2O		1380.3	7.2448	1378.4	7.2549	18.6	0.0975*
		1383.7	7.2271	1383.7	7.2271	–	–
CH_3CH_2OH : CO		–	–	–	–	–	–
CH_3CH_2OH : CH_3OH		1381.7	7.2372	1381.3	7.2397	14.3	0.0752**
CH_3CH_2OH : CO : CH_3OH		1381.7	7.2372	1381.7	7.2372	14.0	0.0734**
CH_3CH_2OH	160	–	–	–	–	–	–
CH_3CH_2OH : H_2O		1380.3	7.2448	1380.3	7.2448	18.9	0.0994
CH_3CH_2OH : CO		–	–	–	–	–	–
CH_3CH_2OH : CH_3OH		–	–	–	–	–	–
CH_3CH_2OH : CO : CH_3OH		–	–	–	–	–	–

Notes. (*)FWHM result of two or more blended peaks. (**)FWHM uncertain/not determined owing to uncertain matrix subtraction.

3.B.4 Ethanol normalized band areas

Table 3.19: Integrated absorbance ratios of selected transitions in pure ethanol.

Temp. (K)	CC stretch. 11.36 μm	CO stretch. 9.514 μm	CH_3 rock. 9.170 μm	CH_2 tors. 7.842 μm	OH deform. 7.518 μm	CH_3 s-deform. 7.240 μm
15	0.23	1.00	0.59	0.06	0.35	0.20
30	0.24	1.00	0.63	0.06	0.34	0.20
70	0.24	1.00	0.65	0.06	0.38	0.23
100	0.25	1.03	0.66	0.06	0.42	0.25
120	0.28	1.04	0.64	0.05	0.47	0.23
130	0.29	1.03	0.64	0.04	0.43	0.20
140	0.28	1.02	0.64	0.04	0.44	0.21
150	0.26	0.96	0.59	0.04	0.41	0.20

Table 3.20: Integrated absorbance ratios of selected transitions in CH_3CH_2OH:H_2O.

Temp. (K)	CC stretch. 11.36 μm	CO stretch. 9.514 μm	CH_3 rock. 9.170 μm	CH_2 tors. 7.842 μm	OH deform. 7.518 μm	CH_3 s-deform. 7.240 μm
15	0.16	1.00	0.35	0.04	0.24	0.17
30	0.17	1.01	0.35	0.05	0.28	0.19
70	0.16	1.01	0.34	0.05	0.28	0.20
100	0.12	0.97	0.33	0.05	0.30	0.21
120	0.12	0.93	0.33	0.05	0.30	0.21
130	0.12	0.93	0.33	0.04	0.27	0.21
140	0.11	0.88	0.35	0.04	0.26	0.20
150	0.11	0.86	0.36	0.04	0.21	0.16
160	0.09	0.74	0.32	0.03	0.17	0.14

Table 3.21: Integrated absorbance ratios of selected transitions in CH_3CH_2OH:CH_3OH.

Temp. (K)	CC stretch. 11.36 μm	CO stretch. 9.514 μm	CH_3 rock. 9.170 μm	CH_2 tors. 7.842 μm	OH deform. 7.518 μm	CH_3 s-deform. 7.240 μm
15	1.00	–	0.99	0.16	1.50	0.57
30	1.00	–	1.09	0.16	1.83	0.62
70	1.01	–	1.38	0.19	3.14	0.81
100	1.00	–	1.36	0.18	2.38	0.66
120	1.05	–	1.12	0.18	–	0.85
130	0.97	–	0.92	0.10	–	0.67
140	0.98	–	1.12	0.09	–	0.66
150	0.90	–	0.99	0.10	–	0.54

Table 3.22: Integrated absorbance ratios of selected transitions in CH_3CH_2OH:CO:CH_3OH.

Temp. (K)	CC stretch. 11.36 μm	CO stretch. 9.514 μm	CH_3 rock. 9.170 μm	CH_2 tors. 7.842 μm	OH deform. 7.518 μm	CH_3 s-deform. 7.240 μm
15	1.00	–	0.87	0.19	1.73	0.66
30	1.00	–	1.09	0.19	1.89	0.91
70	0.94	–	1.37	0.19	2.80	0.79
100	0.94	–	1.39	0.23	2.40	0.69
120	0.77	–	1.03	0.11	–	0.61
130	0.87	–	1.20	0.11	–	0.62
140	0.90	–	1.16	0.12	–	0.57
150	0.89	–	1.06	0.12	–	0.54

3.B.5 Dimethyl ether

Table 3.23: Peak position and FWHM of the dimethyl ether COC stretching mode at 10.85 μm.

Mixture	Temp.	$\lambda_{\mathrm{peak},-\mathrm{baseline}}$		$\lambda_{\mathrm{peak},-\mathrm{matrix}}$		FWHM	
	(K)	(cm^{-1})	(μm)	(cm^{-1})	(μm)	(cm^{-1})	(μm)
CH_3OCH_3	15	921.8	10.848	–	–	10.6	0.1245
CH_3OCH_3 : H_2O		898.2	11.133	898.2	11.133	–	–
		913.1	10.951	913.1	10.951	27.9	0.3406*
CH_3OCH_3 : CO		921.8	10.848	–	–	2.1	0.0248
CH_3OCH_3 : CH_3OH		911.2	10.974	911.7	10.968	–	–
		919.4	10.876	919.4	10.876	15.5	0.1846*
CH_3OCH_3 : CO : CH_3OH		912.2	10.962	912.6	10.957	15.9	0.1904*
		920.8	10.859	921.3	10.853	–	–
CH_3OCH_3	30	921.3	10.853	–	–	10.6	0.1243
CH_3OCH_3 : H_2O		897.7	11.139	898.2	11.133	–	–
		914.1	10.939	913.6	10.945	27.5	0.3358*
CH_3OCH_3 : CO		921.8	10.848	–	–	2.2	0.0253
CH_3OCH_3 : CH_3OH		911.2	10.974	911.7	10.968	–	–
		919.4	10.876	919.9	10.871	9.0	0.1062
CH_3OCH_3 : CO : CH_3OH		912.6	10.957	912.6	10.957	16.2	0.1933*
		921.3	10.853	921.3	10.853	–	–
CH_3OCH_3	70	914.1	10.939	–	–	–	–
		918.0	10.893	–	–	4.1	0.0492
CH_3OCH_3 : H_2O		896.3	11.157	898.2	11.133	–	–
		913.6	10.945	913.6	10.945	15.2	0.1834
CH_3OCH_3 : CO		–	–	–	–	–	–
CH_3OCH_3 : CH_3OH		910.7	10.980	911.2	10.974	–	–
		919.9	10.871	919.9	10.871	6.9	0.0815
CH_3OCH_3 : CO : CH_3OH		911.2	10.974	911.2	10.974	–	–
		920.4	10.865	920.4	10.863	6.1	0.0723
CH_3OCH_3	90	914.1	10.939	–	–	–	–
		918.0	10.893	–	–	6.3	0.0755*
CH_3OCH_3 : H_2O		–	–	898.7	11.127	–	–
		913.6	10.945	913.6	10.945	15.0	0.1807
CH_3OCH_3 : CO		–	–	–	–	–	–
CH_3OCH_3 : CH_3OH		910.7	10.980	911.2	10.974	–	–
		919.9	10.871	920.4	10.865	6.4	0.0760
CH_3OCH_3 : CO : CH_3OH		911.2	10.974	911.2	10.974	–	–
		919.9	10.871	919.9	10.871	6.4	0.0755

Continued on next page

Table 3.23 – continued from previous page

Mixture	Temp.	$\lambda_{\mathrm{peak,-baseline}}$		$\lambda_{\mathrm{peak,-matrix}}$		FWHM	
	(K)	(cm^{-1})	(μm)	(cm^{-1})	(μm)	(cm^{-1})	(μm)
CH_3OCH_3	100	914.6	10.934	–	–	–	–
		918.0	10.893	–	–	6.3	0.0744
CH_3OCH_3 : H_2O		–	–	898.2	11.133	–	–
		913.1	10.951	913.6	10.945	14.0	0.1688
CH_3OCH_3 : CO		–	–	–	–	–	–
CH_3OCH_3 : CH_3OH		910.7	10.980	910.7	10.980	–	–
		920.4	10.865	920.4	10.865	6.3	0.0744
CH_3OCH_3 : CO : CH_3OH		911.2	10.974	911.2	10.974	–	–
		920.4	10.865	920.4	10.865	6.4	0.0754
CH_3OCH_3	120	–	–	–	–	–	–
CH_3OCH_3 : H_2O		912.6	10.957	913.6	10.945	13.8	0.1656
CH_3OCH_3 : CO		–	–	–	–	–	–
CH_3OCH_3 : CH_3OH		907.3	11.021	911.7	10.968	–	–
		918.4	10.888	919.4	10.876	19.5	0.2327
CH_3OCH_3 : CO : CH_3OH		–	–	–	–	–	–
CH_3OCH_3	140	–	–	–	–	–	–
CH_3OCH_3 : H_2O		912.6	10.957	914.6	10.934	13.9	0.1659
CH_3OCH_3 : CO		–	–	–	–	–	–
CH_3OCH_3 : CH_3OH		–	–	–	–	–	–
CH_3OCH_3 : CO : CH_3OH		–	–	–	–	–	–
CH_3OCH_3	160	–	–	–	–	–	–
CH_3OCH_3 : H_2O		913.1	10.951	913.1	10.951	13.2	0.1580
CH_3OCH_3 : CO		–	–	–	–	–	–
CH_3OCH_3 : CH_3OH		–	–	–	–	–	–
CH_3OCH_3 : CO : CH_3OH		–	–	–	–	–	–

Notes. $^{(*)}$FWHM result of two or more blended peaks.

Table 3.24: Peak position and FWHM of the dimethyl ether COC stretching + CH_3 rocking mode at 9.141 μm.

Mixture	Temp.	$\lambda_{\mathrm{peak,-baseline}}$		$\lambda_{\mathrm{peak,-matrix}}$		FWHM	
	(K)	(cm^{-1})	(μm)	(cm^{-1})	(μm)	(cm^{-1})	(μm)
CH_3OCH_3	15	1094.4	9.1374	–	–	10.9	0.0912
CH_3OCH_3 : H_2O		1074.6	9.3055	1074.6	9.3055	–	–
		1087.7	9.1941	1088.1	9.1900	24.7	0.2111*
CH_3OCH_3 : CO		1093.9	9.1414	–	–	2.0	0.0168
CH_3OCH_3 : CH_3OH		1092.0	9.1576	1092.0	9.1576	12.5	0.1055*
CH_3OCH_3 : CO : CH_3OH		1087.2	9.1982	1087.2	9.1982	13.8	0.1162

Continued on next page

Table 3.24 – continued from previous page

Mixture	Temp.	$\lambda_{\mathrm{peak},-\mathrm{baseline}}$		$\lambda_{\mathrm{peak},-\mathrm{matrix}}$		FWHM	
	(K)	(cm^{-1})	(μm)	(cm^{-1})	(μm)	(cm^{-1})	(μm)
CH_3OCH_3	30	1093.9	9.1414	–	–	10.9	0.0909
$CH_3OCH_3 : H_2O$		1074.2	9.3096	1074.2	9.3096	–	–
		1087.7	9.1941	1087.7	9.1941	23.4	0.1994*
$CH_3OCH_3 : CO$		1094.4	9.1374	–	–	2.2	0.0182
$CH_3OCH_3 : CH_3OH$		1092.5	9.1535	1092.5	9.1535	8.6	0.0723*
$CH_3OCH_3 : CO : CH_3OH$		1086.7	9.2023	1086.7	9.2023	–	–
		1093.0	9.1495	1093.0	9.1495	14.2	0.1195*
$CH_3OCH_3^{***}$	70	1091.5	9.1616	–	–	3.9	0.0326
$CH_3OCH_3 : H_2O$		1074.2	9.3096	1074.2	9.3096	–	–
		1088.1	9.1900	1088.6	9.1860	11.8	0.0997
$CH_3OCH_3 : CO$		–	–	–	–	–	–
$CH_3OCH_3 : CH_3OH$		1093.0	9.1495	1093.0	9.1495	6.6	0.0554
$CH_3OCH_3 : CO : CH_3OH$		1093.0	9.1495	1093.0	9.1495	6.1	0.0508
$CH_3OCH_3^{***}$	90	1091.5	9.1616	–	–	3.6	0.0299
$CH_3OCH_3 : H_2O$		1074.2	9.3096	1074.2	9.3096	–	–
		1088.6	9.1859	1088.6	9.1859	11.3	0.0957
$CH_3OCH_3 : CO$		–	–	–	–	–	–
$CH_3OCH_3 : CH_3OH$		1093.0	9.1495	1093.0	9.1495	6.2	0.0517
$CH_3OCH_3 : CO : CH_3OH$		1093.0	9.1495	1093.0	9.1495	6.2	0.0515
$CH_3OCH_3^{***}$	100	1091.5	9.1616	–	–	3.5	0.0294
$CH_3OCH_3 : H_2O$		1073.7	9.3138	1072.7	9.3222	–	–
		1088.6	9.1859	1088.6	9.1859	11.1	0.0940
$CH_3OCH_3 : CO$		–	–	–	–	–	–
$CH_3OCH_3 : CH_3OH$		1093.0	9.1495	1093.0	9.1495	6.0	0.0506
$CH_3OCH_3 : CO : CH_3OH$		1093.0	9.1495	1093.0	9.1495	6.2	0.0522
$CH_3OCH_3^{***}$	120	–	–	–	–	–	–
$CH_3OCH_3 : H_2O$		1073.7	9.3138	1073.2	9.3180	–	–
		1088.6	9.1859	1088.6	9.1859	12.1	0.1016
$CH_3OCH_3 : CO$		–	–	–	–	–	–
$CH_3OCH_3 : CH_3OH$		1084.8	9.2186	1085.2	9.2145	–	–
		1093.0	9.1495	1093.4	9.1454	15.5	0.1305
$CH_3OCH_3 : CO : CH_3OH$		–	–	–	–	–	–
$CH_3OCH_3^{***}$	140	–	–	–	–	–	–
$CH_3OCH_3 : H_2O$		1089.6	9.1778	1089.6	9.1778	–	–
		1095.9	9.1253	1095.9	9.1253	13.3	0.1121
$CH_3OCH_3 : CO$		–	–	–	–	–	–
$CH_3OCH_3 : CH_3OH$		–	–	–	–	–	–
$CH_3OCH_3 : CO : CH_3OH$		–	–	–	–	–	–
$CH_3OCH_3^{***}$	160	–	–	–	–	–	–
$CH_3OCH_3 : H_2O$		1090.5	9.1697	1090.5	9.1697	–	–
		1095.9	9.1253	1095.9	9.1253	10.9	0.0911
$CH_3OCH_3 : CO$		–	–	–	–	–	–
$CH_3OCH_3 : CH_3OH$		–	–	–	–	–	–
$CH_3OCH_3 : CO : CH_3OH$		–	–	–	–	–	–

Notes. $^{(*)}$FWHM result of two or more blended peaks. $^{(***)}$Transition likely saturated.

Table 3.25: Peak position and FWHM of the dimethyl ether COC stretching and CH_3 rocking mode at 8.592 μm.

Mixture	Temp.	$\lambda_{\mathrm{peak},-\mathrm{baseline}}$		$\lambda_{\mathrm{peak},-\mathrm{matrix}}$		FWHM	
	(K)	(cm^{-1})	(μm)	(cm^{-1})	(μm)	(cm^{-1})	(μm)
CH_3OCH_3	15	1164.3	8.5888	–	–	9.7	0.0714
CH_3OCH_3 : H_2O		1161.4	8.6102	1161.4	8.6102	12.5	0.0924
CH_3OCH_3 : CO		1165.3	8.5817	–	–	2.4	0.0177
CH_3OCH_3 : CH_3OH		1162.9	8.5994	1162.9	8.5994	9.6	0.0712
CH_3OCH_3 : CO : CH_3OH		1163.3	8.5959	1163.3	8.5959	8.2	0.0608
CH_3OCH_3	30	1163.8	8.5923	–	–	9.7	0.0712
CH_3OCH_3 : H_2O		1161.9	8.6066	1161.9	8.6066	12.1	0.0895
CH_3OCH_3 : CO		1165.8	8.5781	–	–	2.7	0.0196
CH_3OCH_3 : CH_3OH		1162.9	8.5994	1162.9	8.5994	9.0	0.0668
CH_3OCH_3 : CO : CH_3OH		1163.3	8.5959	1163.3	8.5959	7.8	0.0578
CH_3OCH_3***	70	1163.8	8.5923	–	–	3.9	0.0291
CH_3OCH_3 : H_2O		1162.4	8.6030	1162.4	8.6030	10.2	0.0759
CH_3OCH_3 : CO		–	–	–	–	–	–
CH_3OCH_3 : CH_3OH		1162.9	8.5994	1163.3	8.5959	7.8	0.0576
CH_3OCH_3 : CO : CH_3OH		1163.8	8.5923	1163.8	8.5923	7.0	0.0514
CH_3OCH_3***	90	1163.8	8.5923	–	–	3.6	0.0268
CH_3OCH_3 : H_2O		1162.4	8.6030	1162.4	8.6030	9.4	0.0697
CH_3OCH_3 : CO		–	–	–	–	–	–
CH_3OCH_3 : CH_3OH		1163.3	8.5959	1163.3	8.5959	7.2	0.0534
CH_3OCH_3 : CO : CH_3OH		1163.3	8.5959	1163.3	8.5959	7.2	0.0531
CH_3OCH_3***	100	1163.8	8.5923	–	–	3.7	0.0270
CH_3OCH_3 : H_2O		1162.4	8.6030	1162.9	8.5994	9.1	0.0673
CH_3OCH_3 : CO		–	–	–	–	–	–
CH_3OCH_3 : CH_3OH		1163.3	8.5959	1163.3	8.5959	7.1	0.0522
CH_3OCH_3 : CO : CH_3OH		1163.3	8.5959	1163.3	8.5959	7.2	0.0535
CH_3OCH_3	120	–	–	–	–	–	–
CH_3OCH_3 : H_2O		1163.3	8.5959	1163.3	8.5959	8.8	0.0651
CH_3OCH_3 : CO		–	–	–	–	–	–
CH_3OCH_3 : CH_3OH		1160.9	8.6137	1161.4	8.6102	10.4	0.0770
CH_3OCH_3 : CO : CH_3OH		–	–	–	–	–	–
CH_3OCH_3	140	–	–	–	–	–	–
CH_3OCH_3 : H_2O		1165.8	8.5781	1165.8	8.5781	9.0	0.0661
CH_3OCH_3 : CO		–	–	–	–	–	–
CH_3OCH_3 : CH_3OH		–	–	–	–	–	–
CH_3OCH_3 : CO : CH_3OH		–	–	–	–	–	–
CH_3OCH_3	160	–	–	–	–	–	–
CH_3OCH_3 : H_2O		1167.2	8.5675	1167.2	8.5675	8.8	0.0648
CH_3OCH_3 : CO		–	–	–	–	–	–
CH_3OCH_3 : CH_3OH		–	–	–	–	–	–
CH_3OCH_3 : CO : CH_3OH		–	–	–	–	–	–

Notes. $^{(***)}$Transition likely saturated.

Table 3.26: Peak position and FWHM of the dimethyl ether CH_3 rocking mode at 8.011 μm.

Mixture	Temp.	$\lambda_{\mathrm{peak},-\mathrm{baseline}}$		$\lambda_{\mathrm{peak},-\mathrm{matrix}}$		FWHM	
	(K)	(cm^{-1})	(μm)	(cm^{-1})	(μm)	(cm^{-1})	(μm)
CH_3OCH_3	15	1248.2	8.0115	–	–	9.6	0.0617
CH_3OCH_3 : H_2O		1250.1	7.9992	1250.1	7.9992	8.4	0.0540
CH_3OCH_3 : CO		1244.8	8.0333	–	–	2.8	0.0180
CH_3OCH_3 : CH_3OH		1247.7	8.0146	1247.7	8.0146	11.9	0.0761
CH_3OCH_3 : CO : CH_3OH		1251.6	7.9899	1251.6	7.9899	11.4	0.0728
CH_3OCH_3	30	1248.2	8.0115	–	–	9.6	0.0614
CH_3OCH_3 : H_2O		1249.6	8.0023	1249.6	8.0023	8.3	0.0534
CH_3OCH_3 : CO		1245.3	8.0301	–	–	3.1	0.0200
CH_3OCH_3 : CH_3OH		1247.7	8.0146	1247.7	8.0146	11.1	0.0710
CH_3OCH_3 : CO : CH_3OH		1252.1	7.9869	1252.1	7.9869	12.1	0.0775
CH_3OCH_3	70	1250.1	7.9992	–	–	3.4	0.0219
CH_3OCH_3 : H_2O		1249.6	8.0023	1249.6	8.0023	7.6	0.0484
CH_3OCH_3 : CO		–	–	–	–	–	–
CH_3OCH_3 : CH_3OH		1246.8	8.0209	1246.8	8.0208	9.7	0.0624
CH_3OCH_3 : CO : CH_3OH		1245.8	8.0270	1245.8	8.0270	7.4	0.0478
CH_3OCH_3	90	1249.6	8.0023	–	–	3.4	0.0221
CH_3OCH_3 : H_2O		1249.6	8.0023	1249.6	8.0023	7.7	0.0490
CH_3OCH_3 : CO		–	–	–	–	–	–
CH_3OCH_3 : CH_3OH		1245.8	8.0270	1245.8	8.0270	8.5	0.0546
CH_3OCH_3 : CO : CH_3OH		1245.3	8.0301	1245.3	8.0301	7.8	0.0502
CH_3OCH_3	100	1249.2	8.0054	–	–	3.5	0.0226
CH_3OCH_3 : H_2O		1249.6	8.0023	1249.6	8.0023	7.5	0.0479
CH_3OCH_3 : CO		–	–	–	–	–	–
CH_3OCH_3 : CH_3OH		1245.8	8.0270	1245.8	8.0270	8.7	0.0559
CH_3OCH_3 : CO : CH_3OH		1245.3	8.0301	1245.3	8.0301	9.8	0.0630
CH_3OCH_3	120	–	–	–	–	–	–
CH_3OCH_3 : H_2O		1249.6	8.0023	1249.6	8.0023	7.7	0.0493
CH_3OCH_3 : CO		–	–	–	–	–	–
CH_3OCH_3 : CH_3OH		1248.2	8.0115	1247.7	8.0146	9.6	0.0614
CH_3OCH_3 : CO : CH_3OH		–	–	–	–	–	–
CH_3OCH_3	140	–	–	–	–	–	–
CH_3OCH_3 : H_2O		1249.2	8.0054	1249.2	8.0054	8.3	0.0530
CH_3OCH_3 : CO		–	–	–	–	–	–
CH_3OCH_3 : CH_3OH		–	–	–	–	–	–
CH_3OCH_3 : CO : CH_3OH		–	–	–	–	–	–
CH_3OCH_3	160	–	–	–	–	–	–
CH_3OCH_3 : H_2O		1248.7	8.0084	1248.7	8.0084	8.7	0.0556
CH_3OCH_3 : CO		–	–	–	–	–	–
CH_3OCH_3 : CH_3OH		–	–	–	–	–	–
CH_3OCH_3 : CO : CH_3OH		–	–	–	–	–	–

3.B.6 Dimethyl ether normalized band areas

Table 3.27: Integrated absorbance ratios of selected transitions in pure dimethyl ether.

Temp. (K)	COC stretch. 10.85 μm	COC stretch. + CH_3 rock. 9.141 μm	COC stretch. + CH_3 rock. 8.592 μm	CH_3 rock. 8.011 μm
15	0.49	0.83	1.00	0.06
30	0.49	0.83	0.99	0.07
70	0.48	0.79	0.85	0.06
90	0.48	0.78	0.84	0.06
100	0.46	0.74	0.80	0.06

Table 3.28: Integrated absorbance ratios of selected transitions in CH_3OCH_3:H_2O.

Temp. (K)	COC stretch. 10.85 μm	COC stretch. + CH_3 rock. 9.141 μm	COC stretch. + CH_3 rock. 8.592 μm	CH_3 rock. 8.011 μm
15	0.36	1.00	0.74	0.08
30	0.40	0.99	0.80	0.08
70	0.38	0.94	0.79	0.07
90	0.37	0.91	0.78	0.07
100	0.34	0.89	0.78	0.07
120	0.30	0.84	0.80	0.06
140	0.17	0.71	0.79	0.05
160	0.10	0.61	0.73	0.04

Table 3.29: Integrated absorbance ratios of selected transitions in CH_3OCH_3:CO.

Temp. (K)	COC stretch. 10.85 μm	COC stretch. + CH_3 rock. 9.141 μm	COC stretch. + CH_3 rock. 8.592 μm	CH_3 rock. 8.011 μm
15	0.45	0.66	1.00	0.06
30	0.45	0.70	1.00	0.07

Table 3.30: Integrated absorbance ratios of selected transitions in CH_3OCH_3:CH_3OH.

Temp. (K)	COC stretch. 10.85 μm	COC stretch. + CH_3 rock. 9.141 μm	COC stretch. + CH_3 rock. 8.592 μm	CH_3 rock. 8.011 μm
15	0.71	0.71	1.00	0.10
30	0.69	0.77	1.04	0.09
70	0.65	0.83	1.04	0.09
90	0.63	0.84	1.08	0.08
100	0.60	0.82	1.05	0.08
120	0.29	0.39	0.38	0.04

Table 3.31: Integrated absorbance ratios of selected transitions in CH_3OCH_3:CO:CH_3OH.

Temp. (K)	COC stretch. 10.85 μm	COC stretch. + CH_3 rock. 9.141 μm	COC stretch. + CH_3 rock. 8.592 μm	CH_3 rock. 8.011 μm
15	0.81	0.88	1.00	0.13
30	0.83	1.02	1.13	0.12
70	0.63	0.86	1.04	0.08
90	0.63	0.83	1.00	0.08
100	0.51	0.67	0.77	0.07

3.C Spectroscopic data of selected bands

3.C.1 Acetaldehyde

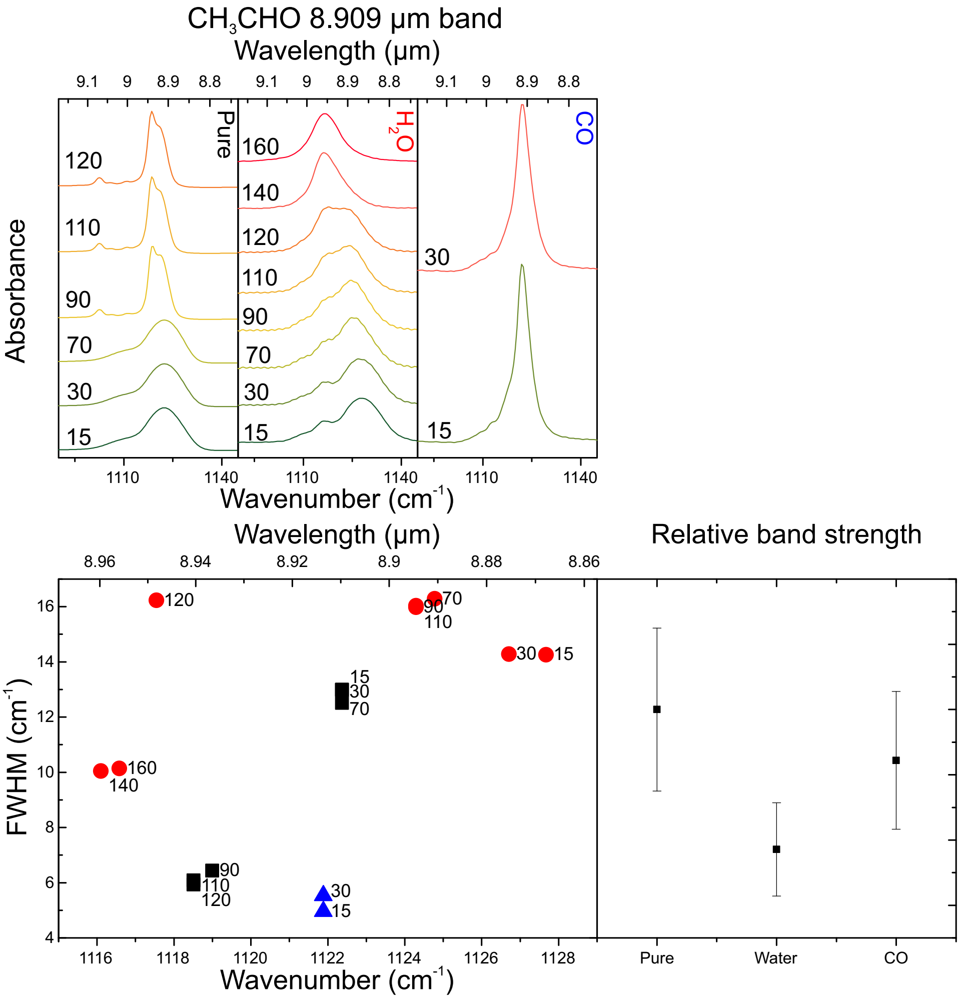

Figure 3.10: Top: from left to right the acetaldehyde 8.909 μm band pure (black) and in water (red) and CO (blue) at various temperatures. Bottom left: peak position vs. FWHM plot, using the same colour coding. Bottom right: the relative band strength for the 8.909 μm band at 15 K in various matrices.

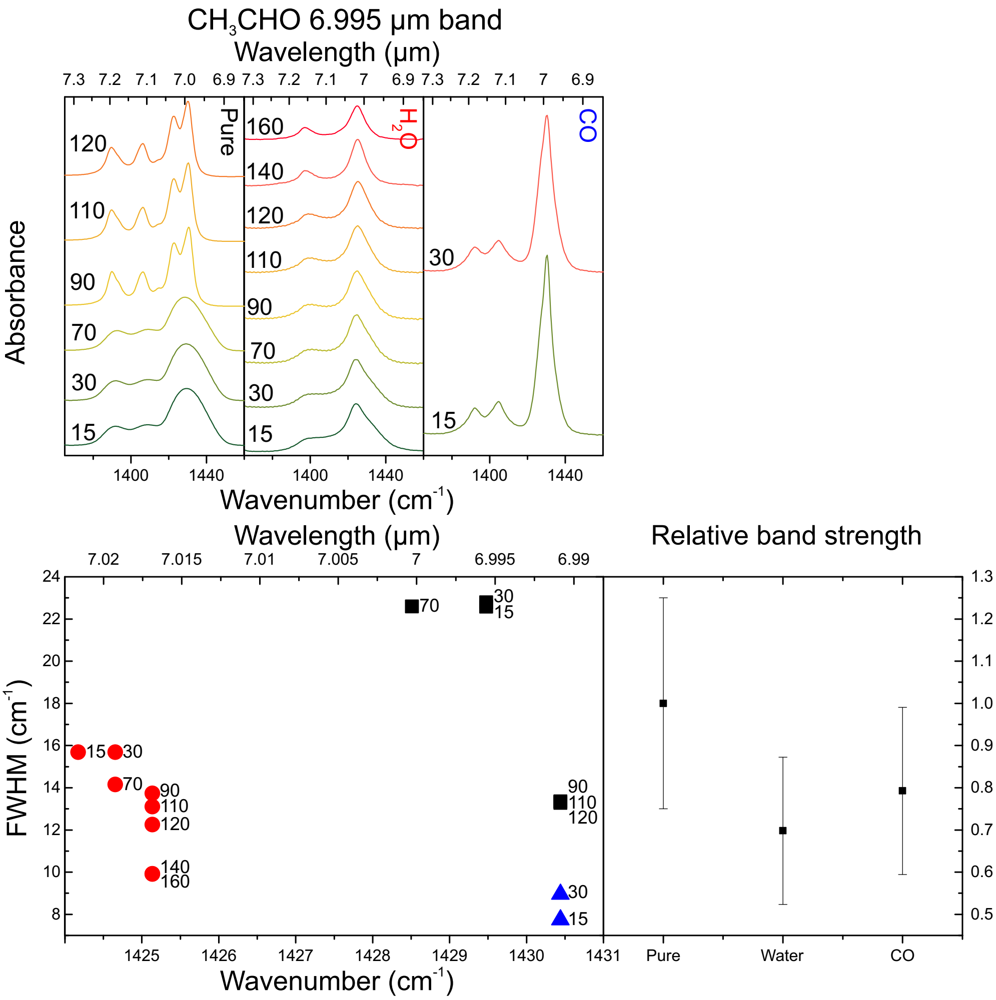

Figure 3.11: Top: from left to right the acetaldehyde 6.995 μm band pure (black) and in water (red) and CO (blue) at various temperatures. Bottom left: peak position vs. FWHM plot, using the same colour coding. Bottom right: the relative band strength for the 6.995 μm band at 15 K in various matrices.

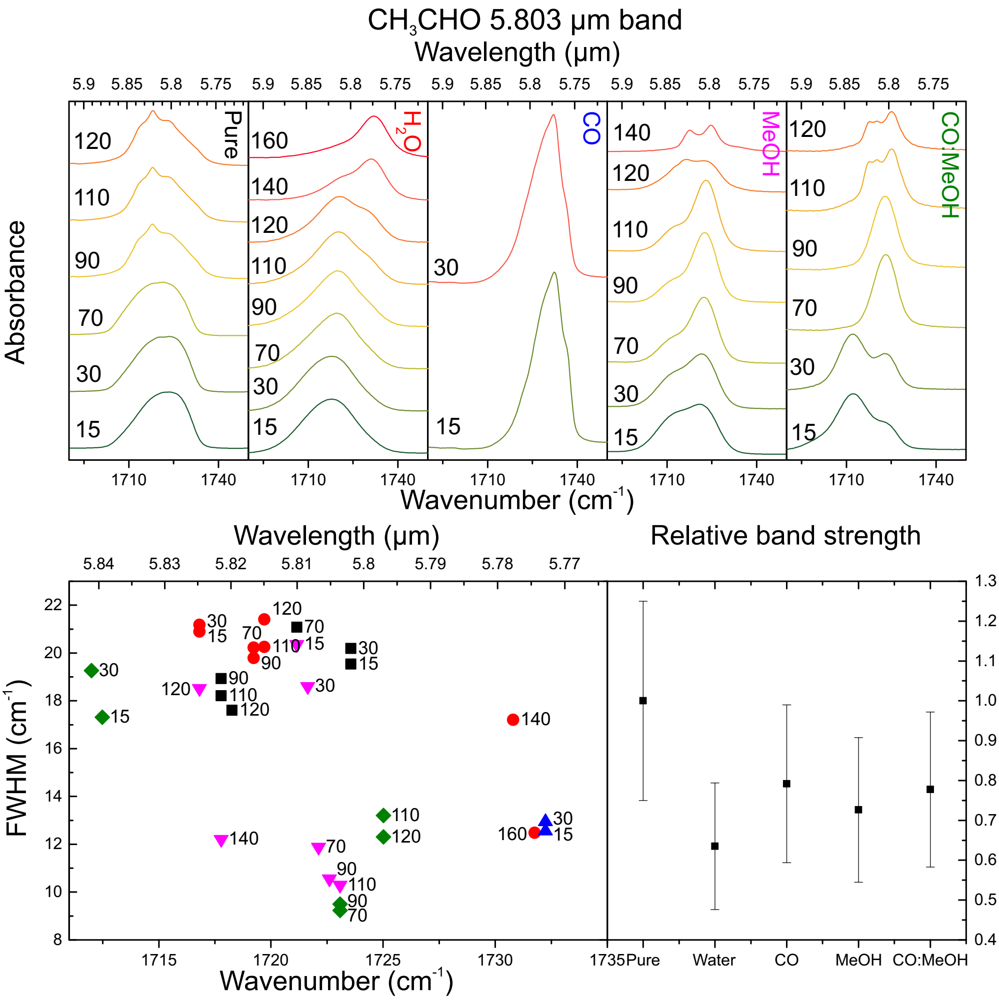

Figure 3.12: Top: from left to right the acetaldehyde 5.803 μm band pure (black) and in water (red), CO (blue), methanol (purple), and CO:CH$_3$OH (green) at various temperatures. Bottom left: peak position vs. FWHM plot, using the same colour coding. Bottom right: the relative band strength for the 5.803 μm band at 15 K in various matrices.

3.C.2 Ethanol

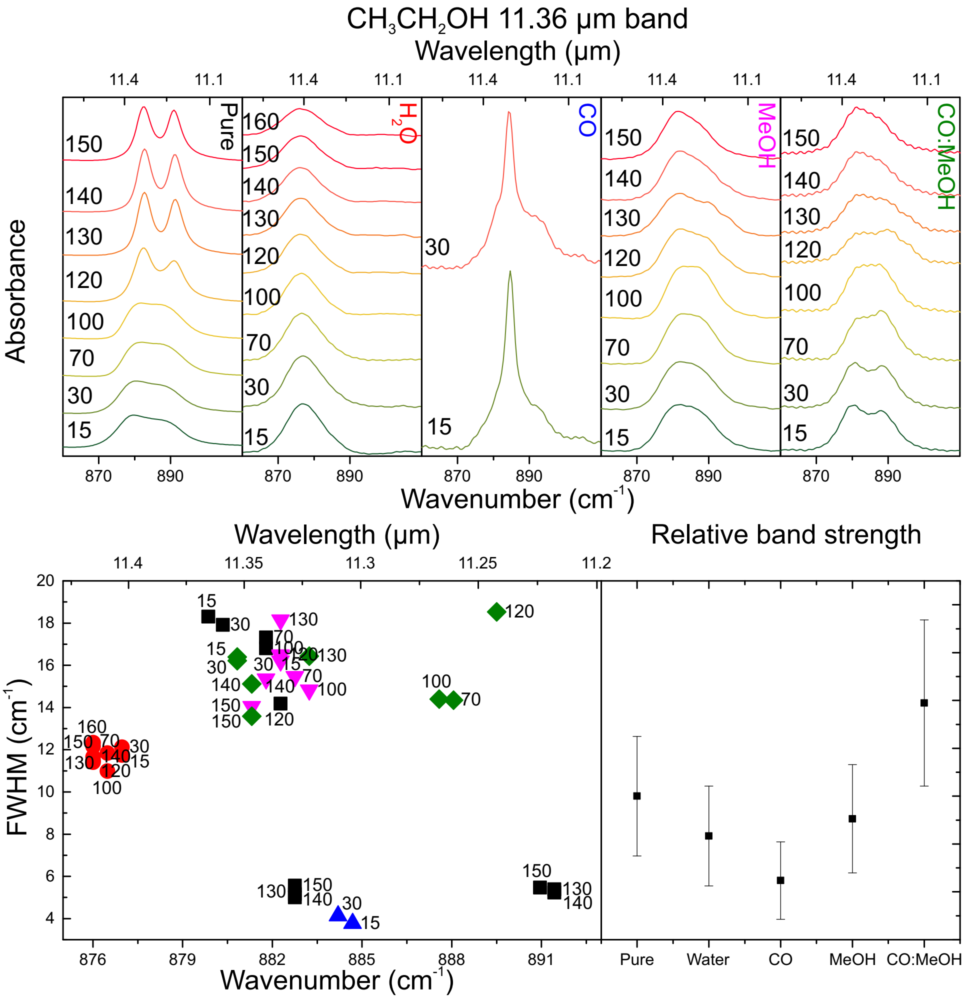

Figure 3.13: Top: from left to right the ethanol 11.36 μm band pure (black) and in water (red), CO (blue), methanol (purple), and CO:CH_3OH (green) at various temperatures. Bottom left: peak position vs. FWHM plot, using the same colour coding. Bottom right: the relative band strength for the 11.36 μm band at 15 K in various matrices.

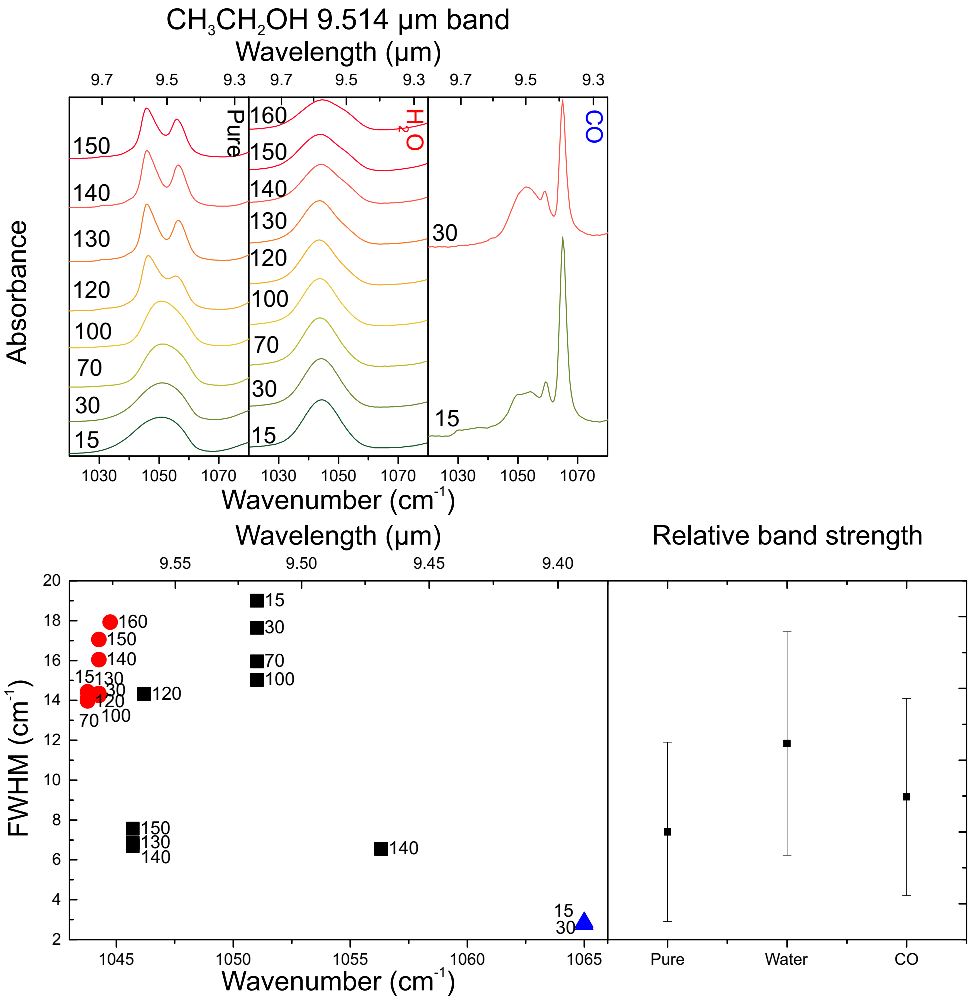

Figure 3.14: Top: from left to right the ethanol 9.514 μm band pure (black) and in water (red) and CO (blue) at various temperatures. Bottom left: peak position vs. FWHM plot, using the same colour coding. Bottom right: the relative band strength for the 9.514 μm band at 15 K in various matrices.

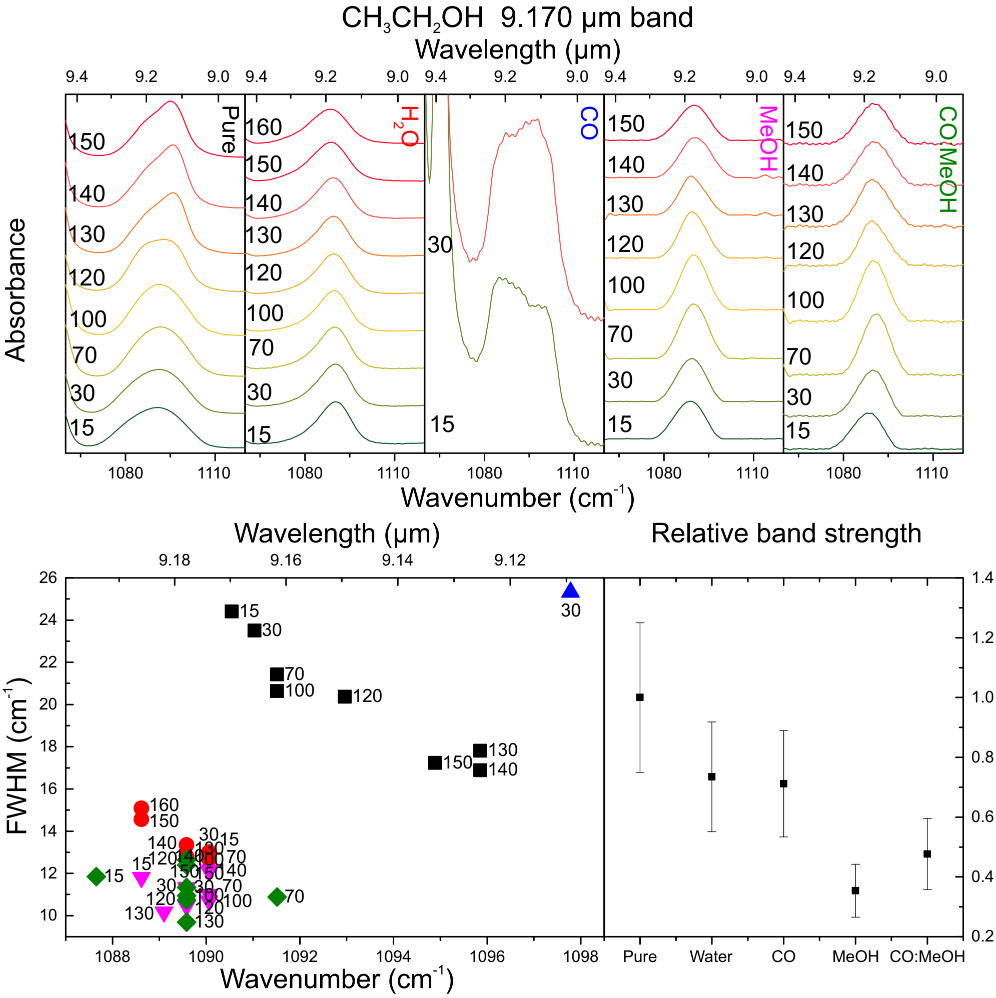

Figure 3.15: Top: from left to right the ethanol 9.170 μm band pure (black) and in water (red), CO (blue), methanol (purple), and CO:CH$_3$OH (green) at various temperatures. Bottom left: peak position vs. FWHM plot, using the same colour coding. Bottom right: the relative band strength for the 9.170 μm band at 15 K in various matrices.

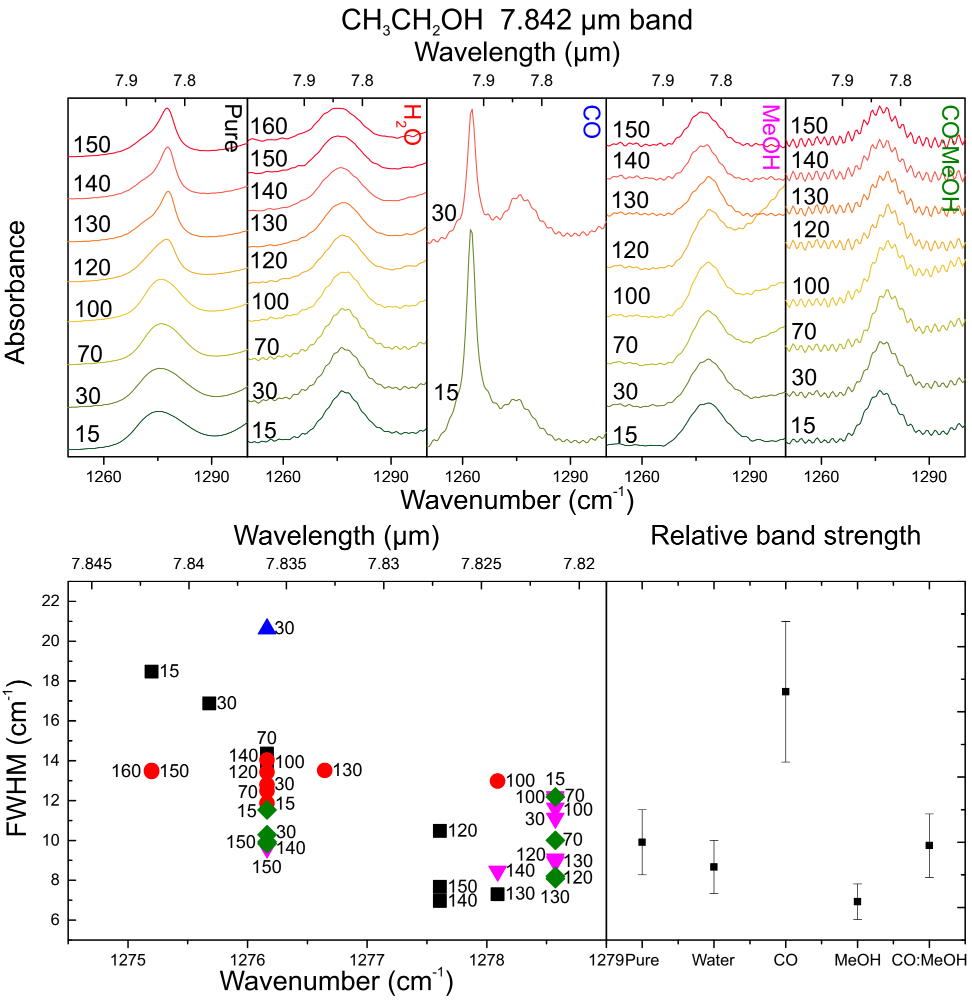

Figure 3.16: Top: from left to right the ethanol 7.842 μm band pure (black) and in water (red), CO (blue), methanol (purple), and CO:CH$_3$OH (green) at various temperatures. Bottom left: peak position vs. FWHM plot, using the same colour coding. Bottom right: the relative band strength for the 7.842 μm band at 15 K in various matrices.

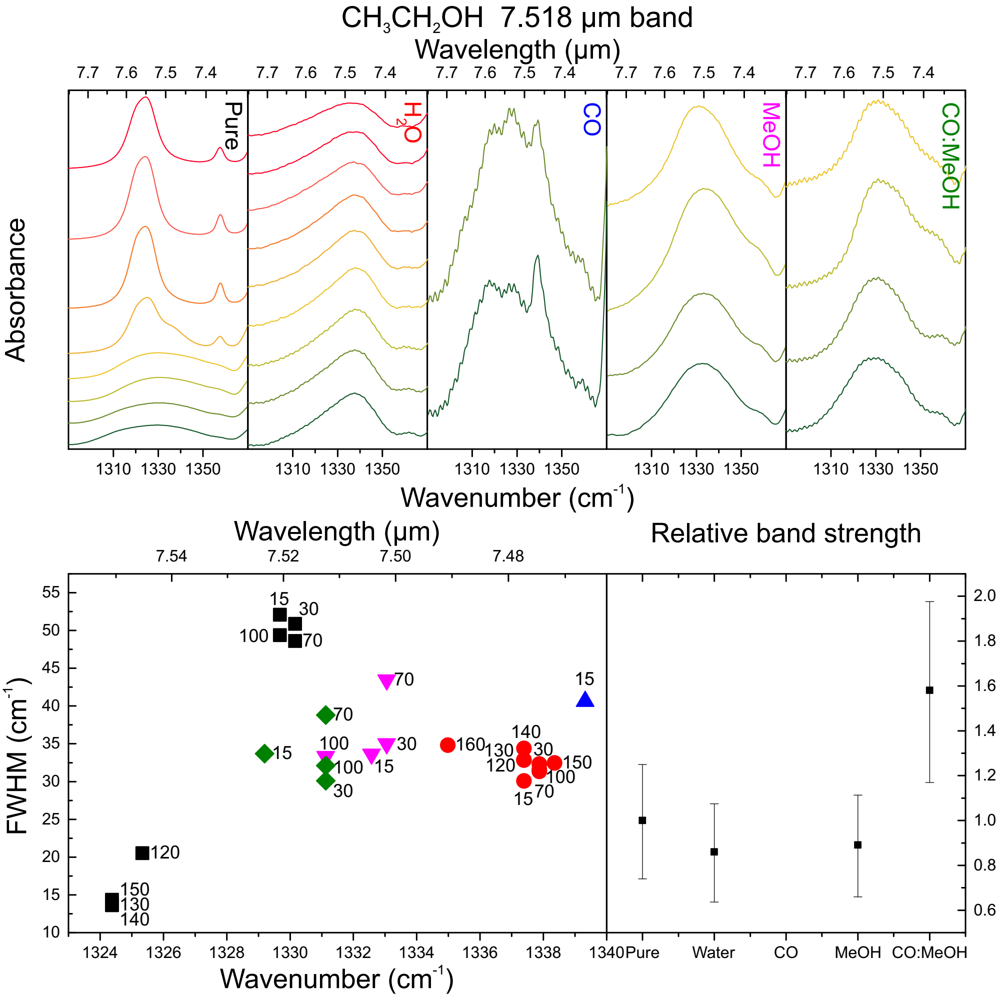

Figure 3.17: Top: from left to right the ethanol 7.518 μm band pure (black) and in water (red), CO (blue), methanol (purple), and CO:CH_3OH (green) at various temperatures. Bottom left: peak position vs. FWHM plot, using the same colour coding. Bottom right: the relative band strength for the 7.518 μm band at 15 K in various matrices.

3.C.3 Dimethyl ether

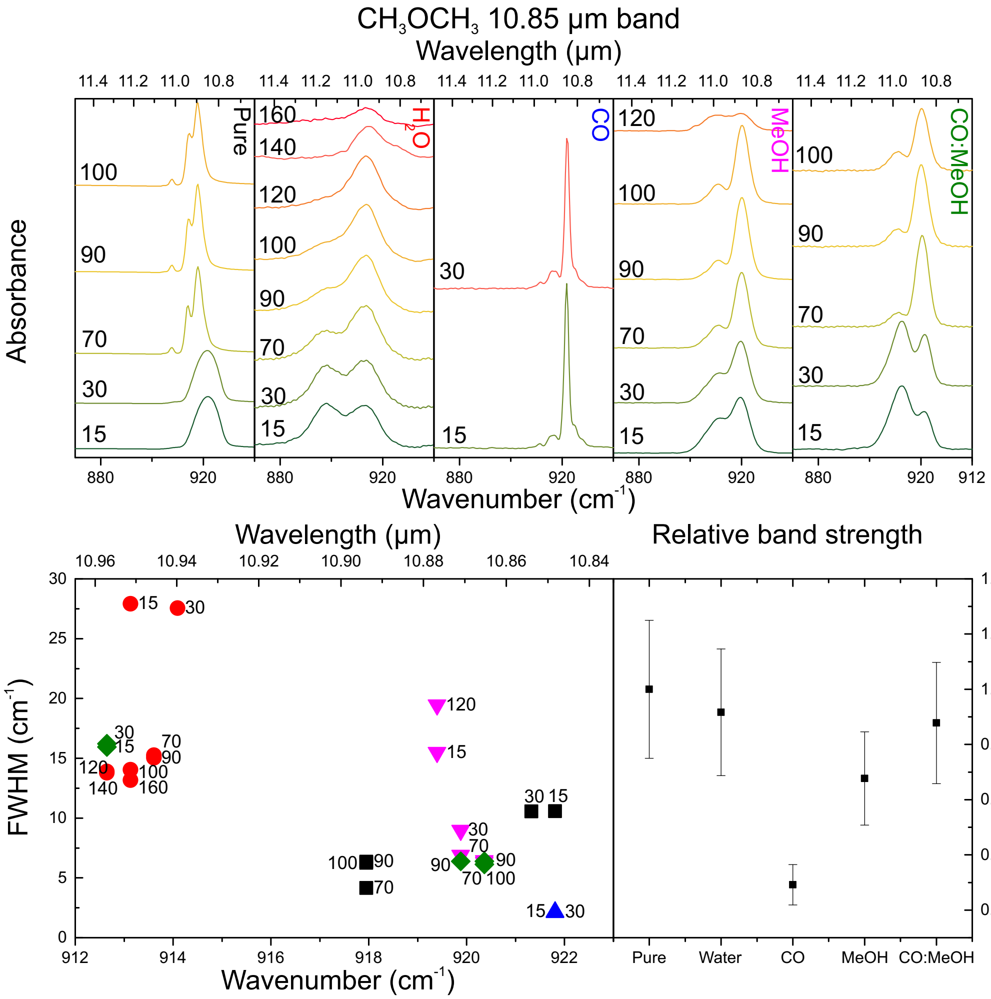

Figure 3.18: Top: from left to right the dimethyl ether 10.85 μm band pure (black) and in water (red), CO (blue), methanol (purple), and CO:CH$_3$OH (green) at various temperatures. Bottom left: peak position vs. FWHM plot, using the same colour coding. Bottom right: the relative band strength for the 10.85 μm band at 15 K in various matrices.

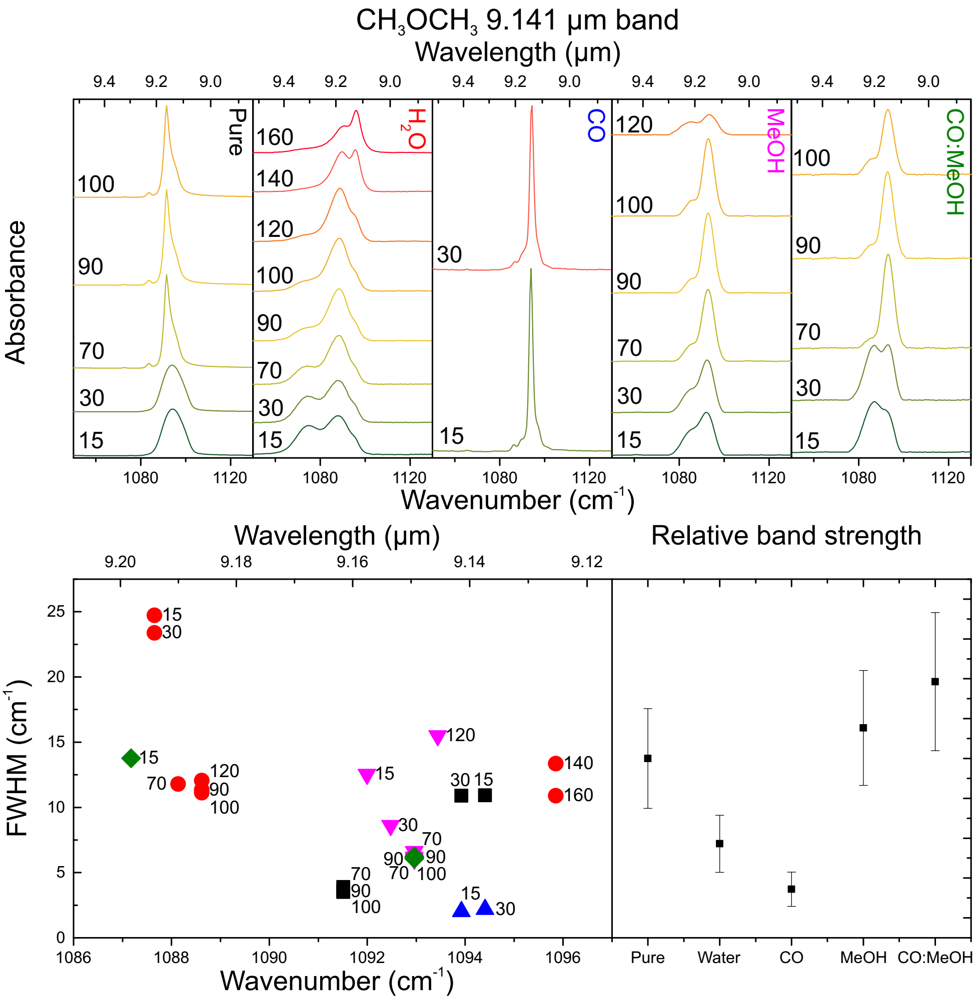

Figure 3.19: Top: from left to right the dimethyl ether 9.141 μm band pure (black) and in water (red), CO (blue), methanol (purple), and CO:CH$_3$OH (green) at various temperatures. Bottom left: peak position vs. FWHM plot, using the same colour coding. Bottom right: the relative band strength for the 9.141 μm band at 15 K in various matrices.

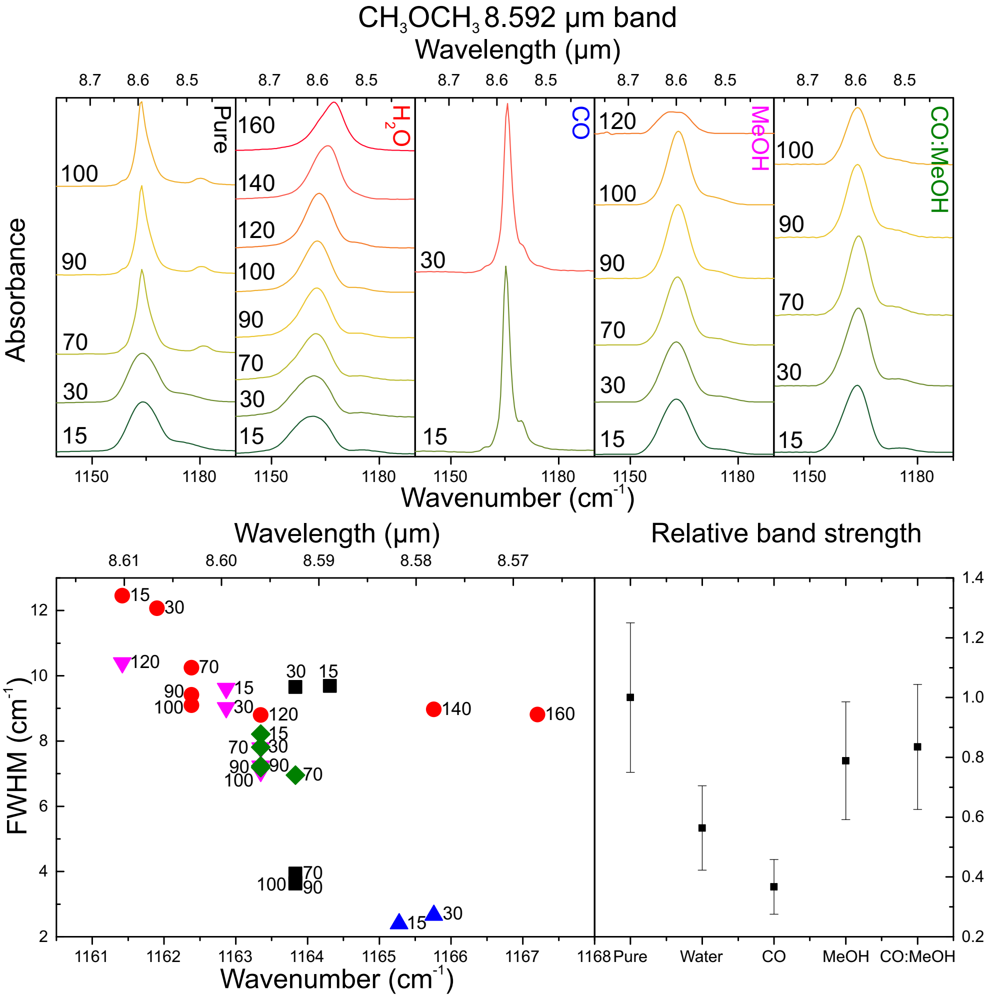

Figure 3.20: Top: from left to right the dimethyl ether 8.592 μm band pure (black) and in water (red), CO (blue), methanol (purple), and CO:CH$_3$OH (green) at various temperatures. Bottom left: peak position vs. FWHM plot, using the same colour coding. Bottom right: the relative band strength for the 8.592 μm band at 15 K in various matrices.
]

4

INFRARED SPECTRA OF COMPLEX ORGANIC MOLECULES IN ASTRONOMICALLY RELEVANT ICE MATRICES. III. METHYL FORMATE AND ITS TENTATIVE SOLID-STATE DETECTION

Jeroen Terwisscha van Scheltinga, Giulia Marcandalli, Melissa K. McClure, Michiel R. Hogerheijde, Harold Linnartz, 2021, A&A, 651 A95

Abstract

Infrared spectroscopy of star- and planet-forming regions is at the dawn of a new age with the upcoming *James Webb* Space Telescope (JWST). Its high resolution and unprecedented sensitivity allows us to probe the chemical complexity of planet forming regions, such as dense clouds, embedded protostars, and protoplanetary disks, both in the solid state and gas phase. In support of these observations, laboratory spectra are required to identify complex organic molecules in the ices that cover the dust grains in these regions.

The work presented in this chapter aims to provide the necessary reference spectra to firmly detect methyl formate ($HCOOCH_3$) in the different evolutionary stages of star- and planet-forming regions. Methyl formate is mixed in astronomically relevant matrices, and the peak positions, full width at half maximum, and relative band intensities are characterized for different temperatures to provide an analytical tool for astronomers.

To derive the targeted spectra, methyl formate was deposited at 15 K on a cryogenically cooled infrared transmissive window under high-vacuum conditions. Specifically, methyl formate was deposited pure and mixed with CO, H_2CO, CH_3OH, H_2O, and CO:H_2CO:CH_3OH combined. The sample was linearly heated until all solid-state constituents were desorbed. Throughout the experiment, infrared spectra were acquired with a Fourier transform infrared spectrometer in the range from 4000 to 500 cm^{-1} (2.5–20 μm) at a spectral resolution of 0.5 cm^{-1}.

Here the characterization of five solid-state methyl formate vibrational modes is presented in pure and astronomically relevant ice matrices. The five selected vibrational modes, namely the C=O stretch (5.804 μm), the C−O stretch (8.256 μm), CH_3 rocking (8.582 μm), O−CH_3 stretching (10.98 μm), and OCO deformation (13.02 μm), are best suited for a JWST identification of methyl formate. For each of these vibrational modes, and each of the mixtures the temperature versus spectra heatmaps, peak position versus full width at half maximum and relative band intensities are given. All spectra are publicly available on the Leiden Ice Database. Additionally, the acquired reference spectra of methyl formate are compared with archival *Spitzer* observations of HH 46. A tentative detection of methyl formate provides an upper limit to the column density of 1.7×10^{17} cm^{-2}, corresponding to an upper limit relative to water of $\leq 2.2\%$ and $\leq 40\%$ with respect to methanol.

4.1 Introduction

The number of identified molecular species in the different evolutionary stages of planet forming systems is continuously increasing (McGuire 2018). The growing complexity of newly detected species suggests that chemistry in the inter- and circumstellar medium is active and diverse. The majority of these molecules are detected in the gas phase with state-of-the-art facilities such as the Atacama Large Millimeter/submillimeter Array (ALMA), but a dozen are also found in the solid state, for example, H_2O and CH_3OH. These are detected through either ground-based telescopes such as the NASA Infrared Telescope Facility (IRTF), or space-based observatories such as the Infrared Space Observatory (ISO) and *Spitzer* Space Telescope.

Infrared facilities probe the vibrational modes of molecules residing in ice-covered dust grains. These grains are present throughout the different evolutionary stages of star and planet forming regions. To date, only small species such as water (H_2O), carbon monoxide (CO), carbon dioxide (CO_2), methane (CH_4), and ammonia (NH_3) have been identified in the solid state (e.g., Boogert et al. 2015). The largest molecule firmly identified to date in the solid-state is methanol (CH_3OH), a species which by definition is considered a complex organic molecule (COM). This is interesting as methanol is a stepping stone toward larger COMs, such as acetaldehyde (CH_3CHO), ethanol (CH_3CH_2OH), dimethyl ether (CH_3OCH_3), methyl formate ($HCOOCH_3$), and glycolaldehyde ($HOCH_2CHO$), as shown by laboratory studies (e.g., Bennett & Kaiser 2007; Öberg et al. 2009b; Modica et al. 2012; Muñoz Caro et al. 2014; Chuang et al. 2016; Fedoseev et al. 2017). Of these larger COMs, two, acetaldehyde and ethanol ice, have been tentatively detected in the massive embedded protostar W33A (Schutte et al. 1999; Öberg et al. 2011). COMs are, however, frequently observed in the gas phase with ground-based telescopes such as ALMA and the Institut de Radioastronomie Millimetrique (IRAM; Öberg et al. 2015; Jørgensen et al. 2016; Bergner et al. 2017; Ligterink et al. 2017, 2018a; Ceccarelli et al. 2017; McGuire et al. 2017; Bøgelund et al. 2019a,b; Manigand et al. 2020; van Gelder et al. 2020; Yang et al. 2021; Nazari et al. 2021). For example, the recent PErseus ALMA CHEmistry Survey (PEACHES) revealed that 58% of their 50 observed embedded (Class 0/I) protostars have COM emission (Yang et al. 2021). Both oxygen- and nitrogen-bearing COMs have been detected, including, but not limited to, methanol (CH_3OH), methyl cyanide (CH_3CN), formamide (NH_2CHO), methyl formate ($HCOOCH_3$), and ethyl cyanide (CH_3CH_2CN).

The changing physical conditions between the different stages of star and planet formation provide a wide range of different (non)energetic triggers that allow the molecular complexity to increase in both the gas phase and in the solid state. Chemical models attempt to reproduce observed COM abundances, with varying degrees of success. Such models describe the formation and destruction of COMs in laboratory or astronomical settings, and they include gas-phase chemistry and/or solid-state chemistry (Garrod 2013; Taquet et al. 2016; Vasyunin et al. 2017; Quénard et al. 2018; Ruaud & Gorti 2019; Simons et al. 2020; Jin & Garrod 2020; Wang et al. 2021). In general, the formation of COMs is deemed more likely to occur in the solid state compared to the gas phase. However, gas-phase COM signatures are also detected in cold regions with temperatures well below their thermal desorption value. This requires either unexplored gas-phase reactions or nonthermal desorption of COMs from the solid state. Methyl formate is one such molecule which is expected to form in the solid state and yet it is observed in cold gas-phase environments, for example, the cold prestellar cores L1689B (Bacmann et al. 2012) and low-mass protostar B1-b (Öberg et al. 2010; Cernicharo et al. 2012). In addition to the observation of methyl formate in cold environments, it is also seen in environments such as hot cores of massive star-forming regions and protostars (see e.g., Belloche et al. 2013; Jørgensen et al. 2016; van Gelder et al. 2020).

Several gas-phase formation pathways have been proposed to form methyl formate through ion-molecule and subsequently dissociative recombination reactions. One of the generally used gas-phase formation channels is the formation of protonated methyl formate from protonated methanol and formaldehyde (reaction (4.1)). This protonated methyl formate then recombines with an electron to form methyl formate (reaction (4.2)).

$$[\mathrm{CH_3OH_2}]^+ + \mathrm{H_2CO} \rightarrow [\mathrm{HC(OH)OCH_3}]^+ + \mathrm{H_2} \tag{4.1}$$

$$[\mathrm{HC(OH)OCH_3}]^+ + e \rightarrow \mathrm{HCOOCH_3} + \mathrm{H}. \tag{4.2}$$

This reaction, with assumed high reaction rates, has been proposed to produce significant amounts of methyl formate within 10^4–10^5 years in chemical models of hot cores (Millar et al. 1991; Caselli et al. 1993; Charnley et al. 1995). Horn et al. (2004), however, investigated several ion-molecule pathways, including reaction (4.1), to form protonated methyl formate in a quantum chemical study. They reported that these reactions have significant activation barriers that prohibit these pathways from efficiently contributing to the observed abundances of methyl formate in hot cores.

The authors tested an alternative association reaction between methyl ions and formic acid (HCOOH; reaction (4.3))

$$\mathrm{CH_3^+} + \mathrm{HCOOH} \rightarrow [\mathrm{HC(OH)OCH_3}]^+, \tag{4.3}$$

which was found to be more efficient. However, despite its higher rate, this pathway is still not able to reproduce the observed methyl formate abundances in hot cores.

Recent modeling attempts by Balucani et al. (2015) suggest that nonthermally desorped methanol ice could potentially feed the formation of COMs in the gas phase. The gas-phase methanol reacts with a hydroxyl radical to form methoxy (reaction (4.4)). These methoxy radicals can then subsequently react with methyl radicals to form dimethyl ether ($\mathrm{CH_3OCH_3}$) through reaction (4.5). Methyl formate is formed through the oxidation of the $\mathrm{CH_2OCH_3}$ radicals (reaction (4.8)), which are created through hydrogen abstraction of dimethyl ether (Eqs. (4.6) & (4.7)). With these reactions incorporated in their model, it is able to retrieve abundances that are in agreement with upper limits derived from observations.

$$\mathrm{CH_3OH} + {}^\bullet\mathrm{OH} \rightarrow {}^\bullet\mathrm{OCH_3} + \mathrm{H_2O} \tag{4.4}$$

$${}^\bullet\mathrm{OCH_3} + {}^\bullet\mathrm{CH_3} \rightarrow \mathrm{CH_3OCH_3} + h\nu \tag{4.5}$$

$$\mathrm{CH_3OCH_3} + \mathrm{F} \rightarrow {}^\bullet\mathrm{CH_2OCH_3} + \mathrm{HF} \tag{4.6}$$

$$\mathrm{CH_3OCH_3} + \mathrm{Cl} \rightarrow {}^\bullet\mathrm{CH_2OCH_3} + \mathrm{HCl} \tag{4.7}$$

$${}^\bullet\mathrm{CH_2OCH_3} + \mathrm{O} \rightarrow \mathrm{HCOOCH_3} + \mathrm{H}. \tag{4.8}$$

In addition to gas-phase reactions, it is also possible to form methyl formate in the solid state through both energetic and non-energetic processes. The associated radicals to form methyl formate in the solid state are formyl and methoxy (reaction (4.9)), and both radicals can be formed through energetic and non-energetic processing.

$$^{\bullet}\mathrm{CHO} + {}^{\bullet}\mathrm{OCH_3} \rightarrow \mathrm{HCOOCH_3}. \tag{4.9}$$

Öberg et al. (2009b) investigated the formation of different COMs through the UV irradiation of pure CH_3OH ice and CH_3OH mixed with either CO or CH_4. In their work, the formation of methyl formate was confirmed and reaction (4.9) was proposed as the underlying reaction pathway. Apart from UV-photon triggered formation, it is also possible to form methyl formate through cosmic ray irradiation (Modica & Palumbo 2010). In their work pure methanol and mixtures of methanol and CO were irradiated with 200 keV protons, and methyl formate was identified through its fundamental CH_3 rocking vibrational mode in the infrared. Methyl formate can also be formed in the solid state through a non-energetic process involving hydrogen addition and abstraction reactions. The hydrogenation of CO is known to form H_2CO and CH_3OH (Hiraoka et al. 1994, 2002; Watanabe & Kouchi 2002a; Hidaka et al. 2004; Watanabe et al. 2004; Fuchs et al. 2009). The work by Chuang et al. (2016) shows that the intermediate radicals – HCO, CH_3O, and CH_2OH – can also react with each other in radical-radical recombinations and form COMs, such as methyl formate, glycolaldehyde, and ethylene glycol. As is evident from these laboratory experiments, there are sufficient pathways to form COMs in the ices that cover dust grains.

Observational results suggest that the ices on dust grains are comprised of two layers, a polar and an apolar layer (e.g., Boogert et al. 2015). The radicals that form methyl formate in the solid state are part of the CO hydrogenation family. It is thus likely that methyl formate is mixed with CO, H_2CO, and CH_3OH and therefore resides in the apolar layer on interstellar dust grains.

The observational identification of COMs will receive a new impetus with the upcoming *James Webb* Space Telescope (JWST). It will be possible to probe these icy grains with higher spatial and spectral resolution than previously available. This creates an opportunity to look for COMs in the different evolutionary stages of star and planet forming regions. In preparation for these observations, this manuscript is the third in a series where COMs are spectroscopically characterized in the infrared for different astronomically relevant ice matrices (Terwisscha van Scheltinga et al. 2018; Rachid et al. 2020). Each molecule has it own spectroscopic signature that consists of a series of vibrational modes and allows for unambiguous identifications. In the solid state, vibrational transition properties are influenced by the physical structure, temperature, and surrounding molecules (Palumbo 2005; Dawes et al. 2007; Öberg et al. 2007, 2009a; Bossa et al. 2012; Isokoski et al. 2014; He et al. 2017). These changes in transition properties are reflected in the spectroscopic shape of the transitions, that is, peak position, full width at half maximum (FWHM), and apparent band strengths. The characterization of these changes offers not only a tool to identify species, but also to characterize temperatures and mixing rates. For this, systematic laboratory data are needed. Here the spectroscopic data for methyl formate are presented.

The paper is structured as follows. Section 2 describes the experimental setup and how it was used to measure the spectra. In Section 3 the results are discussed and Section 4 explores how these features can be used to interpret astronomical observations. In Section 5 we conclude with a summary.

4.2 Experimental

4.2.1 Setup

The experiments in this manuscript were measured on the high-vacuum (HV) setup in the Laboratory for Astrophysics at Leiden Observatory. This setup consists of a stainless steel chamber which is evacuated to a pressure as low as 10^{-7} mbar at room temperature. The sample on which the ice was deposited is a ZnSe window, which can be cooled down to 12 K by a closed cycle helium refrigerator. The temperature of the sample was monitored and controlled with a LakeShore 330 temperature controller and silicon diode temperature sensor. The spectra were acquired with a Fourier transform infrared (FTIR) Varian 670-IR spectrometer. This system covers the infrared range from 4000–500 cm^{-1}, which corresponds to 2.5–20 μm. The best achievable spectral resolution is up to 0.1 cm^{-1}, but in this work a resolution of 0.5 cm^{-1} is used which is more than sufficient. Gas mixtures for sample deposition are prepared in a separate multiline gas mixing system, which is able to produce gas mixtures with a maximum error of $< 10\%$. The specific gas and liquids used in this study are methyl formate (Sigma Aldrich, 99.0%), carbon monoxide (Linde gas, 99.997%), paraformaldehyde (Sigma Aldrich, 95.0%), methanol (Sigma Aldrich, $\geq 99.8\%$), and Milli-Q H_2O (Type I). The paraformaldehyde was exteriorly heated with water at 80 °C to enhance depolymerization and increase the vapor pressure of pure formaldehyde during sample preparation. During deposition, samples containing formaldehyde are similarly heated to prevent polymerization back into paraformaldehyde. For more details on the experimental setup, see Chapter 2, 3, and references therein.

4.2.2 Measurement protocol

The different gas samples, whether pure or mixed, are prepared in the gas mixing system and stored in a 2 liter glass bulb at a pressure of 20 mbar. The ratio at which the matrix constituents are mixed with methyl formate is 20:1. This ratio ensures a balance between sufficient dilution to investigate spectroscopic changes and adequate signal-to-noise for quantitative analysis of the spectroscopic features. Any further dilution is not expected to result in strong deviation of the observed results for methyl formate. This bulb is then connected to the HV setup and the gas is subsequently dosed onto the substrate through a needle valve. The 20 mbar pressure in the 2 liter glass bulb ensures a large enough reservoir to have a constant deposition rate over time. During deposition the growth of the ice is traced with the FTIR spectrometer. The measured absorption features can be translated to a column density, $N_{species}$, according to the following relation:

$$N_{species} = \ln(10) \frac{\int_{band} \log_{10}\left(\frac{I_0(\tilde{\nu})}{I(\tilde{\nu})}\right) d\tilde{\nu}}{A'}, \tag{4.10}$$

where $\int_{band} \log_{10}\left(\frac{I_0(\tilde{\nu})}{I(\tilde{\nu})}\right) d\tilde{\nu}$ is the area of an absorption feature with $I_0(\tilde{\nu})$ and $I(\tilde{\nu})$ as the incoming flux and transmitted flux through the sample, respectively, and the apparent band strength is given by A'. The deposition is stopped when the column density reaches a value of approximately 2.0×10^{18} mol cm^{-2}. This is equal to 2000 monolayers (ML), where one ML equals 10^{15} mol cm^{-2}. The 2000 ML coverage ensures that, over time, the measurement is not significantly contaminated by H_2O

Table 4.1: Selected transitions of methyl formate for solid-state identification.

Species	Vibrational mode	Peak position$^{(*)}$		A'
		cm^{-1}	μm	cm mol.$^{-1}$
Methyl formate	C=O stretch.	1723.1	5.804	$4.96 \times 10^{-17(a)}$
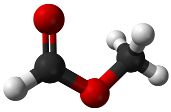	C$-$O stretch.	1211.3	8.256	$2.93 \times 10^{-17(a)}$
	CH_3 rock.	1165.3	8.582	$1.96 \times 10^{-17(a)}$
	O$-$$CH_3$ stretch.	910.7	10.98	$4.82 \times 10^{-18(a)}$
	OCO deform.	768.3	13.02	$1.25 \times 10^{-18(a)}$

Notes. (*) Peak position of the pure molecule at 15 K.
References. (a) Taken from Modica & Palumbo (2010).

background gas deposition in the setup which is 30 ML h^{-1}. A typical deposition takes one hour which results in a contamination by background H_2O deposition of 1.5%. In order to derive the column densities, the apparent band strengths for each of the molecules used in this study are taken from the literature and those of methyl formate are given in Table 4.1 (Modica & Palumbo 2010; Bouilloud et al. 2015). It should be noted that high sample coverage combined with strong absorption features may lead to saturation and the inaccurate determination of column densities. To avoid this, the column density was traced with multiple features during deposition.

After deposition, spectra were acquired with a resolution of 0.5 cm^{-1} and a scan average of 256. Once a spectrum had been acquired at 15 K, the sample was linearly heated and spectra were continuously acquired until the ice fully desorbed from the sample. The heating ramp, 0.5 K min^{-1}, and the time it takes to measure one spectrum, $\sim$ 7 min, results in an acquisition every 3.5 K. This combination allows for an optimal balance between signal-to-noise and temperature resolution per spectrum. These spectra allow for the characterization of their peak position and FWHM as a function of the temperature.

4.2.3 Analysis

The number of spectra acquired per experiment, that is to say for a specific gas mixture, is roughly 35. A selected few spectra at characteristic temperatures of 15, 30, 50, 80, 100, and 120 K are shown in this manuscript and all other spectra are publicly available from the Leiden Ice Database[1]. Each spectrum was baseline subtracted with a cubic spline using fit points that were chosen by eye. In the pure spectra the points were chosen in featureless regions, and in the diluted sample spectra the main constituent features were incorporated in the baseline. This allows for more accurate determination of the peak position and FWHM of the selected methyl formate transitions. As the sample was heated the molecules started to orientate themselves in more energetically favorable positions, which changes the vibrational transition properties. This translates itself into a changing absorption feature shape and absorption wavelength. Upon ice crystallization, for example, spectral features may narrow. An in-depth investigation of how vibrational modes change in the solid state with changing

---

[1] https://icedb.strw.leidenuniv.nl

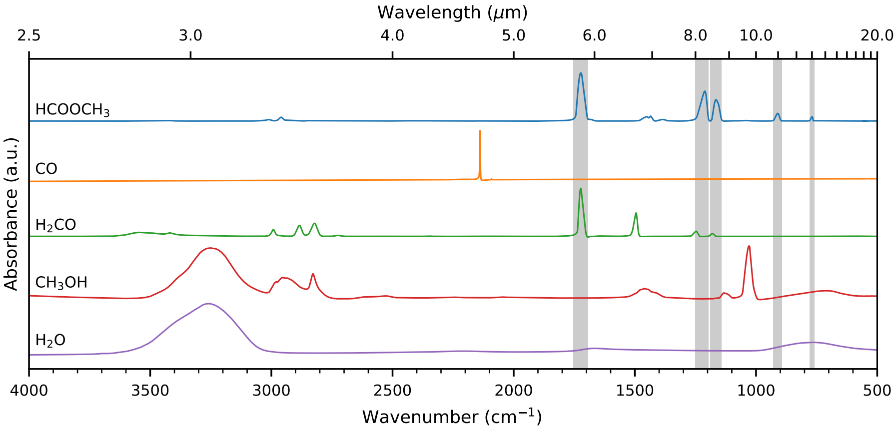

Figure 4.1: Pure normalized spectra of methyl formate ($HCOOCH_3$) and the matrix constituents (CO, H_2CO, CH_3OH, and H_2O) acquired at 15 K. The shaded areas highlight the features of methyl formate investigated in this study.

environmental ice conditions is beyond the scope of this work. In this work, the transitions are characterized by the peak positions and the FWHMs. Certain transitions, for example, O–CH_3 stretching mode, are a combination of different transitions, which overlap when the sample is in amorphous form but become independently visible when it crystallizes. In some specific cases, it is evident that there are two or more features, but at half maximum the features are still blended. In these cases the peak position of the strongest transition is given with the combined FWHM and is indicated by an asterisk. The assignments of the vibrational modes investigated in this work are given in Table 4.1 and are taken from literature (Modica & Palumbo 2010).

4.3 Results and discussion

In this section, we discuss the analysis of the spectra of methyl formate in pure form and mixed with astronomically relevant matrices. The spectra of methyl formate and separate matrix constituents are shown in Figure 4.1. The shaded areas highlight the absorption features of pure methyl formate that are potential candidates for a JWST identification. The O−CH_3 stretching mode (910.5 cm^{-1}/10.98 μm) analysis is shown here, and the results for the other vibrational modes mentioned in Table 4.1 are given in the appendices. In order to visualize the large amount of data acquired, several types of figures and tables are presented in this work. Temperature versus Spectra (TvS) heatmaps were made for a quick and general overview of the effects of temperature and different neighboring molecules on a single transition, see, for example, Figure 4.2. Each panel visualizes a different ice sample, that is, pure methyl formate or methyl formate mixed with abundant or chemically related precursor species. A horizontal cut at a given temperature would give a regular absorption spectrum at that given experimental temperature. Methyl formate crystallizes at approximately 90 K and this can be seen in the top left panel by the sudden shift and intensity change. In the top right panel, the mixture of methyl formate with CO shows that when CO

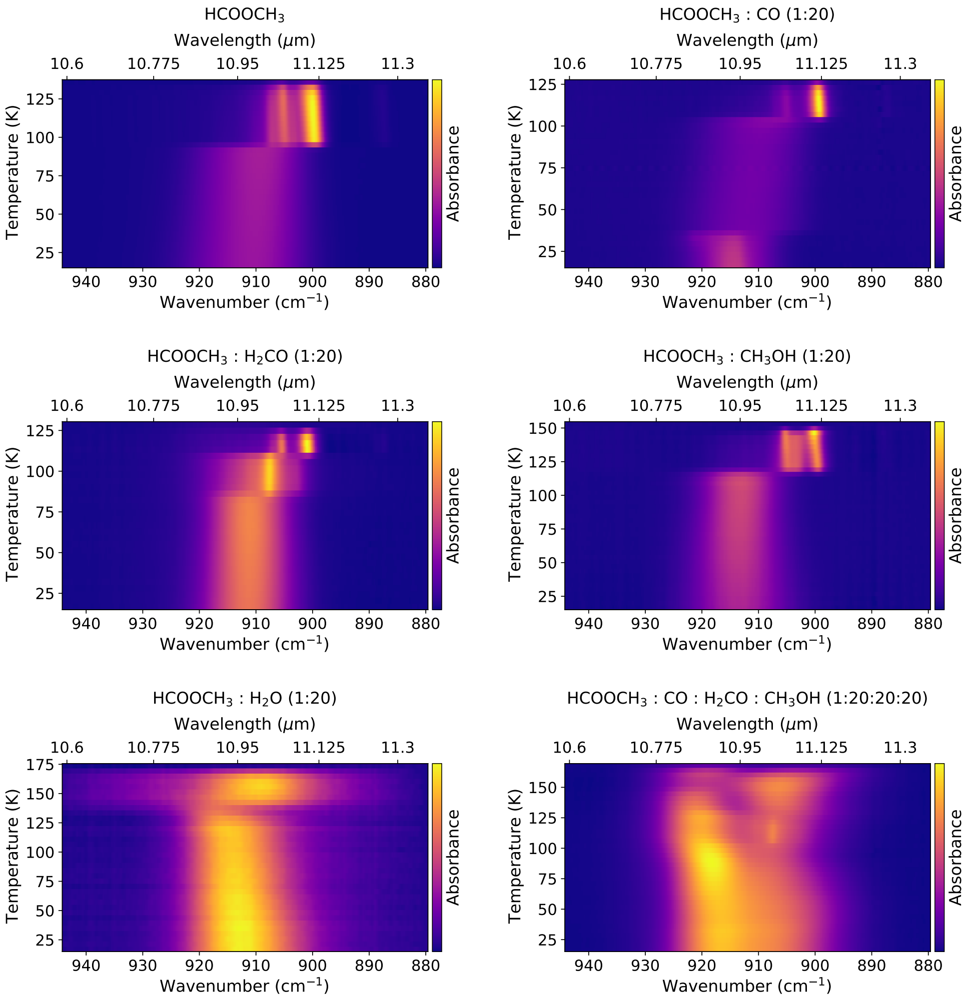

Figure 4.2: Temperature versus Spectra (TvS) heatmaps of the O$-$CH$_3$ stretching mode (910.5 cm^{-1}/10.98 μm) of HCOOCH$_3$ in the astronomically relevant ice matrices as a function of temperature.

is still present in the solid state, T $<$ 35 K, the O$-$CH$_3$ stretching mode feature is blue shifted and narrower. After CO desorption, this band returns to its “original” position. However, crystallization then occurs after 100 K, and the secondary peak is less prominent compared to the pure sample. Even though CO is no longer in the solid state, it has left an imprint on the absorption spectrum of methyl formate. In aid of future astronomical identifications, a more in-depth characterization of the absorption features is given for the five selected transitions, see Figure 4.1. For these transitions, the FWHMs as a function of the peak position and the relative band intensities are given for the selected temperatures, see, for example, Figure 4.3. Lastly, the exact peak position, FWHM, and relative band intensity are given in the tables found in the appendices. The error on the peak position and FWHM are 0.5 and 0.8 cm^{-1}, respectively.

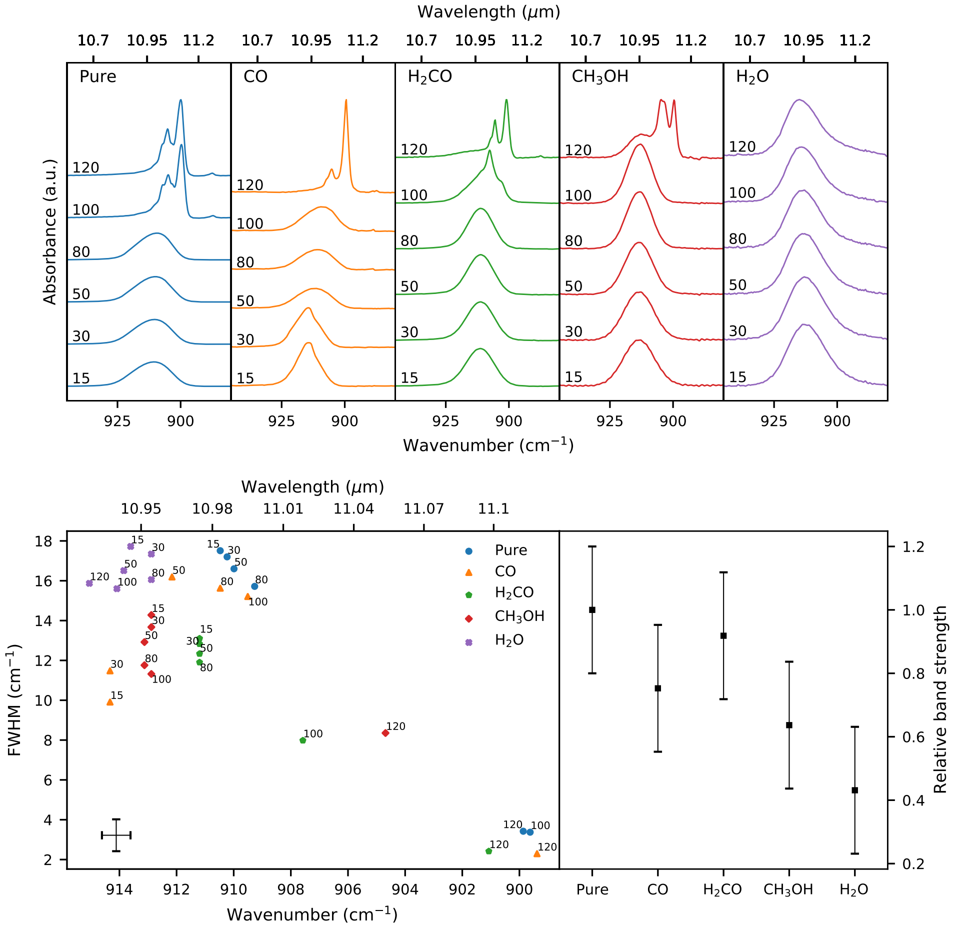

Figure 4.3: Top panel: absorption feature of the O$-$CH$_3$ stretching vibrational mode (910.5 cm^{-1}/10.98 μm) for each of the mixtures at selected temperatures. Bottom left panel: FWHM as a function of peak position at the selected temperatures. The error bar of each individual point is given in the bottom left. Bottom right panel: relative band strengths for methyl formate in the different ice matrices at 15 K with respect to the pure band strength.

4.3.1 The O$-$CH$_3$ stretching mode

The O$-$CH$_3$ stretching vibrational mode is positioned at 910.7 cm^{-1} (10.98 μm) in a pure methyl formate ice sample at 15 K. The TvS heatmaps of this vibrational mode are shown in Figure 4.2. The pure TvS heatmap shows that around 100 K, solid-state methyl formate changes from an amorphous structure to a crystalline structure. This changes the vibrational properties and expresses itself in peak splitting and a red shift to 899.6 cm^{-1} (11.12 μm) for the main peak and 904.9 cm^{-1} (11.05 μm) for the secondary peak. In general, when methyl formate is diluted in one of the matrix constituents (Table 4.2), the O$-$CH$_3$ stretching mode is blue shifted and the FWHM decreases with the exception of the H$_2$O matrix where the FWHM stays comparable.

Table 4.2: Peak position and FWHM of the methyl formate O−CH_3 stretching mode at 15 K in various matrices.

Mixture	Temperature	λ_{peak}		FWHM	
	(K)	(cm^{-1})	(μm)	(cm^{-1})	(μm)
$HCOOCH_3$		910.47	10.983	17.51	0.2108
$HCOOCH_3$: CO		914.33	10.937	9.909	0.1184
$HCOOCH_3$: H_2CO	15	911.20	10.975	13.10	0.1577
$HCOOCH_3$: CH_3OH		912.88	10.954	14.28	0.1711
$HCOOCH_3$: H_2O		913.61	10.946	17.72	0.2131

Notes. Excerpt from Table 4.4.

In Figure 4.3, the O−CH_3 stretching vibrational band is shown as well as the FWHM versus peak position for each of the characteristic temperatures, that is, 15, 30, 50, 80, 100, and 120 K. The bottom right panel of Figure 4.3 shows the relative band strength compared to the pure band strength in different matrices at 15 K.

The apolar (CO:H_2CO:CH_3OH) matrix analysis is omitted for the O−CH_3 stretching vibrational mode as H_2CO and CH_3OH have a vibrational matrix interaction at approximately 915 cm^{-1} (10.9 μm). This matrix interaction is interesting as it takes place between two main interstellar ice constituents. It is likely that this interaction scales with a mixing ratio and depends on whether the ice is fully mixed or layered. We are not aware of an earlier mention of this interaction. A more detailed investigation is beyond the scope of this work.

4.3.2 The OCO deformation mode

The OCO deformation mode is positioned at 768.3 cm^{-1} (13.02 μm) in a pure methyl formate ice sample at 15 K. As crystallization occurs around 90 K, the mode splits into two modes. The main peak is blue shifted to 769.0 cm^{-1} (13.00 μm) and the secondary peak to 775.2 cm^{-1} (12.90 μm). This is the weakest of the transitions selected for analysis, but it is in a favorable position as it only overlaps with the H_2O libration mode and CH_3OH torsion mode. These two modes are easily fitted into the baseline and subtracted. Acetaldehyde (CH_3CHO) has a vibrational mode at a similar wavenumber, but, the presence or absence of other vibrational modes of methyl formate will allow for distinction from acetaldehyde. The TvS heatmaps of the OCO deformation mode in the pure and astronomically relevant matrices are given in Figure 4.6. The general trend is that the FWHM decreases compared to the pure spectrum of methyl formate when mixed with other astronomically relevant constituents. An exception to this is the H_2O matrix: here the FWHM is almost doubled by the interaction with the H_2O matrix, and the peak position blue shifts nearly 10 cm^{-1}. The matrices containing H_2CO blue shift the peak position by a couple of wavenumbers. This is visually summarized in Figure 4.7 and the specifics are given in Table 4.3.

4.3.3 The CH_3 rocking mode

The CH_3 rocking vibrational mode is positioned at 1165.3 cm^{-1} (8.582 μm) in a pure methyl formate ice sample at 15 K. The mode splits into multiple features after crystallization with the main peak at 1165.8 cm^{-1} (8.578 μm) and secondary peaks at 1177.1 cm^{-1} (8.496 μm) and 1158.8 cm^{-1} (8.630 μm). This evolution of the vibrational mode as a function of the temperature in pure form and mixed astronomically relevant matrices is shown in Figure 4.8. The CH_3 rocking mode is blended in the mixtures containing H_2CO with the CH_2 wagging vibrational mode of H_2CO. This mode of H_2CO is positioned at 1178 cm^{-1} (8.489 μm), which is in the blue wing of the methyl formate CH_3 rocking mode. This blending results in a larger FWHM, but it is still smaller than the FWHM of the pure methyl formate spectra, as shown in Figure 4.9. One should be cautious using the derived peak positions, FWHMs, and relative band strength intensities for the mixtures containing H_2CO. These values are influenced by and depend on the ratio to which H_2CO and $HCOOCH_3$ are deposited, in this case 20:1. The mixtures containing CH_3OH show a feature around 1130 cm^{-1} (8.85 μm), which is the CH_3 vibrational rocking mode of CH_3OH. Although this feature of CH_3OH is close to the CH_3 rocking mode of methyl formate, there is no overlap in this study. Any signal associated with the CH_3OH mode is omitted from the analysis.

4.3.4 The C−O stretching mode

The C−O vibrational stretching mode is positioned at 1211.3 cm^{-1} (8.256 μm) in a pure methyl formate ice sample at 15 K. After crystallization, the peak is slightly red shifted to 1210.4 cm^{-1} (8.262 μm), no band splitting is found, and the FWHM decreases. However, there is a significant broad blue wing below the half maximum. The TvS heatmaps of the pure and mixed methyl formate spectra as a function of the temperature are shown in Figure 4.10. The CH_2 rocking mode of H_2CO is positioned at approximately 1247 cm^{-1} (8.019 μm), which introduces a slight overlap with the blue wing of the C−O stretching mode. This CH_2 rocking mode of H_2CO is omitted from analysis by introducing a cut-off at 1234.5 cm^{-1} (8.100 μm). The spectra, peak positions, and corresponding FWHMs at the characteristic temperatures of the C−O stretching mode are given in Figure 4.11. Most remarkable are the spectra of methyl formate mixed in H_2O where at 15 K the peak position is blue shifted to 1233.7 cm^{-1} (8.106 μm) and the FWHM is 40 cm^{-1}, which is 10 cm^{-1} larger compared to the pure spectra. This feature therefore allows us to tell whether methyl formate resides in a polar or an apolar matrix environment. Notably, at low temperatures the apolar mixture has a FWHM of approximately 50 cm^{-1} due to blending with the CH_2 rocking mode of H_2CO.

4.3.5 The C=O stretching mode

The C=O stretching mode is the strongest vibrational mode of methyl formate at 1723.1 cm^{-1} (5.804 μm) in a pure methyl formate ice sample at 15 K, as shown in Figure 4.1. After crystallization, the main peak shifts to the red to a new position of 1698.0 cm^{-1} (5.889 μm). A secondary peak is seen at 1709.8 cm^{-1} (5.849 μm), and a blue-wing plateau is seen. The C=O stretching mode is, however, a common vibrational mode that is also seen in other molecules, such as formaldehyde (H_2CO), formic acid (HCOOH), formamide (NH_2CHO), acetaldehyde (CH_3CHO), and acetone

(CH_3COCH_3). The TvS heatmaps and detailed analysis, that is, FWHM versus peak position and relative band strength intensities, are shown in Figures 4.12 and 4.13, respectively. The C=O stretching mode of methyl formate mixed in H_2O shows a red-wing access and has an approximately 20% larger relative band strength. This is due to a less precise baseline subtraction of the bending mode of H_2O which overlaps with this feature, see Figure 4.1.

Since there is an overlap with the C=O stretch of H_2CO, the matrices containing H_2CO are omitted in our analysis. In general a feature observed around 1720 cm^{-1} (5.81 μm) likely consists of multiple different organic molecules with a C=O bond. This makes it difficult to identify a specific molecule on this vibrational mode alone. This region is, however, ideal to get an estimate on the total amount of molecules in the solid state containing a C=O functional group in their chemical structure. As such, this feature also can act as a diagnostic tool for a family of molecules. This concept is explored in Section 4.4.3.

4.4 Infrared observations

The experiments and data analysis performed in this study will be a valuable analytical tool for astronomers using JWST for ice surveys. The spectroscopic characterization of methyl formate, and other COMs in the solid state (see e.g., Terwisscha van Scheltinga et al. 2018; Rachid et al. 2020; Hudson & Ferrante 2020; Hudson et al. 2020; Gerakines & Hudson 2020), is a prerequisite for their identification in astronomical environments such as dense clouds, embedded protostars, and inclined protoplanetary disks. Previous observations with ISO and *Spitzer* have observed such sources and their spectral resolution and sensitivity allowed for the detection of some smaller solid-state species, including methanol (e.g., Boogert et al. 2015). A few COMs have been tentatively identified in the massive embedded protostar W33A, namely acetaldehyde, ethanol, and formic acid (Schutte et al. 1999; Öberg et al. 2011). The reanalysis of the ISO W33A spectrum with laboratory spectra in Terwisscha van Scheltinga et al. (2018) shows that it is likely possible to determine with JWST in which astronomically relevant ice matrix these COMs reside.

The infrared fingerprint region covered here spans the 2000–400 cm^{-1} (5–25 μm) region. An unambiguous identification of a species in this region from a single vibrational band is challenging, but the presence of multiple vibrational bands considerably helps in the assignment. Methyl formate has five potential candidates for identification in the fingerprint region. These are the C=O stretching mode (5.804 μm), the C−O stretching (8.256 μm), CH_3 rocking (8.582 μm), O−CH_3 stretching (10.98 μm), and OCO deformation (13.02 μm) mode. The C=O stretching mode (5.804 μm) is the strongest absorption feature, but it overlaps with absorption bands of other molecules containing a C=O in their chemical structure. This makes it less favorable to identify methyl formate ice, but it should be visible when other features of methyl formate are observed. The combination of the O−CH_3 stretching (10.98 μm) and OCO deformation (13.02 μm) modes is most suited for an unambiguous solid-state methyl formate identification. These vibrational modes have the lowest apparent band strengths of the selected transitions, but they do not have interfering overlap with other species. They will be superimposed on the H_2O libration and CH_3OH torsion modes, though. These are broad features on which the superimposed methyl formate modes are clearly visible. The C−O stretching (8.256 μm) and CH_3 rocking (8.582 μm) modes have more favorable apparent band strengths, but they overlap with two of the vibrational modes of H_2CO. Since formaldehyde is chemically related to the radicals that form methyl formate, it is reasonable to assume that these two species are mixed in the ice and thus identification on solely these two modes is uncertain. From this it becomes clear that an identification of methyl formate ice is not straightforward from one transition. The unambiguous identification of methyl formate requires multiple transitions, even if some are partially overlapping with features of other species. For overlapping species it is important to consider the relative absorbance ratios of the individual transitions, see Appendix 4.F.

4.4.1 Methyl formate in HH 46

Current available infrared spectra lack the spectral resolution and sensitivity to firmly identify methyl formate ice. However, observations toward some protostars are found to have an additional absorption on the red wing of the 10 μm silicate feature, between 11 and 12 μm. The O$-$CH$_3$ stretching at 10.98 μm is a potential candidate for this observed absorption feature. HH 46, a low-mass protostar, is one of these protostars and we used its spectrum to derive an upper limit of frozen methyl formate in this source. This upper limit was approximated through a best fit by eye of a laboratory spectrum of methyl formate matched to the HH 46 spectrum observed by *Spitzer* (Boogert et al. 2008). These authors corrected the HH 46 spectrum by subtraction of a standard interstellar silicate spectrum (GCS 3; Kemper et al. 2004) and a laboratory spectrum of pure H_2O ice at a temperature of 40 K (Hudgins et al. 1993). As the spectral quality did not allow us to make a distinction as to in which matrix the methyl formate resides, a pure amorphous spectrum was used. Figure 4.4 shows the *Spitzer* spectrum of HH 46 from roughly 5.5 to 14 μm with the laboratory methyl formate spectrum that was fitted by eye to the observed spectrum of HH 46. Additionally, the spectral locations of some previously detected ice species, for example, NH_3, CH_4, and CH_3OH, are shown in Figure 4.4 by vertically dashed lines.

The C=O stretch (5.804 μm), C$-$O stretch (8.256 μm), and CH$_3$ rocking (8.582 μm) modes of methyl formate match with the observation, but they do not reproduce the full pattern. It should be noted that in the blue wing of the astronomical 9 μm feature, there appears to be two weak bumps at approximately 8.2 and 8.6 μm that line up with the C$-$O stretch and CH$_3$ rocking modes of methyl formate. From 11 to 12 μm, there is a broad absorption that seems to be composed of multiple features, of which at least two are positioned at 11.1 and 11.6 μm. The O$-$CH$_3$ stretching mode at approximately 11 μm fits the blue wing of the 11.1 μm feature. The weakest transition, the OCO deformation (13.02 μm), is in this case the important transition that gives a strict upper limit on the methyl formate column density. As shown in the inset of Figure 4.4, there is a potential absorption feature around 12.98 μm. The inset also shows the methyl formate spectrum at that wavelength. The laboratory spectrum is slightly red shifted and wider compared to the absorption feature in HH 46. However, the FWHM versus peak position analysis, see Figure 4.7, of this mode shows that this feature can be attributed to methyl formate. An upper limit of 1.7×10^{17} cm^{-2} was found for methyl formate in HH 46. With respect to water, the upper limit abundances of methyl formate is $\leq$ 2.2%, given a H_2O column density of 7.8×10^{18} cm^{-2}, and $\leq$ 40% with respect to methanol, given a column density of 4.3×10^{17} cm^{-2} (Boogert et al. 2008).

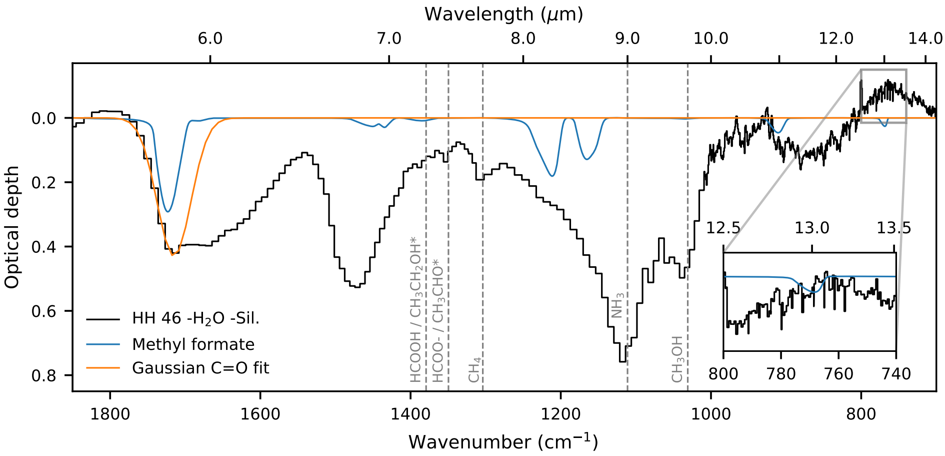

Figure 4.4: *Spitzer* spectrum of HH 46 with subtraction of the continuum, H_2O, and silicates. Additionally, the spectrum of amorphous methyl formate and a Gaussian fit to estimate all molecules containing a C=O bond around 5.8 μm are shown in blue and orange, respectively. The inset in the bottom right zooms in on the 13 μm feature where the laboratory spectrum is vertically offset to match the optical depth of the HH 46 spectrum. Vertical dashed lines indicate the locations of previously detected species, where the asterisk indicates tentative detections.

4.4.2 The 11 μm feature

Infrared absorption features around 7 μm toward protostars show potential for COM identification with JWST, for example, in W33A the absorption features at 7.25 and 7.41 μm are tentatively identified as ethanol and acetaldehyde, respectively (Schutte et al. 1999; Öberg et al. 2011; Terwisscha van Scheltinga et al. 2018). Another example of this type of potential region is the 11 μm region, since some protostars have an additional feature on the 10 μm silicate feature. Here we briefly look at *Spitzer* IRS Short-High spectra taken from the CASSIS database of three protostars, that is, HH 46, R CrA IRS5, and IRAS 15398 (Lebouteiller et al. 2011, 2015). Figure 4.5 shows these normalized absorption features and how they compare to one another. In HH 46, the feature seems to be composed of at least two components with their respective peaks at approximately 11.1 and 11.6 μm. For R CrA IRS5, only the feature at 11.1 μm is seen, but with a comparable optical depth. The third source is IRAS 15398, which has a broader feature compared to the other two. The optical depth is substantially higher, but the signal-to-noise is worse. Throughout the literature, different possible carriers for features in this region have been proposed. Bregman et al. (2000) attribute the observed absorption feature at 11.2 μm in Monoceros R2 IRS 3 to a C–H out-of-plane vibrational mode of polycyclic aromatic hydrocarbon (PAH) molecules. Surveys with both ground- and space-based telescopes have shown that across the different environments, that is to say interstellar medium, young stars, and evolved stars, the 11 μm feature can be attributed to crystalline silicates, specifically forsterite (Kessler-Silacci et al. 2005; Wright et al. 2016; Do-Duy et al. 2020). Based on the data obtained in this and previous studies, we propose a third carrier as a possible

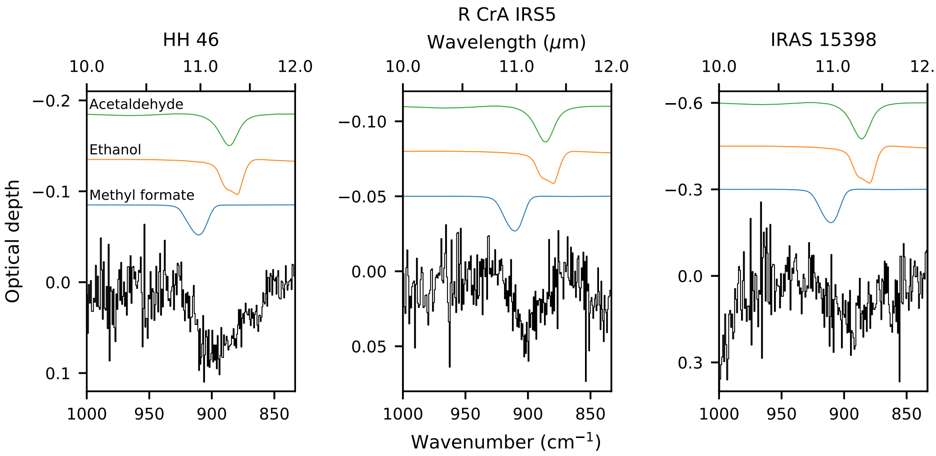

Figure 4.5: *Spitzer* CASSIS pipeline spectra of R Cra IRS5, HH 46, and IRAS 15398 (from left to right) in the 10-14 μm region. The spectra on top are derived from labortory data for pure acetaldehyde, ethanol, and methyl formate recorded at 15 K.

candidate for the absorption feature between 11 and 12 μm, namely COMs. On top of the infrared spectra of the three sources, Figure 4.5 shows the laboratory spectra of three COMs: acetaldehyde (CH_3CHO), ethanol (CH_3CH_2OH), and methyl formate ($HCOOCH_3$). The laboratory spectra are offset and scaled with arbitrary factors to show the overlap with the observed absorption features between 11 and 12 μm. A combination of these and other COMs with vibrational transitions in this region could, partially, or fully be responsible for the absorption features observed.

4.4.3 The C=O functional group

Different molecules with a common functional group (i.e., a CH_3, NH_2, or CO group) exhibit some similar spectral features in the infrared as the involved vibrational bands are the same. The C=O stretching mode is a very common functional group in COMs containing carbon and oxygen atoms. Although each molecule has this feature at its distinctive peak position, in general they are relatively close to each other and overlap when ice is composed of different C=O containing molecules. The apparent band strengths of the different C=O stretching modes can be averaged to make an estimate on the total amount of molecules with a C=O in their chemical structure. In this way, a spectral feature is not assigned to a specific molecule but to a specific class of molecules that generally are chemically related as well. This average apparent band strength was approximated by averaging the apparent band strengths of the molecules mentioned in Section 4.3.5 in a one-to-one ratio (Schutte et al. 1999; Modica & Palumbo 2010; Bouilloud et al. 2015; Hudson et al. 2018). For the HH 46 spectrum, we fit a Gaussian at 5.831 μm with a FWHM of 0.0544 μm, see Figure 4.4. The average apparent band strength of the C=O band is derived to be approximately 3.2×10^{-17} cm^{-1}, resulting in a column density of 7.6×10^{17} cm^{-2} using a Gaussian fit of the integrated band area. The abundance of molecules with C=O in their chemical structure for HH 46 with respect to solid-state water is 9.5%. The upper limit to the column density of methyl formate in HH 46 from Section 4.4.1, together with the estimate of molecules containing a C=O functional group, provide an upper limit of $\leq 23\%$ to the contribution of methyl formate to the family of molecules containing the C=O bond.

4.5 Conclusions

In this study we present the characterization of solid-state methyl formate in the infrared. Spectra for pure methyl formate and mixed in astronomical matrix environments are analyzed and the TvS heatmaps, peak positions versus FWHM, and relative band intensities are given for five selected methyl formate transitions. We conclude the following:

1. Of the five selected transitions, the combination of the $O-CH_3$ stretching (10.98 μm) and OCO deformation (13.02 μm) modes is most suited for the unambiguous detection of methyl formate ice. The other three transitions, C=O stretch (5.804 μm), C−O stretch (8.256 μm), and CH_3 rocking (8.582 μm), potentially overlap with chemically related species. However, these overlapping features are still diagnostic when considering their relative intensities compared to the $O-CH_3$ stretching and OCO deformation modes.

2. The peak position versus FWHM analysis shows that, compared to the pure spectra, the apolar mixtures generally blue shift and decrease the FWHM of the selected transitions. The features in a water matrix are clearly distinguishable from the apolar constituents, for example, the C−O stretching mode in a water matrix is blue shifted by approximately 20 cm^{-1}.

3. Comparing the reference spectra of methyl formate with *Spitzer* observations of HH 46 provides a column density upper limit of 1.7×10^{17} cm^{-2}. With respect to water, the upper limit abundances of methyl formate are $\leq 2.2\%$ and $\leq 40\%$ with respect to methanol.

4. The observed 11 μm feature has previously been attributed to polycyclic aromatic hydrocarbons or crystalline silicates. Several COMs show features in this region and may be contributing carriers of this absorption feature.

5. The total amount of molecules containing a functional C=O group in their chemical structure is estimated to be 7.6×10^{17} cm^{-2}, which in respect to water is equal to 9.5% for the embedded protostar HH 46.

The JWST mid-infrared instrument (MIRI) is most suited for the detection of COMs and is expected to have a continuum signal-to-noise ratio of at most 300. This means JWST will detect absorption features down to 1% of the continuum flux at a 3σ level. A detection of frozen COMs such as methyl formate ice following the spectroscopic data presented here, will be challenging with JWST, and possibly limited to chemically evolved inter- and circumstellar regions.

Appendix

4.A The OCO deformation mode

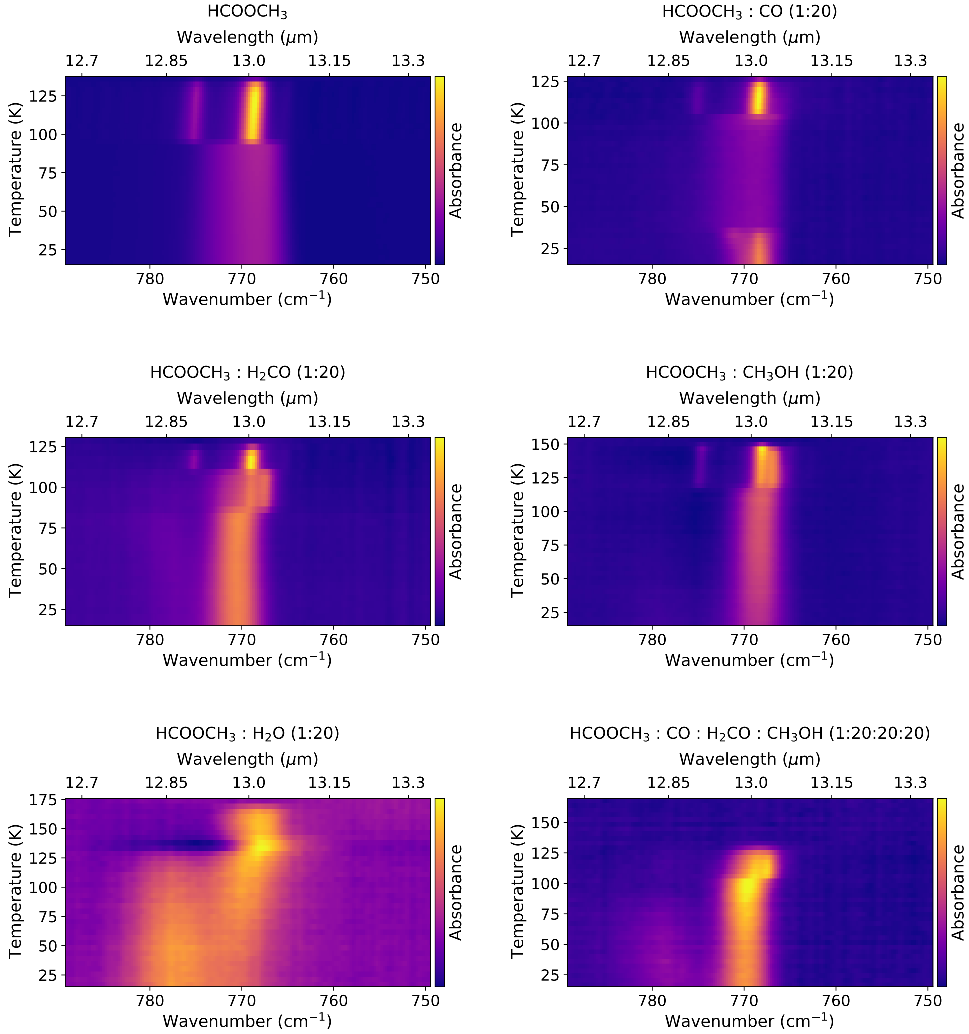

Figure 4.6: Temperature versus Spectra (TvS) heatmaps of the OCO deformation mode (768.3 cm^{-1}/13.02 μm) of $HCOOCH_3$ in the astronomically relevant ice matrices as a function of the temperature.

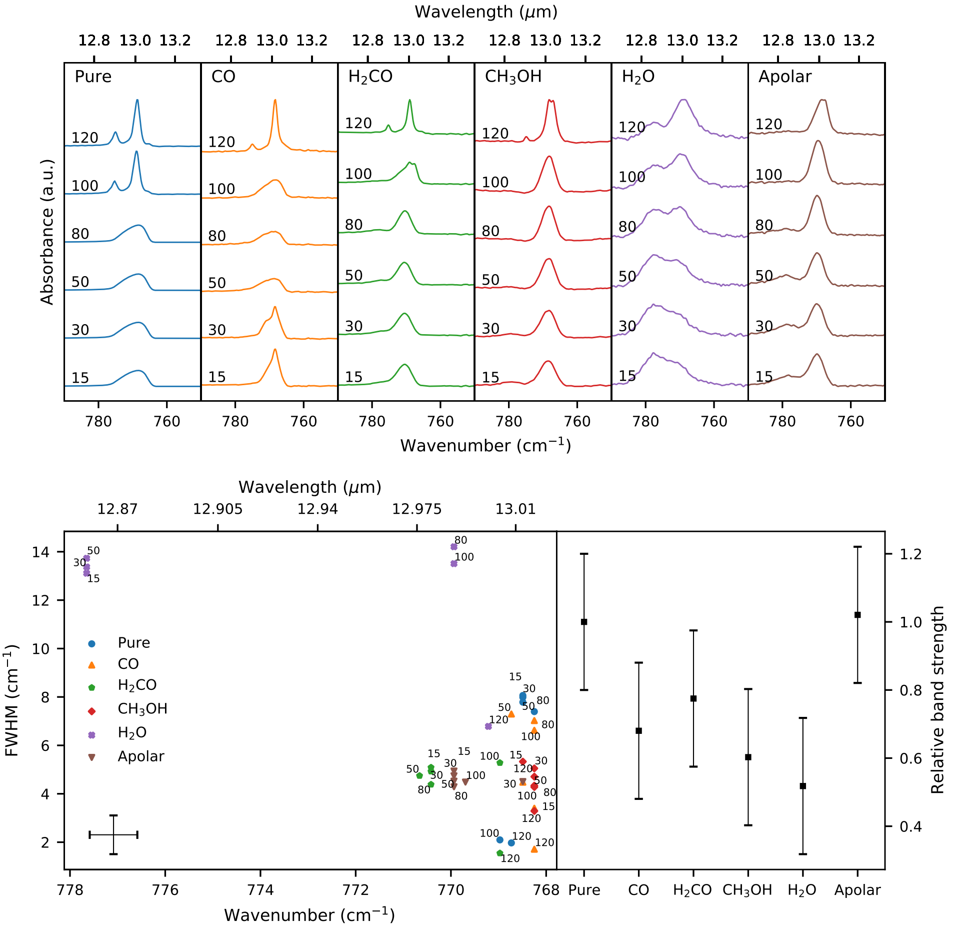

Figure 4.7: Top panel: absorption feature of the OCO deformation vibrational mode (768.3 cm^{-1}/13.02 μm) for each of the mixtures at selected temperatures. Bottom left panel: FWHM as a function of the peak position at the selected temperatures. The error bar of each individual point is given in the bottom left. Bottom right panel: relative band strengths for methyl formate in the different ice matrices at 15 K with respect to the pure band strength.

Table 4.3: Peak position and FWHM of the methyl formate OCO deformation stretching mode (768.3 cm^{-1}/13.02 μm) in various matrices.

Mixture	Temperature	λ_{peak}		FWHM	
	(K)	(cm^{-1})	(μm)	(cm^{-1})	(μm)
$HCOOCH_3$	15	768.48	13.012	8.061	0.1361
$HCOOCH_3$: CO		768.25	13.017	3.404	0.0576
$HCOOCH_3$: H_2CO		770.42	12.980	5.089	0.0857
$HCOOCH_3$: CH_3OH		768.49	13.013	5.329	0.0902
$HCOOCH_3$: H_2O		777.65	12.859	13.11*	0.2184*
$HCOOCH_3$: Apolar		769.94	12.988	4.941	0.0833
$HCOOCH_3$	30	768.49	13.012	7.987	0.1349
$HCOOCH_3$: CO		768.49	13.012	4.479	0.0757
$HCOOCH_3$: H_2CO		770.42	12.980	4.927	0.0829
$HCOOCH_3$: CH_3OH		768.25	13.017	5.050	0.0855
$HCOOCH_3$: H_2O		777.65	12.859	13.37*	0.2228*
$HCOOCH_3$: Apolar		769.94	12.988	4.743	0.0800
$HCOOCH_3$	50	768.49	13.012	7.785	0.1314
$HCOOCH_3$: CO		768.73	13.008	7.296	0.1231
$HCOOCH_3$: H_2CO		770.66	12.976	4.747	0.0799
$HCOOCH_3$: CH_3OH		768.25	13.017	4.709	0.0797
$HCOOCH_3$: H_2O		777.65	12.859	13.73*	0.2289*
$HCOOCH_3$: Apolar		769.94	12.988	4.523	0.0763
$HCOOCH_3$	80	768.25	13.017	7.396	0.1249
$HCOOCH_3$: CO		768.25	13.017	7.025	0.1186
$HCOOCH_3$: H_2CO		770.42	12.980	4.385	0.0739
$HCOOCH_3$: CH_3OH		768.25	13.017	4.336	0.0734
$HCOOCH_3$: H_2O		769.94	12.988	14.21*	0.2374*
$HCOOCH_3$: Apolar		769.94	12.988	4.290	0.0724
$HCOOCH_3$	100	768.97	13.004	2.095	0.0354
		775.24	12.899	–	–
$HCOOCH_3$: CO		768.25	13.017	6.623	0.1119
$HCOOCH_3$: H_2CO		768.97	13.004	5.281	0.0892
$HCOOCH_3$: CH_3OH		768.25	13.017	4.279	0.0725
$HCOOCH_3$: H_2O		769.94	12.988	13.51*	0.2261*
$HCOOCH_3$: Apolar		769.69	12.992	4.484	0.0757
$HCOOCH_3$	120	768.73	13.008	1.971	0.0333
		775.00	13.008	–	–
$HCOOCH_3$: CO		768.45	13.017	1.710	0.0287
		775.24	12.899	–	–
$HCOOCH_3$: H_2CO		768.97	13.004	1.546	0.0262
		775.24	12.899	–	–
$HCOOCH_3$: CH_3OH		768.25	13.017	3.289	0.0558
		775.24	12.899	–	–
$HCOOCH_3$: H_2O		769.21	13.000	6.784	0.1147
$HCOOCH_3$: Apolar		768.49	13.013	4.505	0.0762

Notes. $^{(*)}$ FWHM result of two or more blended peaks.

4.B The O−CH_3 stretching mode

Table 4.4: Peak position and FWHM of the methyl formate O−CH_3 stretching mode (910.5 cm^{-1}/10.98 μm) in various matrices.

Mixture	Temperature	λ_{peak}		FWHM	
	(K)	(cm^{-1})	(μm)	(cm^{-1})	(μm)
$HCOOCH_3$	15	910.47	10.983	17.51	0.2108
$HCOOCH_3$: CO		914.33	10.937	9.909	0.1184
$HCOOCH_3$: H_2CO		911.20	10.975	13.10	0.1577
$HCOOCH_3$: CH_3OH		912.88	10.954	14.28	0.1711
$HCOOCH_3$: H_2O		913.61	10.946	17.72	0.2131
$HCOOCH_3$	30	910.23	10.986	17.20	0.2071
$HCOOCH_3$: CO		914.33	10.937	11.48	0.1371
$HCOOCH_3$: H_2CO		911.20	10.975	12.83	0.1544
$HCOOCH_3$: CH_3OH		912.88	10.954	13.67	0.1638
$HCOOCH_3$: H_2O		912.88	10.954	17.34	0.2085
$HCOOCH_3$	50	909.99	10.989	16.60	0.2000
$HCOOCH_3$: CO		912.16	10.963	16.19	0.1945
$HCOOCH_3$: H_2CO		911.20	10.975	12.36	0.1485
$HCOOCH_3$: CH_3OH		913.12	10.951	12.92	0.1548
$HCOOCH_3$: H_2O		913.85	10.943	16.51	0.1982
$HCOOCH_3$	80	909.27	10.998	15.72	0.1896
$HCOOCH_3$: CO		910.47	10.983	15.63	0.1882
$HCOOCH_3$: H_2CO		911.20	10.975	11.90	0.1434
$HCOOCH_3$: CH_3OH		913.12	10.951	11.13	0.1335
$HCOOCH_3$: H_2O		912.88	10.954	16.06	0.1927
$HCOOCH_3$	100	899.63	11.116	3.374	0.0417
		904.93	11.051	–	–
$HCOOCH_3$: CO		909.51	10.995	15.21	0.1836
$HCOOCH_3$: H_2CO		907.58	11.018	7.982	0.0966
$HCOOCH_3$: CH_3OH		912.88	10.954	11.32	0.1357
$HCOOCH_3$: H_2O		914.09	10.940	15.60	0.1871
$HCOOCH_3$	120	899.87	11.113	3.422	0.0422
		905.17	11.048	–	–
$HCOOCH_3$: CO		899.38	11.119	2.295	0.0284
		905.17	11.048	–	–
$HCOOCH_3$: H_2CO		901.07	11.098	2.418	0.0298
		905.41	11.045	–	–
$HCOOCH_3$: CH_3OH		904.69	11.054	8.354*	0.1025*
		899.63	11.116	–	–
$HCOOCH_3$: H_2O		915.05	10.928	15.87	0.1901

Notes. $^{(*)}$ FWHM result of two or more blended peaks.

4.C The CH_3 rocking mode

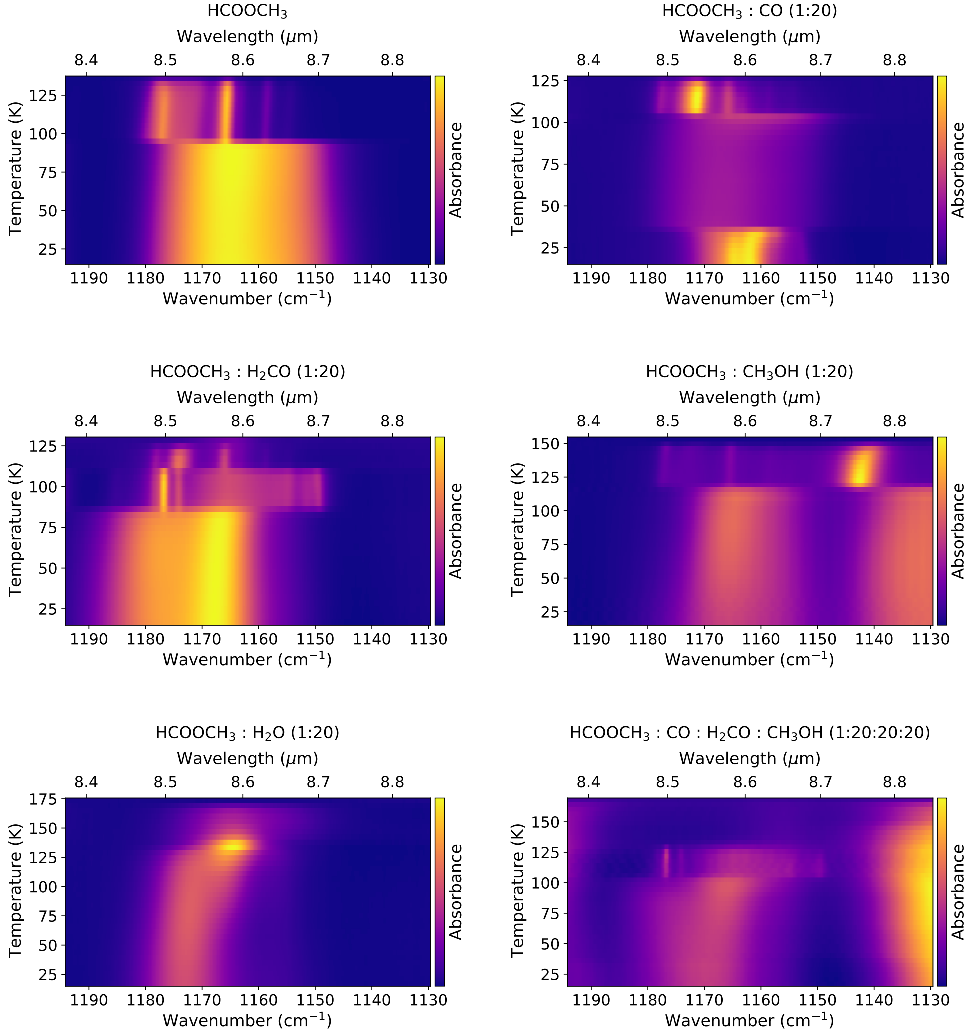

Figure 4.8: Temperature versus Spectra (TvS) heatmaps of the CH_3 rocking mode (1165.3 cm^{-1}/8.582 μm) of $HCOOCH_3$ in the astronomically relevant ice matrices as a function of the temperature.

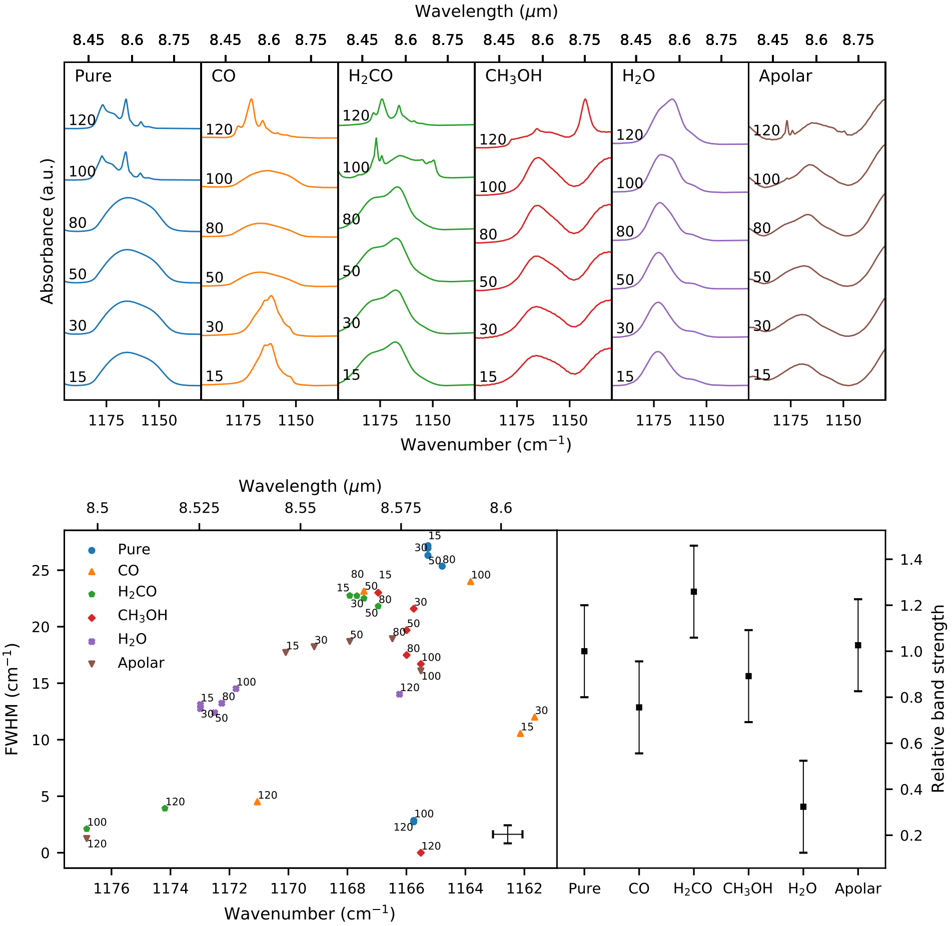

Figure 4.9: Top panel: absorption feature of the CH_3 rocking vibrational mode (1165.3 cm^{-1}/8.582 μm) for each of the mixtures at selected temperatures. Bottom left panel: FWHM as a function of the peak position at the selected temperatures. The error bar of each individual point is given in the bottom right. Bottom right panel: relative band strengths for methyl formate in the different ice matrices at 15 K with respect to the pure band strength.

Table 4.5: Peak position and FWHM of the methyl formate CH_3 rocking mode (1165.3 cm^{-1} / 8.582 μm) in various matrices.

Mixture	Temperature	λ_{peak}		FWHM	
	(K)	(cm^{-1})	(μm)	(cm^{-1})	(μm)
$HCOOCH_3$	15	1165.3	8.5817	27.17	0.2009
$HCOOCH_3$: CO		1162.1	8.6048	10.53	0.0777
$HCOOCH_3$: H_2CO		1167.9	8.5622	22.75	0.1654*
$HCOOCH_3$: CH_3OH		1167.0	8.5693	23.01	0.1701
$HCOOCH_3$: H_2O		1173.0	8.5253	13.11	0.0953
$HCOOCH_3$: Apolar		1170.1	8.5463	17.72	0.1293
$HCOOCH_3$	30	1165.3	8.5817	26.94	0.1992
$HCOOCH_3$: CO		1161.6	8.6084	12.01	0.0887
$HCOOCH_3$: H_2CO		1167.7	8.5634	22.73	0.1653*
$HCOOCH_3$: CH_3OH		1165.8	8.5782	21.59	0.1596
$HCOOCH_3$: H_2O		1173.0	8.5253	12.75	0.0927
$HCOOCH_3$: Apolar		1169.1	8.5534	18.23	0.1331
$HCOOCH_3$	50	1165.3	8.5817	26.31	0.1945
$HCOOCH_3$: CO		1167.4	8.5658	23.14	0.1704
$HCOOCH_3$: H_2CO		1167.4	8.5658	22.50	0.1637*
$HCOOCH_3$: CH_3OH		1166.0	8.5763	19.69	0.1455
$HCOOCH_3$: H_2O		1172.5	8.5288	12.38	0.0901
$HCOOCH_3$: Apolar		1167.9	8.5622	18.70	0.1366
$HCOOCH_3$	80	1164.8	8.5853	25.35	0.1875
$HCOOCH_3$: CO		1167.4	8.5658	23.16	0.1706
$HCOOCH_3$: H_2CO		1167.0	8.5693	21.70*	0.1580*
$HCOOCH_3$: CH_3OH		1166.0	8.5764	17.49	0.1293
$HCOOCH_3$: H_2O		1172.3	8.5305	13.23	0.0964
$HCOOCH_3$: Apolar		1166.5	8.5728	18.94	0.1385
$HCOOCH_3$	100	1165.8	8.5782	2.854	0.0210
		1177.1	8.4956	–	–
$HCOOCH_3$: CO		1163.8	8.5924	24.00	0.1776
$HCOOCH_3$: H_2CO		1176.8	8.4973	2.113	0.0153
$HCOOCH_3$: CH_3OH		1165.5	8.5799	16.70	0.1235
$HCOOCH_3$: H_2O		1171.8	8.5340	14.51	0.1060
$HCOOCH_3$: Apolar		1165.5	8.5799	16.09	0.1186
$HCOOCH_3$	120	1165.8	8.5782	2.742	0.0202
		1176.8	8.4973	–	–
$HCOOCH_3$: CO		1171.1	8.5393	4.508	0.0328
		1165.8	8.5782	–	–
$HCOOCH_3$: H_2CO		1174.2	8.5165	3.921	0.0285
		1166.0	8.5764	–	–
$HCOOCH_3$: CH_3OH		1165.5	8.5799	–**	–**
$HCOOCH_3$: H_2O		1166.2	8.5746	14.03	0.1027
$HCOOCH_3$: Apolar		1176.8	8.4973	1.258	0.0091
		1164.5	8.5870	–	–

Notes. (*) FWHM result of two or more blended peaks. (**) Due to severe blending with the matrix constituent, there is no FWHM determination.

4.D The C–O stretching mode

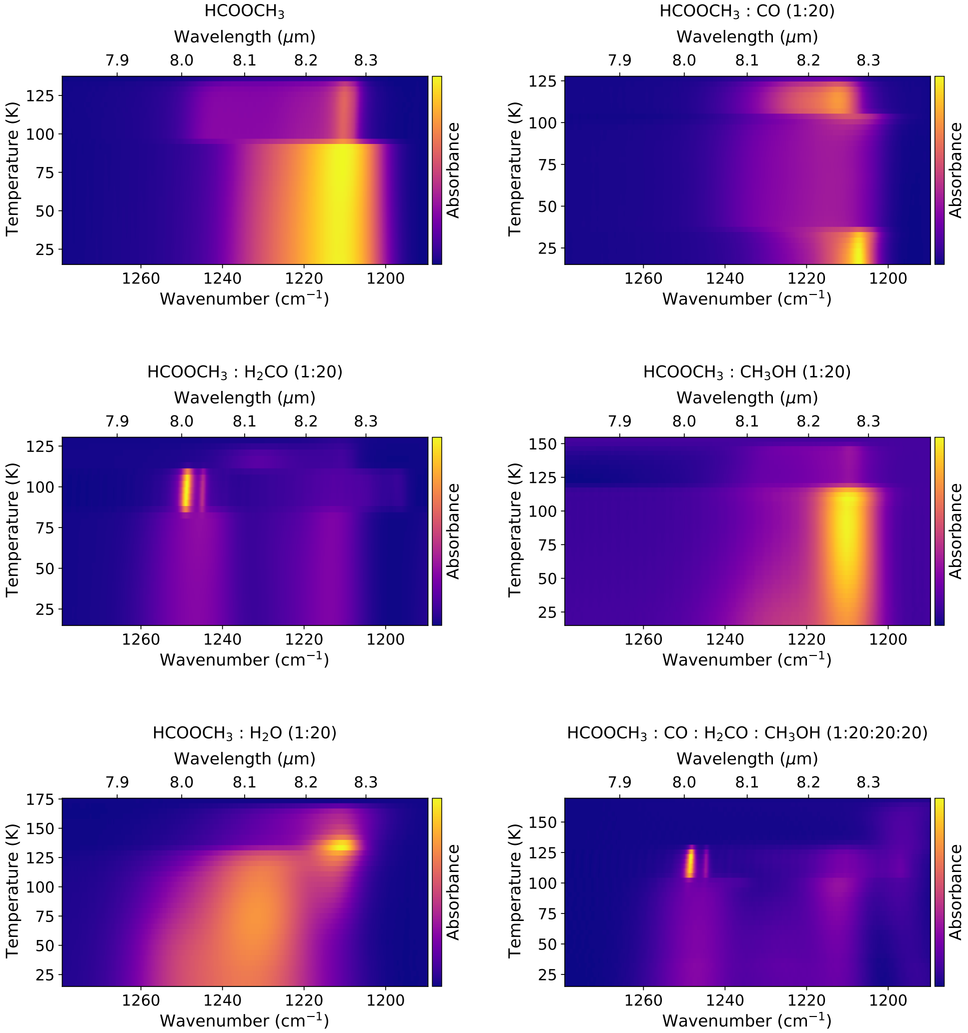

Figure 4.10: Temperature versus Spectra (TvS) heatmaps of the C–O stretching mode (1211.3 cm^{-1}/8.256 μm) of $HCOOCH_3$ in the astronomically relevant ice matrices as a function of the temperature.

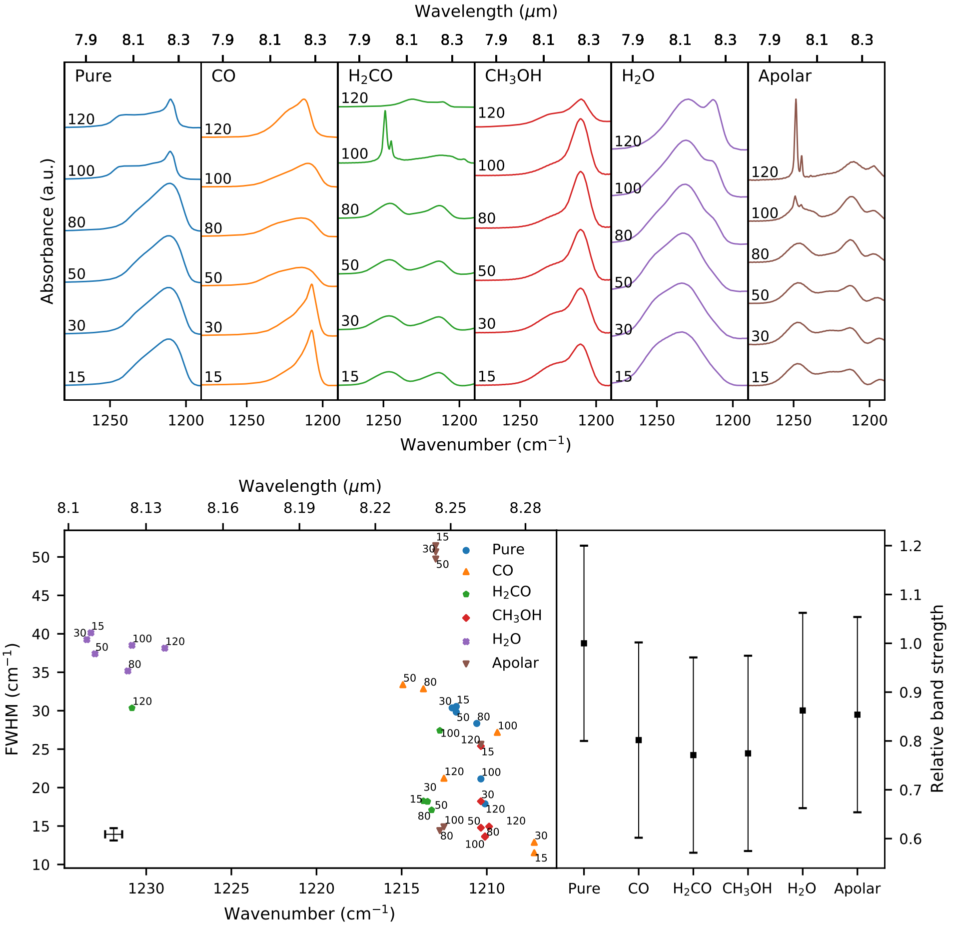

Figure 4.11: Top panel: absorption feature of the C–O stretching vibrational mode (1211.3 cm^{-1}/8.256 μm) for each of the mixtures at selected temperatures. Bottom left panel: FWHM as a function of the peak position at the selected temperatures. The error bar of each individual point is given in the bottom left. Bottom right panel: relative band strengths for methyl formate in the different ice matrices at 15 K with respect to the pure band strength.

Table 4.6: Peak position and FWHM of the methyl formate C−O stretching mode (1211.3 cm^{-1}/8.256 μm) in various matrices.

Mixture	Temperature	λ_{peak}		FWHM	
	(K)	(cm^{-1})	(μm)	(cm^{-1})	(μm)
$HCOOCH_3$	15	1211.8	8.2522	30.55	0.2063
$HCOOCH_3$: CO		1207.2	8.2835	11.53	0.0788
$HCOOCH_3$: H_2CO		1213.7	8.2391	18.26	0.1234
$HCOOCH_3$: CH_3OH		1210.3	8.2621	25.40	0.1718
$HCOOCH_3$: H_2O		1233.2	8.1087	40.13	0.2621
$HCOOCH_3$: Apolar		1213.0	8.2440	51.47*	0.3389*
$HCOOCH_3$	30	1212.0	8.2506	30.37	0.2051
$HCOOCH_3$: CO		1207.2	8.2835	12.88	0.0880
$HCOOCH_3$: H_2CO		1213.5	8.2408	18.20	0.1230
$HCOOCH_3$: CH_3OH		1210.3	8.2621	18.22	0.1239
$HCOOCH_3$: H_2O		1233.5	8.1071	39.24	0.2563
$HCOOCH_3$: Apolar		1213.0	8.2440	50.66*	0.3338*
$HCOOCH_3$	50	1211.8	8.2522	29.82	0.2015
$HCOOCH_3$: CO		1214.9	8.2309	33.38	0.2242
$HCOOCH_3$: H_2CO		1213.5	8.2408	18.17	0.1229
$HCOOCH_3$: CH_3OH		1210.3	8.2621	14.78	0.1008
$HCOOCH_3$: H_2O		1233.0	8.1102	37.40	0.2445
$HCOOCH_3$: Apolar		1213.0	8.2440	49.73*	0.3279*
$HCOOCH_3$	80	1210.6	8.2604	28.34	0.1917
$HCOOCH_3$: CO		1213.7	8.2391	32.85	0.2208
$HCOOCH_3$: H_2CO		1213.2	8.2424	17.08	0.1156
$HCOOCH_3$: CH_3OH		1210.1	8.2637	13.60	0.0928
$HCOOCH_3$: H_2O		1231.1	8.1230	35.17	0.2312
$HCOOCH_3$: Apolar		1212.8	8.2457	14.40	0.0978
$HCOOCH_3$	100	1210.4	8.2621	21.13	0.1426
$HCOOCH_3$: CO		1209.4	8.2687	27.18	0.1840
$HCOOCH_3$: H_2CO		1212.8	8.2457	27.42	0.1857
$HCOOCH_3$: CH_3OH		1210.1	8.2637	13.66	0.0932
$HCOOCH_3$: H_2O		1230.8	8.1246	38.50*	0.2548*
$HCOOCH_3$: Apolar		1212.5	8.2473	14.90	0.1013
$HCOOCH_3$	120	1210.1	8.2637	17.89	0.1211
$HCOOCH_3$: CO		1212.5	8.2473	21.22	0.1430
$HCOOCH_3$: H_2CO		1230.8	8.1246	30.35	0.2026
$HCOOCH_3$: CH_3OH		1209.9	8.2654	14.93	0.1017
$HCOOCH_3$: H_2O		1228.9	8.1373	38.13*	0.2537*
		1213.0	8.2440	–	–
$HCOOCH_3$: Apolar		1210.3	8.2621	25.64*	0.1760*

Notes. $^{(*)}$ FWHM result of two or more blended peaks.

4.E The C=O stretching mode

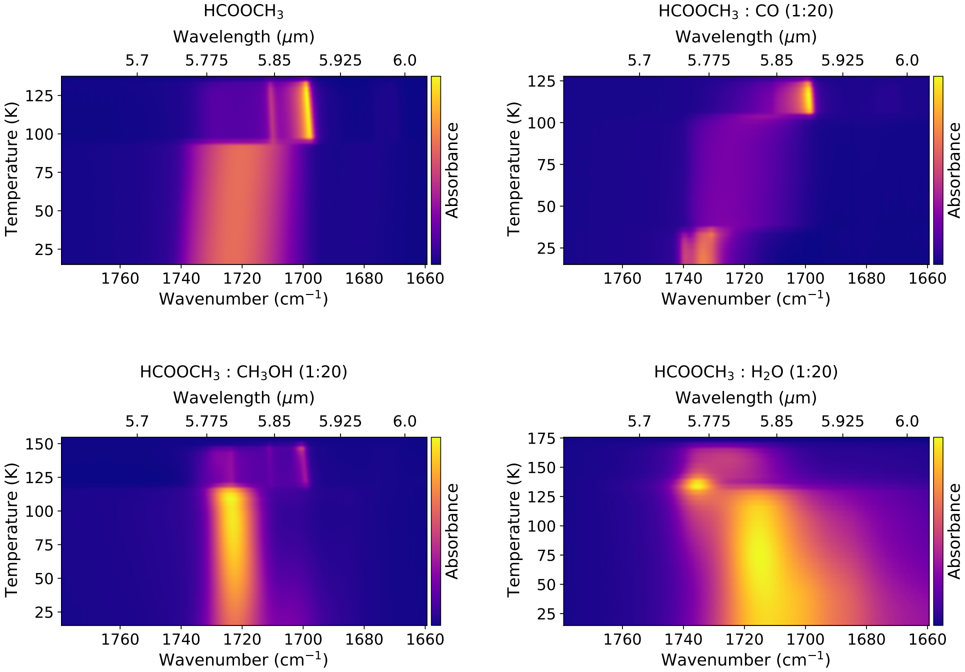

Figure 4.12: Temperature versus Spectra (TvS) heatmaps of the C=O stretching mode (1723.1 cm^{-1}/5.804 μm) of $HCOOCH_3$ in the astronomically relevant ice matrices as a function of the temperature.

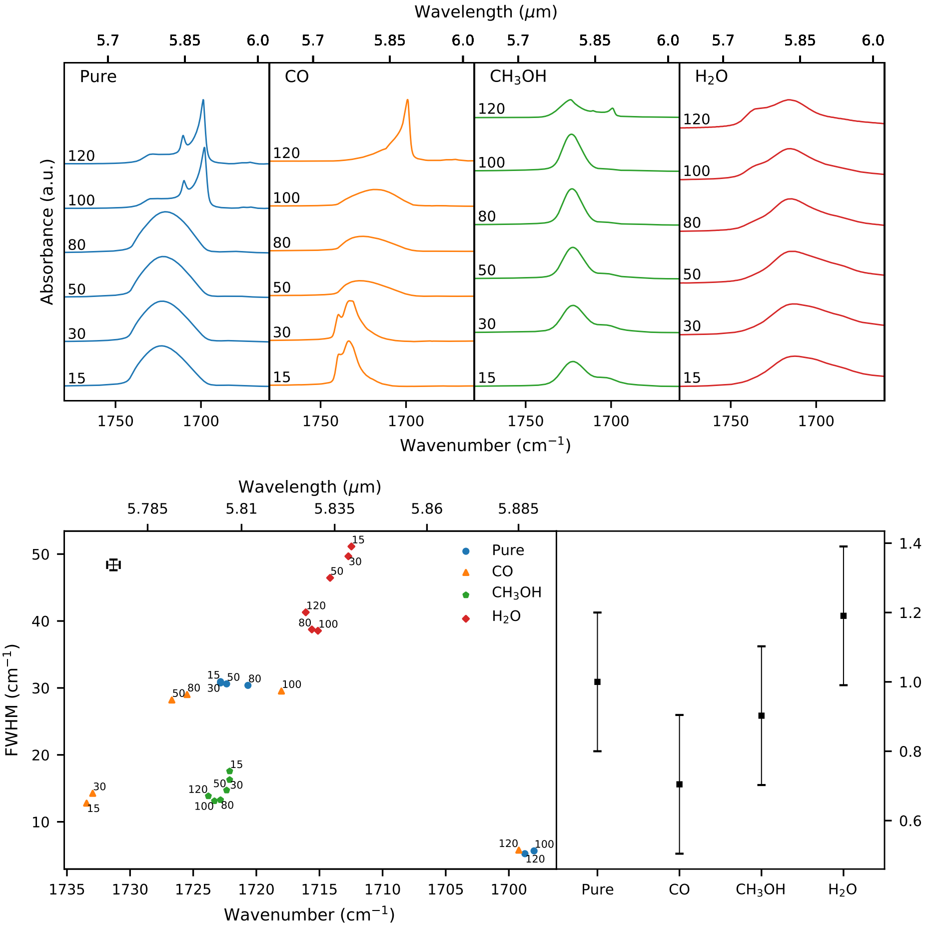

Figure 4.13: Top panel: absorption feature of the C=O stretching vibrational mode (1723.1 cm^{-1}/5.804 μm) for each of the mixtures at selected temperatures. Bottom left panel: FWHM as a function of the peak position at the selected temperatures. The error bar of each individual point is given in the top left. Bottom right panel: relative band strengths for methyl formate in the different ice matrices at 15 K with respect to the pure band strength.

Table 4.7: Peak position and FWHM of the methyl formate C=O stretching mode (1723.1 cm^{-1}/5.804 μm) in various matrices.

Mixture	Temperature	λ_{peak}		FWHM	
	(K)	(cm^{-1})	(μm)	(cm^{-1})	(μm)
$HCOOCH_3$	15	1722.8	5.8044	30.94	0.1043
$HCOOCH_3$: CO		1733.4	5.7689	12.80*	0.0425*
$HCOOCH_3$: CH_3OH		1722.1	5.8068	17.57	0.0593
$HCOOCH_3$: H_2O		1712.5	5.8395	51.14*	0.1762*
$HCOOCH_3$	30	1722.8	5.8044	30.75	0.1038
$HCOOCH_3$: CO		1733.0	5.7705	14.26*	0.0474*
		1739.5	5.7489	–	–
$HCOOCH_3$: CH_3OH		1722.1	5.8068	16.28	0.0549
$HCOOCH_3$: H_2O		1712.7	5.8387	49.67*	0.1711*
$HCOOCH_3$	50	1722.4	5.8060	30.61	0.1033
$HCOOCH_3$: CO		1726.7	5.7914	28.20	0.0950
$HCOOCH_3$: CH_3OH		1722.4	5.8060	14.72	0.0496
$HCOOCH_3$: H_2O		1714.2	5.8338	46.45*	0.1597*
$HCOOCH_3$	80	1720.7	5.8117	30.38	0.1027
$HCOOCH_3$: CO		1725.5	5.7955	29.02	0.0978
$HCOOCH_3$: CH_3OH		1722.8	5.8044	13.27	0.0447
$HCOOCH_3$: H_2O		1715.6	5.8289	38.74*	0.1325*
$HCOOCH_3$	100	1698.0	5.8893	5.659	0.0196
		1709.8	5.8486	–	–
$HCOOCH_3$: CO		1718.0	5.8207	29.54	0.1000
$HCOOCH_3$: CH_3OH		1723.3	5.8028	13.11	0.0442
$HCOOCH_3$: H_2O		1715.1	5.8305	38.54*	0.1312*
$HCOOCH_3$	120	1698.7	5.8868	5.239	0.0181
		1710.5	5.8461	–	–
$HCOOCH_3$: CO		1699.2	5.8851	5.769	0.0200
$HCOOCH_3$: CH_3OH		1723.8	5.8011	13.85	0.0466
		1699.2	5.8851	–	–
$HCOOCH_3$: H_2O		1716.1	5.8272	41.30*	0.1398*

Notes. (*) FWHM result of two or more blended peaks.

4.F Integrated absorbance ratios of the selected methyl formate transitions

Table 4.8: Integrated absorbance ratios of methyl formate for each of the selected transitions and temperatures, for both pure and mixed with astronomically relevant matrices, with respect to the C−O stretching mode (1211.3 cm^{-1}/8.256 μm).

Mixture	Temperature (K)	OCO deform. (13.02 μm)	O−CH_3 stretch. (10.98 μm)	CH_3 rock. (8.582 μm)	C−O stretch. (8.256 μm)	C=O stretch. (5.804 μm)
$HCOOCH_3$	15	0.038	0.150	0.602	1.000	1.659
$HCOOCH_3$: CO		0.032	0.141	0.567	1.000	1.458
$HCOOCH_3$: H_2CO		0.038	0.178	0.983	1.000	–**
$HCOOCH_3$: CH_3OH		0.030	0.123	0.693	1.000	1.934
$HCOOCH_3$: H_2O		0.023	0.075	0.226	1.000	2.291
$HCOOCH_3$: Apolar		0.046	–*	0.723	1.000	–**
$HCOOCH_3$	30	0.038	0.150	0.598	1.000	1.669
$HCOOCH_3$: CO		0.035	0.140	0.566	1.000	1.451
$HCOOCH_3$: H_2CO		0.038	0.180	0.983	1.000	–**
$HCOOCH_3$: CH_3OH		0.029	0.131	0.714	1.000	1.972
$HCOOCH_3$: H_2O		0.022	0.076	0.224	1.000	2.253
$HCOOCH_3$: Apolar		0.043	–*	0.727	1.000	–**
$HCOOCH_3$	50	0.038	0.151	0.592	1.000	1.683
$HCOOCH_3$: CO		0.029	0.142	0.467	1.000	1.396
$HCOOCH_3$: H_2CO		0.037	0.183	0.979	1.000	–**
$HCOOCH_3$: CH_3OH		0.027	0.143	0.759	1.000	2.055
$HCOOCH_3$: H_2O		0.023	0.069	0.221	1.000	2.181
$HCOOCH_3$: Apolar		0.039	–*	0.759	1.000	–**
$HCOOCH_3$	80	0.039	0.154	0.595	1.000	1.718
$HCOOCH_3$: CO		0.028	0.143	0.461	1.000	1.416

Continued on next page

Table 4.8 – continued from previous page

Mixture	Temperature (K)	OCO deform. (13.02 μm)	O$-$CH$_3$ stretch. (10.98 μm)	CH$_3$ rock. (8.582 μm)	C$-$O stretch. (8.256 μm)	C=O stretch. (5.804 μm)
$HCOOCH_3 : H_2CO$		0.037	0.189	0.965	1.000	$-$**
$HCOOCH_3 : CH_3OH$		0.029	0.153	0.796	1.000	2.145
$HCOOCH_3 : H_2O$		0.022	0.066	0.239	1.000	2.075
$HCOOCH_3$: Apolar		0.035	$-$*	0.769	1.000	$-$**
$HCOOCH_3$	100	0.088	0.362	0.436	1.000	1.967
$HCOOCH_3 : CO$		0.032	0.156	0.569	1.000	1.591
$HCOOCH_3 : H_2CO$		0.036	0.237	0.718	1.000	$-$**
$HCOOCH_3 : CH_3OH$		0.026	0.156	0.797	1.000	2.188
$HCOOCH_3 : H_2O$		0.021	0.062	0.268	1.000	2.035
$HCOOCH_3$: Apolar		0.034	$-$*	0.696	1.000	$-$**
$HCOOCH_3$	120	0.089	0.366	0.439	1.000	1.992
$HCOOCH_3 : CO$		0.026	0.122	0.389	1.000	1.625
$HCOOCH_3 : H_2CO$		0.015	0.218	0.378	1.000	$-$**
$HCOOCH_3 : CH_3OH$		0.111	0.496	1.597	1.000	4.295
$HCOOCH_3 : H_2O$		0.020	0.071	0.320	1.000	2.007
$HCOOCH_3$: Apolar		0.026	$-$*	0.578	1.000	$-$**

Notes. (*) Cannot be determined due to H_2CO and CH_3OH matrix interaction, see Section 4.3.1. (**) Due to the overlapping C=O stretching modes of H_2CO and $HCOOCH_3$, the relative intensity cannot be determined, see Section 4.3.5.

5

The TW Hya Rosetta Stone Project. II. Spatially resolved emission of formaldehyde hints at low-temperature gas-phase formation

Jeroen Terwisscha van Scheltinga, Michiel R. Hogerheijde, L. Ilsedore Cleeves,
Ryan A. Loomis, Catherine Walsh, Karin I. Öberg, Edwin A. Bergin,
Jennifer B. Bergner, Geoffrey A. Blake, Jenny K. Calahan, Paolo Cazzoletti,
Ewine F. van Dishoeck, Viviana V. Guzmán, Jane Huang, Mihkel Kama,
Chunhua Qi, Richard Teague, David J. Wilner, 2021, ApJ, 906, 111

Abstract

Formaldehyde (H_2CO) is an important precursor to organics like methanol (CH_3OH). It is important to understand the conditions that produce H_2CO and prebiotic molecules during star and planet formation. H_2CO possesses both gas-phase and solid-state formation pathways, involving either UV-produced radical precursors or CO ice and cold ($\lesssim 20$ K) dust grains. To understand which pathway dominates, gaseous H_2CO's ortho-to-para ratio (OPR) has been used as a probe, with a value of 3 indicating "warm" conditions and < 3 linked to cold formation in the solid state. This chapter presents spatially resolved Atacama Large Millimeter/submillimeter Array observations of multiple ortho- and para-H_2CO transitions in the TW Hya protoplanetary disk to test H_2CO formation theories during planet formation. We find disk-averaged rotational temperatures and column densities of 33 ± 2 K, $(1.1 \pm 0.1) \times 10^{12}$ cm^{-2} and 25 ± 2 K, $(4.4 \pm 0.3) \times 10^{11}$ cm^{-2} for ortho- and para-H_2CO, respectively, and an OPR of 2.49 ± 0.23. A radially resolved analysis shows that the observed H_2CO emits mostly at rotational temperatures of 30–40 K, corresponding to a layer with $z/R \geq 0.25$. The OPR is consistent with 3 within 60 au, the extent of the pebble disk, and decreases beyond 60 au to 2.0 ± 0.5. The latter corresponds to a spin temperature of 12 K, well below the rotational temperature. The combination of relatively uniform emitting conditions, a radial gradient in the OPR, and recent laboratory experiments and theory on OPR ratios after sublimation, lead us to speculate that *gas-phase* formation is responsible for the observed H_2CO across the TW Hya disk.

5.1 Introduction

The incorporation of complex organic molecules (COMs) into forming planets is essential to solving the puzzle of life's origins (e.g., Herbst & van Dishoeck 2009). The answer to how and where prebiotic molecules are formed is an important step in this investigation, and starts with the study of the chemical precursors of COMs. Even for one of the simplest COMs, methanol (CH_3OH), the origin of its precursor molecule formaldehyde (H_2CO) has yet to be fully constrained in protoplanetary disks (Loomis et al. 2015; Öberg et al. 2017). Specifically, H_2CO presents a challenge in that it can potentially form via reactions in the gas phase and via formation in the ice mantles of cold grains, followed by nonthermal desorption or sublimation (Qi et al. 2013; Loomis et al. 2015; Öberg et al. 2017). The relative occurrence of both paths is important, because they take place in different environments and thus contribute differently to the formation of methanol and other COMs. Furthermore, an unsolved question is whether the observed organic reservoir is close enough to the midplane where planets form.

Solid-state formation of H_2CO starts with the hydrogenation of CO; further hydrogenation, though with a small barrier of 400–500 K, leads to efficient formation of CH_3OH (Hiraoka et al. 1994, 2002; Watanabe & Kouchi 2002a; Hidaka et al. 2004; Watanabe et al. 2004; Fuchs et al. 2009). From CH_3OH, a complex and varied chemistry can be seeded by the subsequent formation of simple sugars and sugar alcohols like glycerol, an important building block for cell membranes (Chuang et al. 2017; Fedoseev et al. 2017). In contrast, gas-phase formation of H_2CO occurs most efficiently through the reaction between atomic oxygen and methyl radicals (CH_3; Fockenberg & Preses 2002; Atkinson et al. 2006) as well as CH_2 and hydroxyl radicals (OH). Therefore, the gas-phase formation pathway is particularly efficient where these radicals can be generated, primarily in the UV-irradiated surface where there is efficient photodesorption and photodissociation (Aikawa et al. 2002; Loomis et al. 2015).

The first protoplanetary disks in which H_2CO was detected are those around DM Tau and GG Tau (Dutrey et al. 1997). These detections were followed by the detection of H_2CO in LkCa 15 (Aikawa et al. 2003; Thi et al. 2004). Although groundbreaking, the detections were only in the best case marginally spatially resolved and comparison to models to disentangle the origin of H_2CO was not feasible.

Recent high-resolution observations with the Atacama Large Millimeter/Submillimeter Array (ALMA) of H_2CO transitions in 20 protoplanetary disks suggests that both gas-phase and solid-state formation of formaldehyde occurs, with their relative contributions varying across different disks (van der Marel et al. 2014; Loomis et al. 2015; Öberg et al. 2017; Carney et al. 2017; Kastner et al. 2018; Guzmán et al. 2018; Podio et al. 2019; Pegues et al. 2020; Garufi et al. 2020). Parametric model fits to resolved observations of H_2CO 3_{12}–2_{11} and 5_{15}–4_{14} in the disk of T Tauri star TW Hya find both warm and cold H_2CO components in compact and extended regions, respectively (Öberg et al. 2017). These studies have demonstrated that observations of multiple transitions allow for an improved determination of the rotational temperature and column density, which provides further constraints on the radial *and* vertical location of the emitting molecules and their origin. For example, in the disk of the Herbig Ae star HD 163296, Guzmán et al. (2018) derived for the first time a disk-averaged column density ratio of the ortho and para isomers of H_2CO in the range 1.8–2.8 with a rotational temperature of 24 K.

As first proposed by Kahane et al. (1984), the ortho-to-para ratio (OPR) of H_2CO could additionally shed light on the formation origins of this molecule. For example, H_2CO formed in warm gas would thermalize at the statistically expected OPR of 3.0, while cold formation, such as the CO-ice hydrogenation pathways, would equilibrate the OPR to a lower value consistent with the grain temperature. The expectation is that the OPR is conserved from the moment of formation, since radiative transitions between ortho- and para-H_2CO are strictly forbidden. However, recent experimental work by Hama et al. (2018) showed that for *water*, desorption *resets* the OPR to 3.0. If this is the case for H_2CO, other explanations for the observed low H_2CO OPR values are necessary and a cold-grain formation route cannot be inferred.

The disk around TW Hya is an ideal laboratory to study the chemical origin of formaldehyde in detail. TW Hya is the closest Sun-like star surrounded by a gas-rich protoplanetary disk, with a distance of 60.1 pc (Gaia Collaboration et al. 2018). Its disk has been studied extensively, in millimeter continuum and near-infrared scattered light, in various molecules including CO and isotopologues, and in a variety of chemical tracers (e.g., Andrews et al. 2012, 2016; Akiyama et al. 2015; Walsh et al. 2016; Öberg et al. 2017; Huang et al. 2018; Teague et al. 2018). Spatially resolved observations of two H_2CO lines, 3_{12}–2_{11} ($0\farcs45 \times 0\farcs45$) and 5_{15}–4_{14} ($0\farcs47 \times 0\farcs41$), in the TW Hya disk by Öberg et al. (2017) suggested that gas-phase formation dominates in the inner regions of the disk (< 10 au) while grain-surface formation contributes beyond 15 au.

In the current paper, we use a comprehensive multiline data set, including a wider range of upper-state energies, 21–141 K, and now in both ortho- and para-spin isomers, taken with ALMA toward the TW Hya disk. These data allow us to *directly* infer the radial and vertical structure of H_2CO, without having to rely on parametric models like those used by Öberg et al. (2017). We aim to elucidate the formation of this key simple organic. Our data were obtained as part of an ALMA study ("TW Hya as a Chemical Rosetta Stone", PI L.I. Cleeves) aimed at a deep understanding of this object's chemistry, and by extension, of that of other gas-rich protoplanetary disks. In this paper, observations of H_2CO from this ALMA project, together with archival ALMA data, are presented and used to explore the rotational temperature, column density, and OPR of H_2CO in TW Hya. Section 5.2 describes the observational details and data reduction, Section 5.3 describes the resulting radial emission and excitation profiles, and Section 5.4 discusses the implications for the chemical origin of H_2CO across the TW Hya disk. Section 5.5 summarizes the main findings.

5.2 Observations and reduction

The data presented here were obtained as part of the ALMA project "TW Hya as a chemical Rosetta stone" (2016.1.00311.S, PI Cleeves); additional, archival H_2CO data were taken from ALMA projects 2013.1.00114.S and 2016.1.00464.S. The observational details (number of antennas, baseline ranges, on-source time, and calibrators) are summarized in Table 5.1. All data sets were processed through the standard ALMA calibration pipeline, after which self-calibration was applied. Data from 2013.1.00114.S is phase and amplitude self-calibrated on the continuum in the H_2CO spectral window using CASA 4.5 with timescales of 10–30 s. This improved the signal-to-noise ratio of the emission by a factor of ≈ 3. Phase self-calibration is applied to the data from 2016.1.00311.S using line-free portions of the continuum. The solution interval is set to 30 s and polarization is averaged. Furthermore, the spectral windows are

Table 5.1: ALMA Observations.

ALMA Project Code	Date	Antennas	Baselines (m)	On-source (minutes)	Calibrators Bandpass	Calibrators Phase	Calibrators Flux
2013.1.00114.S[a]	2014 Jul 19[1]	32	34-650	42.0	J1037–2934	J1037–2934	Pallas
2016.1.00311.S[b]	2016 Dec 16[2]	45	15-449	23.9	J1037–2934	J1037–2934	J1037–2934
	2017 Feb 01[3]	41	14-256	28.3	J1058+0133	J1037–2934	J1107–4449
	2017 Apr 08[4]	40	15-379	28.8	J1037–2934	J1037–2934	J1058+0133
	2017 May 05[2]	45	16-1120	39.3	J1037–2934	J1037–2934	J1107–4449
	2017 May 07[2]	51	16-1079	39.3	J1037–2934	J1037–2934	J1107–4449
	2017 May 21[4]	45	15-1097	47.8	J1037–2934	J1037–2934	J1037–2934
	2018 Jan 23[3]	43	14-1386	47.1	J1058+0133	J1037–2934	J1037–2934
	2018 Sep 20[3]	44	14-1385	47.1	J1037–2934	J1037–2934	J0904–5735
2016.1.00464.S[c]	2016 Dec 03[5−7]	40	14-662	48.3	J1058+0133	J1037–2934	J1037–2934
	2016 Dec 05[5−7]	46	15-648	48.3	J1058+0133	J1037–2934	J1058+0133
	2016 Dec 07[5−7]	45	14-609	48.3	J1058+0133	J1037–2934	J1037–2934
	2016 Dec 07[5−7]	45	15-648	48.3	J1058+0133	J1037–2934	J1058+0133
	2016 Dec 07[5−7]	39	15-596	48.3	J1058+0133	J1037–2934	J1037–2934
	2016 Dec 10[5−7]	46	15-648	48.3	J1058+0133	J1037–2934	J1058+0133
	2016 Dec 11[5−7]	46	15-636	48.3	J1058+0133	J1037–2934	J1037–2934

Notes. For (a), (b), and (c) the principal investigators are K. I. Öberg, L. I. Cleeves, and C. Walsh, respectively. (1)-(7) Link the transitions from Table 5.2 to the observation in which they are observed.

separately calibrated with a minimum signal-to-noise of 3 and minimum of six baselines per antenna. Data from 2016.1.00464.S is phase and amplitude self-calibrated with CASA 4.7.2 with two rounds of phase calibration, one over 30 second intervals and one over the integration time, and a single round of amplitude calibration. The signal-to-noise ratio in a CLEANed continuum image improved by a factor of ≈ 20. The final calibration tables are applied to the line-containing spectral windows.

Subsequent data processing was performed with CASA 5.6.1 (McMullin et al. 2007). The continuum is subtracted using the UVCONTSUB task. Image reconstruction was performed with the TCLEAN algorithm using the multiscale deconvolver (Högbom 1974; Cornwell 2008) to reduce side lobes and increase the signal-to-noise ratio. Scales of $0''$, $0\farcs5$, $1\farcs0$, $2\farcs5$ and $5\farcs0$ were used for the multiscale deconvolver. No masking is applied as no significant difference was observed between the images with and without masking. Furthermore, masking creates a bias as scales used by the multiscale deconvoler larger then the masks are ignored by CLEAN. For the imaging of H_2CO 3_{03}–2_{02} Briggs weighting with a robust parameter of 0.5 was used, resulting in a synthesized beam of $0\farcs49 \times 0\farcs33$ and a good balance between the angular resolution and recovery of flux on all scales. All other H_2CO transitions were imaged with a robust parameter of 2.0, resulting in angular resolutions that closely match that of the 3_{03}–2_{02} line and optimizing the sensitivity. The 3_{12}–2_{11} transition is observed in only one execution block with a Maximum Recoverable Scale (MRS) of $2\farcs3$, less than the size of the disk line emission in several channels. Therefore, for this specific transition some “smooth” flux on larger scales may be missing with the exact amount depending on the details of the imaging reconstruction (for example, simple CLEAN versus multiscale CLEAN as applied by us). Given that the emission is not “flat” and is primarily peaked toward the star, missing flux is not expected to be a large contributor to the overall flux.

All images were CLEANed to three times the noise found by the IMSTAT task in line-free channels. The spectral resolution (channel width) of all cubes was set to 0.25 km s^{-1}, close to the native resolution of the lowest resolution data (0.22 km s^{-1} for the 5_{15}–4_{14} transition). For several of the observed transition our data combine observations from different ALMA configurations and require corrections to obtain correct flux densities and noise levels. This stems from disparities between the flux scale in jansky per synthesized beam of the (CLEAN-recovered) emission and jansky per dirty beam for the noise residuals (R.A. Loomis et al., in prep.). A final flux calibration uncertainty of 10% is included in the further analysis as suggested by the ALMA Technical Handbook.

The CLEANed data cubes are masked according to the expected Keplerian rotation of TW Hya. Pixels are masked on a per channel basis where no emission is expected to occur when the emitting gas in the protoplanetary disk around TW Hya follows Keplerian rotation, (e.g., Salinas et al. 2017). The mask is created with the disk parameters: PA 152°, inclination 5°, and stellar mass 0.88 $M_\odot$ from Huang et al. (2018) with a systematic velocity of 2.83 km s^{-1} ($V_{\rm LSR}$) and outer radius of 220 au, which corresponds to the edge of the gas disk as measured by CO (Huang et al. 2018). Due to the nature of Keplerian masked moment-zero maps there is a nonuniform rms across the map, as described by Bergner et al. (2018), Pegues et al. (2020). We follow these authors and bootstrap the uncertainty of the moment-zero maps and integrated flux densities by evaluating the rms of a large number of extractions across a similar number of randomly chosen line-free channels.

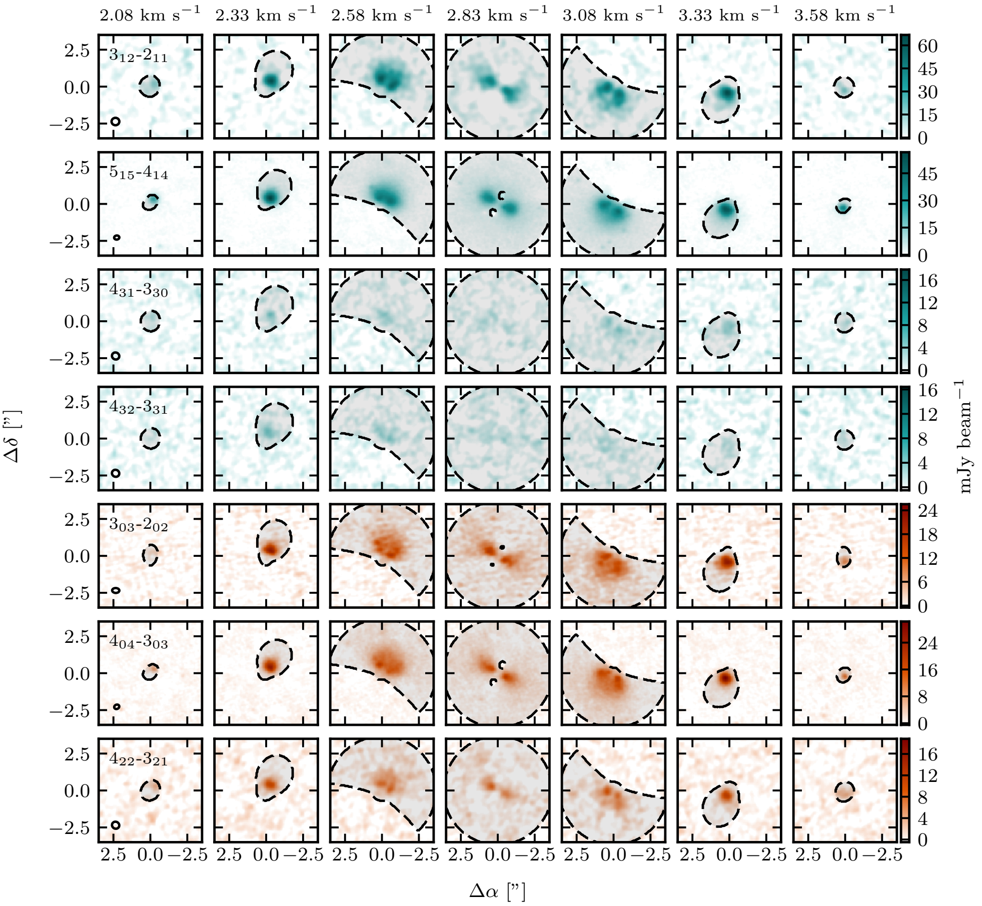

Figure 5.1: Channel maps from the observed transitions at native spatial resolution with the Keplerian masked overlayed. The channel velocities are labelled on top in the $V_{\rm LSR}$ reference frame. The teal and bronze color correspond to the ortho- and para-spin isomers, respectively. Beam sizes are indicated by the ellipse in the left-bottom corner of the first column.

5.3 Results

5.3.1 Observational results

Emission in all seven targeted H_2CO transitions is clearly detected. Figure 5.1 shows the channel maps of the emission. Table 5.2 lists integrated flux densities of each transition extracted using Keplerian masking on the emission cubes. Values range from 1118 ± 7 mJy km s^{-1} for the o-H_2CO 5_{15}–4_{14} line to 22 ± 4 mJy km s^{-1} for the o-H_2CO 4_{32}–3_{31} line. Figure 5.2 shows the spectra integrated over the disk after Kepler masking.

Table 5.2: Observed Formaldehyde Transitions.

Transition	$\mathrm{Log}_{10}[A_{ij}]$ (s^{-1})	E_u (K)	Robust[a]	Beam ($'' \times ''$, $^\circ$)	Channel rms[b] (mJy beam^{-1})	Mom-0 rms[c] (mJy beam^{-1} km s^{-1})	Int. Flux Density[d] (mJy km s^{-1})
3_{03}–2_{02}(p)^2	−3.55037	20.96	0.5	0.49×0.33, −87.8	1.46	0.49	283 ± 4
3_{12}–2_{11}(o)^1	−3.55724	33.45	2.0	0.53×0.50, 88.7	2.65	0.98	402 ± 7
4_{04}–3_{03}(p)^3	−3.16102	34.90	2.0	0.35×0.29, 64.7	1.62	0.41	519 ± 5
4_{22}–3_{21}(p)^5	−3.27994	82.12	2.0	0.51×0.47, −60.3	0.93	0.36	62 ± 3
4_{31}–3_{30}(o)^6	−3.51653	140.9	2.0	0.51×0.47, −62.2	0.93	0.35	24 ± 4
4_{32}–3_{31}(o)^7	−3.51684	140.9	2.0	0.51×0.47, −62.2	0.93	0.36	22 ± 4
5_{15}–4_{14}(o)^4	−2.92013	62.45	2.0	0.35×0.28, 83.5	2.67	0.60	1118 ± 7

Notes. The rest frequency, Einstein *A* coefficient, and upper state energy are taken from the LAMDA database. (1)-(7) Link the observations from Table 5.1 to the transitions.

[a] The robust parameter used for Briggs weighting in the CLEAN process.

[b] The channel rms is given at a common spectral resolution of 0.25 km s^{-1}.

[c] The moment-zero rms is determined through the bootstrapping described in Section 5.2.

[d] The integrated flux density is retrieved through summation of the emission retrieved by Keplerian masking of the emission cube.

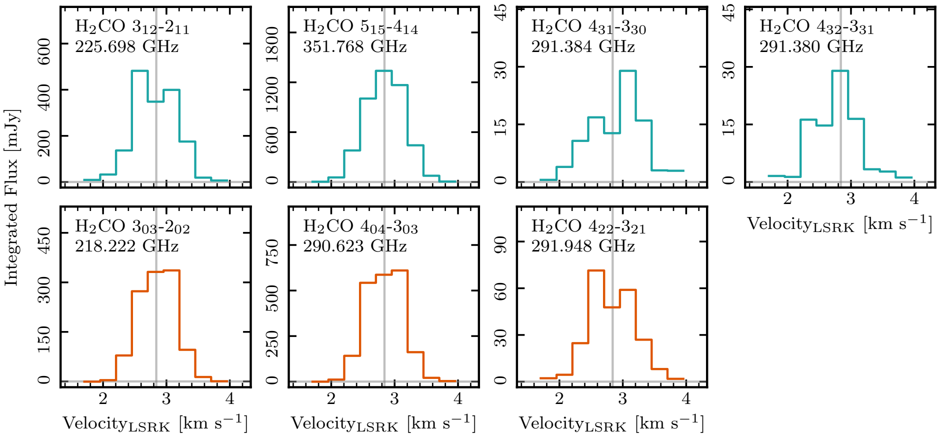

Figure 5.2: Integrated spectra of the seven observed Keplerian masked H_2CO transitions, i.e., pixels are masked according to a model predicting the Keplerian rotation of TW Hya. Top row, from left to right: o-H_2CO 3_{12}–2_{11}, 5_{15}–4_{14}, 4_{31}–3_{30}, and 4_{32}–3_{31}. Bottom row, from left to right: p-H_2CO 3_{03}–2_{02}, 4_{04}–3_{03}, and 4_{22}–3_{21}. The vertical line indicates the systematic velocity of TW Hya.

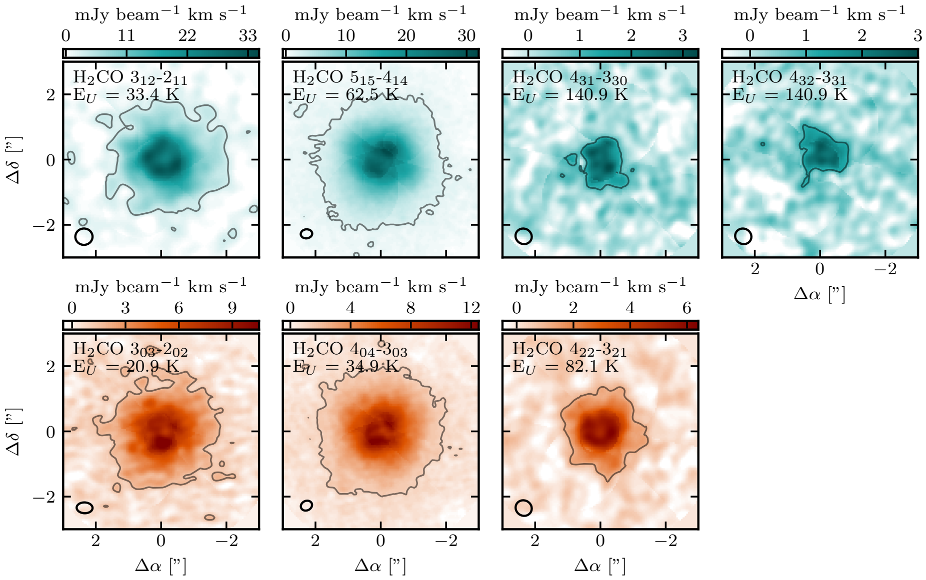

Figure 5.3: Keplerian masked velocity integrated emission of observed H_2CO transitions at native spatial resolution ($V_{\rm LSR}$ = 1.83–3.83 km s^{-1}). Top row: ortho-spin isomer transitions; bottom row: para-spin isomer transitions. The contour in each panel depicts 3σ, where σ for each transition is taken from Table 5.2. Beam sizes are indicated by the ellipse in the left-bottom corner of each panel.

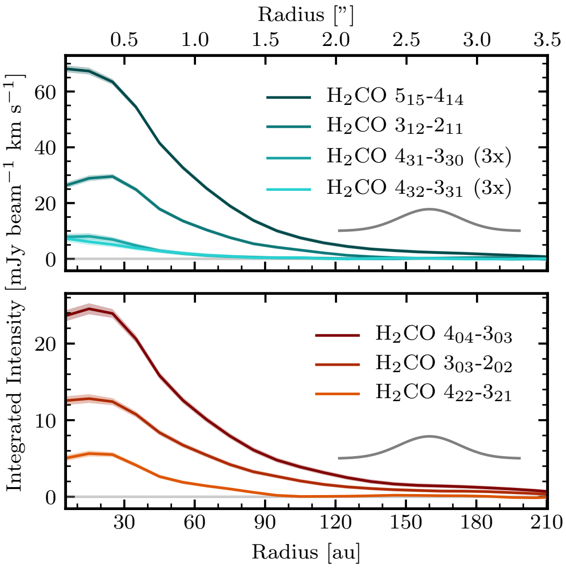

Figure 5.4: Radial intensity profiles of the observed ortho (top panel) and para (bottom panel) H_2CO transitions retrieved from the Keplerian masked moment-zero maps. The displayed uncertainties do not contain the 10% flux calibration error. All data have a common spatial resolution of 30 au depicted by the Gaussian in the bottom right.

The channel maps clearly show that the emission follows the velocity pattern of a disk in Keplerian rotation. Using the expected region of emission in each velocity channel integrated intensity (zero moment) maps are obtained and shown in Figure 5.3. These images show that the H_2CO emission is concentrated in a ring with a radius of $0\farcs3$ (18 au), with a broad fainter brim of emission as was also seen by Öberg et al. (2017). From these Keplerian masked integrated intensity images, radial emission profiles are extracted by annular averaging in 10 au wide bins (Figure 5.4). Uncertainty levels of the radially averaged intensities are calculated by dividing the moment-zero rms with the square-root of the number of independent beams present in that bin. To bring all data on the same angular resolution of $0\farcs5$, the H_2CO 3_{03}–2_{02}, 4_{04}–3_{03}, and 5_{15}–4_{14} were re-imaged using CLEAN and respective UVTAPER of $[0\farcs0, 0\farcs35, -87.8°]$, $[0\farcs23, 0\farcs33, 64.7°]$, and $[0\farcs18, 0\farcs30, 83.5°]$ before the radial intensity profiles of these transitions were extracted. It should be noted that the 4_{31}–3_{30} and 4_{32}–3_{31} transitions have very similar excitation parameters and are thus difficult to distinguish in Figure 5.4.

5.3.2 H_2CO excitation temperature and column density

5.3.2.1 Rotational diagram analysis

The wide range of upper-state energies of 21–141 K of the detected H_2CO lines allow for well-constrained estimates of the excitation temperatures and column densities of the ortho and para isomers through a rotation diagram analysis (e.g., Goldsmith & Langer 1999). Since the gas densities in the disk (as estimated from the models of Cleeves et al. 2015; Kama et al. 2016) typically exceed the critical density of the targeted transitions, $n_{\mathrm{H_2}} \sim 10^6$–$10^7$ cm^{-3}, the molecule's excitation is likely in local thermal equilibrium (LTE), even in the outer region of the disk. Derived excitation temperatures therefore are a reliable estimate of the kinetic temperature of the emitting gas, provided that the emission is optically thin. In the treatment outlined below, specific allowance is made for moderately optically thick emission.

The line intensity, I_ν, follows from the column density of the upper-state level in the optically thin limit, N^{thin}, as

$$I_\nu = \frac{A_{ul} N_u^{\text{thin}} hc}{4\pi \Delta v}, \tag{5.1}$$

where A_{ul} is the Einstein A coefficient and Δv the velocity width of the emission line. Rewriting equation 5.1 and substituting the source brightness I_ν as flux per solid angle, S_ν/Ω, gives

$$N_u^{\text{thin}} = \frac{4\pi S_\nu \Delta v}{A_{ul} \Omega hc}. \tag{5.2}$$

Here, S_ν is the flux density extracted from the integrated spectra or the radial flux profiles, and Ω is the total solid angle from which the emission is extracted. If the emission is not fully optically thin, the column density of the upper-state level, N_u, follows from the optically thin limit by applying a correction for line optical depth,

$$N_u = N_u^{\text{thin}} \frac{\tau}{1 - e^{-\tau}} \tag{5.3}$$

where τ is the optical depth at the center of the line. This line opacity τ is given by

$$\tau = \frac{A_{ul} N_u^{\text{thin}} c^3}{8\pi \nu^3 \Delta v} (e^{h\nu/kT_{\text{rot}}} - 1) \tag{5.4}$$

where ν is the rest-frequency of the transition. An upper limit to the opacity follows from assuming a line width Δv equal to the disk-averaged FWHM of the intrinsic line, estimated to be 0.275 km s^{-1}. This value is estimated from the FWHM of the Keplerian corrected integrated spectra acquired with GoFish (Teague 2019). Finally, the total column density, N_{tot}, is related to the upper-state level populations through the Boltzmann equation,

$$\frac{N_u}{g_u} = \frac{N_{\text{tot}}}{Q(T_{\text{rot}})} e^{-E_u/kT_{\text{rot}}}, \tag{5.5}$$

where g_u is the degeneracy of the corresponding upper-state level, Q the partition function of H_2CO, E_u the upper-state level energy, and T_{rot} the rotational temperature of H_2CO. The upper-state degeneracy, upper-state energy, Einstein A coefficient, and frequency of each transition are extracted from the Leiden Atomic and Molecular Database (LAMDA; Schöier et al. 2005). The partition function for H_2CO is constructed from the rotational ground states taken from the ExoMol database (Al-Refaie et al. 2015; Wang et al. 2020). In order to independently investigate the nuclear-spin isomers a separate partition function is created for each of the isomers. The ExoMol database assumes an OPR of three. This OPR is incorporated in their state degeneracies and is removed by dividing by three to match the state degeneracies of the LAMDA database. The partition function is constructed by summing over the possible internal H_2CO ground states,

$$Q(T_{\text{rot}}) = \sum_i g_i e^{-E_i/kT} \tag{5.6}$$

where g_i is the degeneracy and E_i the energy of state i. These separate partition functions allow independent determination of the column densities of each spin isomer. As is customary for rotation diagram analyses, the column density N_{tot} and rotation

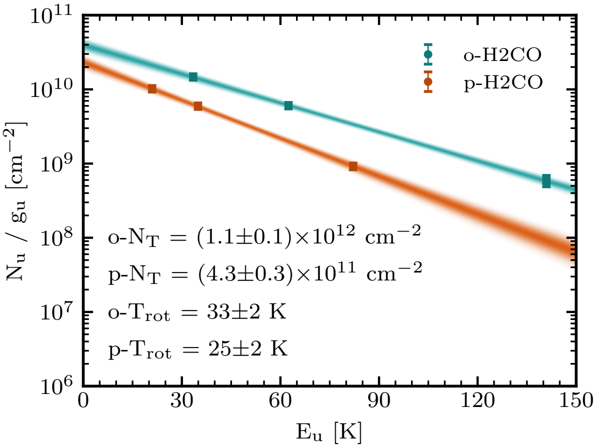

Figure 5.5: Rotational diagram of disk-averaged H_2CO flux density values from Table 5.2. The teal and bronze color represent the level populations of the ortho- and para-spin isomers, respectively. The markers show the data and the lines show random draws from the posterior distribution retrieved by the EMCEE fitting procedure.

temperature $T_{\rm rot}$ are retrieved from the intercept and slope, respectively, of $\ln(N_u/g_u)$ vs E_u (Figure 5.5). Following Loomis et al. (2018) and Teague et al. (2018), we create a likelihood function from Equation 5.5 and use EMCEE (Foreman-Mackey et al. 2013) to retrieve posterior distributions for $T_{\rm rot}$ and $N_{\rm tot}$ from the observed H_2CO transitions. This rotational diagram fitting procedure is applied to each of the spin isomers separately.

5.3.2.2 Disk-averaged rotational diagram

The disk integrated flux densities of Table 5.2, analysing each spin isomer separately, yields disk averaged column densities and rotational temperatures of $(1.1 \pm 0.1) \times 10^{12}$ cm^{-2}, 33 ± 2 K and $(4.3 \pm 0.3) \times 10^{11}$ cm^{-2}, 25 ± 2 K for ortho- and para-H_2CO, respectively. These values result in a disk-averaged OPR of 2.49 ± 0.23. Uncertainties are the 16th and 84th percentiles of the posterior distributions, corresponding to 1σ. The disk-averaged line opacities range from 0.002–0.049, confirming the assumption of optically thin emission. However, one should note that this assumes a uniform distribution of H_2CO across the entire disk which is not the case, as seen in Figure 5.4. The opacities will be larger in the inner region where column densities are higher, as shown in Section 5.3.2.3.

Carney et al. (2019) investigated the disk-averaged ratio of CH_3OH with respect to H_2CO for the protoplanetary disks around HD 163296 and TW Hya. Specifically for TW Hya they found a CH_3OH/H_2CO ratio of 1.27 ± 0.13. In their work the average H_2CO and CH_3OH column densities are derived self-consistently from the integrated line intensity of one transition and an assumed excitation temperature, (see Equation (1) of Carney et al. 2019). The H_2CO column density is found to be 3.7×10^{12} cm^{-2}, which is approximately 2.4 times higher than the derived average total H_2CO column density of $(1.5 \pm 0.1) \times 10^{12}$ cm^{-2} in this work. The lower total H_2CO column density derived through rotational diagram analysis pushes the CH_3OH/H_2CO ratio up to a value of 3.1 ± 0.4. However, it should be noted that the CH_3OH column density used in this work is taken from Carney et al. (2019) and is thus not derived self consistent with the H_2CO column density.

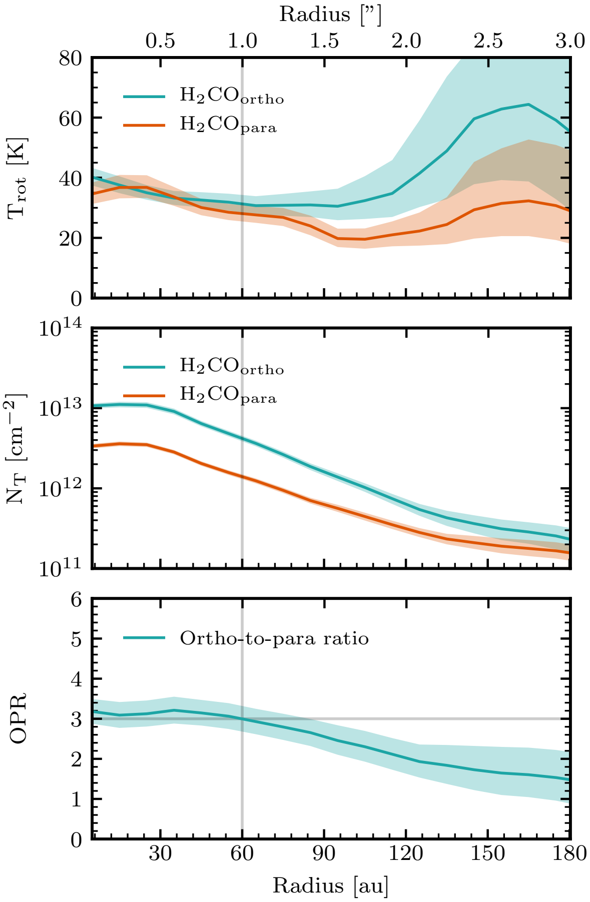

Figure 5.6: Radially resolved H_2CO temperature (top panel), column densities (middle panel), and OPR (bottom panel) of H_2CO obtained from our rotational diagram analysis using the radial emission profiles of Figure 5.4. Teal and bronze colors represent the ortho- and para-spin isomers, respectively. Shaded areas depict 1σ uncertainties. The gray vertical and horizontal line depict the millimeter-dust continuum edge and the high temperature OPR limit of 3.0, respectively.

The rotational temperatures of both spin isomers are not identical, with a slightly higher value of 33 K found for ortho-H_2CO compared to 26 K for para-H_2CO. If the OPR is in thermal equilibrium, such a difference is expected: the ortho isomer is the more abundant in warmer gas compared to the para isomer, resulting in a higher rotational temperature for the former when averaging its emission over the disk. However, there may also be a systematic bias, because the detected o-H_2CO lines extend over a larger range of upper-level energies (up to 141 K) compared to the p-H_2CO lines (up to 82 K), thus naturally probing higher excitation gas. Section 5.3.2.3 explores further explanations, folding in spatially resolved information.

5.3.2.3 Radially resolved rotational diagram

The same rotational diagram analysis as carried out above for the disk-integrated fluxes, can also be performed as function of radius, using the Keplerian masked moment-zero images, all restored to a common resolution of $0''.5$, and the corresponding radial intensity profiles of Figure 5.4. As depicted in Figure 5.6, the column densities in the $0''.5$ beam peak at $\sim$ 20 au with values of $(1.1 \pm 0.1) \times 10^{13}$ cm^{-2} and $(3.6 \pm 0.3) \times 10^{12}$ cm^{-2} for o-H_2CO and p-H_2CO, respectively. The opacities are largest in the inner region where column densities are highest. The largest optical

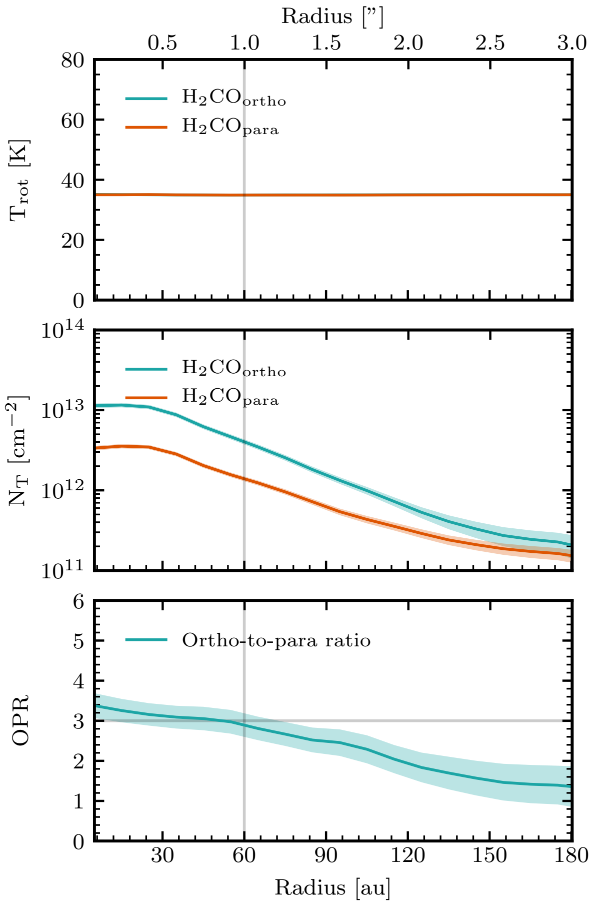

Figure 5.7: Radially resolved H_2CO temperature (top panel), column densities (middle panel), and OPR (bottom panel) of H_2CO obtained from our rotational diagram analysis with a fixed rotational temperature at 35 K. Teal and bronze colors represent the ortho- and para-spin isomers, respectively. Shaded areas depict 1σ uncertainties. The gray vertical and horizontal line depict the millimeter-dust continuum edge and the high temperature OPR limit of 3.0, respectively.

depths are found to be $\tau = 0.47$ and $\tau = 0.35$ for the 5_{15}–4_{14} and 3_{12}–2_{11} transition, respectively. Beyond 85 au all the opacities drop to a value of $\tau < 0.1$. Therefore, all transitions only require a moderate correction for opacity.

The rotational temperatures of both the ortho- and para-H_2CO are found to be consistent with each other within 80 au. The averaged rotational temperatures drops as function of radius from 37 ± 5 K at the center of the first radial bin (5 au), to 29 ± 5 K at 75 au. These observed rotational temperature are below the freeze-out temperature of gas-phase H_2CO at approximately 80 K (Noble et al. 2012; Pegues et al. 2020). Beyond 80 au the rotational temperatures deviate from each other with a two sigma tension. This explains the observed difference in rotational temperatures from the disk-averaged analysis. At radii beyond 120 au no meaningful constraints on the temperature are found due to the low signal-to-noise ratio in the majority of the transitions.

The observed temperature difference between the ortho- and para-spin isomer from the disk-averaged analysis can be traced back to two transitions: 3_{12}–2_{11} and 4_{22}–3_{21}. The 3_{12}–2_{11} transition is observed with an MRS of $2''\!.3$. This transition has an upper-state energy of 33 K, the lowest of the ortho-spin isomers in this data set. With potentially missing extended emission on scales of $2''\!.3$ and larger, the fit may result in higher rotational temperatures on these scales. The 4_{22}–3_{21} transition has an upper-state energy of 82 K, which is the highest of the para-spin isomers in this data set. Combined with the drop in emission of the radial profile from 90–140 au, this may result in lower rotational temperatures in this region. Additional observations with a more robust coverage of the extended emission are needed to determine the H_2CO emitting temperature more robustly.

Dividing the column density profiles of o-H_2CO and p-H_2CO yields the radially resolved OPR, which is consistent with an OPR of 3.0, the high temperature limit, in the inner 60 au and drops to lower values at larger radii, that is, 2.0 ± 0.5 at a distance of 120 au. We rule out that the temperature bias described in the previous paragraph has an impact on the derived OPR. Repeating the analysis at fixed rotational temperatures ranging from 30–40 K, and omitting the 3_{12}–2_{11} transition that may miss extended emission, we recover the same downward OPR trend. The fixed rotational temperature model of 35 K is shown in Figure 5.7. We therefore conclude that the radial decrease in the OPR beyond the millimeter-dust continuum is robust.

5.4 Discussion

5.4.1 The inner H_2CO line emission decrease

Our resolved, multiline observations of H_2CO in TW Hya broadly indicate a flattening or decrease in flux interior to 20 au. An inner deficit in the intensity profile has been seen in other disks and other molecular lines, and can be attributed either to real decreases in column density or to line or continuum opacity (Andrews et al. 2012; Cleeves et al. 2016; Isella et al. 2016; Loomis et al. 2017). Continuum oversubtraction due to optically thick lines can be ruled out in this case, given the consistently low optical line depths (< 0.5, see Section 5.3.2). Continuum opacity is also likely not the only explanation, because emission of other molecules at similar wavelengths are centrally peaked (e.g., $C^{18}O$ $J = 3 - 2$ imaged by Schwarz et al. 2016). However, it should be noted that Huang et al. (2018) found the millimeter wavelength spectral index inside $<$ 20 au to be 2.0, indicative of optically thick continuum emission. Depending on the height where the line emission originates, *some* of the drop in emission may be due to an optically thick continuum. Nonetheless, our data show evidence of H_2CO inside of 20 au, the approximate CO snow line location in this disk (Schwarz et al. 2016; van 't Hoff et al. 2017; Zhang et al. 2017), indicative of active gas-phase H_2CO chemistry as was also found in Öberg et al. (2017).

5.4.2 Gas-phase versus grain-surface formation of H_2CO

In interstellar environments, H_2CO forms by a combination of CO-ice hydrogenation and neutral–neutral gas-phase reactions, specifically CH_3 + O and CH_2 + OH (e.g., Loomis et al. 2015). For CO ice to exist in abundance, the dust grain temperature must be quite low, below 25 K depending on the binding surface. This temperature is much lower than the thermal desorption temperature of H_2CO, therefore H_2CO formed by this mechanism requires subsequent nonthermal desorption to produce observable gas-phase quantities. Previous work by Loomis et al. (2015) and Öberg et al. (2017) found that a combination of gas-phase and solid-state chemistry likely contributes to the observed gaseous H_2CO in disks. In TW Hya specifically, Öberg et al. (2017)

suggested that the H_2CO ring near the CO snow line could be evidence of a CO-ice regulated chemistry (see also Qi et al. 2013). In addition, a number of sources, for example, HD 163296, CI Tau, DM Tau, and AS 209 (see Pegues et al. 2020), show an increase or ring in H_2CO in the outer disk. A clear example of a secondary increase is found in HD 163296 at a radius of $\sim$ 250 au (Carney et al. 2017). These authors suggest that an additional formation route related to CO ice may be opening up at this location, or that increased penetration of ultraviolet radiation boosts gas-phase formation of H_2CO.

Previous work by Öberg et al. (2017) showed a similar emission bump in the 3_{12}–2_{11} transition near the millimeter-dust continuum edge at 60 au. Our imaging of the same data at similar spatial resolution does not show this emission bump. We attribute the difference to the MRS of $2\farcs3$ of this data set in combination with the different applied CLEAN method (multiscale CLEAN), since this method is expected to yield a more reliable result for extended emission.

The near-constant rotational temperature of 30–40 K found here for H_2CO suggests that the emission arises from an elevated layer in TW Hya's disk, well above the CO snow surface. In models of the TW Hya disk (Bergin et al. 2013; Cleeves et al. 2015; Kama et al. 2016; Calahan et al. 2021), these temperatures are found at normalized heights of $z/R \geq 0.25$. Additionally, recent observations of the edge-on younger embedded disk IRAS 04302 also show that the bulk of the H_2CO emission arises from $z/R \sim 0.21$–0.28 (Podio et al. 2020; van't Hoff et al. 2020). At these heights, sufficient UV can penetrate to induce photodesorption of H_2CO since the bulk of the small dust has grown and is very settled (e.g., Dullemond & Dominik 2004; Testi et al. 2014). These same UV photons also induce efficient gas-phase formation of H_2CO by radical production, since the two radical-radical gas-phase reactions that form H_2CO are barrierless. Teague & Loomis (2020) found CN at similar heights in TW Hya, a molecule which is formed mainly through UV irradiation (Cazzoletti et al. 2018). Our data therefore suggest that gas-phase formation is likely important to explain the observed gas-phase H_2CO across the entire disk of TW Hya.

Interestingly, Loomis et al. (2015) found that gas-phase chemistry alone underproduced the observed column density of H_2CO in the DM Tau protoplanetary disk. However, it is important to note that the modeling carried out in Loomis et al. (2015) either fully turned off CO hydrogenation or left on the full CO-hydrogenation pathway up to forming CH_3OH. While detailed chemical modeling is beyond the scope of the present paper, we examined the reaction rates from the existing Cleeves et al. (2015) TW Hya chemical model with a dust surface area reduction of 85%. The latter is invoked to emulate the effects of dust settling and radial drift, which significantly reduce the effective solid surface for ice chemistry to occur (Hogerheijde et al. 2011; Bergin & Cleeves 2018). In the layer where H_2CO is abundant ($z/R > 0.25$), the two gas-phase pathways with O and OH are far more efficient than CO-ice hydrogenation due to the warm temperatures of the surface layers. From these initial tests it also appears that, although H_2CO formed in the gas phase is easily photodissociated, subsequent freeze-out of the resulting HCO radicals reforms H_2CO, as the hydrogenation step involved is barrierless (Fuchs et al. 2009). Further modeling is needed to confirm this symbiotic gas-grain relationship in H_2CO formation. The key role of UV-induced gas-phase chemistry has been seen in other models. Walsh et al. (2014) find that H_2CO can be efficiently formed through gas-phase chemistry alone around a typical T Tauri star. They found a fractional abundance with respect to n_{H} of 10^{-10}–10^{-9}, which translates in their models to column densities between 10^{12} and 10^{13} cm^{-2}, very similar to the values obtained from our observations. It should be noted that although gas-phase chemistry is sufficient to explain observed *gas-phase* column densities it does not imply that *solid-state* formation does not occur in the disk midplane. The chemical models generally produce five orders of magnitude more solid-state H_2CO in the disk midplane.

5.4.3 Constraints from the H_2CO OPR on the formation

The smooth radial H_2CO column density profile and near-constant excitation temperature are consistent with a single origin of the observed H_2CO, namely gas-phase formation. Is this consistent with the radial gradient in OPR that is also observed? As first proposed by Kahane et al. (1984), the OPR of H_2CO – if distributed according to a Boltzmann distribution – drops below 3.0 for spin temperatures below $\sim$ 35 K and reaches 2.0 for a spin temperature of $\sim$ 12 K (see Figure 10 of Kahane et al. 1984). The spin temperature is thought to correspond to the formation temperature of the molecule since the gas-phase nuclear-spin conversion time for nonreactive collisions is longer than the H_2CO lifetime (Tudorie et al. 2006). Within 60 au, the inferred *rotational* temperatures of 30–40 K are consistent with the *spin* temperatures of $\gtrsim$ 27 K found from the OPR. Outside 60 au, and especially outside 120 au, the OPR suggest a spin temperature of 10–17 K while the (poorly constrained) rotational temperature exceeds 20 K (1σ).

A low OPR and corresponding low formation temperature have been invoked as evidence of the formation of H_2CO in the ice, during the prestellar phase or in cold regions of the disk, and subsequent release in the gas. This is based on the expectation that the OPR is conserved from the moment of formation, because radiative transitions between ortho- and para-H_2CO are strictly forbidden. However, recent experimental work by Hama et al. (2018) shows that nonthermal desorption of para-enriched water ice at 11 K causes the OPR to revert to 3.0, as expected for higher temperatures. For water, this is explained by the fact that water molecules in the ice cannot rotate because of hydrogen bonds in the ice matrix. This restriction results in a quasi-degeneracy of the ortho- and para-H_2O states in the solid state. Furthermore, theoretical studies on solid-state H_2O propose that rapid nuclear-spin conversion in the solid-state is possible through intermolecular proton–proton magnetic dipolar interactions (Limbach et al. 2006; Buntkowsky et al. 2008). Similar to H_2O, H_2CO will also be rotationally hindered in the solid state, and an OPR of 3.0 may be expected on release into the gas phase, even when formed at low temperatures. However, the extent of rotational hindrance of H_2CO in an apolar CO matrix has to be investigated theoretically or experimentally before a conclusive statement can be made.

If we accept that the OPR reflects the temperature of the H_2CO formation in the ice, our observed values indicate that only outside 60 au does the observed H_2CO emission contain a contribution originating in the ice. Although not very well constrained, the rotational temperature at these radii exceeds the freeze-out temperature of CO, < 21 K (Schwarz et al. 2016), suggesting that some vertical transport of H_2CO formed in the midplane through hydrogenation is required. Given the low turbulence in the TW Hya disk (Flaherty et al. 2018), it is not immediately clear what mechanism can efficiently explain this vertical transport. Alternatively, solid-state H_2CO can be inherited from the prestellar stage (e.g., Visser et al. 2011). This inherited H_2CO ice could then non-thermally desorb in an elevated layer in the protoplanetary disk stage before it settles to the disk midplane. If, however, the observed H_2CO has an inherited origin and we assume the OPR is preserved we would expect a constant value. The observed OPR ranging from 3.0–2.0 in this single monotonic component would thus require an external influence, that is, different desorption conditions or subsequent disk gas-phase chemistry. This inherently implies that the OPR of the inherited ice is not wholly preserved. It is possible that due to beam smearing multiple components are hidden in what now seems to be a single component. However, the OPR drops across three beam sizes making this scenario unlikely.

If, on the other hand, we accept that the OPR is reset to 3.0 on desorption as suggested by the experiments discussed above, the lower OPR values found outside 60 au mean that ice formation cannot play a significant role here. Instead, gas formation is required. To explain the low OPR requires either low-temperature formation or a *chemical* explanation. The former can be explained by deeper penetration of UV radiation at large radii, producing the required radicals closer to the midplane and at lower temperatures. The latter requires detailed modeling including the spin state chemistry, and the role of H_2 spin. The extent to which the *rotational* temperature in the outer disk deviates from the *spin* temperature corresponding to the observed OPR cannot be assessed with the current data. Future ALMA observations with higher signal-to-noise ratio and additional transitions with lower upper-state energies are needed for this.

Additionally, in this scenario the observed OPR of 3.0 inside 60 au is both consistent with gas-phase formation and nonthermal desorption from the solid state. However, H_2CO formed in the solid state from CO hydrogenation during the protoplanetary disk stage requires vertical transport, which is unlikely in TW Hya due to the lack of turbulence, as described above. This raises the question, what does create the H_2CO ring emission at ~ 20 au if it is not linked to the CO snowline? The observations of the edge-on younger embedded disk IRAS 04302 also find that H_2CO decreases in the inner region (Podio et al. 2020; van't Hoff et al. 2020). In this younger and warmer disk CO does not freeze-out due to higher midplane temperatures (van 't Hoff et al. 2018a). Furthermore, $C^{17}O$ emission in the IRAS 04302 disk does not decrease in the inner region, ruling out dust opacity (van't Hoff et al. 2020). The authors thus argue that the decrease of H_2CO in the inner region is due to lower abundances of parent radicals in the gas-phase instead of an optically thick continuum. This mechanism could still be at play in an older protoplanetary disk like TW Hya and will be investigated in a follow-up paper with chemical modeling.

5.5 Summary

We report the most comprehensive survey of spatially and spectrally resolved ortho- and para-H_2CO emission in a protoplanetary disk to date, TW Hya. We detect H_2CO emission across the entire disk out to 180 au, with a partially filled emission ring at 20 au and a smooth decrease beyond this radius. A rotational diagram analysis shows that the emission originates from a layer with a nearly constant temperature between 30 and 40 K, which corresponds to $z/R \geq 0.25$. We find column densities of a few times 10^{13} cm^{-2} in the inner disk decreasing to $\sim 10^{12}$ cm^{-2} in the outer disk, and an OPR consistent with 3 in the inner 60 au decreasing to a value of ~ 2 at 120 au. Unlike some other disks, for example, HD 163296, CI Tau, DM Tau, and AS 209, no secondary increase in the H_2CO emission or column density is seen in the outer disk. The results and discussion presented in this work have led us to speculate that the low OPR of H_2CO in the disk of TW Hya does not reflect direct ice formation, as is commonly assumed, but instead hints at predominantly gas-phase formation. Several lines of evidence lead to this speculation: (1) the smooth emission profiles that suggests a single formation path across the disk, (2) the radially decreasing OPR, (3) the lack of vertical mixing to return H_2CO ice from the disk midplane, and (4) the recent results on the reset of the OPR to 3 upon desorption of H_2O. Instead, a cold *gas-phase* origin of the gaseous H_2CO molecules responsible for the emission appears a more likely scenario for TW Hya. In other disks (e.g., DM Tau, Loomis et al. 2015), ice formation may play a larger role, and even in TW Hya the *bulk* of the H_2CO likely resides (unobserved) in ice near the midplane. Gas-phase formation is supported by the presence of abundant H_2CO in the same region where there is a deficit of solid mass, specifically outside of the millimeter pebble disk. This is the same region where the OPR begins to drop. This scenario will be tested in a follow-up study with forward models that include chemistry, spin states, and radiative transfer to better understand the observed OPR and its implications for organic formation in disks during planet formation.

6 FORMATION OF CO_2 THROUGH CONSUMPTION OF GAS-PHASE CO ON VACUUM-UV IRRADIATED WATER ICE

Jeroen Terwisscha van Scheltinga, N.F.W. Ligterink, A.D. Bosman,
Michiel R. Hogerheijde, Harold Linnartz, Submitted to Astronomy & Astrophysics

Abstract

Recent observations of protoplanetary disks suggest that they are depleted in gas-phase CO up to a factor of 100 with respect to predictions from physical-chemical (or thermo-chemical) models. It has been posed that gas-phase CO is chemically consumed and converted into less volatile species through gas-grain processes. Observations of interstellar ices reveal a CO_2 component in a polar (H_2O) ice matrix, suggesting potential co-formation or co-evolution.

The aim of the work in this chapter is to experimentally verify the interaction of gas-phase CO with solid-state OH radicals on the surface of water ice above the sublimation temperature of CO.

For this amorphous solid water (ASW) is deposited in an UHV setup and irradiated with vacuum-UV (VUV) photons (140–170 nm, produced with a microwave discharge hydrogen lamp) to dissociate H_2O and create OH radicals. Gas-phase CO is simultaneously admitted and only adsorbs with a short residence time on the ASW. Formed products are studied both in the infrared through Fourier transform infrared spectroscopy and quadrupole mass spectrometry.

The experiments presented in this chapter show that gas-phase CO is converted into CO_2 when interacting with ASW that is VUV irradiated in the temperature range of 40–120 K. Between 40 and 90 K, CO_2 production is constant, above 90 K, CO_2 production is reduced in favor of O_2 production. In the temperature range of 40–60 K, the CO_2 remains in the solid state, while at temperatures ≥ 70 K the majority of the formed CO_2 is released into the gas phase.

At the end of this chapter we conclude that gas-phase CO reacts with OH radicals, created on the surface of ASW with VUV irradiation, above its canonical sublimation temperature. The diffusion during the short, but nonzero, residence times of CO on the surface of ASW suggests that a Langmuir-Hinshelwood type reaction is involved. Formation of CO_2 is seen up to 120 K, with a constant production at 40–90 K, gradually yielding to O_2 production at higher temperatures. This mechanism could explain (part of) the observed presence of CO_2 embedded in water-rich ices when it occurs during the build up of the H_2O ice mantle. It may also contribute to the observed lack of gas-phase CO in planet-forming disks, as previously suggested. It should be noted though that our experiments indicate a lower efficiency than originally adopted in model descriptions of planet-forming disks.

6.1 Introduction

In typical laboratory astrochemistry experiments the processes that occur in the solid state and gas phase are investigated independently. However, there are conditions in the interstellar medium where these are intimately intertwined and could potentially affect each other. In this work, we explore experimentally the interaction between gas-phase carbon monoxide (CO) and UV irradiated water ice (H_2O) and place the results in astrophysical context.

In the study of planet forming disks, CO and its isotopes are common tracers of the total gas mass, but are often found to be depleted by factors up to 10–100, even after taking into account freeze-out of CO in the coldest disk regions (Ansdell et al. 2016; Miotello et al. 2017; Trapman et al. 2021). Recent chemical models by Bosman et al. (2018) suggest that gas-phase CO could be converted into CO_2 after interaction with a UV-irradiated H_2O ice surface, at temperatures just above the CO sublimation temperature. Under realistic disk conditions, this pathway was found by Bosman et al. (2018) to convert significant amounts of CO into CO_2. However, little experimental work exists to confirm this mechanism. If efficient, the UV-irradiated edges of molecular clouds could be another environment where this gas-grain reaction can occur. This could possibly explain (part of) the observed presence of CO_2 in polar ices (Pontoppidan et al. 2008), if gas-phase CO conversion happens on the surface during the build up of the H_2O ice mantle and adding to contributions from other pathways already studied.

The solid-state formation of CO_2 has been investigated both theoretically (see e.g., Goumans et al. 2008; Goumans & Andersson 2010; Arasa et al. 2013) and experimentally resulting in several energetic and non-energetic pathways:

1. Ground-state CO reacts with an electronically excited CO* to form CO_2 and atomic carbon (Gerakines et al. 1996; Palumbo et al. 1998; Loeffler et al. 2005; Jamieson et al. 2006; Bennett et al. 2009; Ioppolo et al. 2009),
2. CO reacts with atomic oxygen to form CO_2 (Roser et al. 2001; Madzunkov et al. 2006; Raut & Baragiola 2011; Ioppolo et al. 2013; Minissale et al. 2013),
3. CO reacts with a hydroxyl (OH) radical to form CO_2 and atomic hydrogen (Watanabe & Kouchi 2002b; Watanabe et al. 2007; Ioppolo et al. 2009; Oba et al. 2010, 2011; Ioppolo et al. 2011; Noble et al. 2011; Zins et al. 2011; Yuan et al. 2014),
4. Formaldehyde (H_2CO) reacts with atomic oxygen and forms CO_2 and molecular hydrogen (Minissale et al. 2015).

All of the above pathways efficiently produce CO_2 in the solid state and only the last pathway does not include CO. The majority of these solid-state experiments are performed at temperatures below 20 K, representative of dark cloud or disk midplane (> 20 AU) conditions. This is well below the CO sublimation temperature, which is approximately 20 and 30 K for interstellar and laboratory timescales, respectively. The low temperatures in these experiments ensure that CO stays adsorbed on the surface and is able to react with the other ice constituents. The experimental studies by Oba et al. (2011) and Yuan et al. (2014) have investigated the formation of CO_2 from CO at substrate temperatures above the sublimation temperature of CO. In the former, CO_2 was formed when CO and OH radicals were co-deposited on a substrate in the temperature range from 40 to 60 K. The latter observed formation of CO_2 when gas-phase CO interacted with OH radicals produced by UV photons on the surface of water ice at 76 K. Both works show that CO can interact with OH radicals in the solid state above its canonical desorption temperature.

In this work, we set out to experimentally investigate the conversion of gas-phase CO into CO_2 on the surface of vacuum-UV (VUV) irradiated water ice (40–120 K), and asses the efficiency in astrophysical settings. Specifically, amorphous solid water (ASW) is irradiated at a temperature of the ASW, $\geq$ 40 K, which ensures that the majority of the gas-phase CO in our experimental chamber does not freeze-out onto our ASW sample. Section 6.2 describes the methods used to investigate this process, and analyze the data. Results are written down in Section 6.3 and are discussed in Section 6.4. The astrophysical implications are given in Section 6.5, and concluding remarks are written down in Section 6.6.

6.2 Methods

6.2.1 CryoPAD2

All reported laboratory measurements are performed in the Leiden Laboratory for Astrophysics using CryoPAD2 (Chapter 2, Ligterink et al. 2017, 2018b). This setup operates under ultra-high vacuum conditions ($P_{\mathrm{mc}} \sim 5 \times 10^{-11}$ mbar at 15 K). It accommodates a gold-coated substrate which is positioned in the center of a stainless steel chamber and acts as an analogue for an interstellar dust grain surface. On top of the chamber a closed-cycle helium cryostat is positioned which cools the gold-coated surface down to temperatures of 15 K. A Lakeshore 350 temperature controller sets the temperature of the surface through PID-controlled Joule heating in the range of 15 to 300 K with an absolute and relative accuracy of 2 and 1 K, respectively. In order to further simulate the interstellar environments in which these dust grains reside, a microwave-discharge hydrogen-flow lamp (MDHL) is connected to the chamber. These type of sources generally produce VUV photons at 121.6 nm, Lyman-α, and between 140 to 170 nm, which corresponds to photon energies of 7.5 to 10.2 eV. However, in the present experiments a MgF_2 window is used which absorbs Lyman-α photons, see Appendix 6.A for the UV spectrum. The flux of the MDHL at the location of the substrate is determined with a NIST-calibrated photodiode (SXUV-100) as $(2.5 \pm 0.3) \times 10^{14}$ photons s^{-1} cm^{-2}.

The reactions induced by VUV irradiation under these conditions are diagnosed using InfraRed (IR) spectroscopy and mass spectrometry. The collimated beam of a Fourier-Transform InfraRed Spectrometer (Agilent 660 FTIRS), is used for Reflection Absorption InfraRed Spectroscopy (RAIRS). In this method the incoming FTIR beam is reflected from the substrate under a grazing incidence angle, improving the sensitivity. This *in situ* diagnostic allows us to probe, qualitatively and quantitatively, the molecular content in the ice adsorbed on the substrate. The infrared spectra are acquired continuously during the experiments to investigate and track the chemical evolution in the solid state under the influence of VUV irradiation.

The second diagnostic tool is a Hiden HAL/3F PIC 1000 series quadrupole mass spectrometer (QMS). During VUV irradiation some molecular species desorb from the substrate into the gas phase. The QMS probes the molecular content of the

Table 6.1: Overview of the performed experiments.

Series	Molecules	Temp[a] (K)	H_2O col. den.[b] (monolayers)	Notes
Main experiments	$H_2{}^{18}O$ (s) + $^{13}C^{18}O$ (g)	40 (15)	57.8	–
	$H_2{}^{18}O$ (s) + $^{13}C^{18}O$ (g)	50 (15)	56.7	–
	$H_2{}^{18}O$ (s) + $^{13}C^{18}O$ (g)	60 (15)	57.6	–
	$H_2{}^{18}O$ (s) + $^{13}C^{18}O$ (g)	70 (15)	61.8	–
	$H_2{}^{18}O$ (s) + $^{13}C^{18}O$ (g)	80 (15)	62.9	–
	$H_2{}^{18}O$ (s) + $^{13}C^{18}O$ (g)	90 (15)	57.8	–
	$H_2{}^{18}O$ (s) + $^{13}C^{18}O$ (g)	100 (15)	56.8	–
	$H_2{}^{18}O$ (s) + $^{13}C^{18}O$ (g)	120 (15)	58.3	–
Control experiments	$H_2{}^{18}O$ (s)	40 (15)	70.2	Water only.
	$H_2{}^{18}O$ (s) + ^{13}CO (g)	60 (15)	63.2	$^{13}C^{16}O$.
	$H_2{}^{18}O$ (s) + $^{13}C^{18}O$ (g)	40 (15)	66.4	No VUV.

Notes. (a) The first temperature is the temperature at which the ASW is VUV irradiated and the second temperature in parenthesis is the deposition temperature. (b) The H_2O column density is derived through the integrated area of the OH-stretching mode (boundaries, 3800–2950 cm^{-1}) through Eq. 6.1, where A' is taken to be 1.5×10^{-16} cm $molec^{-1}$ ($H_2{}^{16}O$, Bouilloud et al. 2015).

atmosphere in the chamber. This allows for qualitative assignment of species released and/or produced during the experiments through their characteristic mass fragmentation patterns. Furthermore, after calibration of the QMS through the procedure described in Section 6.2.3.2, it is possible to derive the quantitative amount of a species released into the gas phase. After VUV irradiation, the substrate temperature is linearly increased with time in a temperature programmed desorption (TPD) experiment until all adsorbed species have thermally desorbed. During TPD, species are released into the gas phase at their canonical desorption temperature, and are subsequently measured by the QMS. Upon ionization, in our case with 70 eV electrons, molecules fragment into a characteristic fragmentation pattern, which allows for assignment of newly formed species, complementary to the IR. Isotopically enriched precursors are used to discriminate from background gas contributions and to add additional diagnostic information to the RAIRS and TPD experiments.

6.2.2 Experimental protocol

The following molecules are used in the experiments: Milli-Q H_2O (Type I), $H_2{}^{18}O$ (Sigma-Aldrich, 97%), regular CO (Linde gas, 99.997%), and $^{13}C^{18}O$ (Sigma-Aldrich, 99% ^{13}C and 95% ^{18}O). The experiment is started by depositing a layer of ASW onto the substrate. The gas-phase H_2O enters the chamber roughly 1 cm away from the substrate, and is deposited under normal incidence to the substrate. The temperature of the substrate during H_2O deposition is set at 15 K. This ensures that the deposited H_2O is porous-ASW. A precision leak valve is used to guarantee consistent column densities of H_2O throughout the measurements. Before the experiments continue, the chamber is left to settle for at least 30 minutes. This ensures that the pressure in the main chamber (P_{mc}) is below 2.0×10^{-10} mbar and that the amount of residual gas-phase H_2O can be neglected. After this, the substrate temperature is slowly increased to a specific temperature at which the experiments are performed, typically with a rate of 2 K min^{-1}. Once the desired sample temperature is reached, the MDHL is started and gas-phase CO is released into the chamber. The gas-phase CO enters the chamber at roughly 5 cm distance from the substrate, and under 45 degrees with respect to the substrate normal. The precision leak valve is set to have a constant P_{mc} of 5.0×10^{-8} mbar. This translates into the ASW surface being exposed to approximately 5×10^{13} CO molecules cm^{-2} s^{-1}. The ASW is exposed in total 300 minutes to VUV irradiation (with a total incident fluence of 4.5×10^{18} photons) and CO molecules, after which TPD is performed to sublimate parent and newly-formed species. During VUV irradiation the shutter between the MDHL and vacuum chamber is closed to measure the baseline signals of the chamber without VUV irradiation. A list of experiments performed in this study is given in Table 6.1, which also provides information on the variable experimental parameters.

6.2.3 Data analysis

6.2.3.1 RAIRS vibrational spectroscopy

The infrared spectra are acquired in RAIRS mode with the FTIR and are subsequently analysed. The column density, N_{species}, of the probed molecules on the substrate is derived through the following relationship with the measured absorbance

$$N_{\mathrm{species}} = \ln(10) \cdot \frac{\int_{band} \log_{10}\left(\frac{I_0(\tilde{\nu})}{I(\tilde{\nu})}\right) d\tilde{\nu}}{R \cdot A'}, \tag{6.1}$$

where the absorbance, the ratio of the incoming flux, $I_0(\tilde{\nu})$, and reflected flux, $I(\tilde{\nu})$, is integrated over a range that encompasses the full absorption feature, and A' is the apparent band strength. The apparent band strengths are taken from literature from transmission experiments; for RAIRS these values need to be corrected with a value R in order to retrieve accurate column densities. The RAIRS correction factor is determined through isothermal desorption of CO and results in a setup-specific value (see e.g., Öberg et al. 2009c). We assume that the area probed by the infrared beam on our substrate amounts to 1.0 cm^2 and thus the amount of molecules, N_{species}, is also the column density, given in molecules cm^{-2}. As stated before and shown in Table 6.1, all main experiments are performed with $^{13}C^{18}O$ and $H_2{}^{18}O$ resulting in the formation of $^{13}C^{18}O_2$. To our knowledge the apparent band strength of this specific isotope of CO_2 is unknown and thus the apparent band strength of $^{13}CO_2$, 6.8×10^{-17} cm $molecule^{-1}$ (Bouilloud et al. 2015), is used to approximate the column density of $^{13}C^{18}O_2$.

As will be shown in Section 6.3, multiple CO_2 features are observed in the IR. In order to follow the growth of these different CO_2 features, the three prominent ones are approximated by fitting a Gaussian profile to each of them in order to deconvolve the spectra. The CURVE_FIT function from SCIPY is used to fit a Gaussian profile to each absorption component through least squares regression (Virtanen et al. 2020). A 3-Gaussian fit reproduces the integrated absorbance to $\leq 10\%$, and suffices as a fit, given the variation in observed profile shapes due to (small) changes in physical/chemical environment and spectroscopic artifacts in the spectra.

6.2.3.2 QMS calibration

RAIRS allows determination of the column density in the solid state, while the QMS allows tracing of molecules released from the solid state into the gas phase. In order to use the QMS for quantitative purposes mass signals need to be calibrated and this is realized, through the photodesorption of CO (see e.g., Fayolle et al. 2013; Martín-Doménech et al. 2015). The loss of CO in the solid state, which is traced with RAIRS, is correlated to the CO signal measured by the QMS. This calibration allows for the conversion of any CO QMS signal, released under VUV irradiation, to a CO column density released from the solid state. For other molecules, one needs to take into account the partial electron-impact ionization cross section, and the mass sensitivity of the molecule in question with respect to CO. The following relation is used to quantify the amount of CO_2 formed and released into the gas phase

$$N_{\mathrm{CO_2}} = S_{\mathrm{CO_2}} \cdot \frac{\sigma_{\mathrm{CO}}}{\sigma_{\mathrm{CO_2}}} \cdot \frac{F(\mathrm{CO^+/CO})}{F(\mathrm{CO_2^+/CO_2})} \cdot \frac{M(\mathrm{CO})}{M(\mathrm{CO_2})} \cdot \frac{N_{\mathrm{CO(ice)}}}{S_{\mathrm{CO(gas)}}\ t}, \tag{6.2}$$

where $N_{\mathrm{CO_2}}$ is the column density of CO_2 released from the solid state, σ the total electron-impact ionization cross-section, F the fragmentation fraction of the ionized species, and M the mass sensitivity function of the QMS. The variables in the last term of Eq. 6.2 are determined in a separate experiment where $N_{\mathrm{CO(ice)}}$ is the amount of CO that desorbs from the solid state due to photodesorption measured by the FTIRS, S_{CO} the measured CO signal by the QMS, and t the time over which the $N_{\mathrm{CO(ice)}}$ photodesorbed.

6.3 Results

In this section we present the results of the experiments mentioned in Table 6.1. In general, irradiation of ASW with VUV photons in the presence of gas-phase CO produces CO_2. Additionally, in the experiments at the higher end of the temperature range, (> 90 K), formation of molecular oxygen (O_2) is observed. To understand the processes that occur on and/or in the solid state we consider the infrared and QMS results, and how these change with temperature.

6.3.1 Infrared spectroscopy results

We observe the formation of CO_2 in the solid state through RAIRS. In Figure 6.1 we present five difference RAIRS spectra at experimental temperatures of 40 and 60 K. Such spectra are obtained by subtracting the initial ASW spectrum, before VUV irradiation, from the subsequently acquired spectra during irradiation. The spectra shown here are obtained at five different VUV fluence intervals where ASW was simultaneously exposed to gas-phase CO. It is apparent from these spectra that three distinct absorption features grow with increasing VUV fluence. The three features are positioned at 2279, 2260, and 2243 $\mathrm{cm^{-1}}$ and are all attributed to CO_2, namely $^{13}C^{18}O_2$ cluster islands on top of the water ice, $^{13}C^{16}O^{18}O$ bound to water, and $^{13}C^{18}O_2$ bound to water, respectively (Lehmann et al. 1977; He et al. 2017). The ^{16}O in $^{13}C^{16}O^{18}O$ originates from isotope impurities in the $H_2{}^{18}O$ and $^{13}C^{18}O$ samples.

The lowest ASW temperature at which the experiments are performed is 40 K. This ensures that the majority of the gas-phase CO molecules that enter the vacuum

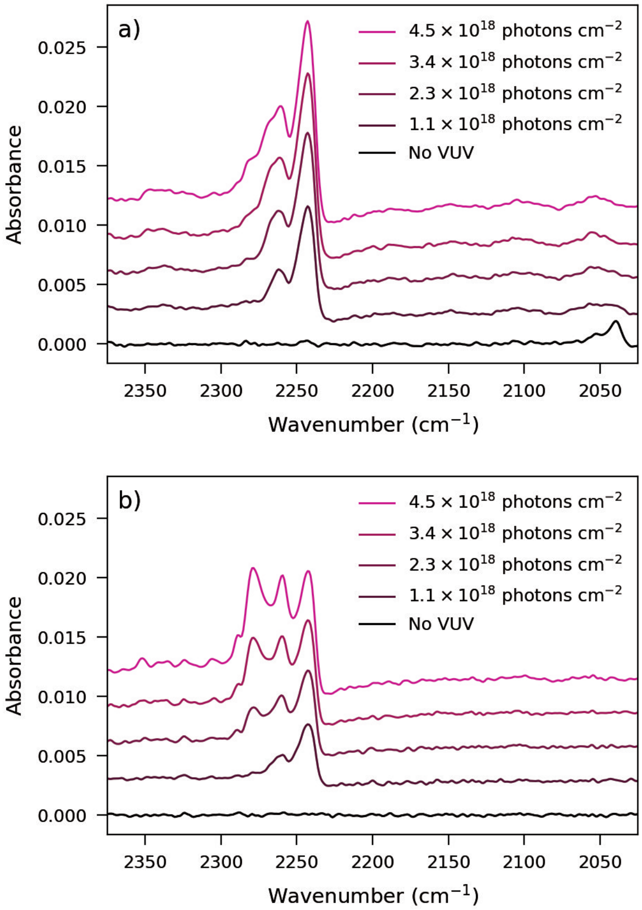

Figure 6.1: Five difference RAIRS spectra following VUV irradiation of ASW ($H_2{}^{18}O$) at 40 K (top) and 60 K (bottom) with gas-phase $^{13}C^{18}O$ at different VUV fluences, increasing from low to high.

chamber cannot adsorb onto our sample, as it is above the canonical desorption temperature of CO. However, as is shown by He et al. (2016b), the sticking coefficient of CO on nonporous-ASW (np-ASW) is close to unity at 40 K. Once the ASW is covered with CO, no additional CO freeze-out occurs. This is seen in the experiment at 40 K through the infrared signal around 2040 cm^{-1} where, preceding VUV-irradiation, the ASW is briefly exposed to gas-phase CO only (Figure 6.1a). In this short 5 minute window, CO adsorbs on top of the ASW with a column density of $\sim$ 1.1 monolayers, where one monolayer equals 10^{15} molecules cm^{-2}. This ice grows within 60 s and does not further increase. As soon as VUV irradiation starts, this solid-state CO on the surface of the ASW is consumed. At ASW temperatures $\geq$ 50 K no adsorption of CO is seen (Figure 6.1b). This is expected as the sticking coefficient of CO on ASW significantly drops at temperatures $\geq$ 50 K. An upper limit of $\leq$ 0.1 monolayers is derived for CO on top of ASW at temperatures $\geq$ 50 K.

Figure 6.2 shows the combined results of the experiment with ASW at 40 K. The upper and lower panels show results of both the infrared and QMS experiments during VUV irradiation and TPD, respectively. Figure 6.2a shows the growth of the combined and each individual CO_2 component during VUV irradiation (shaded areas), while

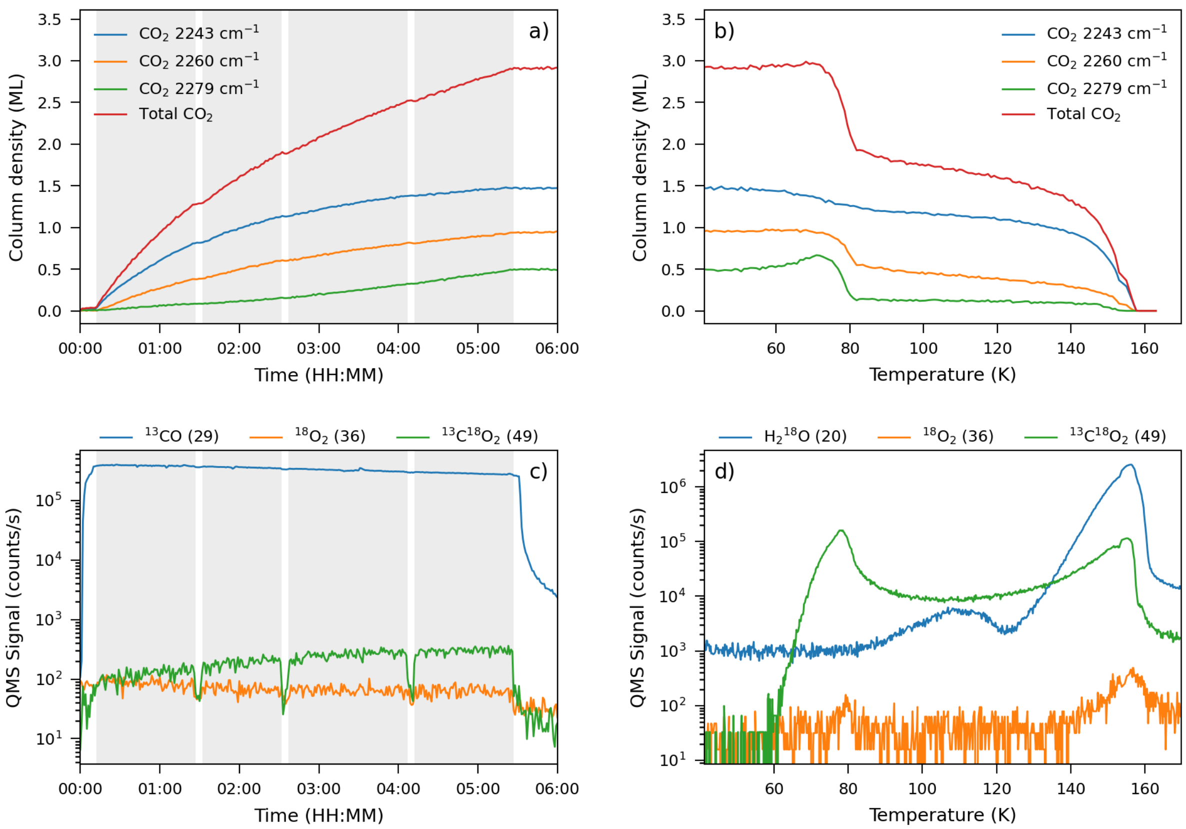

Figure 6.2: Results of the experiment of ASW at a temperature of 40 K. In the top row the deconvolved infrared components are given and in the bottom row the data for the quadrupole mass spectrometer (QMS) is presented. The left column shows data acquired during VUV irradiation (shaded area is with VUV shutter open) and on the right during temperature programmed desorption (TPD). ^{13}CO is shown in panel c), as measuring the main isotope (^{13}C^{18}O) would saturate the QMS and the ^{16}O isotope is present in the CO sample at a level of 5%.

Figure 6.2b shows the decrease, but during TPD. It is evident that the deconvolved components grow at different rates. The CO_2 component at 2243 cm^{-1} is the first to grow and levels off as the VUV fluence increases. This component is attributed to $^{13}C^{18}O_2$ bound to the ASW surface, as this initial CO_2 can only interact with the ASW. The 2279 cm^{-1} component has a delayed start and is attributed to $^{13}C^{18}O_2$ clusters on the surface of ASW (cf. He et al. 2017, who observed the same features, but shifted by $\sim$ 100 cm^{-1} due to the isotope shift.) As the ASW temperature increases, the diffusion of CO_2 also increases. The growth of CO_2 clusters starts earlier and the amount of molecules in clusters is increased with ASW temperature, see Figures 6.2, 6.8 (50 K), and 6.9 (60 K). Additionally, due to the increased temperature of the ASW, less binding sites are occupied by CO_2 due to reduced residence times. This is reflected in less CO_2 molecules bound to the ASW and more CO_2 molecules in clusters with increasing temperature. The component at 2260 cm^{-1} is due to $^{13}C^{16}O^{18}O$, formed from isotope impurities, on the ASW surface. Additionally, in the fitting of these three CO_2 components the 2260 cm^{-1} component comprises contribution from the 2243 and 2279 cm^{-1} features, as a Gaussian profile does not accurately represent these solid-state CO_2 absorption features. This makes an unique assignment for the 2260 cm^{-1} component difficult.

The decrease of the total CO_2 and each of the separate components during TPD is shown in Figure 6.2b. The CO_2 sublimates in two steps, the first desorption event occurs at $\sim$ 80 K and the second at $\sim$ 150 K. The former is in line with the canonical desorption temperature of CO_2, and the latter with the canonical desorption temperature of H_2O. The component at 2279 cm^{-1} drops around $\sim$ 80 K, which is in line with clusters of CO_2. The component at 2243 cm^{-1} gradually drops as the temperature of the ASW increases and disappears with the desorption of H_2O at 156 K, which is in agreement with CO_2 bound to ASW surface.

At ASW temperatures $\geq$ 70 K, the majority of the formed CO_2 is released back into the gas phase (see e.g., Figure 6.3). At 70 and 80 K, however, some of the initially formed CO_2 remains in the solid state, see Figure 6.3a and Appendix 6.10a, respectively. This CO_2 is formed during the initial moments of VUV irradiation and is bound to the deep binding sites on the ASW surface that are able to "trap" CO_2. The column densities of trapped CO_2 at 70 and 80 K are 0.6 and 0.12 monolayers, respectively. No solid-state CO_2 is detected in the experiments with ASW temperatures $\geq$ 90 K, and the upper limit of solid-state CO_2 is derived to be $\leq$ 0.02 monolayers.

6.3.2 QMS results

The QMS allows tracing of gas-phase species in the chamber during VUV irradiation and afterwards during TPD. The signals measured during TPD are only used for identification. In the following two sections we focus first on the QMS analysis of CO_2 that remained in the solid state (40–60 K) and then on CO_2 released into the gas phase (> 60 K) after formation.

6.3.2.1 Solid-state CO_2 (40–60 K)

The majority of the CO_2 formed at ASW temperatures of 40–60 K remains in the solid state, as is found in the infrared experiments. This solid-state CO_2 is released into the gas phase during TPD due to thermal desorption, and subsequently measured with the QMS. However, during VUV irradiation there is some gas-phase CO_2 signal

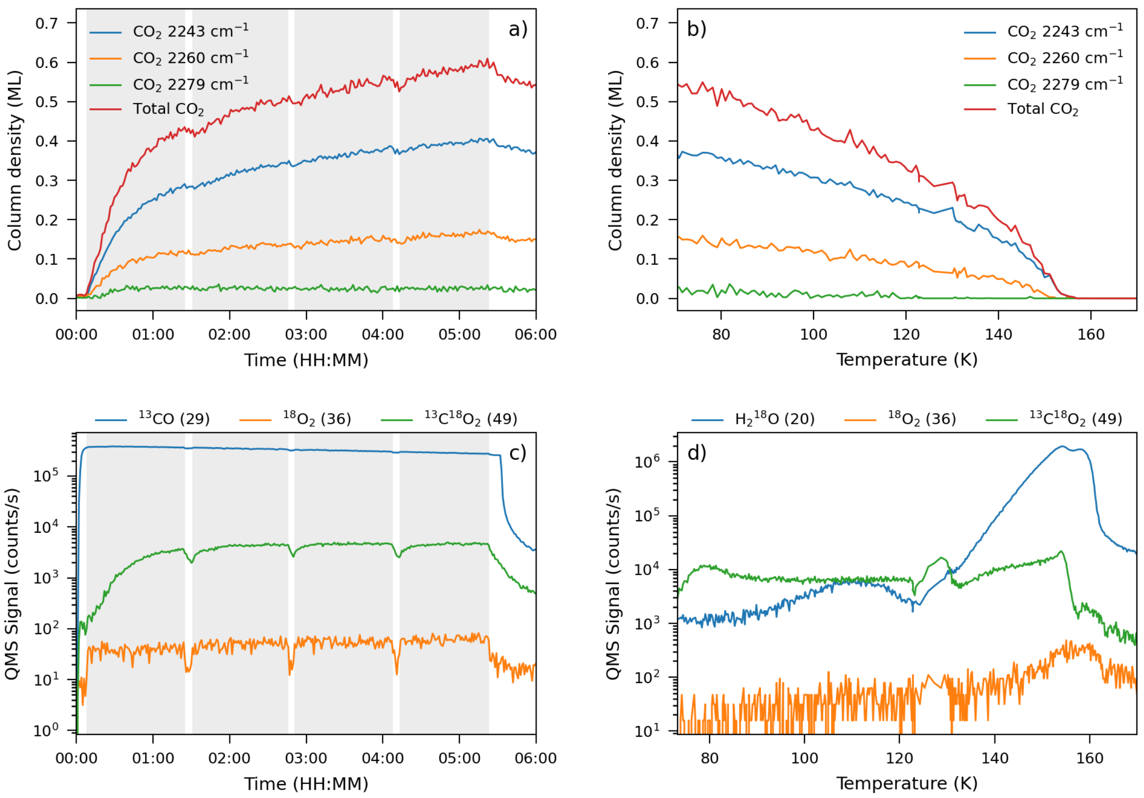

Figure 6.3: Results of the experiment of ASW at a temperature of 70 K. In the top row the deconvolved infrared components are given and in the bottom row the data for the quadrupole mass spectrometer (QMS) is presented. The left column shows data acquired during VUV irradiation (shaded area is with VUV shutter open) and on the right during temperature programmed desorption (TPD). ^{13}CO is shown in panel c), as measuring the main isotope (^{13}C^{18}O) would saturate the QMS and the ^{16}O isotope is present in the CO sample at a level of 5%. The increased signal in panel d) during the TPD between 120–130 K is due an unfortunate nonlinear temperature artifact.

measured by the QMS. This is illustrated in Figure 6.2c (shaded areas) by the signal at mass-to-charge ratio $(m/z) = 49$, which is associated with the main mass-fragmentation peak of $^{13}C^{18}O_2$. The increase of this CO_2 QMS signal follows approximately the same trend as the growth of the CO_2 column density measured in the infrared (Figure 6.2a). When the VUV shutter is closed, unshaded areas, the signal at $m/z = 49$ drops. We attribute this gas-phase CO_2 QMS signal to photodesorbed CO_2 from the solid state (Fillion et al. 2014).

During TPD, there are two distinct desorption peaks of CO_2 with an elevated plateau between them (see e.g., Figure 6.2d). The first desorption peak occurs at 78 K, the canonical desorption temperature of CO_2. The CO_2 molecules that desorb at this temperature, are those in CO_2 cluster islands. The second desorption peak coincides with the water desorption peak observed at 156 K. Both are in agreement with the deconvolved infrared components at 2279 and 2243 cm^{-1} (see e.g., Figure 6.2b).

6.3.2.2 Gas-phase CO_2 ($>$ 60 K)

In the remainder of the main experiments, Figures 6.3, 6.10–6.13, the temperature of the ASW ranges from 70–120 K. During these experiments equal amounts of CO are converted into CO_2. However, the majority of the formed CO_2 is released into the gas phase after formation. Similar to Figure 6.2, we present the results of ASW at 70 K in Figure 6.3. During this experiment $\sim$ 20% of the formed CO_2 stays on the surface of ASW, while the remainder is released into the gas phase. The release of CO_2 into the gas phase is slightly below the canonical CO_2 desorption temperature, 78 K. This is no surprise as the binding energy of CO_2 bound to H_2O equals 2250 K, while the binding energy between CO_2 molecules is higher at 2415 K (He et al. 2017). During the first hour of VUV irradiation, the ASW surface "traps" some of the formed CO_2 in its deep binding sites, but once these are occupied, most of the subsequently formed CO_2 is released into the gas phase. This is reflected by the initial rapid build up of CO_2 in the infrared during the first VUV irradiation interval (Figure 6.3a). Additionally, in Figure 6.3c it is shown that the gas-phase CO_2 builds up during the initial VUV interval, where it reaches steady state at the same time when the growth of solid-state CO_2 levels off. Lastly, during TPD the two main desorption features clearly appear, but not as prominent as in the 40–60 K experiments. The majority of the CO_2 is released during TPD in the "plateau" region between 85–145 K, that is, between the canonical desorption of CO_2 cluster islands and H_2O, as is shown in Figure 6.3d.

In the experiments with ASW temperatures between 90 and 120 K (Figures 6.11–6.13), no solid-state CO_2 is observed in the infrared (column density $\leq 2.0 \times 10^{13}$ cm^{-2}). The TPDs in this temperature range, however, do reveal that some CO_2 is still bound to the surface of the ASW. Following the trend as seen in the experiments with ASW at 70 and 80 K, the amount of CO_2 that remains on the ASW surface decreases with increasing temperature, see Figures 6.11–6.13. This is in line with the decrease of absolute signal of the "plateau" during TPD. Interestingly, a significant amount of O_2 formation is observed in this temperature range, as shown by the QMS signal at $m/z = 36$ representing $^{18}O_2$. The formation of O_2 increases with temperature at the cost of CO_2. At 120 K the formation of CO_2 is almost completely quenched and over 90% of the formed products is O_2.

Figure 6.4: Column densities of the formed products when ASW is VUV irradiated and exposed to gas-phase CO as function of temperature. Solid-state column densities are derived through FTIRS and gas-phase column densities through the QMS as described in Section 6.2.3.

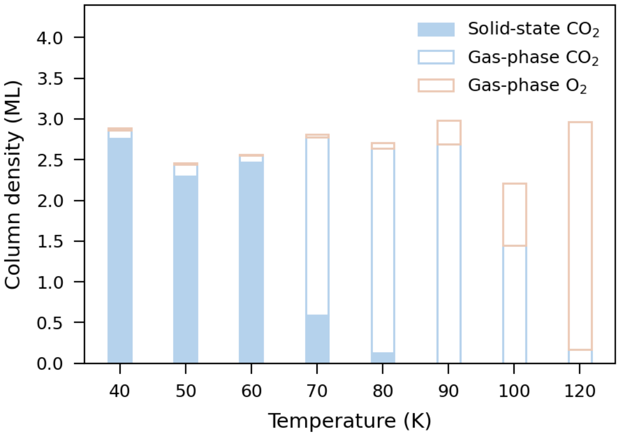

6.3.3 CO_2 and O_2 column densities

For each of the main experiments the column densities of the products are summarized in Figure 6.4. The column density of solid-state CO_2 is derived through the combined integrated absorbance area of the three infrared CO_2 features. The CO_2 and O_2 gas-phase column densities are derived through the calibration of the QMS described in Section 6.2.3.2. In short, in the temperature range 40–60 K the main product is solid-state CO_2. As the substrate temperature is increased above 60 K, the CO_2 is detected in the gas phase, and at even higher temperatures, that is, ≥ 90 K, O_2 formation is observed at the cost of CO_2.

6.4 Discussion

It is clear from the presented results that CO_2 is formed in our experiments, and that the temperature of the ASW influences the physical appearance of CO_2. In the following section we explore the different pathways to CO_2, which one results in the formation of CO_2 in our experiments, under which conditions, and what the efficiency is of this process.

6.4.1 Exploring the reaction network

In the introduction we mentioned several pathways that can form CO_2. The formation of CO_2 in our experiments is driven by VUV irradiation of ASW that interacts with gas-phase CO. This is different from most earlier studies where CO was embedded and intimately mixed with water ice. Such experiments are relevant for astronomical scenarios in which H_2O and CO are mixed in the solid state. However, these are not the scenarios discussed later in this paper, that is, protoplanetary disks (Section 6.5.1) and molecular cloud edges (Section 6.5.2).

There are two potential pathways to form CO_2 in our experiments, which involve both H_2O and CO, and three possible pathways that could lead to the observed formation of O_2 at higher temperatures. Figure 6.5 gives a schematic overview of the below described reactions.

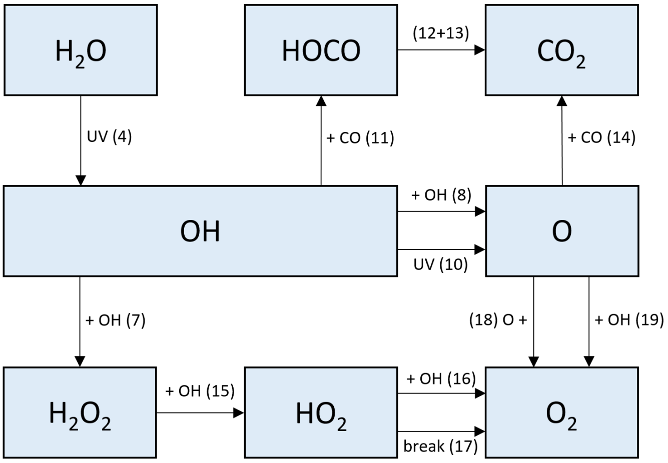

Figure 6.5: Schematic overview of the reactions that potentially occur in our experiments with VUV irradiation of solid-state H_2O in the presence of gas-phase CO. The numbers in parenthesis correspond to the reactions in Section 6.4.1. Backward, recombination, and by-products of reactions are not shown for clarity.

UV photons generally dissociate H_2O in the ice through its excited $\tilde{\text{A}}$ and $\tilde{\text{B}}$ states, which mainly lead to the formation of OH radicals and atomic oxygen,

$$H_2O + h\nu \rightarrow H + OH, \tag{6.3}$$

$$H_2O + h\nu \rightarrow H_2 + O(^1D). \tag{6.4}$$

Stief et al. (1975) reported quantum efficiencies of 0.89 and ≥ 0.99 for reaction (6.3), and quantum efficiencies of 0.11 and ≤ 0.01 for reaction (6.4) for the wavelength intervals 105-145 nm and 145-185 nm, respectively. In this study we use a MgF_2 window with no Lyman-α transmission between the MDHL and vacuum chamber. This ensures that Lyman-α photons are absorbed, and that the majority of the UV photons are in the 140–170 nm (7.3–8.9 eV) range, see Appendix 6.A. This, combined with the reported quantum efficiencies, results in the dissociation of H_2O only through the excited $\tilde{\text{A}}$, and produces OH radicals through reaction (6.3).

The formed H and OH proceed in different ways depending on the depth in the solid state at which dissociation occurs. The molecular dynamics calculations by Andersson & van Dishoeck (2008) showed that in the top three monolayers the majority of the photodissocation events results in the desorption of H and trapping of OH. At four monolayers or deeper most of the photodissocation events result in trapping of both species or recombination, reforming H_2O through reaction (6.5),

$$H + OH \rightarrow H_2O. \tag{6.5}$$

The desorption of H in the top three monolayers results in an enrichment of OH radicals on the surface. It was found in these calculations that the OH radicals can diffuse up to 60 Å on top of the H_2O surface at 10 K. This diffusion occurs on picosecond timescales, and does not include any thermal diffusion on longer timescales. Hama et al. (2009) showed that the OH radicals produced through reaction (6.3) are hot and have a translational temperature of 1300 ± 300 K. This significant amount of translational energy allows for additional diffusion, and increases the probability of two OH radicals to meet and react with each other. This reaction either forms hydrogen peroxide (H_2O_2) or H_2O and atomic oxygen, see reactions (6.6) and (6.7), respectively. The branching ratio between reactions (6.6) and (6.7) was found to be 0.8 and 0.2, respectively, for two non-energetic OH radicals reacting with each other at 40–60 K (Oba et al. 2011),

$$\mathrm{OH} + \mathrm{OH} \rightarrow \mathrm{H_2O_2}, \tag{6.6}$$

$$\mathrm{OH} + \mathrm{OH} \rightarrow \mathrm{H_2O} + \mathrm{O(^3P)}. \tag{6.7}$$

As the abundance of the H_2O_2 increases, the amount of H_2O_2 dissociated by VUV photons increases through reaction (6.8),

$$\mathrm{H_2O_2} + h\nu \rightarrow \mathrm{OH} + \mathrm{OH}. \tag{6.8}$$

The translational temperature of these OH radicals was found to be 7500 ± 1000 K, which potentially allows for even further diffusion of OH radicals across the surface (Hama et al. 2009). These OH radicals on the surface, or those below for that matter, can be subsequently dissociated by VUV photons forming atomic hydrogen and oxygen, see reaction (6.9),

$$\mathrm{OH} + h\nu \rightarrow \mathrm{H} + \mathrm{O(^3P)}. \tag{6.9}$$

The OH radicals formed through reactions (6.3) and (6.8) are potential candidates for CO_2 formation when reacting with gas-phase CO. In the experimental study by Oba et al. (2010) the formation of CO_2 was observed from co-deposition of non-energetic OH radicals, cooled to 100 K prior to deposition, and CO molecules at 10 and 20 K. The authors proposed that CO_2 forms through reactions (6.10), (6.11), and (6.12),

$$\mathrm{CO} + \mathrm{OH} \rightarrow trans\mathrm{-HOCO}, \tag{6.10}$$

$$trans\mathrm{-HOCO} \rightarrow cis\mathrm{-HOCO}, \tag{6.11}$$

$$cis\mathrm{-HOCO} \rightarrow \mathrm{CO_2} + \mathrm{H}. \tag{6.12}$$

Ground-state atomic oxygen formed through reactions (6.7) and (6.9) also has the potential to react with CO and form CO_2 through reaction (6.13),

$$\mathrm{CO} + \mathrm{O(^3P)} \rightarrow \mathrm{CO_2}. \tag{6.13}$$

The addition of ground-state atomic oxygen to CO has been experimentally shown to work between 5 and 20 K, where CO is adsorbed on a bare substrate (Roser et al. 2001; Madzunkov et al. 2006; Raut & Baragiola 2011; Ioppolo et al. 2013). The same reaction has also been investigated on top of ASW by Minissale et al. (2013). These authors show that the CO_2 is formed through reaction (6.13) when CO and O are co-deposited on the surface of ASW in the temperature range 10–50 K.

The initially formed O, OH, and H_2O_2 can react with each other to form the hydroperoxyl radical (HO_2) and O_2. The HO_2 radical is formed through subsequent reactions of H_2O_2 with OH, see reaction (6.14). O_2 can be formed through different means, 1) an HO_2 radical reacts with OH, see reaction (6.15), 2) the HO_2 radical falls apart, see reaction (6.16), 3) atomic oxygen reacts with OH, see reaction (6.17), or 4) atomic oxygen reacts with another atomic oxygen, see reaction (6.18).

$$\mathrm{H_2O_2} + \mathrm{OH} \rightarrow \mathrm{HO_2} + \mathrm{H_2O}, \tag{6.14}$$

$$\mathrm{HO_2} + \mathrm{OH} \rightarrow \mathrm{O_2} + \mathrm{H_2O}, \tag{6.15}$$

$$\mathrm{HO_2} \rightarrow \mathrm{H} + \mathrm{O_2}, \tag{6.16}$$

$$\mathrm{O} + \mathrm{OH} \rightarrow \mathrm{O_2} + \mathrm{H}, \tag{6.17}$$

$$\mathrm{O} + \mathrm{O} \rightarrow \mathrm{O_2}. \tag{6.18}$$

6.4.2 CO_2 formation pathway

In order to disentangle which of the above formation pathways is active in our experiments, we look at the following aspects: 1) the temperature dependence of CO_2 formation, 2) isotopologue behaviour, and 3) comparison with other work, available from literature. Across the temperature range of 40–90 K, the total column density of formed CO_2 is constant, but above 90 K the efficiency of CO_2 formation decreases due to the competing formation of O_2, see Figure 6.4. This temperature dependence contains significant amount of information, which allows us to constrain the formation of CO_2 to one pathway.

Our experiments show that CO_2 is formed through the reaction between gas-phase CO and solid-state OH radicals. These OH radicals are the primary product of H_2O dissociation in our experiments, and are thus most likely to react with CO. This particular reaction pathway to CO_2 has been investigated extensively (Watanabe & Kouchi 2002b; Watanabe et al. 2007; Ioppolo et al. 2009; Oba et al. 2010, 2011; Ioppolo et al. 2011; Noble et al. 2011; Zins et al. 2011; Yuan et al. 2014). However, the majority of these studies were performed at temperatures where CO is in the solid state, and mixed with H_2O. Oba et al. (2010) looked at the formation of CO_2 through co-deposition of CO and non-energetic OH radicals at a temperature of 10 and 20 K. Besides CO_2, the authors also observed the intermediate products cis- and trans-HOCO radicals at 1774 and 1812 cm^{-1}, respectively. They found that the HOCO absorption features disappear at $T > 40$ K, which is in line with the experimental work of Milligan & Jacox (1971). This is most likely the reason why the cis- and trans-HOCO radicals are not detected in the infrared spectra of our experiments (spectra not shown). In a follow-up study, Oba et al. (2011) investigated the same reactions, but in the temperature range 40–60 K. Formation of CO_2 was observed in the IR, but the efficiency at which CO was converted into CO_2 decreased with increasing temperature. The conversion rates were found to be 1.4%, 0.8%, and 0.3% at 40, 50, and 60 K, respectively. This decrease was attributed to the decreasing residence times with increasing surface temperature of both CO and OH. In our experiments this efficiency decrease is not observed, even when only considering solid-state CO_2. A possible explanation to this is the different origin of the OH radicals; in our work the radicals are formed *in situ*, whereas in previous studies OH radicals are deposited.

The other proposed formation pathway to CO_2 in which atomic oxygen reacts with gas-phase CO can be excluded. Given the temperature range, 40–120 K in which CO_2 is formed, and that O_2 is significantly formed at temperatures ≥ 90 K, it is unlikely that atomic oxygen is involved due to its short residence times, and that it is a secondary product of OH radicals through reactions (6.7) and (6.9) in our work. Additionally, on ASW atomic oxygen and CO have similar binding energies, that is, 1320 and 1350 K, respectively, and thus their residence times on the surface are comparable (Minissale et al. 2016; He et al. 2016a). Because of their similar residence times, no difference should be observed between the formation of CO_2 and O_2 with experimental temperature. However, as this difference is observed, this is additional proof that atomic oxygen is not involved in the formation of CO_2. Lastly, Minissale et al. (2013) investigated the formation of CO_2 through co-deposition of CO and atomic oxygen on top of ASW. It was found that the efficiency of CO_2 formation peaked at 35 K and dropped to zero at 60 K. As CO_2 formation is observed in our experiments up to 120 K, this is again evidence that atomic oxygen is not involved in the formation of CO_2. It should be noted that experimental conditions are not identical, as in our experiments the atomic oxygen would be formed *in situ* instead of co-deposited with CO. However, since atomic oxygen is in the ground state, for both our work and that of Minissale et al. (2013), no clear differences are expected.

Formation of CO_2 through excited CO reacting with another CO molecule on the surface of ASW can also be ruled out. This is unlikely to occur, because it would require a CO molecule to be excited during its short, but nonzero, residence time and react with another CO molecule which has an equally short residence time. Additionally, in the control experiment with $H_2{}^{18}O$ and $^{13}C^{16}O$, the formed CO_2 is measured with the QMS during TPD at $m/z = 47$, corresponding to $^{13}C^{16}O^{18}O$, see Appendix 6.14. If the CO_2 is formed through excited CO and another CO molecule it is expected to be observed at $m/z = 45$, corresponding to $^{13}C^{16}O_2$.

From above results and discussion it is most likely that CO_2 is formed through the interaction between CO and OH radicals, formed by UV dissociation of H_2O. However, it is not yet clear if CO directly interacts with OH radicals from the gas phase, that is, an Eley-Rideal type reaction, or if CO adsorbs onto the ASW, diffuses, and subsequently reacts with OH radicals, that is, a Langmuir-Hinshelwood type reaction. Additionally, the formation location of CO_2 is also not yet clear; is it formed on the surface or embedded in the ASW? Both of these topics will be discussed in the following section.

6.4.3 The formation location of CO_2

It is possible to estimate the time a species resides on a surface given a temperature and binding energy to that surface. We derived that CO has residence times on ASW of 4.5×10^2–7.7×10^{-8} s in the range from 40 to 120 K. This is found through the Arrhenius equation, which can be written as

$$k = Ae^{-\frac{E_{bind}}{T}}, \tag{6.19}$$

where k is the rate constant, A the frequency factor, which is taken to be 10^{12} s^{-1}, E_{bind} the binding energy of a species to a specific surface in K, and T the temperature of the surface in K. The residence time is then given by the reciprocal of the rate constant from Eq. 6.19. For CO on ASW, the binding energy is dependent on the CO surface coverage, ranging from 1000–1700 K at 1–10^{-3} monolayer coverage, respectively (He et al. 2016a). The above residence times are estimated given an average binding energy of 1350 K for CO on ASW. For comparison, the binding energy of CO on the CO–CO interface is 855 ± 25 K (Öberg et al. 2005).

Even within these short residence times, some diffusion across the surface is expected. The number of binding sites CO visits on ASW, before desorption occurs, is estimated to be 7.2×10^{10}–4.2×10^3 in the range 40–120 K. This is also derived through Eq. 6.19. Specifically, the amount a CO can diffuse across different binding sites before a species desorbs is approximated by dividing the diffusion rate by the desorption rate. The diffusion rate is estimated by exchanging the E_{bind} term in Eq. 6.19 for the diffusion energy (E_{diff}). The rate constant is then a proxy of the number of hops a species makes between different binding sites per second. The diffusion energy for CO on ASW has recently been measured *in situ* with transmission electron microscopy (TEM), and was found to be 350 ± 50 K (Kouchi et al. 2020).

Given these residence times and amount of binding sites that are "visited" before desorption occurs, we conclude that CO spends sufficient time on the surface of ASW to react with OH radicals through a Langmuir-Hinshelwood type reaction. This is different from Yuan et al. (2014), who investigated this reaction under similar experimental conditions and attributed it to an Eley-Rideal type of reaction. Yuan et al. (2014) employed a slightly higher binding energy of 0.125 eV (1450 K) for CO on H_2O, which results in a residence time of $\sim 2 \times 10^{-4}$ s at their experimental temperature of 76 K. The residence time is used to calculate the fractional coverage of CO on H_2O and was found to be 1×10^{-6} ML. The resulting fractional coverage of OH was derived to be 0.05 ML, over four orders of magnitude higher, which led to the conclusion of an Eley-Rideal type of reaction. However, diffusion of CO during this (short) residence time was not considered. At these temperatures, CO visits approximately 10^6 binding sites during its residence time, and thus, the effective surface scanned by CO is ~ 1 ML even though the fractional coverage of CO is only 1×10^{-6} ML. This supports that the involved mechanism follows a Langmuir-Hinshelwood type reaction.

Furthermore, we see no evidence of significant CO diffusion, and subsequent trapping, into the *bulk* of the H_2O ice. However, there is some trapping of CO in the surface and/or pores of the ASW. This is shown in a control experiment where ASW is exposed to CO molecules, but not to VUV irradiation. During TPD of this control experiment, as is shown in Appendix 6.15, the majority of the CO desorbs at approximately 50 K. Only a small amount of CO “volcano” desorbs when the ASW crystallizes. It is most likely that this CO got trapped in ASW due to pore collapse, instead of actually diffusing into the bulk ASW.

6.4.4 Temperature dependent formation, CO_2 vs O_2

Now that it is clear that the CO_2 in our experiments is formed through a Langmuir-Hinshelwood type reaction between solid-state OH radicals and solid-state CO molecules, be it with very short residence times, we can look at the reason why at temperatures > 90 K the CO_2 formation becomes less effective. Given the short residence time of atomic oxygen on ASW at temperatures > 90 K, that is, $< 2.3 \times 10^{-6}$ s, that atomic oxygen is a secondary product through reactions (6.7) and (6.9), and is not involved in the formation of CO_2 (see Section 6.4.2), we expect that atomic oxygen is also not involved in the observed formation of O_2 in our experiments.

This leaves the formation of O_2 involving a HO_2 radical, which is formed through the reaction of an OH radical with H_2O_2, reaction (6.14). This H_2O_2 is formed from two OH radicals through reaction (6.8). The formation of CO_2 and O_2 is thus both dependent on the availability of OH radicals. Given the temperature dependence it is likely that the mobility of the OH radical holds the answer to why these pathways are in competition. This is an interesting pathway to form O_2 at high temperatures, especially compared to the “standard” pathways with atomic oxygen, reactions (6.17) and (6.18). In this work we only explore this as a way to explain the decrease in CO_2 formation at temperatures > 90 K. A more in-depth investigation of this pathway to O_2 is beyond the scope of this work and will be presented in the near future.

6.4.5 Conversion rate of CO into CO_2

In order to demonstrate that the gas-grain pathway to convert CO into CO_2 is a process of importance in astrophysical environments, we discuss in this section its conversion rate and limiting factors. In total ~ 60 monolayers of water ice are deposited on the substrate in preparation of our experiments. However, as this conversion of CO into

CO_2 occurs on the surface, not all of this H_2O is available to act as a reacting medium. Classically, the surface of solid-state H_2O contains approximately 10^{15} molecules per cm^2. However, due to the porous nature of our ASW, the available H_2O surface for CO to adsorb on is expected to be larger. Additionally, with hydrogen released from the top three monolayers upon UV dissociation of H_2O, and the mobility of the OH radicals, we assume that OH radicals formed in the top three monolayers are available to convert CO into CO_2 (Andersson & van Dishoeck 2008). These top three monolayers, that is, 3.0×10^{15} H_2O molecules cm^{-2}, are henceforth the reactive surface.

In this reactive surface UV photons are absorbed by H_2O with an average VUV absorption cross section of $(3.4 \pm 0.2) \times 10^{-18}$ cm^2 (Cruz-Diaz et al. 2014). Given this cross section, roughly 1% of the total incident VUV fluence is absorbed by H_2O in the reactive surface, and equals 4.5×10^{16} photons. On the assumption that H_2O dissociation is 100% efficient, this produces an equal amount of OH radicals in the reactive surface. In the temperature range 40–90 K, approximately 2.7×10^{15} CO_2 molecules are formed, and thus an equal amount of OH radicals is consumed. This means that, for our assumptions, only 6% of the available 4.5×10^{16} OH radicals are involved in the conversion of CO into CO_2.

In our experiments OH, and not CO, is the limiting factor in the reaction. In the temperature range of 40–90 K, the formation of CO_2 is considered to be constant. However, the residence time of CO is lowered by a factor of 10^8 and the binding sites visited by CO by a factor of 10^5 from 40 to 90 K. That is to say, once CO finds an OH radical on the surface that is available, the conversion into CO_2 is (close to) unity.

The small fraction (6%) of UV absorption events resulting in CO_2 production, may be a consequence of inefficient H_2O dissociation or OH + H recombination. There is the possibility that 94% of the OH radicals are not good “candidates” for reacting with CO in this reactive surface. This would be surprising, because even non-energetic OH radicals in the ground state are able to form CO_2 with CO at 10 K (Oba et al. 2010). However, in the interest of the argument, lets assume that indeed 94% of the OH radicals do not convert CO into CO_2. This leaves an OH rich surface, since the hydrogen atoms desorb upon H_2O dissociation in this reactive surface. This large quantity of OH radicals should largely find each other and react to form H_2O_2 and O_2. The infrared does not show any of the vibrational modes of H_2O_2 within our detection limits (spectra not shown), especially not with the expected H_2O_2 column density of ~ 20 monolayers, and only at temperatures ≥ 90 K significant amounts of O_2 are observed, but only at column densities of ~ 3, not 20 monolayers (at 120 K; see Figure 6.4). In itself this column density is already questionable, as it is approximately seven times larger than the available H_2O molecules in this reactive surface. A control experiment where ASW is irradiated at 40 K and gas-phase CO is omitted, does show the formation of H_2O_2 and O_2, see Appendix 6.16. This shows that in the presence of gas-phase CO the formation of H_2O_2 and O_2 in the reactive surface is quenched, and that in the main experiments all available OH radicals react with CO into CO_2.

The amount of CO_2 produced, and lack of H_2O_2 and/or O_2 at $T < 90$ K, in the experiments is in conflict with the amount of OH radicals that should be produced with 100% dissociation efficiency of H_2O. Does not every VUV absorption event result in the dissociation of H_2O or is recombination after VUV dissociation a lot more efficient in our experiments? Fully answering this question is beyond the scope of this work, but it leads to a conundrum that requires future attention. It is unlikely that recombination to H_2O is significantly more efficient than predicted by molecular dynamics calculations. Photodissociation and desorption occur on picosecond timescales after UV absorption in these simulations, and thus, diffusion of atomic hydrogen within this time window is improbable. It should be noted that in molecular dynamics calculations only a single event is considered per simulation, and thus for H_2O recombination to occur the atomic hydrogen needs to find its original OH partner before it desorbs. It could be that in our experiments the atomic hydrogen reforms H_2O with previously formed OH radicals due to the high UV photon fluxes 2.5×10^{14} photons s^{-1} cm^{-2}. Molecular dynamics calculations of H_2O photodissociation and recombination with neighbouring OH radicals are needed to test the efficiency of this channel.

The lack of efficient H_2O recombination points toward inefficient photodissociation of H_2O upon absorption of a UV photon in the excited $\tilde{A}$ state. However, in Figure 2 of Andersson & van Dishoeck (2008) the fraction probabilities of photodissociation pathways for H_2O are given per *absorbed* photon and sum to (near) unity. This is in conflict with our results as we only observe 6% (effective) dissociation efficiency of H_2O. Schriever et al. (1990) investigated the absolute photodissociation quantum yield of H_2O in an argon matrix (ratio 1:500). It was found that at 160 nm and 5 K the photodissociation efficiency of isolated H_2O in argon equals 20–30%. It should be noted that in the work by Schriever et al. (1990) the H_2O is isolated and trapped in the bulk, which cannot necessarily be extrapolated to our work. However, it does hint that photodissociation of H_2O with VUV, under laboratory conditions, is not 100%. More investigation is needed here, as this is key for a correct incorporation of the laboratory results into astrochemical models.

Interestingly, the molecular dynamics calculations by Arasa et al. (2013) find a similar conversion factor, that is, ~ 0.03 per absorbed photon, for the interaction between CO and OH. In their work different CO-H_2O systems were investigated, where H_2O was dissociated through the first excited state with ultraviolet photons at 10 K. They found that CO needs to be embedded in H_2O for it to be converted into CO_2 with a probability of $(3.6 \pm 0.7) \times 10^{-4}$ per absorbed photon. However, it was found that the intermediate HOCO complex has a significant higher formation probability of $(3.00 \pm 0.07) \times 10^{-2}$ per absorbed photon. This was explained by the HOCO complex being trapped in the solid state and losing its internal energy to the surrounding molecules, which prevents further reaction to $CO_2 + H$. In our experiments the HOCO complex is not observed. However, it could very well be that this HOCO complex still is involved in the formation of CO_2 in our experiments due to the increased ASW temperature, as seen in Milligan & Jacox (1971) and Oba et al. (2011). If this is the case, then our formation efficiency of 0.06 per absorbed photon is in agreement with that from Arasa et al. (2013). It should be noted that the authors assume that each absorbed photon leads to dissociation into H and OH.

Although our formation efficiency is comparable to that of Arasa et al. (2013), the motivation is different. In the molecular dynamics calculations the location and orientation of the reaction products are the limiting factor, while in our experiments, due to the lack of other reaction products, it seems that photodissociation of H_2O in the solid state is not efficient. A possible source of error in our determination of the formation efficiency are the experimental assumptions. Using Gaussian error propagation, we estimate the error in our formation efficiency of CO_2 per *absorbed* VUV photon in the reactive surface to be 60%, and thus ranges from 2–10%.

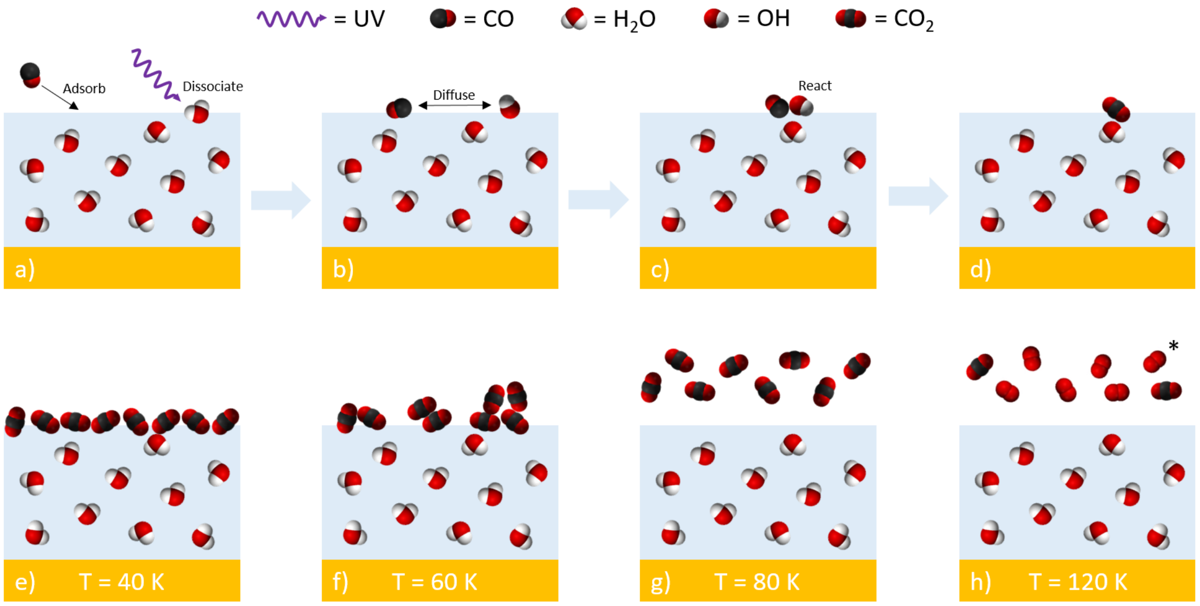

Figure 6.6: Simplistic representation of the processes that occur in our experiments. Panel a) through d) show the proposed Langmuir-Hinshelwood reaction that creates CO_2 in our experiments. Panels in the bottom row schematically show the structure or phase in which the formed products end up after formation, given a certain experimental temperature. $^{(*)}$ Molecular oxygen is not formed through the depicted reaction, for details see Section 6.4.1 & 6.4.4.

6.5 Astrophysical implications

The above results and discussion are summarized in a simplified cartoon (see Figure 6.6). In the top row of this figure, the formation process is visualized. Formation of CO_2 on the surface of ASW through VUV irradiation of H_2O and interaction with gas-phase CO is discussed in detail in Section 6.4. In short, CO has a short, but nonzero, residence time on ASW even though its temperature is above the canonical desorption temperature of CO. This combined with VUV irradiation of H_2O results in the formation of OH radicals. The diffusion of CO and OH radicals allows them to react with each other and form CO_2 in a Langmuir-Hinshelwood type reaction. The bottom row of Figure 6.6 illustrates the physical appearance of the formed CO_2 with changing substrate temperature. A full analysis of the experiments is given in Section 6.3, but briefly, in the lower end of the experimental temperature range, that is, 40–60 K, the formed CO_2 remains in the solid state. Specifically, at 40 K (Figure 6.6e) the CO_2 is not mobile enough and the majority of the CO_2 stays bound to the ASW surface. However, in the experiment at 60 K (Figure 6.6f), the CO_2 has significant mobility and starts diffusing across the surface, and forms CO_2 cluster islands on top of the ASW. As shown in Figure 6.6g, the formed CO_2 is released into the gas phase at 80 K, and at higher temperatures, the formation of O_2 starts competing with CO_2, which is shown in Figure 6.6h. In the 40–90 K range, our experiments show that 2–10% of the *absorbed* UV photons in the reactive surface, that is, top three monolayers of ASW, result in the conversion of gas-phase CO into CO_2. In the following section, we look at two astrophysical environments, that is, protoplanetary disks and molecular clouds, where this pathway could play an important role.

6.5.1 CO conversion in protoplanetary disks

In planet forming disks, the gas mass, as derived through CO isotopologues, often comes out factors 10–100 lower than expected based on the dust content. This finding is based on physical-chemical modeling that includes photodissociation and freeze out of CO and its isotopes (Miotello et al. 2014, 2016, 2017). One interpretation is that these disks have already lost a significant fraction of their total gas mass. Another is that some unknown process locks up gas-phase CO on grains. A correct interpretation is essential for models of planet formation that rely on the available gas-mass reservoir as well as on the gas-to-dust ratio. Other gas-mass tracers are problematic, as H_2 is undetectable and HD has only been observed in a few sources (see e.g., Bergin et al. 2013; McClure et al. 2016; Trapman et al. 2017; Kama et al. 2020), where, incidentally, the HD data support the notion of gas-phase CO being locked up. The CO into CO_2 conversion has been proposed as a possible pathway to convert gas-phase CO into a species that is much more difficult to detect.

Chemical-modeling work by Bosman et al. (2018) looked at several pathways through which CO could be converted into less volatile species to explain the low observed CO fluxes. These models are successful in this conversion on timescales shorter than average protoplanetary disk lifetimes, that is, $\sim$ 3 Myr. It should be noted that it was found in these models that gas-phase CO is in competition with atomic hydrogen for OH radicals on the surface (see Bosman et al. 2018, for more details). Furthermore, these results depend on the adopted binding energies, reaction rates, and formation of H_2. For example, the binding energy of CO in these models is kept constant at 855 K, no matter the environment. However, it has been found that the binding energy of CO on ASW can be as high as 1700 K (He et al. 2016a). In a similar fashion, Trapman et al. (2021) used `DALI` models to investigate the low CO fluxes in the Lupus star-forming region. Disk regions with $T_{\mathrm{gas}} > 35$ K were excluded in these models for gas-phase CO conversion, as verification models showed that CO conversion through grain-surface chemistry was negligible at these temperatures, but again this was tested with a CO binding energy of 855 K.

Including the correct binding energy for CO on ASW in these types of models is crucial. This increased binding energy will allow gas-phase CO to compete with atomic hydrogen for OH radicals in a larger temperature range, and thus a larger region in protoplanetary disks where CO can be removed from the gas phase. In our experiments and the models by Bosman et al. (2018) and Trapman et al. (2021), the amount of gas-phase CO that is converted into CO_2 depends on the availability of OH radicals. The authors assume in their models that once H_2O absorbs an UV photon, dissociation is 100% efficient. As discussed in Section 6.4.5, our experiments show an efficiency for OH production of 2–10% per absorbed UV photon as opposed to the 100% adopted in the models. Further modeling is required, also including the correct binding energy of CO on ASW, to fully assess the impact of our results on the model predictions.

6.5.2 CO_2 formation in edges of molecular clouds

Observations of icy grains surrounding young stars suggest that large amounts of the solid-state CO_2 are embedded in a water-rich environment. Here we explore if the conversion of gas-phase CO into solid-state CO_2 could explain the puzzling presence of this solid-state CO_2. It is generally assumed that the ice that covers dust grains is composed of two layers: a polar and an apolar layer, where the apolar layer is on top of the polar layer (see e.g., Boogert et al. 2015). A polar ice layer is dominated by species with larger dipole moments, such as H_2O, and an apolar ice layer mainly contains species with smaller or no dipole moments, such as CO and N_2. The *Spitzer* “Cores to Disks” program showed that in embedded young low-mass stars the majority of the observed solid-state CO_2 is mixed in a polar water-rich environment (Pontoppidan et al. 2008). Given this H_2O-dominated environment, it is possible that a substantial fraction of this CO_2 is formed through reactions between CO and OH radicals. This would require CO to freeze out during H_2O formation in order to be intimately mixed and subsequently to be converted into CO_2.

Infrared observations show that it is unlikely that CO is mixed in a water-rich environment. The observed CO absorption feature can be deconvolved into three components, namely 4.665 μm (2143.7 cm^{-1}), 4.673 μm (2139.7 cm^{-1}), and 4.681 μm (2136.5 cm^{-1}). The blue component (4.665 μm) is assigned to CO in an apolor environment, specifically, it is linked to mixtures of solid-state CO and CO_2 (Boogert et al. 2002; van Broekhuizen et al. 2006) or crystalline CO (Pontoppidan et al. 2003). The middle component (4.673 μm) is generally attributed to pure CO (see e.g., Boogert et al. 2002). The red component (4.681 μm) has a broader “footprint” compared to the other two and is linked to CO in a polar environment. This polar environment could be H_2O and would set the scene for solid-state formation of CO_2 in a polar environment. However, Sandford et al. (1988) showed that if CO would reside in H_2O, one can expect a feature at 4.647 μm (2151.9 cm^{-1}) due to the dangling OH bond, which has not been seen in interstellar spectra. It is thus unlikely that this CO is mixed with H_2O. Mixtures of CO with CH_3OH, however, do reproduce the red component in both peak position and width (Cuppen et al. 2011). A mixture of CO and CH_3OH is also more likely, as CH_3OH is formed through hydrogenation of CO (Hiraoka et al. 1994, 2002; Watanabe & Kouchi 2002a; Hidaka et al. 2004; Watanabe et al. 2004; Fuchs et al. 2009).

In order to explain the solid-state CO_2 embedded in water-rich environments without invoking the need for CO embedded in H_2O ice, we look at the initial build-up of water ice on dust grains. Water can be formed through both gas-phase and solid-state pathways. However, the gas-phase ion-molecule chemistry produces only a fraction of the total observed water abundances, and thus water is mainly formed through the addition of hydrogen to atomic oxygen on the surface of dust grains (see reviews by van Dishoeck et al. 2014; Linnartz et al. 2015, and references therein). This formation process of solid-state H_2O takes place in the edges of molecular clouds at intermediate extinction (A_V). At this extinction, CO is already present, but still resides in the gas phase. For example, in the Taurus molecular cloud water ice is detected at a threshold extinction, that is, the extinction at which a species is detected in the solid state, of 3.2 ± 0.1 A_V, while for CO the threshold extinction was determined to be 6.7 ± 1.6 A_V (Whittet et al. 2001, 2010). Physical-chemical models of molecular clouds show that the dust-grain temperature at the edge of a cloud equals 31 K, with an external FUV field strength of 100 G_0, where G_0 is a scaling factor in multiples of the average local interstellar radiation field, which is indeed sufficient to keep CO in the gas phase (Hollenbach et al. 2009). For CO_2 to be mixed with H_2O it has to form simultaneously, and since CO is in the gas-phase during H_2O formation, CO_2 can be formed through the process described in this work. The OH radicals required for the conversion of CO into CO_2 are readily available in this region. They are the intermediate product to H_2O formation, and the external UV field is still sufficient at this extinction to photodissociate already existing H_2O molecules.

The solid-state CO_2 that is observed to be embedded in water-rich environment in the "Cores to Disks" program, has a relative average abundance w.r.t. H_2O of ~ 0.2. Assuming that roughly equal amounts of atomic oxygen go into CO and H_2O, this would imply that approximately 20% of the gas-phase CO would have to be converted into solid-state CO_2 to explain observed abundances. Inclusion of this pathway in physical-chemical models of molecular clouds is required to test how efficient this process is in low-density regions at interstellar timescales and explain the observed solid-state CO_2 abundances.

6.6 Conclusions

In this study we investigate the interaction of gas-phase CO with vacuum-UV irradiated water ice. The temperature of the water ice is varied between 40–120 K, and several control experiments are performed to narrow down the possible interpretations of the results. Our findings are summarized as follows:

1. The interaction between gas-phase CO and vacuum-UV irradiated water ice produces CO_2 up to 120 K. Solid-state CO_2 is observed in the temperature range 40–60 K. At 70 K or higher, the formed CO_2 is released into the gas phase, and above 90 K, O_2 formation is observed at the cost of CO_2 production.

2. CO has a significant residence time on water ice, even though it is above the canonical sublimation temperature of CO. In this short, but nonzero, residence time, each CO is able to diffuse between up to 7.2×10^{10} different binding sites before desorption occurs. This significant diffusion allows CO to find an OH radical, created by UV dissociation of H_2O, and form CO_2 in a Langmuir-Hinshelwood type reaction.

3. Given that gas-phase CO can only interact with the surface of the water ice, this includes pores exposed to the vacuum, we derived a conversion rate of 0.06 per *absorbed* photon in the reactive surface (i.e., three monolayers). The limiting factor in this conversion rate is the production of OH radicals.

4. It is unclear what sets the efficiency of 2–10% of produced CO_2 per absorbed UV photon in the reactive surface, given that no other products, such as H_2O_2, are observed and molecular dynamics calculations indicate that photodissocation is (close to) unity and reformation into H_2O is inefficient.

5. Understanding this process is important for astrophysical regions, such as molecular clouds and planet-forming disks. In clouds, this processs can explain the presence of solid-state CO_2 embedded in water-rich ices. In disks, it has been invoked to explain the lack of gas-phase CO, but our results suggest that the laboratory efficiency of the process falls short to significantly reduce the observed gas-phase CO in protoplanetary disks.

This work demonstrates the wide temperature efficacy of this gas and grain interaction process. Future work, should focus on further experimental and theoretical exploration of the molecular dynamics which include the effects of high fluxes and neighbouring OH radicals on the reforming of H_2O after photodissociation. Additionally, these processes should be included quantitatively in models of planet-forming disk chemistry and molecular clouds. With this work we show that gas and grain chemistry cannot be considered as fully separate, but that, under the right conditions, interaction of the gas with the icy surface results in observable effects.

Appendix

6.A UV spectrum

The spectral energy distribution of the MDHL used in this study is measured *in situ* with a VUV spectrometer (McPherson Model 234/302), which is mounted opposite to the MDHL on the other side of the main chamber. In this work a MgF_2 window was used that does not transmit Lyman-α photons, but does transmit the molecular hydrogen emission lines and continuum between 140–170 nm. The VUV spectrum with which the ASW is irradiated in our experiments is shown in Figure 6.7.

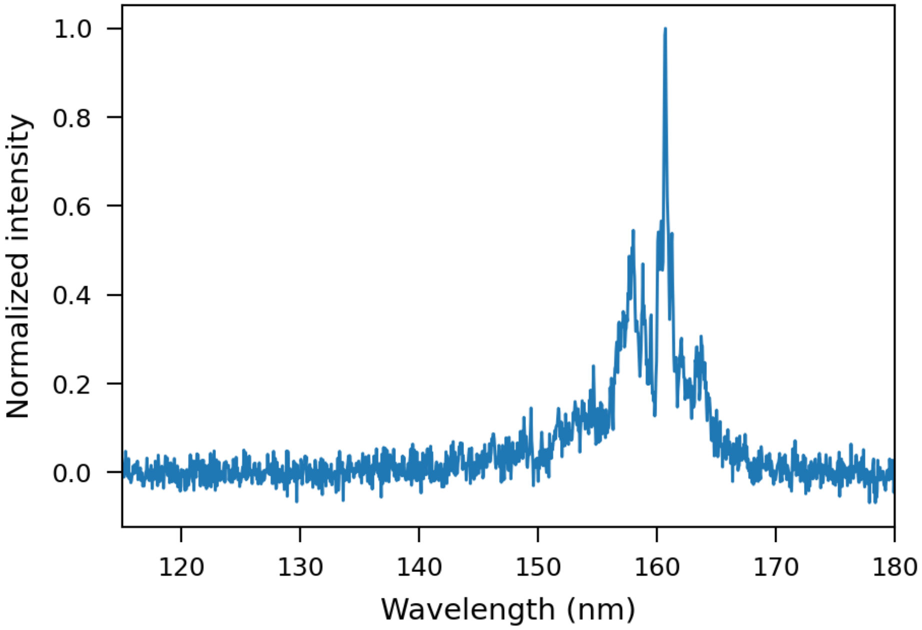

Figure 6.7: UV spectrum of the microwave discharge hydrogen lamp used in our work in combination with a MgF_2 window that absorbs Lyman-α.

6.B Additional experiments

The main experiments at 50, 60, 80, 90, 100, and 120 K and control experiments with ^{13}CO instead of $^{13}C^{18}O$, no VUV irradiation, and no gas-phase CO are presented in this appendix. Due to a nonlinear temperature artifact during TPD, the majority of the experiments show an unexpected and erroneous signal increase in the QMS TPD panels (d). This occurs approximately in the temperature range 120–150 K. In the caption of each figure the exact temperature range is given in which the QMS signals are not reliable.

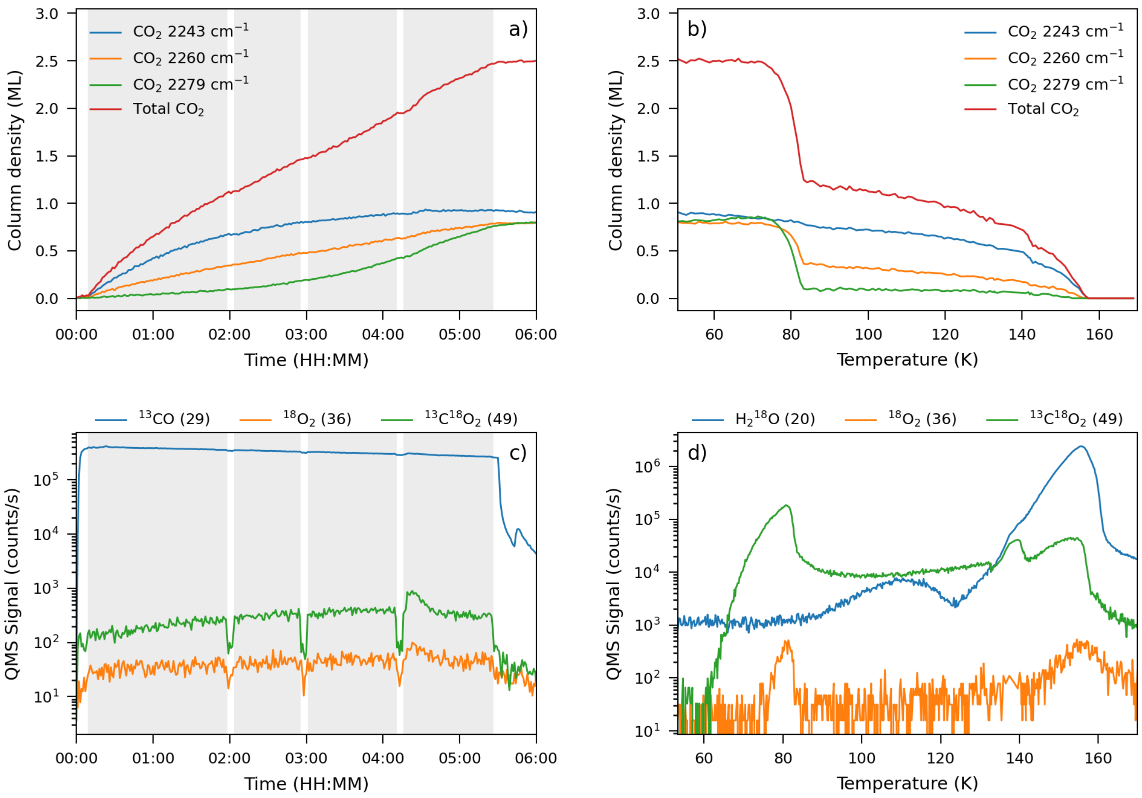

Figure 6.8: Results of the experiment of ASW at a temperature of 50 K. In the top row the deconvolved infrared components are given and in the bottom row the data for the quadrupole mass spectrometer (QMS) is presented. The left column shows data acquired during VUV irradiation (shaded area is with VUV shutter open) and on the right during temperature programmed desorption (TPD). ^{13}CO is shown in panel c), as measuring the main isotope ($^{13}C^{18}O$) would saturate the QMS and the ^{16}O isotope is present in the CO sample at a level of 5%. The increased signal in panel d) during the TPD between 130–140 K is due to nonlinear temperature artifact.

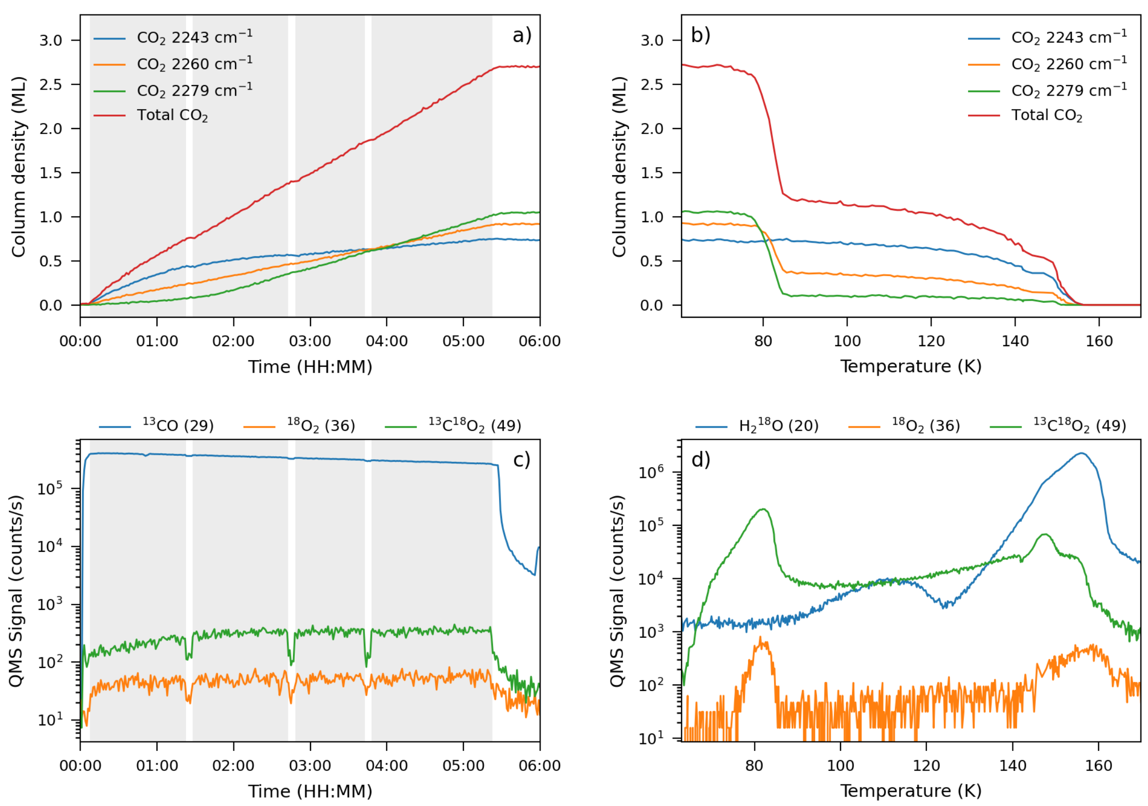

Figure 6.9: Results of the experiment of ASW at a temperature of 60 K. In the top row the deconvolved infrared components are given and in the bottom row the data for the quadrupole mass spectrometer (QMS) is presented. The left column shows data acquired during VUV irradiation (shaded area is with VUV shutter open) and on the right during temperature programmed desorption (TPD). ^{13}CO is shown in panel c), as measuring the main isotope (^{13}C^{18}O) would saturate the QMS and the ^{16}O isotope is present in the CO sample at a level of 5%. The increased signal in panel d) during the TPD between 140–150 K is due to nonlinear temperature artifact.

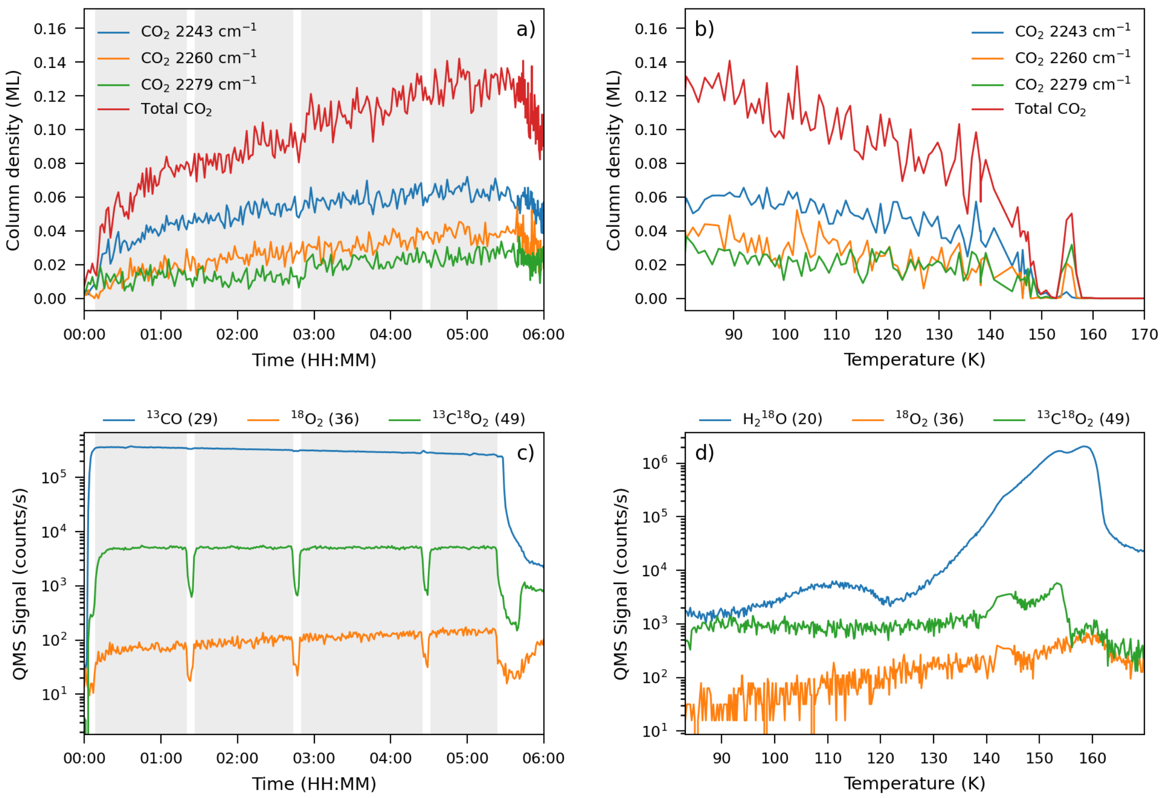

Figure 6.10: Results of the experiment of ASW at a temperature of 80 K. In the top row the deconvolved infrared components are given and in the bottom row the data for the quadrupole mass spectrometer (QMS) is presented. The left column shows data acquired during VUV irradiation (shaded area is with VUV shutter open) and on the right during temperature programmed desorption (TPD). ^{13}CO is shown in panel c), as measuring the main isotope ($^{13}C^{18}O$) would saturate the QMS and the ^{16}O isotope is present in the CO sample at a level of 5%. The increased signal in panel d) during the TPD between 140–150 K is due to nonlinear temperature artifact.

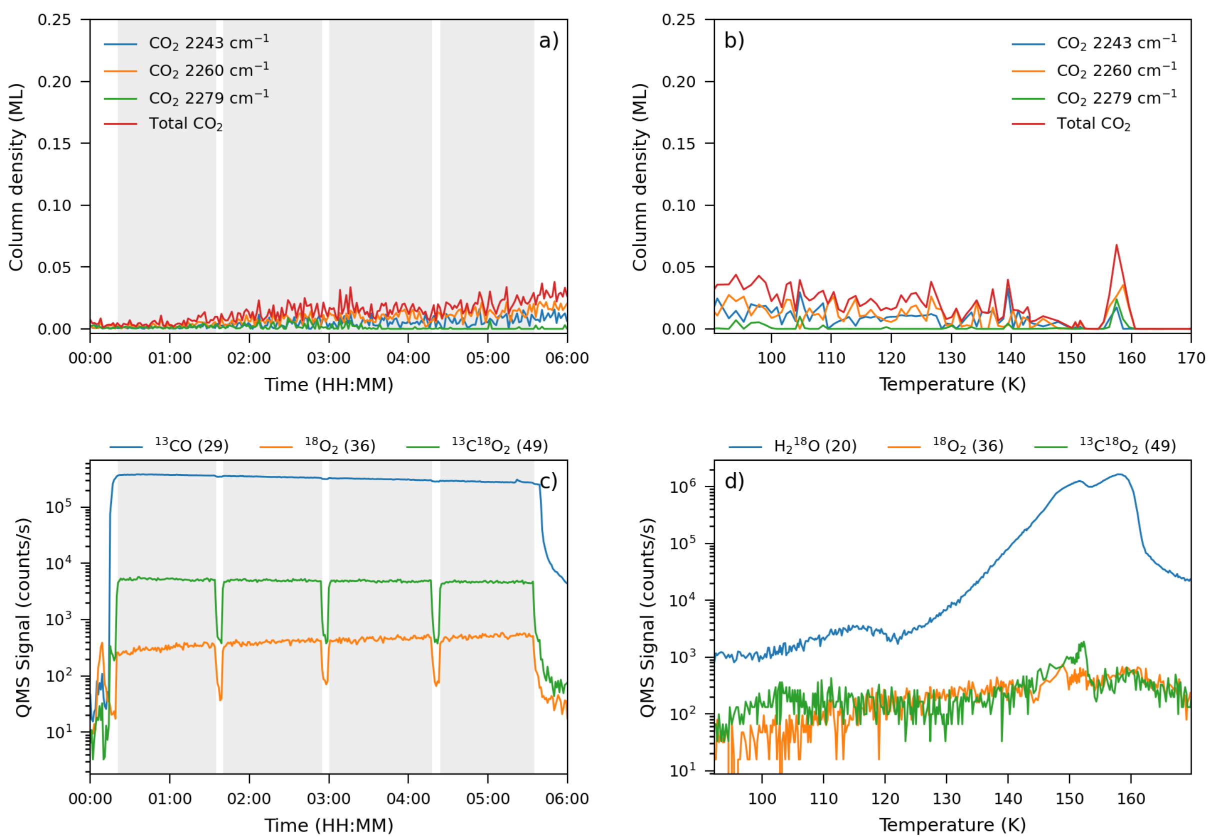

Figure 6.11: Results of the experiment of ASW at a temperature of 90 K. In the top row the deconvolved infrared components are given and in the bottom row the data for the quadrupole mass spectrometer (QMS) is presented. The left column shows data acquired during VUV irradiation (shaded area is with VUV shutter open) and on the right during temperature programmed desorption (TPD). ^{13}CO is shown in panel c), as measuring the main isotope (^{13}C^{18}O) would saturate the QMS and the ^{16}O isotope is present in the CO sample at a level of 5%.

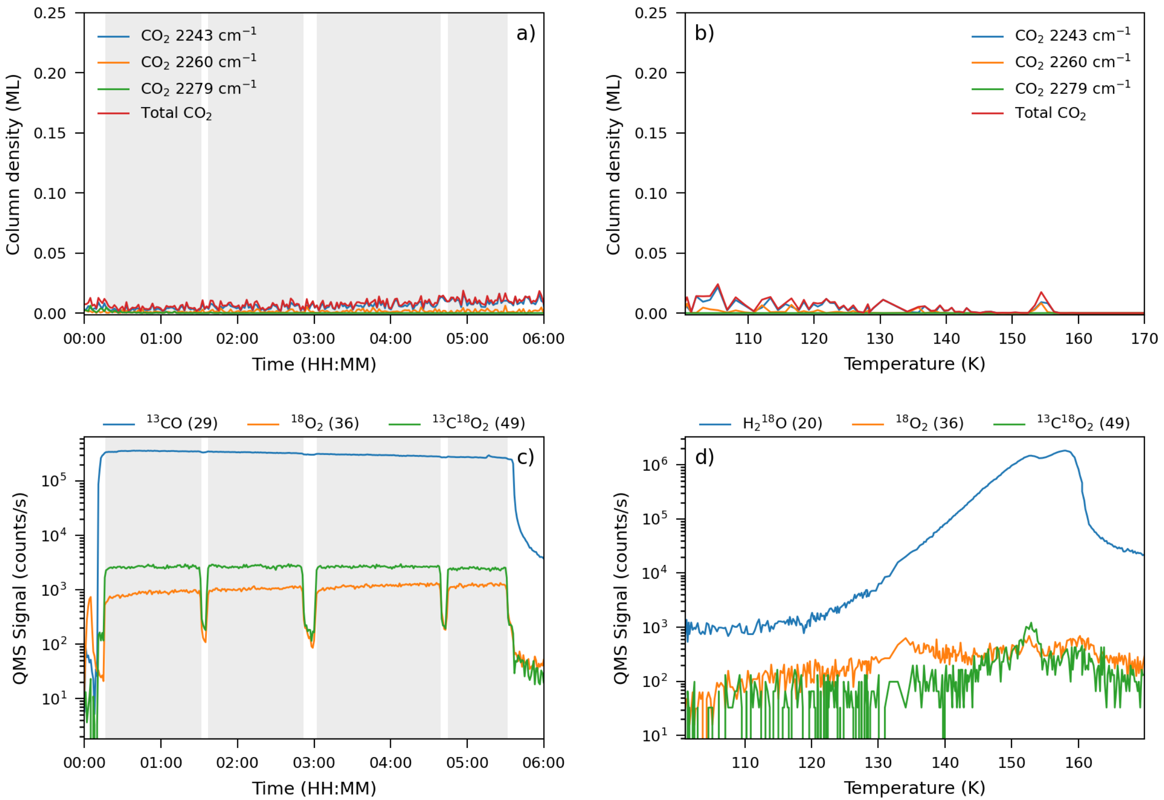

Figure 6.12: Results of the experiment of ASW at a temperature of 100 K. In the top row the deconvolved infrared components are given and in the bottom row the data for the quadrupole mass spectrometer (QMS) is presented. The left column shows data acquired during VUV irradiation (shaded area is with VUV shutter open) and on the right during temperature programmed desorption (TPD). ^{13}CO is shown in panel c), as measuring the main isotope (^{13}C^{18}O) would saturate the QMS and the ^{16}O isotope is present in the CO sample at a level of 5%. The increased signal in panel d) during the TPD between 130–140 K is due to nonlinear temperature artifact.

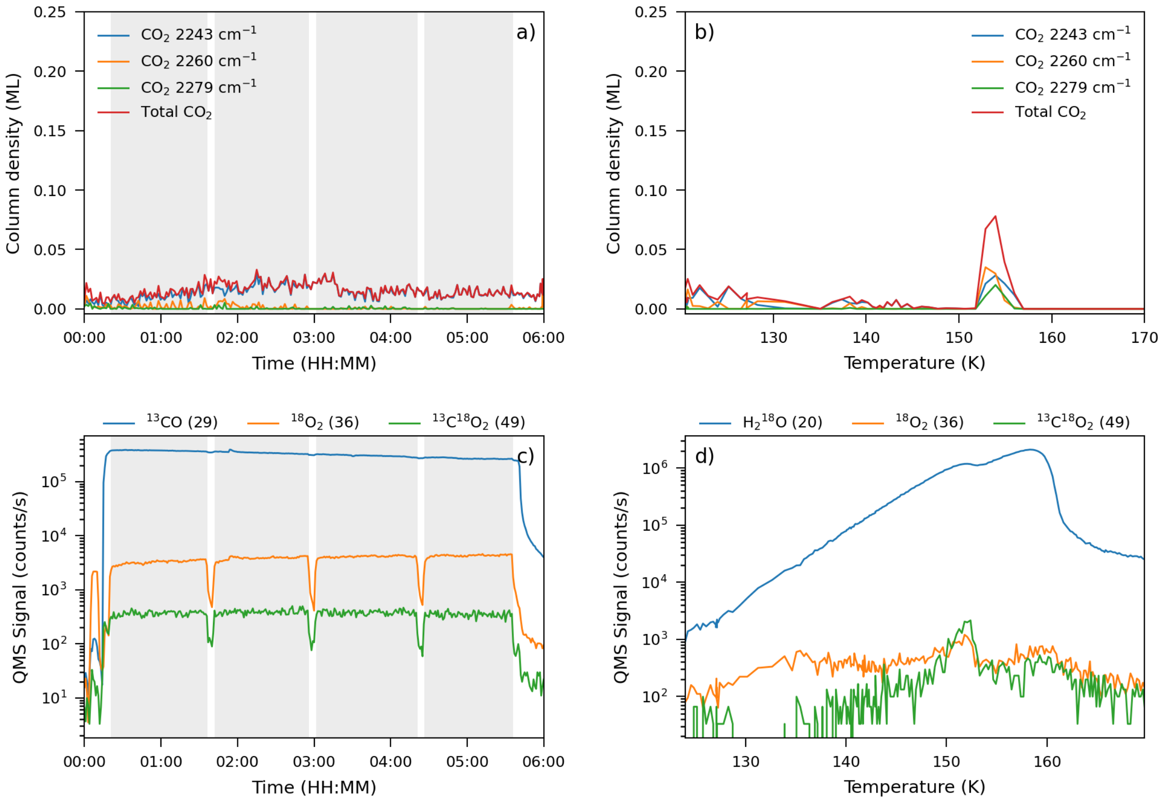

Figure 6.13: Results of the experiment of ASW at a temperature of 120 K. In the top row the deconvolved infrared components are given and in the bottom row the data for the quadrupole mass spectrometer (QMS) is presented. The left column shows data acquired during VUV irradiation (shaded area is with VUV shutter open) and on the right during temperature programmed desorption (TPD). ^{13}CO is shown in panel c), as measuring the main isotope ($^{13}C^{18}O$) would saturate the QMS and the ^{16}O isotope is present in the CO sample at a level of 5%. The increased signal in panel d) during the TPD between 130–140 K is due to nonlinear temperature artifact.

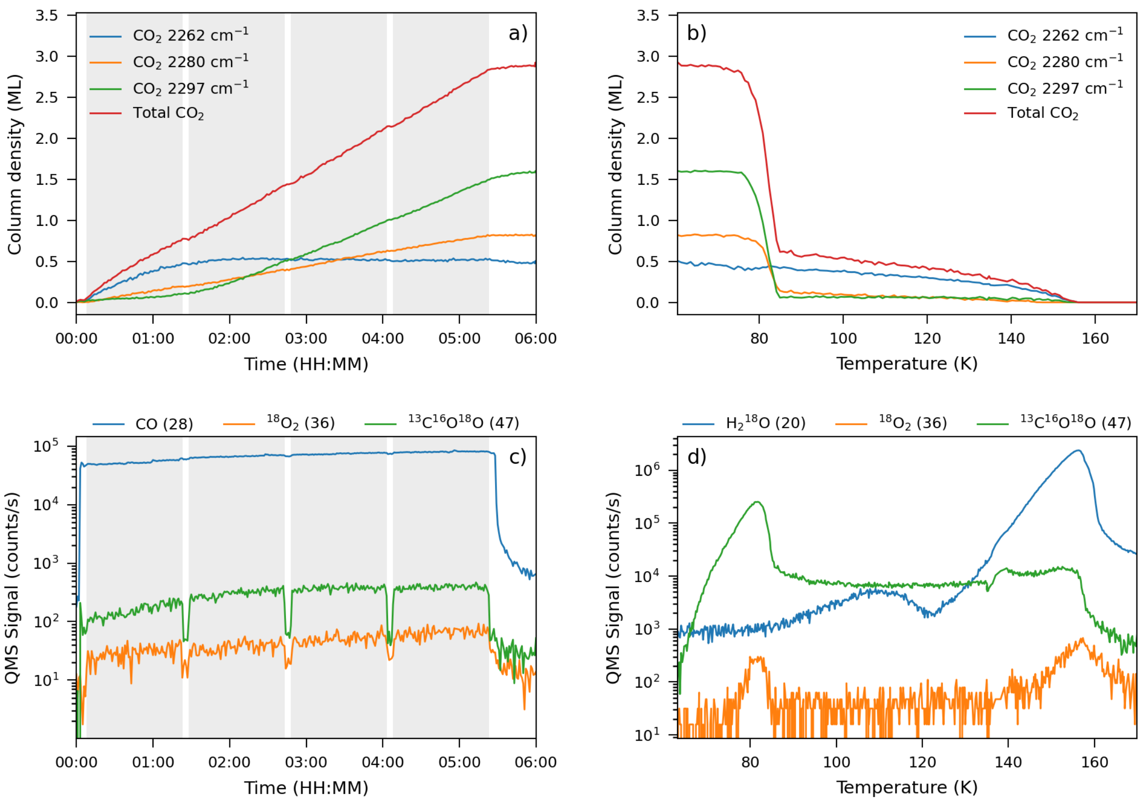

Figure 6.14: Results of the experiment of ASW at a temperature of 60 K with isotopic ^{13}CO instead of ^{13}C^{18}O. In the top row the deconvolved infrared components are given and in the bottom row the data for the quadrupole mass spectrometer (QMS) is presented. The left column shows data acquired during VUV irradiation (shaded area is with VUV shutter open) and on the right during temperature programmed desorption (TPD). ^{12}CO is shown in panel c), as measuring the main isotope (^{13}CO) would saturate the QMS and the ^{16}O isotope is present in the CO sample at a level of 5%. The increased signal in panel d) during the TPD between 130–140 K is due to nonlinear temperature artifact.

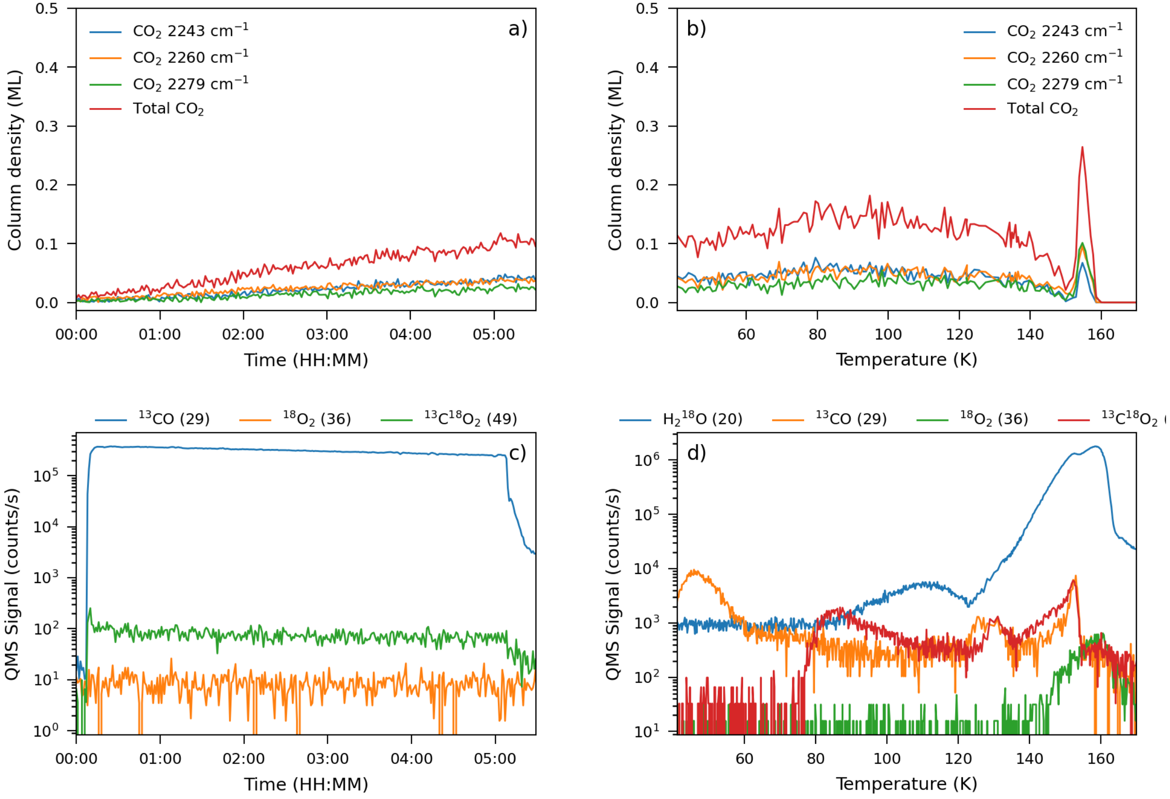

Figure 6.15: Results of the experiment of ASW at a temperature of 40 K without VUV irradiation. In the top row the deconvolved infrared components are given and in the bottom row the data for the quadrupole mass spectrometer (QMS) is presented. The left column shows data acquired during VUV irradiation (shaded area is with VUV shutter open) and on the right during temperature programmed desorption (TPD). ^{13}CO is shown in panel c), as measuring the main isotope ($^{13}C^{18}O$) would saturate the QMS and the ^{16}O isotope is present in the CO sample at a level of 5%.

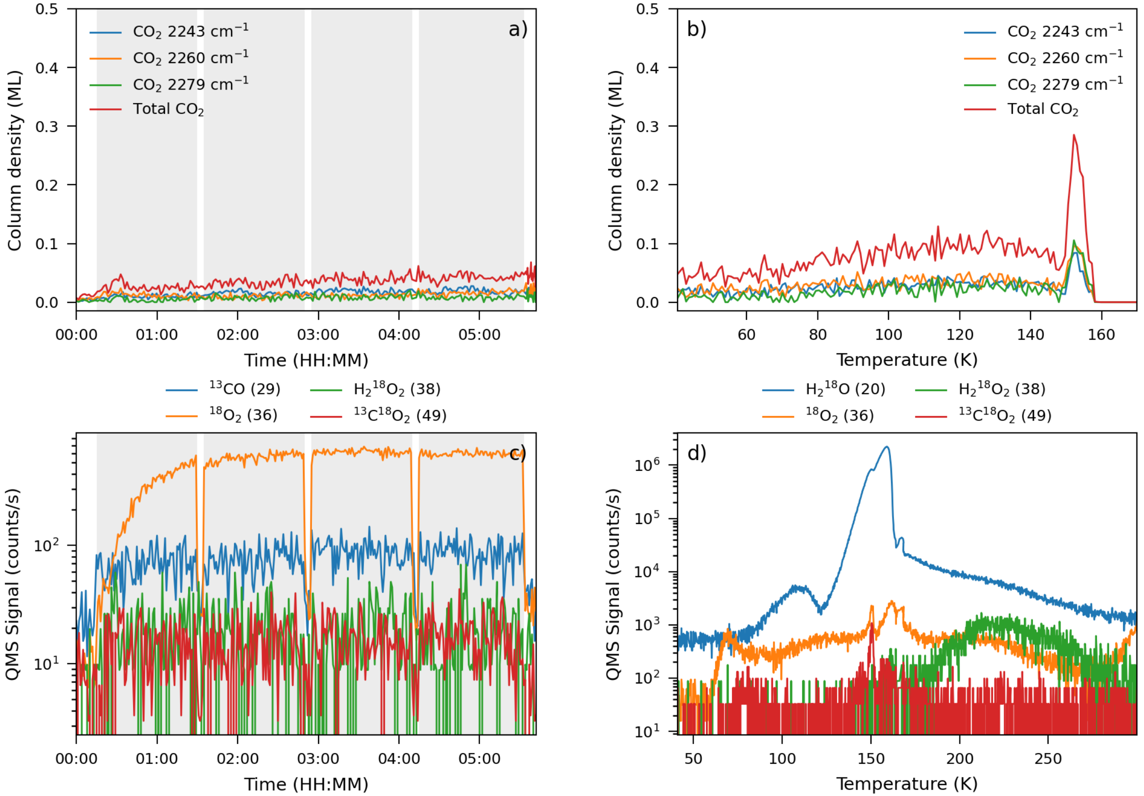

Figure 6.16: Results of the experiment of ASW at a temperature of 40 K without gas-phase CO. In the top row the deconvolved infrared components are given and in the bottom row the data for the quadrupole mass spectrometer (QMS) is presented. The left column shows data acquired during VUV irradiation (shaded area is with VUV shutter open) and on the right during temperature programmed desorption (TPD). TPD is now shown up until 300 K to show the desorption of H_2O_2. ^{13}CO is shown in panel c), to verify that indeed no significant amount of CO is in the gas phase during VUV irradiation.

BIBLIOGRAPHY

Aikawa, Y., Momose, M., Thi, W.-F., et al. 2003, PASJ, 55, 11

Aikawa, Y., van Zadelhoff, G. J., van Dishoeck, E. F., & Herbst, E. 2002, A&A, 386, 622

Akiyama, E., Muto, T., Kusakabe, N., et al. 2015, ApJ, 802, L17

Al-Refaie, A. F., Yachmenev, A., Tennyson, J., & Yurchenko, S. N. 2015, MNRAS, 448, 1704

Allan, A., McKean, D. C., Perchard, J.-P., & Josien, M.-L. 1971, Spectrochim. Act. Part A: Molec. Spectrosc., 27, 1409

Altwegg, K., Balsiger, H., Bar-Nun, A., et al. 2016, Sci. Adv., 2, e1600285

Altwegg, K., Balsiger, H., Berthelier, J. J., et al. 2017, MNRAS, 469, S130

Altwegg, K., Balsiger, H., & Fuselier, S. A. 2019, ARA&A, 57, 113

Andersson, S. & van Dishoeck, E. F. 2008, A&A, 491, 907

Andrews, S. M. 2020, ARA&A, 58, 483

Andrews, S. M., Huang, J., Pérez, L. M., et al. 2018, ApJ, 869, L41

Andrews, S. M., Wilner, D. J., Hughes, A. M., et al. 2012, ApJ, 744, 162

Andrews, S. M., Wilner, D. J., Zhu, Z., et al. 2016, ApJ, 820, L40

Ansdell, M., Williams, J. P., van der Marel, N., et al. 2016, ApJ, 828, 46

Arasa, C., van Hemert, M. C., van Dishoeck, E. F., & Kroes, G. J. 2013, J. Phys. Chem. A., 117, 7064

Atkinson, R., Baulch, D. L., Cox, R. A., et al. 2006, Atmos. Chem. Phys., 6, 3625

Bacmann, A., Taquet, V., Faure, A., Kahane, C., & Ceccarelli, C. 2012, A&A, 541, L12

Balucani, N., Ceccarelli, C., & Taquet, V. 2015, MNRAS, 449, L16

Baratta, G. A. & Palumbo, M. E. 1998, J. Opt. Soc. Am., 15, 3076

Baratta, G. A., Palumbo, M. E., & Strazzulla, G. 2000, A&A, 357, 1045

Barnes, A. J. & Hallam, H. E. 1970, Transactions of the Faraday Society, 66, 1932

Belloche, A., Müller, H. S. P., Menten, K. M., Schilke, P., & Comito, C. 2013, A&A, 559, A47

Bennett, C. J., Chen, S.-H., Sun, B.-J., Chang, A. H. H., & Kaiser, R. I. 2007, ApJ, 660, 1588

Bennett, C. J., Jamieson, C. S., & Kaiser, R. I. 2009, Phys. Chem. Chem. Phys. Incorporat. Faraday Transac., 11, 4210

Bennett, C. J. & Kaiser, R. I. 2007, ApJ, 661, 899

Bergantini, A., Maksyutenko, P., & Kaiser, R. I. 2017, ApJ, 841, 96

Bergin, E. A. & Cleeves, L. I. 2018, Chemistry During the Gas-Rich Stage of Planet Formation (Springer), 137

Bergin, E. A., Cleeves, L. I., Gorti, U., et al. 2013, Nature, 493, 644

Bergner, J. B., Guzmán, V. G., Öberg, K. I., Loomis, R. A., & Pegues, J. 2018, ApJ, 857, 69

Bergner, J. B., Öberg, K. I., Garrod, R. T., & Graninger, D. M. 2017, ApJ, 841, 120

Bisschop, S. E., Fuchs, G. W., van Dishoeck, E. F., & Linnartz, H. 2007a, A&A, 474, 1061

Bisschop, S. E., Jørgensen, J. K., van Dishoeck, E. F., & de Wachter, E. B. M. 2007b, A&A, 465, 913

Boamah, M. D., Sullivan, K. K., Shulenberger, K. E., et al. 2014, Faraday Discussions, 168, 249

Bøgelund, E. G., Barr, A. G., Taquet, V., et al. 2019a, A&A, 628, A2

Bøgelund, E. G., McGuire, B. A., Hogerheijde, M. R., van Dishoeck, E. F., & Ligterink, N. F. W. 2019b, A&A, 624, A82

Bøgelund, E. G., McGuire, B. A., Ligterink, N. F. W., et al. 2018, A&A, 615, A88

Boogert, A. C. A., Gerakines, P. A., & Whittet, D. C. B. 2015, ARA&A, 53, 541

Boogert, A. C. A., Hogerheijde, M. R., & Blake, G. A. 2002, ApJ, 568, 761

Boogert, A. C. A., Huard, T. L., Cook, A. M., et al. 2011, ApJ, 729, 92

Boogert, A. C. A., Pontoppidan, K. M., Knez, C., et al. 2008, ApJ, 678, 985

Boogert, A. C. A., Schutte, W. A., Tielens, A. G. G. M., et al. 1996, A&A, 315, L377

Booth, A. S., Walsh, C., Terwisscha van Scheltinga, J., et al. 2021, Nature Astronomy, 5, 684

Bosman, A. D., Walsh, C., & van Dishoeck, E. F. 2018, A&A, 618, A182

Bossa, J. B., Isokoski, K., de Valois, M. S., & Linnartz, H. 2012, A&A, 545, A82

Bossa, J.-B., Maté, B., Fransen, C., et al. 2015, ApJ, 814, 47

Boudin, N., Schutte, W. A., & Greenberg, J. M. 1998, A&A, 331, 749

Bouilloud, M., Fray, N., Bénilan, Y., et al. 2015, MNRAS, 451, 2145

Bregman, J. D., Hayward, T. L., & Sloan, G. C. 2000, ApJ, 544, L75

Briggs, D. S. 1995, in American Astronomical Society Meeting Abstracts, Vol. 187, American Astronomical Society Meeting Abstracts, 112.02

Buntkowsky, G., Limbach, H.-H., Walaszek, B., et al. 2008, Z. Phys. Chem., 222, 1049

Calahan, J. K., Bergin, E., Zhang, K., et al. 2021, ApJ, 908, 8

Carney, M. T., Hogerheijde, M. R., Guzmán, V. V., et al. 2019, A&A, 623, A124

Carney, M. T., Hogerheijde, M. R., Loomis, R. A., et al. 2017, A&A, 605, A21

Caselli, P. & Ceccarelli, C. 2012, A&A Rev., 20, 56

Caselli, P., Hasegawa, T. I., & Herbst, E. 1993, ApJ, 408, 548

Cazaux, S., Tielens, A. G. G. M., Ceccarelli, C., et al. 2003, ApJ, 593, L51

Cazzoletti, P., van Dishoeck, E. F., Visser, R., Facchini, S., & Bruderer, S. 2018, A&A, 609, A93

Ceccarelli, C., Caselli, P., Fontani, F., et al. 2017, ApJ, 850, 176

Cernicharo, J., Marcelino, N., Roueff, E., et al. 2012, ApJ, 759, L43

Charnley, S. B. 2004, Adv. Space Res., 33, 23

Charnley, S. B., Kress, M. E., Tielens, A. G. G. M., & Millar, T. J. 1995, ApJ, 448, 232

Charnley, S. B. & Rodgers, S. D. 2005, in IAU Symposium, Vol. 231, Astrochemistry: Recent Successes and Current Challenges, ed. D. C. Lis, G. A. Blake, & E. Herbst, 237–246

Chuang, K. J., Fedoseev, G., Ioppolo, S., van Dishoeck, E. F., & Linnartz, H. 2016, MNRAS, 455, 1702

Chuang, K. J., Fedoseev, G., Qasim, D., et al. 2017, MNRAS, 467, 2552

Cleeves, L. I., Bergin, E. A., Qi, C., Adams, F. C., & Öberg, K. I. 2015, ApJ, 799, 204

Cleeves, L. I., Öberg, K. I., Wilner, D. J., et al. 2016, ApJ, 832, 110

Cornwell, T. J. 2008, IEEE J. Sel. Top. Signal Process., 2, 793

Coussan, S., Bouteiller, Y., & Perchard, J. P. 1998, Spectrochim. Act. Part A: Molec. Spectrosc., 102, 5789

Cruz-Diaz, G. A., Muñoz Caro, G. M., Chen, Y. J., & Yih, T. S. 2014, A&A, 562, A119

Cuppen, H. M., Penteado, E. M., Isokoski, K., van der Marel, N., & Linnartz, H. 2011, MNRAS, 417, 2809

Dartois, E., Schutte, W., Geballe, T. R., et al. 1999, A&A, 342, L32

Dawes, A., Mukerji, R. J., Davis, M. P., et al. 2007, J. Chem. Phys., 126, 244711

de Barros, A. L. F., Domaracka, A., Andrade, D. P. P., et al. 2011, MNRAS, 418, 1363

Do-Duy, T., Wright, C. M., Fujiyoshi, T., et al. 2020, MNRAS, 493, 4463

Dulieu, F., Amiaud, L., Congiu, E., et al. 2010, A&A, 512, A30

Dullemond, C. P. & Dominik, C. 2004, A&A, 421, 1075

Dutrey, A., Guilloteau, S., & Guelin, M. 1997, A&A, 317, L55

Ehrenfreund, P. & Charnley, S. B. 2000, ARA&A, 38, 427

Evans, J. & Bernstein, H. 1956, Can. J. Chem., 34

Fayolle, E. C., Bertin, M., Romanzin, C., et al. 2013, A&A, 556, A122

Fedoseev, G., Chuang, K. J., Ioppolo, S., et al. 2017, ApJ, 842, 52

Fedoseev, G., Cuppen, H. M., Ioppolo, S., Lamberts, T., & Linnartz, H. 2015a, MNRAS, 448, 1288

Fedoseev, G., Ioppolo, S., Zhao, D., Lamberts, T., & Linnartz, H. 2015b, MNRAS, 446, 439

Fillion, J.-H., Fayolle, E. C., Michaut, X., et al. 2014, Faraday Discussions, 168, 533

Flaherty, K. M., Hughes, A. M., Teague, R., et al. 2018, ApJ, 856, 117

Fockenberg, C. & Preses, J. M. 2002, J. Phys. Chem. A., 106, 2924

Foreman-Mackey, D., Hogg, D. W., Lang, D., & Goodman, J. 2013, PASP, 125, 306

Fuchs, G. W., Cuppen, H. M., Ioppolo, S., et al. 2009, A&A, 505, 629

Gaia Collaboration, Brown, A. G. A., Vallenari, A., et al. 2018, A&A, 616, A1

Garrod, R. T. 2013, ApJ, 765, 60

Garufi, A., Podio, L., Codella, C., et al. 2020, A&A, 636, A65

Gerakines, P. A. & Hudson, R. L. 2020, ApJ, 901, 52

Gerakines, P. A., Schutte, W. A., & Ehrenfreund, P. 1996, A&A, 312, 289

Gibb, E., Nummelin, A., Irvine, W. M., Whittet, D. C. B., & Bergman, P. 2000a, ApJ, 545, 309

Gibb, E. L. & Whittet, D. C. B. 2002, ApJ, 566, L113

Gibb, E. L., Whittet, D. C. B., Schutte, W. A., et al. 2000b, ApJ, 536, 347

Gillett, F. C. & Forrest, W. J. 1973, ApJ, 179, 483

Goesmann, F., Rosenbauer, H., Bredehöft, J. H., et al. 2015, Science, 349

Goldsmith, P. F. & Langer, W. D. 1999, ApJ, 517, 209

Goumans, T. P. M. & Andersson, S. 2010, MNRAS, 406, 2213

Goumans, T. P. M., Uppal, M. A., & Brown, W. A. 2008, MNRAS, 384, 1158

Guzmán, V. V., Öberg, K. I., Carpenter, J., et al. 2018, ApJ, 864, 170

Hama, T., Kouchi, A., & Watanabe, N. 2018, ApJ, 857, L13

Hama, T., Yabushita, A., Yokoyama, M., Kawasaki, M., & Andersson, S. 2009, J. Chem. Phys., 131, 054508

He, J., Acharyya, K., & Vidali, G. 2016a, ApJ, 825, 89

He, J., Acharyya, K., & Vidali, G. 2016b, ApJ, 823, 56

He, J., Emtiaz, S. M., & Vidali, G. 2017, ApJ, 837, 65

Herbst, E. & van Dishoeck, E. F. 2009, ARA&A, 47, 427

Hidaka, H., Watanabe, M., Kouchi, A., & Watanabe, N. 2011, Phy. Chem. Chem. Phys., 13, 15798

Hidaka, H., Watanabe, N., Shiraki, T., Nagaoka, A., & Kouchi, A. 2004, ApJ, 614, 1124

Hiraoka, K., Ohashi, N., Kihara, Y., et al. 1994, Chem. Phys. Lett., 229, 408

Hiraoka, K., Sato, T., Sato, S., et al. 2002, ApJ, 577, 265

Hiraoka, K., Yamashita, A., Yachi, Y., et al. 1995, ApJ, 443, 363

Högbom, J. A. 1974, A&AS, 15, 417

Hogerheijde, M. R., Bergin, E. A., Brinch, C., et al. 2011, Science, 334, 338

Hollenbach, D., Kaufman, M. J., Bergin, E. A., & Melnick, G. J. 2009, ApJ, 690, 1497

Hollenstein, H. & Günthard, H. H. 1971, Spectrochim. Act. Part A: Molec. Spectrosc., 27, 2027

Horn, A., Møllendal, H., Sekiguchi, O., et al. 2004, ApJ, 611, 605

Huang, J., Andrews, S. M., Cleeves, L. I., et al. 2018, ApJ, 852, 122

Hudgins, D. M., Sandford, S. A., Allamandola, L. J., & Tielens, A. G. G. M. 1993, ApJS, 86, 713

Hudson, R. L. 2017, Spectrochim. Act. Part A: Molec. Spectrosc., 187, 82

Hudson, R. L. & Ferrante, R. F. 2020, MNRAS, 492, 283

Hudson, R. L., Gerakines, P. A., & Ferrante, R. F. 2018, Spectrochim. Act. Part A: Molec. Spectrosc., 193, 33

Hudson, R. L., Yarnall, Y. Y., & Coleman, F. M. 2020, Spectrochim. Act. Part A: Molec. Spectrosc., 233, 118217

Inostroza-Pino, N., Mardones, D., Ge, J. J. X., & MacLeod-Carey, D. 2020, A&A, 641, A14

Ioppolo, S., Fedoseev, G., Chuang, K. J., et al. 2021, Nature Astronomy, 5, 197

Ioppolo, S., Fedoseev, G., Lamberts, T., Romanzin, C., & Linnartz, H. 2013, Rev. Sci. Instrum., 84, 073112

Ioppolo, S., Palumbo, M. E., Baratta, G. A., & Mennella, V. 2009, A&A, 493, 1017

Ioppolo, S., van Boheemen, Y., Cuppen, H. M., van Dishoeck, E. F., & Linnartz, H. 2011, MNRAS, 413, 2281

Isella, A., Guidi, G., Testi, L., et al. 2016, Phys. Rev. Lett., 117, 251101

Isokoski, K., Bossa, J. B., Triemstra, T., & Linnartz, H. 2014, Phys. Chem. Chem. Phys. Incorporat. Faraday Transac., 16, 3456

Jamieson, C. S., Mebel, A. M., & Kaiser, R. I. 2006, ApJS, 163, 184

Jin, M. & Garrod, R. T. 2020, ApJS, 249, 26

Jørgensen, J. K., van der Wiel, M. H. D., Coutens, A., et al. 2016, A&A, 595, A117

Kahane, C., Frerking, M. A., Langer, W. D., Encrenas, P., & Lucas, R. 1984, A&A, 137, 211

Kama, M., Bruderer, S., van Dishoeck, E. F., et al. 2016, A&A, 592, A83

Kama, M., Trapman, L., Fedele, D., et al. 2020, A&A, 634, A88

Kastner, J. H., Qi, C., Dickson-Vandervelde, D. A., et al. 2018, ApJ, 863, 106

Keane, J. V., Tielens, A. G. G. M., Boogert, A. C. A., Schutte, W. A., & Whittet, D. C. B. 2001, A&A, 376, 254

Kemper, F., Vriend, W. J., & Tielens, A. G. G. M. 2004, ApJ, 609, 826

Kessler, M. F., Steinz, J. A., Anderegg, M. E., et al. 1996, A&A, 315, L27

Kessler-Silacci, J. E., Hillenbrand, L. A., Blake, G. A., & Meyer, M. R. 2005, ApJ, 622, 404

Kouchi, A., Furuya, K., Hama, T., et al. 2020, ApJ, 891, L22

Lamberts, T., Cuppen, H. M., Fedoseev, G., et al. 2014, A&A, 570, A57

Lamberts, T., Cuppen, H. M., Ioppolo, S., & Linnartz, H. 2013, Phys. Chem. Chem. Phys., 15, 8287

Larson, R. B. 2003, Rep. Prog. Phys., 66, 1651

Lebouteiller, V., Barry, D. J., Goes, C., et al. 2015, ApJS, 218, 21

Lebouteiller, V., Barry, D. J., Spoon, H. W. W., et al. 2011, ApJS, 196, 8

Lee, J.-E., Lee, S., Baek, G., et al. 2019, Nature Astronomy, 3, 314

Lehmann, B., Wahlen, M., Zumbrunn, R., Oeschger, H., & Schnell, W. 1977, Appl. Phys., 13, 153

Ligterink, N. F. W. 2017, PhD thesis, University of Leiden

Ligterink, N. F. W., Coutens, A., Kofman, V., et al. 2017, MNRAS, 469, 2219

Ligterink, N. F. W., Paardekooper, D. M., Chuang, K. J., et al. 2015, A&A, 584, A56

Ligterink, N. F. W., Terwisscha van Scheltinga, J., Taquet, V., et al. 2018a, MNRAS, 480, 3628

Ligterink, N. F. W., Walsh, C., Bhuin, R. G., et al. 2018b, A&A, 612, A88

Limbach, H.-H., Buntkowsky, G., Matthes, J., et al. 2006, ChemPhysChem, 7, 551

Linnartz, H., Bossa, J.-B., Bouwman, J., et al. 2011, in IAU Symposium, Vol. 280, The Molecular Universe, 390–404

Linnartz, H., Ioppolo, S., & Fedoseev, G. 2015, Int. Rev. Phys. Chem., 34, 205

Loeffler, M. J., Baratta, G. A., Palumbo, M. E., Strazzulla, G., & Baragiola, R. A. 2005, A&A, 435, 587

Loomis, R. A., Cleeves, L. I., Öberg, K. I., et al. 2018, ApJ, 859, 131

Loomis, R. A., Cleeves, L. I., Öberg, K. I., Guzman, V. V., & Andrews, S. M. 2015, ApJ, 809, L25

Loomis, R. A., Öberg, K. I., Andrews, S. M., & MacGregor, M. A. 2017, ApJ, 840, 23

Madzunkov, S., Shortt, B. J., Macaskill, J. A., Darrach, M. R., & Chutjian, A. 2006, Phys. Rev., 73, 020901

Maity, S., Kaiser, R. I., & Jones, B. M. 2015, Phys. Chem. Chem. Phys. Incorporat. Faraday Transac., 17, 3081

Manigand, S., Jørgensen, J. K., Calcutt, H., et al. 2020, A&A, 635, A48

Martín-Doménech, R., Manzano-Santamaría, J., Muñoz Caro, G. M., et al. 2015, A&A, 584, A14

McClure, M. K., Bergin, E. A., Cleeves, L. I., et al. 2016, ApJ, 831, 167

McGuire, B. A. 2018, ApJS, 239, 17

McGuire, B. A., Shingledecker, C. N., Willis, E. R., et al. 2017, ApJ, 851, L46

McMullin, J. P., Waters, B., Schiebel, D., Young, W., & Golap, K. 2007, in Astronomical Society of the Pacific Conference Series, Vol. 376, Astronomical Data Analysis Software and Systems XVI, ed. R. A. Shaw, F. Hill, & D. J. Bell, 127

Mikawa, Y., Brasch, J., & Jakobsen, R. 1971, Spectrochim. Act. Part A: Molec. Spectrosc., 27, 529

Millar, T. J., Herbst, E., & Charnley, S. B. 1991, ApJ, 369, 147

Milligan, D. E. & Jacox, M. E. 1971, J. Chem. Phys., 54, 927

Minissale, M., Congiu, E., & Dulieu, F. 2016, A&A, 585, A146

Minissale, M., Congiu, E., Manicò, G., Pirronello, V., & Dulieu, F. 2013, A&A, 559, A49

Minissale, M., Loison, J. C., Baouche, S., et al. 2015, A&A, 577, A2

Miotello, A., Bruderer, S., & van Dishoeck, E. F. 2014, A&A, 572, A96

Miotello, A., van Dishoeck, E. F., Kama, M., & Bruderer, S. 2016, A&A, 594, A85

Miotello, A., van Dishoeck, E. F., Williams, J. P., et al. 2017, A&A, 599, A113

Miyauchi, N., Hidaka, H., Chigai, T., et al. 2008, Chem. Phys. Lett., 456, 27

Modica, P. & Palumbo, M. E. 2010, A&A, 519, A22

Modica, P., Palumbo, M. E., & Strazzulla, G. 2012, Planet. Space Sci., 73, 425

Muñoz Caro, G. M., Dartois, E., Boduch, P., et al. 2014, A&A, 566, A93

Müller, H. S. P., Belloche, A., Xu, L.-H., et al. 2016, A&A, 587, A92

Nazari, P., van Gelder, M. L., van Dishoeck, E. F., et al. 2021, A&A, 650, A150

Noble, J. A., Dulieu, F., Congiu, E., & Fraser, H. J. 2011, ApJ, 735, 121

Noble, J. A., Theule, P., Mispelaer, F., et al. 2012, A&A, 543, A5

Oba, Y., Miyauchi, N., Hidaka, H., et al. 2009, ApJ, 701, 464

Oba, Y., Watanabe, N., Hama, T., et al. 2012, ApJ, 749, 67

Oba, Y., Watanabe, N., Kouchi, A., Hama, T., & Pirronello, V. 2010, ApJ, 712, L174

Oba, Y., Watanabe, N., Kouchi, A., Hama, T., & Pirronello, V. 2011, Phys. Chem. Chem. Phys. Incorporat. Faraday Transac., 13, 15792

Öberg, K. I. 2016, Chem. Rev., 116, 9631

Öberg, K. I. & Bergin, E. A. 2021, Phys. Rep., 893, 1

Öberg, K. I., Boogert, A. C. A., Pontoppidan, K. M., et al. 2011, ApJ, 740, 109

Öberg, K. I., Bottinelli, S., Jørgensen, J. K., & van Dishoeck, E. F. 2010, ApJ, 716, 825

Öberg, K. I., Fayolle, E. C., Cuppen, H. M., van Dishoeck, E. F., & Linnartz, H. 2009a, A&A, 505, 183

Öberg, K. I., Fraser, H. J., Boogert, A. C. A., et al. 2007, A&A, 462, 1187

Öberg, K. I., Garrod, R. T., van Dishoeck, E. F., & Linnartz, H. 2009b, A&A, 504, 891

Öberg, K. I., Guzmán, V. V., Furuya, K., et al. 2015, Nature, 520, 198

Öberg, K. I., Guzmán, V. V., Merchantz, C. J., et al. 2017, ApJ, 839, 43

Öberg, K. I., van Broekhuizen, F., Fraser, H. J., et al. 2005, ApJ, 621, L33

Öberg, K. I., van Dishoeck, E. F., & Linnartz, H. 2009c, A&A, 496, 281

Palumbo, M. E. 2005, in Journal of Physics Conference Series, Vol. 6, J. Phys. Conf. Ser., 211–216

Palumbo, M. E., Baratta, G. A., Brucato, J. R., et al. 1998, A&A, 334, 247

Palumbo, M. E., Baratta, G. A., Collings, M. P., & McCoustra, M. R. S. 2006, Phys. Chem. Chem. Phys., 8, 279

Palumbo, M. E., Tielens, A. G. G. M., & Tokunaga, A. T. 1995, ApJ, 449, 674

Pegues, J., Öberg, K. I., Bergner, J. B., et al. 2020, ApJ, 890, 142

Penteado, E. M., Boogert, A. C. A., Pontoppidan, K. M., et al. 2015, MNRAS, 454, 531

Plyler, E. 1952, J. Res. Natl. Inst. Stand. Technol., 4, 281

Podio, L., Bacciotti, F., Fedele, D., et al. 2019, A&A, 623, L6

Podio, L., Garufi, A., Codella, C., et al. 2020, A&A, 642, L7

Pontoppidan, K. M. 2006, A&A, 453, L47

Pontoppidan, K. M., Boogert, A. C. A., Fraser, H. J., et al. 2008, ApJ, 678, 1005

Pontoppidan, K. M., Fraser, H. J., Dartois, E., et al. 2003, A&A, 408, 981

Posselt, W., Holota, W., Kulinyak, E., et al. 2004, in Proc. SPIE, Vol. 5487, Optical, Infrared, and Millimeter Space Telescopes, ed. J. C. Mather, 688–697

Qi, C., Öberg, K. I., & Wilner, D. J. 2013, ApJ, 765, 34

Quénard, D., Jiménez-Serra, I., Viti, S., Holdship, J., & Coutens, A. 2018, MNRAS, 474, 2796

Rachid, M. G., Terwisscha van Scheltinga, J., Koletzki, D., & Linnartz, H. 2020, A&A, 639, A4

Raut, U. & Baragiola, R. A. 2011, ApJ, 737, L14

Rejoub, R., Lindsay, B. G., & Stebbings, R. F. 2002, Phys. Rev., 65, 042713

Roser, J. E., Vidali, G., Manicò, G., & Pirronello, V. 2001, ApJ, 555, L61

Ruaud, M. & Gorti, U. 2019, ApJ, 885, 146

Salinas, V. N., Hogerheijde, M. R., Mathews, G. S., et al. 2017, A&A, 606, A125

Sandford, S. A., Allamandola, L. J., Tielens, A. G. G. M., & Valero, G. J. 1988, ApJ, 329, 498

Schöier, F. L., van der Tak, F. F. S., van Dishoeck, E. F., & Black, J. H. 2005, A&A, 432, 369

Schriever, R., Chergui, M., & Schwentner, N. 1990, J. Chem. Phys., 93, 9206

Schutte, W. A., Boogert, A. C. A., Tielens, A. G. G. M., et al. 1999, A&A, 343, 966

Schutte, W. A., Tielens, A. G. G. M., Whittet, D. C. B., et al. 1996, A&A, 315, L333

Schwarz, K. R., Bergin, E. A., Cleeves, L. I., et al. 2016, ApJ, 823, 91

Shu, F. H., Adams, F. C., & Lizano, S. 1987, ARA&A, 25, 23

Simons, M. A. J., Lamberts, T., & Cuppen, H. M. 2020, A&A, 634, A52

Stief, L. J., Payne, W. A., & Klemm, R. B. 1975, J. Chem. Phys., 62, 4000

Swings, P. & Rosenfeld, L. 1937, ApJ, 86, 483

Taquet, V., López-Sepulcre, A., Ceccarelli, C., et al. 2015, ApJ, 804, 81

Taquet, V., Wirström, E. S., & Charnley, S. B. 2016, ApJ, 821, 46

Teague, R. 2019, The Journal of Open Source Software, 4, 1632

Teague, R., Henning, T., Guilloteau, S., et al. 2018, ApJ, 864, 133

Teague, R. & Loomis, R. 2020, ApJ, 899, 157

Terwisscha van Scheltinga, J., Ligterink, N. F. W., Boogert, A. C. A., van Dishoeck, E. F., & Linnartz, H. 2018, A&A, 611, A35

Testi, L., Birnstiel, T., Ricci, L., et al. 2014, in Protostars and Planets VI, ed. H. Beuther, R. S. Klessen, C. P. Dullemond, & T. Henning, 339

Thi, W. F., van Zadelhoff, G. J., & van Dishoeck, E. F. 2004, A&A, 425, 955

Tielens, A. G. G. M. 2013, Rev. Mod. Phys., 85, 1021

Tielens, A. G. G. M., Tokunaga, A. T., Geballe, T. R., & Baas, F. 1991, ApJ, 381, 181

Trapman, L., Bosman, A. D., Rosotti, G., Hogerheijde, M. R., & van Dishoeck, E. F. 2021, A&A, 649, A95

Trapman, L., Miotello, A., Kama, M., van Dishoeck, E. F., & Bruderer, S. 2017, A&A, 605, A69

Tudorie, M., Cacciani, P., Cosléou, J., et al. 2006, A&A, 453, 755

Turner, B. E. 1991, ApJS, 76, 617

Tychoniec, Ł., Manara, C. F., Rosotti, G. P., et al. 2020, A&A, 640, A19

van Broekhuizen, F. A., Groot, I. M. N., Fraser, H. J., van Dishoeck, E. F., & Schlemmer, S. 2006, A&A, 451, 723

van Broekhuizen, F. A., Keane, J. V., & Schutte, W. A. 2004, A&A, 415, 425

van der Marel, N., van Dishoeck, E. F., Bruderer, S., & van Kempen, T. A. 2014, A&A, 563, A113

van Dishoeck, E. F., Bergin, E. A., Lis, D. C., & Lunine, J. I. 2014, in Protostars and Planets VI, ed. H. Beuther, R. S. Klessen, C. P. Dullemond, & T. Henning, 835

van Gelder, M. L., Tabone, B., Tychoniec, Ł., et al. 2020, A&A, 639, A87

van 't Hoff, M. L. R., Tobin, J. J., Harsono, D., & van Dishoeck, E. F. 2018a, A&A, 615, A83

van 't Hoff, M. L. R., Tobin, J. J., Trapman, L., et al. 2018b, ApJ, 864, L23

van 't Hoff, M. L. R., Walsh, C., Kama, M., Facchini, S., & van Dishoeck, E. F. 2017, A&A, 599, A101

van't Hoff, M. L. R., Harsono, D., Tobin, J. J., et al. 2020, ApJ, 901, 166

Vasyunin, A. I., Caselli, P., Dulieu, F., & Jiménez-Serra, I. 2017, ApJ, 842, 33

Virtanen, P., Gommers, R., Oliphant, T. E., et al. 2020, Nature Methods, 17, 261

Visser, R., Doty, S. D., & van Dishoeck, E. F. 2011, A&A, 534, A132

Walsh, C., Loomis, R. A., Öberg, K. I., et al. 2016, ApJ, 823, L10

Walsh, C., Millar, T. J., Nomura, H., et al. 2014, A&A, 563, A33

Wang, Y., Du, F., Semenov, D., Wang, H., & Li, J. 2021, A&A, 648, A72

Wang, Y., Tennyson, J., & Yurchenko, S. N. 2020, Atoms, 8, 7

Watanabe, N. & Kouchi, A. 2002a, ApJ, 571, L173

Watanabe, N. & Kouchi, A. 2002b, ApJ, 567, 651

Watanabe, N., Mouri, O., Nagaoka, A., et al. 2007, ApJ, 668, 1001

Watanabe, N., Nagaoka, A., Shiraki, T., & Kouchi, A. 2004, ApJ, 616, 638

Weidenschilling, S. J. 1977, MNRAS, 180, 57

Werner, M. W., Roellig, T. L., Low, F. J., et al. 2004, ApJS, 154, 1

Wexler, A. 1967, Appl. Spectrosc. Rev., 1, 29

Whittet, D. C. B., Gerakines, P. A., Hough, J. H., & Shenoy, S. S. 2001, ApJ, 547, 872

Whittet, D. C. B., Goldsmith, P. F., & Pineda, J. L. 2010, ApJ, 720, 259

Wolszczan, A. & Frail, D. A. 1992, Nature, 355, 145

Wright, C. M., Do Duy, T., & Lawson, W. 2016, MNRAS, 457, 1593

Wright, G. S., Wright, D., Goodson, G. B., et al. 2015, PASP, 127, 595

Yang, Y.-L., Sakai, N., Zhang, Y., et al. 2021, ApJ, 910, 20

Yuan, C., Cooke, I. R., & Yates, John T., J. 2014, ApJ, 791, L21

Zhang, K., Bergin, E. A., Blake, G. A., Cleeves, L. I., & Schwarz, K. R. 2017, Nature Astronomy, 1, 0130

Zhang, S., Zhu, Z., Huang, J., et al. 2018, ApJ, 869, L47

Zins, E.-L., Joshi, P. R., & Krim, L. 2011, ApJ, 738, 175

NEDERLANDSE SAMENVATTING

Het is gemakkelijk om in de drukte van ons dagelijkse leven te vergeten hoe bijzonder onze aarde is. Een relatief kleine planeet die ongeveer 4,6 miljard jaar geleden is gevormd op de juiste afstand van de zon, en waar sindsdien alles precies zo is verlopen dat wij en elk ander levend wezen kunnen bestaan. Kijk je op een heldere nacht omhoog naar alle sterren die aan de hemel staan, dan stel je vrijwel automatisch de vraag, is de aarde de enige plek in het heelal waar leven is ontstaan? Inmiddels zijn er bijna 5000 exoplaneten ontdekt en weten we dat gemiddeld elke ster minstens één planeet heeft. Een zeer groot deel van deze planeten zal niet geschikt zijn voor leven of in ieder geval het leven zoals wij dat kennen. Dit komt omdat de temperatuur op het oppervlak veel te hoog of te laag is, of doordat de atmosfeer niet geschikt is, denk bijvoorbeeld aan giftige gassen of een te hoge druk. Echter, de hoeveelheid sterren in ons heelal is enorm groot. Het is daarom bijna niet denkbaar, dat er geen andere plek in ons universum is waar, net als op aarde, de fysieke en chemische omstandigheden ook ideaal zijn voor het ontstaan van leven.

Om tot een levend organisme te komen zijn er bepaalde organische bouwstenen nodig. Deze moleculen zijn nodig zodat organismes, eencellig en meercellig, kunnen overleven, gedijen, reproduceren en evolueren. Denk hierbij aan bouwstoffen zoals eiwitten, nucleïnezuren, koolhydraten en lipiden. De grote vraag is, zijn deze organische bouwstenen op aarde gevormd, of waren ze al aanwezig voordat planeten ontstonden? In het laatste geval zou dit kunnen betekenen dat het hele universum gevuld is met de bouwstenen van het leven.

In de laatste 100 jaar is ons begrip van de fysische en chemische processen in het universum significant verbeterd. Eerst dacht men dat onder de extreme condities in de ruimte, dat wil zeggen, zeer lage en zeer hoge temperaturen en intense stralingsvelden, moleculen maar moeizaam gevormd kunnen worden. Inmiddels zijn er meer dan 240 verschillende moleculen ontdekt! Een subgroep van deze moleculen zijn de zogenaamde complexe organische moleculen, ook wel COMs genoemd. Dit zijn moleculen met zes of meer atomen, waarvan minstens één een koolstof atoom is en één ander een zuurstof, stikstof, fosfor of zwavel atoom is. COMs zijn van bijzonder belang omdat zij de kleinere versie zijn van de hiervoor genoemde organische bouwstenen. Door COMs te bestuderen in de ruimte krijgen wij een beter beeld van hoe het leven is ontstaan op aarde, en dus mogelijk ook rondom andere sterren.

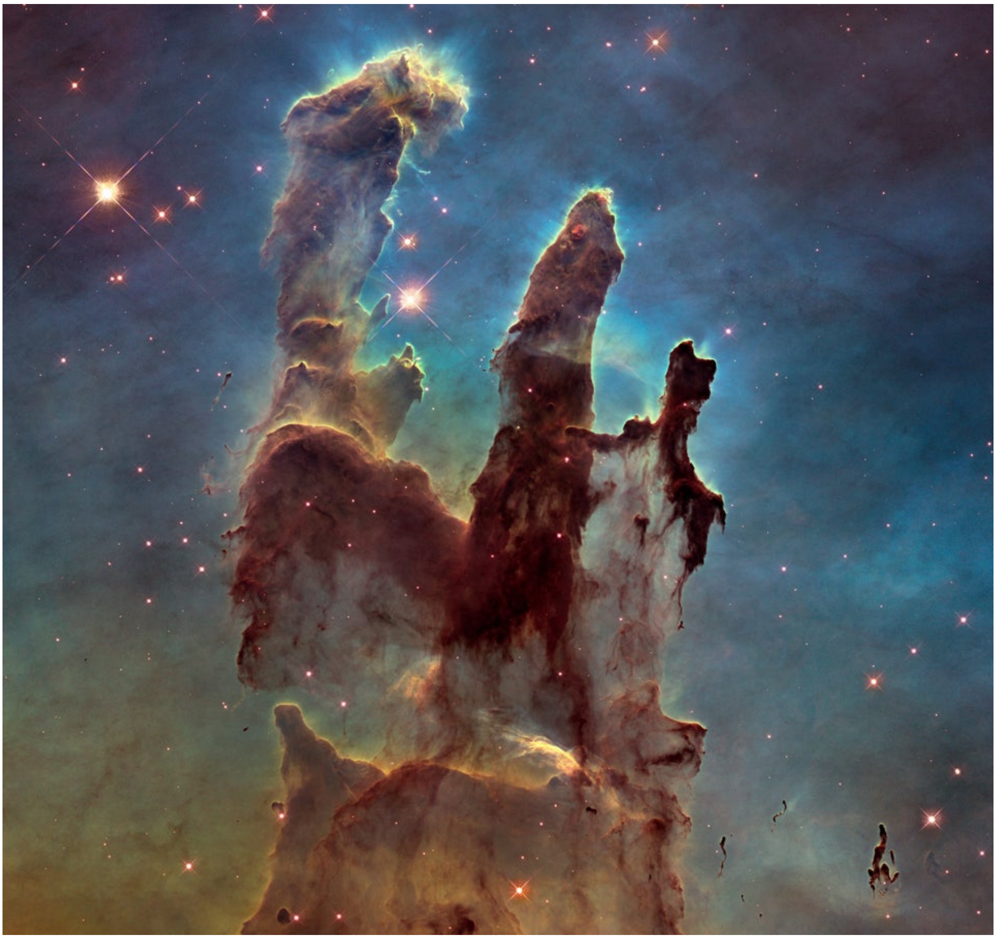

Figuur 1: De ‘Pilaren der Creatie’ die deel uitmaken van de Adelaarsnevel in het sterrenbeeld ‘de slang’, gezien door de *Hubble* ruimtetelescoop. Deze moleculaire wolken zijn donker omdat zij bestaan uit koud gas en stof dat licht van achtergelegen sterren tegenhoudt. De intense kleuren aan de randen van de wolk komen door de interactie van intense straling van nabij gelegen sterren met het stof en gas aan de buitenkant van de moleculaire wolken (Credit: ESA).

Hoe vormen sterren en planeten?

In verhouding tot de leeftijd van ons zonnestelsel worden nieuwe sterren en planeten relatief snel gevormd. Echter, dit proces duurt nog steeds enkele miljoenen jaren en start in een moleculaire wolk. Zo’n moleculaire wolk bestaat uit koud gas en stofdeeltjes, en is vele malen groter dan een planeetstelsel, zo’n 100.000 keer, en in deze wolk kunnen duizenden nieuwe sterren ontstaan. Een voorbeeld van zo’n wolk is de ‘Pilaren der Creatie’, zie Figuur 1. Het gas en stof in deze wolk is niet uniform verdeeld, en dus worden, onder invloed van hun eigen zwaartekracht, de dichte gebieden steeds dichter. Wanneer genoeg materiaal is samengetrokken in een gebied wordt dit een *prestellaire kern* genoemd. Uiteindelijk hoopt het materiaal in zo’n kern zich op rond het gravita-

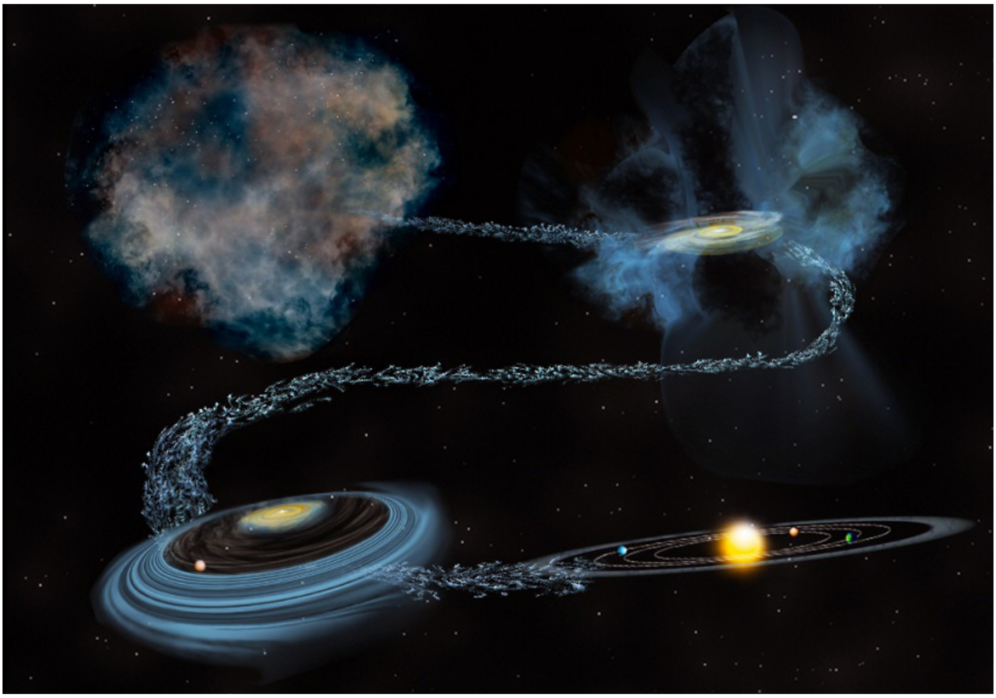

Figuur 2: Visualisatie van de evolutie van moleculaire wolk naar jong planetenstelsel. Een deel van een moleculaire wolk (linksboven) trekt samen onder zijn eigen zwaartekracht en begint uit het beschikbare materiaal een *protoster* en een kleine draaiende schijf te vormen (rechtsboven). Naarmate meer materiaal invalt op de *protoster* groeit ook de *protoplanetaire schijf* (linksonder). Uiteindelijk start kernfusie in de jonge ster en wordt het resterende gas en stof weggeblazen (rechtsonder). Wat overblijft zijn de planeten die in de *protoplanetaire schijf* zijn gevormd (Credit: Bill Saxton, NSF/AUI/NRAO).

tionele centrum en vormt het daar een puntbron, ook wel bekend als een *protoster*. Het initiële materiaal van de moleculaire wolk heeft een bepaald impulsmoment en dit moet worden behouden tijdens het vormen van een ster. Dit heeft tot gevolg dat er rondom de *protoster* een schijf van gas en stof ontstaat. Daarnaast stroomt ook materiaal weg van de *protoster*. Deze zogenaamde *jets* staan loodrecht op de schijf en werpen met hoge snelheden materiaal terug het *interstellaire medium* in. Op dit moment in het vormingsproces vindt er nog geen kernfusie plaats in de *protoster* en wordt het omliggende materiaal voornamelijk verwarmd door de gravitationele energie die vrijkomt bij het invallen van materiaal op de *protoster*. Naarmate meer van het omliggende materiaal invalt op de *protoster* neemt de massa en temperatuur toe en blijft er alleen nog een schijf van gas en stof over die om de protoster heen draait. Deze schijf wordt ook wel de *protoplanetaire schijf* genoemd, en het is in deze schijf waar van het resterende interstellaire manteriaal planeten worden gevormd. Uiteindelijk zal kernfusie van waterstof gaan plaats vinden in de ster en wordt de meerderheid van het stof en gas terug geblazen in het *interstellaire medium*. Het overgebleven materiaal wordt aangetrokken door de jonge planeten en zo vormt een jong planetenstelsel. Deze evolutie van moleculaire wolk naar een jong planetenstelsel is weergegeven in Figuur 2.

Astrochemie

Tot nu toe hebben wij vooral gekeken naar de fysische evolutie van materiaal op grote schaal, maar wat gebeurt er op moleculair niveau? Het gas in een wolk bestaat voornamelijk uit waterstof, maar bevat ook atomen zoals koolstof en zuurstof, en simpele moleculen zoals koolstofmonoxide (CO). De stofdeeltjes zijn klein, typisch een paar tienden tot enkele μm, en bestaan voornamelijke uit silicaten en koolstofhoudende moleculen zoals grafiet en polycyclische aromatische koolwaterstoffen. Door de dichtheid van het stof in de wolken wordt externe straling tegengehouden en daalt de temperatuur naar 10 K (-263 °C). De lage temperatuur van de stofdeeltjes zorgt ervoor dat gasfase deeltjes - atomen en moleculen - kunnen vastvriezen, waarbij een laagje ijs ontstaat. In dit laagje ijs vinden chemische reacties plaats die in de gasfase niet plaats vinden of veel minder efficiënt zijn. De reden hiervoor is dat de ijslaag niet alleen een molecuul reservoir is, maar ook fungeert als oppervlakte katalysator. De overtollige reactie energie wordt daarbij door het ijs geabsorbeerd en stabiliseerd het molecuul, iets wat, als gevolg van de lage dichtheden, in de gasfase veel moeilijker is.

Door toevoeging van atomen aan simpele moleculen kunnen verschillende nieuwe moleculen ontstaan, waaronder COMs. Ook invallende straling of vrije elektronen kunnen chemische reacties initiëren en zo nieuwe moleculen vormen. Gelijktijdig, kunnen UV fotonen of hoog geladen kosmische straling ook moleculen in het ijs uiteen laten vallen. De overgebleven radicalen zijn reactief en reageren dan met andere moleculen om zo tot grotere moleculen te komen. Om een voorbeeld te noemen, bij de zeer lage temperaturen in een donkere wolk, kunnen CO moleculen met waterstof atomen reageren die over een ijsoppervlak bewegen. Daarbij ontstaan formaldehyde (H_2CO) en methanol (CH_3OH). Vervolgens kan, door interactie met een UV foton, de binding tussen de methylgroep (CH_3) en hydroxylgroep (OH) in methanol gebroken worden. Het methylradicaal kan een reactie aangaan met een nabij gelegen hydroxymethyl (CH_2OH) radicaal, insgelijks gevormd door interactie tussen UV en methanol, en zo ethanol (CH_3CH_2OH) vormen. Een 'cruciaal' molecuul dat regelmatig door intelligent leven op aarde wordt genuttigd en het universum zit er vol mee. Op vergelijkbare manier worden ook andere organische bouwstenen als glycine (NH_2CH_2COOH, een aminozuur) en glycolaldehyde ($HOCH_2CHO$, het simpelste suiker) gevormd in radicaal molecuul reacties in en op de ijslagen van interstellaire stofdeeltjes.

Laboratorium en telescopen

Hoe weten wij eigenlijk dat deze organische bouwstenen gevormd worden in de vroege stadia van ster- en planeetformatie? Het is immers niet mogelijk om even langs te gaan en op locatie wat metingen te verrichten. Dit kan op verschillende manieren, namelijk door de chemie te bestuderen onder vergelijkebare omstandigheden in gespecialiseerde experimentele opstellingen, door met (ruimte)telescopen deze gebieden spectroscopisch te bestuderen of door middel van computersimulaties. In dit proefschrift zijn zowel telescopen en laboratorium opstellingen gebruikt, zie Figuur 3 en 4, om tot een beter begrip te komen van de processen die bepalend zijn voor de chemische evolutie.

Beide maken gebruik van spectroscopie en zijn gebaseerd op de interactie van licht met materie. Afhankelijk van het materiaal en de energie van een foton zijn er verschillende uitkomsten. Bijvoorbeeld, fotonen in het optische gebied worden gereflecteerd op wit papier, terwijl hetzelfde licht zal worden geabsorbeerd door zwart papier. Dit

Figuur 3: Foto van de Atacama Large Millimeter/submillimeter Array in de Atacama woestijn in Chili. Deze telescoop is gebruikt voor het werk gepresenteerd in hoofdstuk 5 (Credit: ESO/NAOJ/NRAO).

werkt niet alleen met zichtbaar licht, maar ook met infrarood en microgolf fotonen. Door de absorptie van een infrarood foton kunnen moleculen gaan trillen (vibreren), terwijl de absorptie van een microgolf foton ervoor zorgt dat een molecuul gaat draaien (roteren). Echter, een molecuul absorbeert niet willekeurig op elke golflengte fotonen, maar absorbeert alleen fotonen met golflengtes die kenmerkend zijn voor dat molecuul, een soort moleculaire vingerafdruk. Daarnaast kunnen moleculen ook fotonen uitzenden, en ook dit gebeurt bij specifieke golflengtes. Dit komt omdat moleculen liever geen overtallige energie hebben, en door fotonen uit te zenden raken zij deze energie kwijt. De verzameling van al die golflengtes wordt een spectrum genoemd en is uniek voor verschillende moleculen. Ken je het spectrum van een molecuul, dan kun je dit overal herkennen.

Astronomen gebruiken (ruimte)telescopen om spectra te meten van onder andere ster en planeet vormende gebieden. Uit deze spectra leiden zij dan af welke moleculen aanwezig zijn, en gelijktijdig wordt er informatie verkregen over eigenschappen zoals de temperatuur en de dichtheid van het materiaal. Deze informatie is belangrijk omdat het als vergelijkingsmateriaal wordt gebruikt met computersimulaties van zulke gebieden. Tijdens dit promotieonderzoek is onder andere gebruik gemaakt van de Atacama Large Millimeter/submillimeter Array (ALMA) telescoop, zie Figuur 3. De ALMA telescoop combineert 66 verschillende antennes om zo in het radio domein met hoge ruimtelijke en spectrale resolutie moleculen in de ruimte waar te nemen. ALMA is een interferometer. Dit betekent dat het geen directe afbeeldingen maakt van objecten, echter, elke antenne meet een signaal van het object aan de hemel met een fase en amplitude. Al deze losse signalen worden aan elkaar gekoppeld door middel van een *correlator*, en zo kan een beeld worden gereconstrueerd van het object dat is waargenomen. De kracht van ALMA is dat het deze reconstructies kan maken voor elke golflengte die het waarneemt. Moleculen rondom een jonge ster worden dan in beeld gebracht door naar frequenties te kijken die specifiek zijn voor een bepaald molecuul. Door deze moleculen in kaart te brengen, krijgen wij een beter beeld van de chemische inventaris en de fysische eigenschappen in jonge ster- en planeetvormende gebieden.

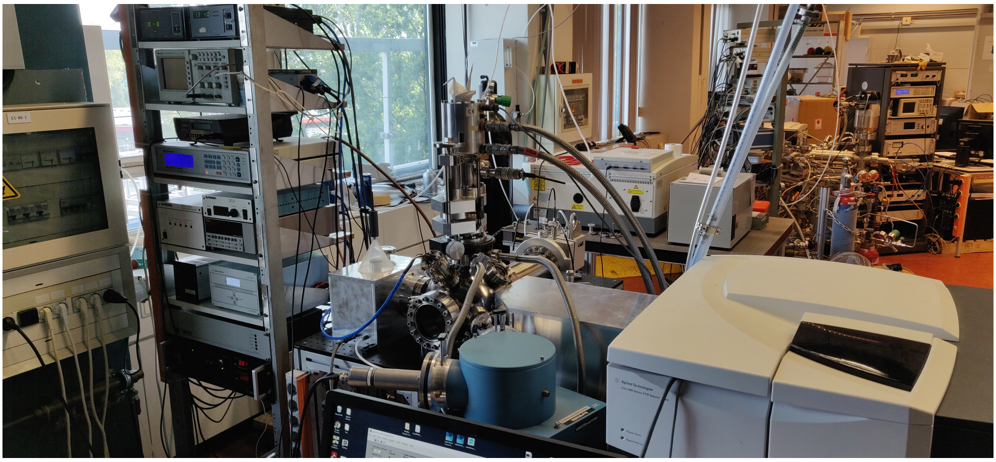

Figuur 4: Foto van de experimentele opstelling CryoPAD2 in het Laboratorium voor astrofysica van de Sterrewacht te Leiden.

In veel astrofysische laboratoria wordt spectroscopie gebruikt om te achterhalen welke processen plaats vinden onder astrofysische omstandigheden. In dit promotieonderzoek is voornamelijk infrarood spectroscopie toegepast om de vorming van moleculen in de vaste stof te onderzoeken en te kijken hoe verschillende moleculen invloed op elkaar uitoefenen in de vaste stof. Om moleculen in de vaste fase te krijgen onder astrofysische omstandigheden zijn gespecialiseerde opstellingen nodig. In het algemeen bestaan deze uit een roestvrij stalen kamer met daaraan de verschillende instrumenten gekoppeld. Deze kamer wordt tot extreem lage drukken ($< 10^{-10}$ mbar) gepompt door een turbomoleculaire pomp. Hierdoor is CryoPAD2 één van de leegste plekken van Nederland. Om dit te visualiseren, stel je voor dat het hele IJsselmeer volledig wordt geleegd en vervolgens gelijkmatig wordt gevuld met een halve liter water en niks anders. Daarnaast worden de moleculen in de opstelling gekoeld naar -258 °C, 15 °C boven het absolute nulpunt, hetgeen de temperatuur nabootst van de koude stofdeeltjes in de ruimte. Onder deze omstandigheden kan gecontroleerd onderzocht worden hoe moleculen elkaar beïnvloeden en hoe nieuwe moleculen vormen onder invloed van bestraling. Voor die bestraling wordt weer een speciale lamp gebruikt, die het ultraviolette licht nabootst zoals dat in de ruimte voorkomt. Uiteindelijk worden laboratorium, waarnemingen en simulaties samengevoegd om zo tot een beter inzicht te komen over beschikbaarheid van organische bouwstenen in ster- en planeetvormende systemen.

Conclusies van dit proefschrift

In dit proefschrift zijn stappen gezet naar een beter begrip van de interactie tussen (organische) moleculen in de gasfase en vaste stof tijdens de vorming van nieuwe sterren en planeten. Het is algemeen geaccepteerd dat de meeste COMs gevormd worden in de ijslagen op interstellaire stofdeeltjes. Tot op heden zijn vrijwel alle COMs alleen in de gasfase geïdentificeerd. Dit is deels een gevolg van het feit dat waarnemingen van gasfase spectra vele malen gevoeliger en molecuul specifiek uitgevoerd kunnen worden. Daarnaast is een meerderheid van deze gasfase COMs gedetecteerd in warmere gebieden waar de vaste stof moleculen zijn gesublimeerd. In koude gebieden is het nog steeds niet helemaal duidelijk hoe de transitie van ijs naar gas verloopt. Met de lancering van de *James Webb* ruimtetelescoop (JWST) komt hier verandering in. Deze infrarood ruimtetelescoop is vele malen gevoeliger dan zijn voorgangers en maakt het mogelijk om met grotere nauwkeurigheid ook ijs in de ruimte te bestuderen. Ter voorbereiding op toekomstige vaste stof waarnemeningen met de JWST zijn in hoofdstukken 3 en 4 infrarood ijs spectra gemeten van aceetaldehyde, dimethylether, ethanol en methylformiaat in de pure vorm, maar ook gemengd met astronomisch relevante moleculen. De uitgebreide karakterisatie in deze hoofdstukken vormt een sterke basis voor astronomen om uit de JWST spectra af te leiden welke COMs zich in het ijs bevinden. In de nabije toekomst zal deze informatie tot een beter beeld leiden van de organische ijs inventaris.

Het enige COM dat tot op heden wel is gedetecteerd in de vaste stof is methanol, en zoals eerder vermeld wordt methanol gevormd via hydrogenatie van CO op de stofdeeltjes in het ijs. Computersimulaties van een *protoplanetaire schijf* suggereren dat methanol in de vaste stof gedeeltelijk naar de gasfase zou moeten sublimeren. Echter, gasfase observaties van *protoplanetaire schijven* laten deze voorspelde hoeveelheid gasfase methanol niet zien. Om hier een beter beeld van te krijgen kan naar het tussenliggende product gekeken worden, namelijk formaldehyde (H_2CO). Gasfase formaldehyde is volop aanwezig in *protoplanetaire schijven*, echter, naast vorming in de vaste stof kan formaldehyde ook efficiënt gevormd worden in de gasfase. In hoofdstuk 5 zijn meerdere rotationele transities van gasfase formaldehyde met ALMA onderzocht. Uit de waarnemingen en analyse daarvan is de fysische structuur, de temperatuur en hoeveelheid formaldehyde gas in de *protoplanetaire schijf* van de jonge ster TW Hya berekend. Deze resultaten geven aanwijzingen dat het geobserveerde gasfase formaldehyde in TW Hya in de gasfase is gevormd, en dus waarschijnlijk niet chemisch gerelateerd is aan het proces dat methanol vormt in het ijs op de stofdeeltjes. Dit werk in TW Hya vormt een uitgangspunt voor een algemeen beter begrip van de oorsprong van formaldehyde in ster- en planeetvormende gebieden.

Tijdens de evolutie van een moleculaire wolk naar een jong planentenstelsel zijn er veel fysische en chemische processen die tegelijk plaats vinden en invloed op elkaar hebben. In het algemeen moet de temperatuur van een stofdeeltje lager zijn dan de sublimatietemperatuur van een molecuul om dit molecuul uit te laten vriezen op een stofdeeltje. In hoofdstuk 6 is onder astrofysische omstandigheden in het laboratorium onderzocht of er een reactie kan plaats vinden op het oppervlakte van water ijs, bestraald met UV fotonen, en gasfase CO. Daarbij is de temperatuur van het water ijs boven de sublimatietemperatuur van CO en kan het dus niet uitvriezen bovenop het water ijs. Uit de resultaten blijkt dat dit process plaats vindt en dit is interessant omdat het laat zien dat gasfase en vaste stof niet als geïsoleerd van elkaar gezien kunnen worden. De interactie tussen gasfase CO en UV bestraald water ijs produceert koolstofdioxide (CO_2) en heeft de potentie om te verklaren waarom in *protoplanetaire schijven* te weinig gasfase CO wordt gezien. Bovendien laten waarnemingen aan ijs in de ruimte zien dat een groot deel van het CO_2 ijs gemengd is met water ijs, terwijl CO ijs niet is gemengd met water ijs, ook dit is te verklaren met het bovenstaande proces.

De hoofd conclusies van dit proefschrift zijn als volgt:

- Om aceetaldehyde, dimethylether, ethanol en methylformiaat te detecteren met de JWST zijn de volgende infrarood absorptiebanden het meest gunstig: 7.427 en 5.803 μm banden voor aceetaldehyde, de 9.141 en 8.011 μm banden voor dimethylether, de 11.36 en 7.240 μm banden voor ethanol, en de 13.02 en 10.98 μm banden voor methylformiaat. Voor een robuste waarneming van één van deze moleculen zijn minstens twee absorptiebanden nodig en in de juiste verhoudingen met elkaar.

- Gasfase formaldehyde in ster- en planeetvormende gebieden heeft niet perse dezelfde chemische oorsprong als methanol, namelijk hydrogenatie van CO. De waarnemingen met ALMA rondom TW Hya laten zien dat de eigenschappen van het gasfase formaldehyde consistent zijn met een gasfase oorsprong.

- De interactie tussen gasfase CO en water ijs laat zien dat het niet alleen belangrijk is om te kijken naar de interactie tussen gas en stof op een fysische manier, maar ook chemische manier. Deze interactie is belangrijk omdat het mogelijk effect heeft op onze interpretatie van de hoeveelheid materiaal die aanwezig is voor planeetformatie.

- Tijdens de bestraling van water ijs is naar boven gekomen dat er minder hydroxylradicalen worden gevormd dan gedacht. Dit heeft twee mogelijke oorzaken, namelijk UV fotonen dissociëren water niet met een 100% efficiency of na dissocatie is de recombinatie van waterstof en het hydroxylradicaal efficiënter.

De resulataten die in dit proefschrift zijn gepresenteerd vormen een sterke basis voor ijsobservaties van complexe organische moleculen en dragen bij aan het in kaart brengen van de organische inventaris in ster- en planeetvormende gebieden door de spectra aan te leveren die nodig zijn voor waarnemingen met de JWST. Verder wordt aangetoond dat het voor gasfase formaldehyde mogelijk is om te achterhalen of dit zijn oorsprong vindt in de gasfase of de vaste stof. Tenslotte is experimenteel voor een eerste keer systematisch gekeken naar de wisselwerking tussen gasfase CO en water ijs en het is gebleken dat dit een nieuw reactiekanaal biedt naar CO_2. Mogelijk is hetzelfde mechanisme actief in andere reacties en dit zal dan van belang zijn om toekomstige modellen verder te verbeteren.

PUBLICATIONS

Refereed publications

1. *Quantification of O_2 formation during UV photolysis of water ice - H_2O and H_2O:CO_2 ices*
   Bulak, M., Paardekooper, D.M., Fedoseev, G., Chuang, K.-J., **Terwisscha van Scheltinga, J.**, Eistrup, C., and Linnartz, H. 2021, accepted for publication in Astronomy & Astrophysics.

2. *Infrared spectra of complex organic molecules in astronomically relevant ice matrices. III. Methyl formate and its tentative solid-state detection*
   Terwisscha van Scheltinga, J., Marcandalli, G., McClure, M.K., Hogerheijde, M.R., Linnartz, H. 2021, Astronomy & Astrophysics, 651, A95.

3. *An inherited complex organic molecule reservoir in a warm planet-hosting disk*
   Booth, A.S., Walsh, C., **Terwisscha van Scheltinga, J.**, van Dishoeck, E.F., Ilee, J.D., Hogerheijde, M.R., Kama, M., Nomura, H. 2021, Nature Astronomy, 5. 684-690.

4. *The TW Hya Rosetta Stone Project. IV. A hydrocarbon-rich disk atmosphere*
   Cleeves, L.I., Loomis, R.A., Teague, R., Bergin, E.A., Wilner, D.J., Bergner, J.B., Blake, G.A., Calahan, J.K., Cazzoletti, P., van Dishoeck, E.F., Guzmán, V.V., Hogerheijde, M.R., Huang, J., Kama, M., Öberg, K.I., Qi, C., **Terwisscha van Scheltinga, J.**, Walsh, C. 2021, The Astrophysical Journal, 911, 29.

5. *The TW Hya Rosetta Stone Project. III. Resolving the gaseous thermal profile of the disk*
   Calahan, J.K., Bergin, E.A., Zhang, K., Teague, R., Cleeves, L.I., Bergner, J.B., Blake, G.A., Cazzoletti, P., Guzmán, V.V., Hogerheijde, M.R., Huang, J., Kama, M., Loomis R.A., Öberg, K.I., Qi, C., van Dishoeck, E.F., **Terwisscha van Scheltinga, J.**, Walsh, C., Wilner D.J. 2021, The Astrophysical Journal, 908, 8.

6. *The TW Hya Rosetta Stone Project. II. Spatially resolved emission of formaldehyde hints at low-temperature gas-phase formation*
   Terwisscha van Scheltinga, J., Hogerheijde, M.R., Cleeves, L.I., Loomis, R.A., Walsh, C., Öberg, K.I., Bergin, E.A., Bergner, J.B., Blake, G.A., Calahan, J.K., Cazzoletti, P., van Dishoeck, E.F., Guzmán, V.V., Huang, J., Kama, M., Qi, C., Teague, R., Wilner, D.J. 2021, The Astrophysical Journal, 906, 111.

7. *The TW Hya Rosetta Stone Project. I. Radial and vertical distributions of DCN and DCO^+*
Öberg, K.I., Cleeves, L.I., Bergner, J.B., Cavanaro, J., Teague, R., Huang, J., Loomis, R.A., Bergin, E.A., Blake, G.A., Calahan, J.K., Cazzoletti, P., Guzmán, V.V., Hogerheijde, M.R., Kama, M., **Terwisscha van Scheltinga, J.**, Qi, C., van Dishoeck, E.F., Walsh, C., Wilner, D.J. 2021, The Astronomical Journal, 161, 38.

8. *Infrared spectra of complex organic molecules in astronomically relevant ice mixtures. II. Acetone*
Rachid, M.G., **Terwisscha van Scheltinga, J.**, Koletzki, D., Linnartz, H. 2020, Astronomy & Astrophysics, 639, A4.

9. *Effect of molecular structure on the infrared signatures of astronomically relevant PAHs*
Bouwman, J., Castellanos, P., Bulak, M., **Terwisscha van Scheltinga, J.**, Cami, J., Linnartz, H., Tielens, A.G.G.M. 2019, Astronomy & Astrophysics, 621, A80.

10. *The formation of peptide-like molecules on interstellar dust grains*
Ligterink, N.F.W., **Terwisscha van Scheltinga, J.**, Taquet, V., Jørgensen, J.K., Cazaux, S., van Dishoeck, E.F., Linnartz, H. 2018, Monthly Notices of the Royal Astronomical Society, 480, 3.

11. *Methanol ice co-desorption as a mechanism to explain cold methanol in the gas-phase*
Ligterink, N.F.W., Walsh, C., Bhuin, R.G., Vissapragada, S., **Terwisscha van Scheltinga, J.**, Linnartz, H. 2018, Astronomy & Astrophysics, 612, A88.

12. *Infrared spectra of complex organic molecules in astronomically relevant ice matrices. I. Acetaldehyde, ethanol, and dimethyl ether*
Terwisscha van Scheltinga, J., Ligterink, N.F.W., Boogert, A.C.A., van Dishoeck, E.F., Linnartz, H., 2018, Astronomy & Astrophysics, 611, A35.

Submitted publications

1. *Formation of CO_2 through consumption of gas-phase CO on vacuum-UV irradiated water ice*
Terwisscha van Scheltinga, J., Ligterink, N.F.W., Bosman, A.D., Hogerheijde, M.R., Linnartz, H. Submitted to Astronomy & Astrophysics.

2. *Ice Age: Chemo-dynamical modeling of Cha-MMS1 to predict new solid-phase species for detection with JWST*
Jin, M., Lam K.H., McClure, M.K., **Terwisscha van Scheltinga, J**, Li, Z.-Y., Boogert, A.C.A., Herbst, E., Davis, S.W., Garrod, R.T. Submitted to The Astrophysical Journal.

CURRICULUM VITAE

My first independent breath of air was on Wednesday the 26th of December 1990. When growing up, my father made and repaired as much as possible by himself. It is thus no surprise that I as kid always wanted to take things apart and see how they worked. This was a great clue that I should become a scientist, but my ambitions as a kid were different, I wanted to build houses.

During my time at high school there was not much that grabbed my attention and I decided that academia was not for me, oh the irony. One thing that I did enjoy during that time was working on my moped. Taking it apart, repairing it, and making it go faster. Sorry mom, it went a lot faster than I said. This interest in mechanics and electronics lead to me enrolling at the "Vak Technische Opleidings Centrum *Fokker*". Here I was trained in the craft of maintaining, troubleshooting, and repairing avionic aircraft systems. As a follow-up of this training I joined the Royal Netherlands Air Force, but that part of my career was rather short as I quickly realized it was not for me. At that time I was 21 and the commercial aviation industry was in a depression, which meant no one was hiring and left me with the question what do I do now?

Having become slightly more mature since high school and having regained some of my curiosity about wanting to know how stuff works, I decided to continue studying. After a chat with the study advisor of Applied Physics, Nico van der Houwen at the Haagse Hogeschool, I was convinced that I wanted to be an engineer. I finished the first year cum laude, but was caught off guard when I got offered a job at a company at which I initially applied. I decided to take the job at AAR Aircraft Component Services. Here I learned to work with electronics at the component level and repair automatic pilot, navigation, and communication systems. However, after a year it no longer satisfied my curiosity and I went back to Applied Physics at the Haagse Hogeschool.

For my internship I got the opportunity to work at ESA-ESTEC with Olivier Witasse and Fabrice Cipriani. This was for me the first exposure to an academic environment and I truly enjoyed it. I worked on a Direct Simulation Monte Carlo model in which the effects of Mars and Solar wind on the regolith of Phobos were simulated. This project left me wanting more and in my final year of Applied Physics I asked my graduation project coordinator, Arjan Lock, if he knew a place where I could dip my toes in the academic world. He got me in touch with Prof. Harold Linnartz of the then Sackler Laboratory of Astrophysics at Leiden University. Impressed with all the scientific equipment and the big questions at play there was no doubt for me, this was the place for me. I wrote my thesis on the characterization of vibrational spectra of ethanol in pure form and astronomically relevant ice matrices. After this, I joined the group as a research assistant to expand my work and prepare it for a scientific publication. I contemplated getting a masters degree in astronomy, but decided that student life was no longer for me and it was time for me to look for a full-time job. This decision did not align with the plan Harold had for me. I remember vividly sitting in his office when I got the question, would you like to start a PhD with me and Michiel Hogerheijde? How could I say no to a once in a life-time opportunity? Arranging the paper work for this unusual situation was going to take some time, and I decided to travel through Southeast Asia in the mean time. On the 7th of June 2017 the plane I was in landed in Hanoi Vietnam and unsuspectingly I turned off airplane mode. Filled with joy, and a bit of disbelief, I read that within a month I would be a scientist who would work on improving the general knowledge about molecules during star and planet formation.

In the four years of my PhD, I worked on the experimental devices CryoPAD2 and HV setup, both cryogenic setups that exploit Fourier transform infrared spectroscopy. Additionally, the CryoPAD2 setup has a quadrupole mass spectrometer and microwave-discharge hydrogen-flow lamp. This allows for investigation of photoprocesses in analogue interstellar ices. Part of my PhD consisted of working with data from the Atacama Large Millimeter/submillimeter Array. This data was part of a large collaboration, the "TW Hya Rosetta Stone" project. As part of this project, I visited the University of Virginia and the National Radio Astronomy Observatory in Charlottesville Virginia. The experimental and observational research in this thesis has been presented during conferences and visits in The Netherlands, The United Kingdom, Italy, and the United States of America. During my time in the Laboratory for Astrophysics I have supervised three students (Giulia Marcandalli, Daniel Koletzki, and Stefan van der Giessen) and was mentor to two PhD students (Marina G. Rachid and Tara Bründl). Additionally, I was the teaching assistant for the master colloquia in which I supervised MSc students in presenting their work. After the defense of my thesis, I will continue as a VICO fellow at the University of Virginia in Charlottesville.

ACKNOWLEDGEMENTS

Although I am the author of this book, non of it would have been written without the trust and support of many people along the way. It is easy to forget how much small things matter. Asking someone to join for a coffee or lunch, listening to their struggles, racing a piece of furniture around the top floor of a building, or just a simple smile. For everyone who did that for me, thank you.

I feel very fortunate to have received the opportunity to pursue a PhD. I am especially grateful to Harold Linnartz and Michiel Hogerheijde who believed that I could succeed without the standard prerequisites. You stuck your necks out for me and this has swayed my life into a direction I could never have imagined. Thank you for all the supervision and patience, and Michiel, I promise that one day I will write the conclusion at the beginning of the paragraph.

Another person who played a fundamental role in my PhD is Niels Ligterink. He supervised me as a BSc student, but was also a great PhD mentor who taught me the ropes of astrochemistry and CryoPAD2. Even after you left to Bern, you were always available for scientific sparring and helping me wrap my head around the mind-boggling struggles that come with a PhD. For the majority of my PhD I have been roomies with Michał Bulak. It was great to have someone to share laboratory struggles with, but also boerenkool with way too much mustard or a good party. Thank you for all the fun and your patience, zapiekanka. Alex, Arthur, Leon, and Merel, you have supported me tremendously. No question was too silly, and (remarkably) no borrel conversation was too weird for you.

No (laboratory) PhD student survives without technical support. I would like to thank David, Eric, Erik, Huib, and Leonardo for all their IT support over the years. However, there is one person from IT who I would like the give a special thanks, Aart Vos. Besides the countless times he helped me or ordered parts for me, he also taught me a great deal in "practical" skills, for example, moving a 5 meter long wooden crate through two university buildings and up five floors. It was not easy, but we managed. A je to! How many golfers does it take to change a light bulb? FORE! If you want more jokes like this, Aart is a great supplier. Martijn Witlox, where would I have been without your mechanical support. Always ready to fix the mess we create in the lab or thinking of ways in which we can improve our science. You are truly a master of scientific machining. Peter van Veldhuizen and Raymond Koehler, thank you for all the electronic support, and trusting me with your precious equipment so that I could figure it out by myself.

Through the years I have worked with many people in the Laboratory for Astrophysics at Leiden Observatory. Andreas, Carlos, Daniel P., Danna, Old Gregg, Gleb, Gwen, Helgi, Jerry, Jiao, Jordy, Julia, Kirstin, Ko-Ju, Marina, Michał, Morgan, Nicolas, Niels, Pablo, Pranjal, Radha, Sanjana, Sergio, Tara, Thanja, Vincent, Will,

Xavier, and Yu thank you for all the enlightening conversation, the games of dominoes, and drinks.

Besides working in the laboratory, I have also worked with ALMA in the group of Michiel. Eva, Leon, Mason, and Vachail (Nico), thank you for all the support and making a lab rat feel welcome in the world of ALMA. I would also like to thank Ewine van Dishoeck who welcomed me in her group meetings and retreats. I have learned a tremendous amount about star and planet formation through those interactions. Alex, Alice, Alvaro, Andres, Anna M., Ardjan, Arthur, Benoit, Christian, Daniel H., Giovanni, Leon, Lisa, Lucas, Łukasz, Margot, Martijn, Melissa, Merel, Nadia, Paolo, Pooneh, Sierk, and Teresa thank you for always being patience and explaining the trivial and nontrivial gaps in my knowledge. I have also had the pleasure to be part of the ALMA collaboration "TW Hya Rosetta Stone" project. This project was lead by Ilse Cleeves and I am very grateful I was able to join. The data reduction was far from standard, but with the help of the ARC node Allegro and Ryan Loomis a beautiful data set was created. The entire team has made my first adventure with ALMA a great success and they have taught me a lot. It gave me the nudge to aspire an academic career, and I could not have been happier when Ilse told my I could join her group as a VICO fellow to work with her. See you soon!

A special mention to Anna G., Dario, Dilovan, Fraser, Kirsty, Lýdia, and Mantas. We did not work together scientifically, but I sure had a lot of fun at or outside of work with you, thank you! Last, but certainly not least, I would like to thank all of my friends outside academia and family who have supported me over the last years and told me "You can do this".